DOCTOR OF PHILOSOPHY

Semiconductor Devices for Generating Terahertz Radiation

Roberts, Daniel

Award date:
2016

Awarding institution:
Bangor University

Semiconductor Devices for Generating Terahertz Radiation

Daniel Rhys Griffin Roberts

PRIFYSGOL
BANGOR
UNIVERSITY

A thesis submitted for the degree of

Doctor of Philosophy

School of Electronic Engineering

Bangor University

July 2016

Declaration and Consent

Details of the Work

I hereby agree to deposit the following item in the digital repository maintained by Bangor University and/or in any other repository authorized for use by Bangor University.

Author Name: Daniel Rhys Griffin Roberts

Title: Semiconductor Devices for Generating Terahertz Radiation

Supervisor/Department: Dr. Iestyn Pierce / School of Electronic Engineering

Funding body (if any): Coleg Cymraeg Cenedlathol

Qualification/Degree obtained: PhD

This item is a product of my own research endeavours and is covered by the agreement below in which the item is referred to as "the Work". It is identical in content to that deposited in the Library, subject to point 4 below.

Non-exclusive Rights

Rights granted to the digital repository through this agreement are entirely non-exclusive. I am free to publish the Work in its present version or future versions elsewhere.

I agree that Bangor University may electronically store, copy or translate the Work to any approved medium or format for the purpose of future preservation and accessibility. Bangor University is not under any obligation to reproduce or display the Work in the same formats or resolutions in which it was originally deposited.

Bangor University Digital Repository

I understand that work deposited in the digital repository will be accessible to a wide variety of people and institutions, including automated agents and search engines via the World Wide Web.

I understand that once the Work is deposited, the item and its metadata may be incorporated into public access catalogues or services, national databases of electronic theses and dissertations such as the British Library's EThOS or any service provided by the National Library of Wales.

I understand that the Work may be made available via the National Library of Wales Online Electronic Theses Service under the declared terms and conditions of use (http://www.llgc.org.uk/index.php?id=4676). I agree that as part of this service the National Library of Wales may electronically store, copy or convert the Work to any approved medium or format for the purpose of future preservation and accessibility. The National Library of Wales is not under any obligation to reproduce or display the Work in the same formats or resolutions in which it was originally deposited.

Statement 1:

This work has not previously been accepted in substance for any degree and is not being concurrently submitted in candidature for any degree unless as agreed by the University for approved dual awards.

Signed …….. (candidate)

Date ……..

Statement 2:

This thesis is the result of my own investigations, except where otherwise stated. Where correction services have been used, the extent and nature of the correction is clearly marked in a footnote(s).

All other sources are acknowledged by footnotes and/or a bibliography.

Signed …….. (candidate)

Date ……..

Statement 3:

I hereby give consent for my thesis, if accepted, to be available for photocopying, for inter-library loan and for electronic storage (subject to any constraints as defined in statement 4), and for the title and summary to be made available to outside organisations.

Signed …….. (candidate)

Date ……..

NB: Candidates on whose behalf a bar on access has been approved by the Academic Registry should use the following version of **Statement 3:**

Statement 3 (bar):

I hereby give consent for my thesis, if accepted, to be available for photocopying, for inter-library loans and for electronic storage (subject to any constraints as defined in statement 4), after expiry of a bar on access.

Signed …… (candidate)

Date ……

<u>Statement 4</u>:

Choose **<u>one</u>** of the following options

a) I agree to deposit an electronic copy of my thesis (the Work) in the Bangor University (BU) Institutional Digital Repository, the British Library ETHOS system, and/or in any other repository authorized for use by Bangor University and where necessary have gained the required permissions for the use of third party material.	
b) I agree to deposit an electronic copy of my thesis (the Work) in the Bangor University (BU) Institutional Digital Repository, the British Library ETHOS system, and/or in any other repository authorized for use by Bangor University when the approved **bar on access** has been lifted.	
c) I agree to submit my thesis (the Work) electronically via Bangor University's e-submission system, however I **opt-out** of the electronic deposit to the Bangor University (BU) Institutional Digital Repository, the British Library ETHOS system, and/or in any other repository authorized for use by Bangor University, due to lack of permissions for use of third party material.	

Options B should only be used if a bar on access has been approved by the University.

In addition to the above I also agree to the following:

1. That I am the author or have the authority of the author(s) to make this agreement and do hereby give Bangor University the right to make available the Work in the way described above.

2. That the electronic copy of the Work deposited in the digital repository and covered by this agreement, is identical in content to the paper copy of the Work deposited in the Bangor University Library, subject to point 4 below.

3. That I have exercised reasonable care to ensure that the Work is original and, to the best of my knowledge, does not breach any laws – including those relating to defamation, libel and copyright.

4. That I have, in instances where the intellectual property of other authors or copyright holders is included in the Work, and where appropriate, gained explicit permission for the inclusion of that material in the Work, and in the electronic form of the Work as accessed through the open access digital repository, *or* that I have identified and removed that material for which adequate and appropriate permission has not been obtained and which will be inaccessible via the digital repository.

5. That Bangor University does not hold any obligation to take legal action on behalf of the Depositor, or other rights holders, in the event of a breach of intellectual property rights, or any other right, in the material deposited.

6. That I will indemnify and keep indemnified Bangor University and the National Library of Wales from and against any loss, liability, claim or damage, including without limitation any related legal fees and court costs (on a full indemnity bases), related to any breach by myself of any term of this agreement.

Signature: …… Date : ……..

Abstract

Semiconductor Devices for Generating Terahertz Radiation

This thesis will investigate different methods for realizing terahertz (THz) radiation. The work will look at the current state of the art in technologies for generating THz radiation using two types of semiconductor laser diodes, the vertical-cavity surface-emitting laser (VCSEL), and the vertical-external-cavity surface-emitting laser (VECSEL).

The work starts by looking at designing a dual-wavelength laser inspired by work presented in the literature; with particular emphasis on reducing the wavelength spacing between the two wavelengths and improving the positions of the quantum-wells (QW) in order to reduce the residual absorption in the QWs. This naturally leads on to investigations into the effects of linewidth, and linewidth enhancement, on the performance of the device. It is found that linewidth enhancement is not a limiting factor in the design of dual-wavelength lasers.

The thesis will then investigate the technique of injection locking, simulated by rate equations, in order to investigate, in detail, the various behavioural regions exhibited by such a scheme under varying injection rates and detuning frequencies. The scheme will consist of a two laser system approach, whereby both unidirectional and bidirectional injection locking will be investigated. The disadvantage to such a scheme is the fact that there will be a zero frequency separation between the lasers frequencies while operating in the locked condition, hence the injection locking scheme will provide a building block for a three laser locking system based on four-wave mixing (FWM).
The interest in injection locking has been proven to be of great interest in the world of optics, ever since the Dutch scientist, Christiaan Huygens, discovered the phenomenon while confined to bed with illness during the 17th century. Such an approach has shown to be durable and efficient in improving the spectral and dynamic performance of directly modulated laser diodes.

The scheme of injection locking will be utilized in order to build a system based on the FWM phenomenon with a nonzero frequency separation between the lasers' frequencies. As with the injection locking scheme, the various behavioural patterns at varying injection rates and detuning frequencies will be thoroughly investigated. The resilience of the system to perturbations (modulation response) will then be investigated, and the performance of the three laser FWM system will be

compared to that of an uncoupled laser, whereby the phasor difference between the first and the second laser is calculated. The amplitude of the resultant wave is then compared to the amplitude of the uncoupled wave in order to establish whether or not the three laser FWM system supresses any of the introduced perturbations. It is found that the more the injection rate is increased, the more the FWM system supresses the effect of the perturbations, where a maximum improvement of 44% over the uncoupled laser is observed. It is also found that the system shows the behaviour of a first order system in series with a second order system in its frequency response.

The contributions made in this thesis include a new dual-wavelength VECSEL structure design, whereby the wavelength spacing between the two wavelengths has been significantly reduced, and the locations of the QWs have been improved.

Also, a system has been modelled utilising the injection locking scheme, in order to produce a nonzero frequency difference between the coupled lasers. For the first time, a thorough investigation of the locking regions has been undertaken at varying injection rates and detuning frequencies, whereby the different behaviours exhibited by the system in each region has been explored. A detailed investigation on the resilience of this new system to introduced perturbations is also presented.

Contents

List of Figures

List of Tables

Acknowledgements

It has been a great pleasure, and most memorable experience, pursuing a PhD at the School of Electronic Engineering at Bangor University over the past four years.

I would firstly like to extend a wholeheartedly thank you to my PhD supervisor, Dr. Iestyn Pierce, for his continued support and guidance from the start of this experience. The countless hours of discussions, support and encouragement have been invaluable throughout my PhD study and research. His guidance has helped me throughout the whole project, and I could not have imagined having a better advisor and mentor for my PhD research.

I would also like to extend my gratitude to the Coleg Cymraeg Cenedlaethol for awarding me a PhD scholarship, and the opportunity to conduct a PhD at Bangor University. I would also like to thank them for not only providing me with the opportunity to conduct a PhD, but also for the opportunity to do so through the medium of Welsh, the first of which to be undertaken at the School of Electronic Engineering. I would also like to thank Gwerddon, for providing me with the opportunity to publish my work through the medium of Welsh. Diolch yn fawr iawn i chi i gyd!

Finally, and by no means least, I would like to thank my family, who have been there from the beginning, not only while pursuing a PhD, but from starting my undergraduate degree at Bangor University back in 2008. Without them guiding me towards the path of electronic engineering, I wouldn't have been here in the first place, and for that, I will be forever grateful.

CHAPTER ONE

INTRODUCTION

Semiconductor lasers have been at the forefront of our daily lives over the past two decades, and many of us use them unknowingly on a regular basis. They have established their place in modern laser technology, and have a greater variety of applications than any other type of laser. Such applications include CD & DVD drives, optical memory, laser printers, barcode readers, optical computer components, medical imaging, and even for some cancer treatments. When compared to solid state or gas lasers, semiconductor lasers have many advantages, including relatively high efficiency, their remarkably small size, their low cost, and their ease of use.

1.1 – The History of the Laser

The laser, which appears today in so many applications, developed from the maser; first published in two papers by Charles Townes *et al*. in the *Physical Review* in 1954 and 1955 [1], [2]. The term maser stands for 'microwave amplification by stimulated emission of radiation', and such a device depended upon the theoretical discovery made by Albert Einstein almost 40 years previously; known today as stimulated emission. In 1916, Albert Einstein had derived the theoretical existence of stimulated emission; this is the process by which electromagnetic waves, travelling at the right frequency, are able to 'stimulate' an excited atom, or a molecule, to fall from a higher energy state to a lower energy state, and hence emit more waves as a result [3]. Willis Lamb and Robert Retherford of Columbia University in New York, successfully used the stimulated emission phenomenon in order to amplify the radiation emitted by hydrogen molecules [3], [4]. This was performed in order to improve the measurement efficiency of the frequency from a specific molecular transition [3], [4].

Charles Townes saw a way to take this further, due to his background and experience in microwave engineering. He figured that if he could assemble a population of excited molecules in a cavity built to the right dimensions, then the radiation that would be emitted by some of these molecules would reflect back into the cavity, and interact with other molecules, causing the phenomenon of stimulated emission to increase. He believed that the 'feedback loop' between the molecules and the cavity would amplify the signal substantially [3].

Townes *et al*. successfully built the first maser in 1954 [1], where they sent a beam of excited ammonia molecules into a resonant cavity. They saw that the emission became self-sustaining as radiation from the molecules in the cavity would stimulate further radiation from the supply of excited molecules

that were continuously being renewed within the cavity [3]. Once Townes had proven his device would work, many other scientists went about replicating his work, and applying variations upon it. In the Bell Laboratories of New Jersey in 1958, Charles Townes and Arthur Schawlow proposed a system that would work at infrared and optical wavelengths [5]. It was not until two years later, in 1960, where the first experimental observation of light amplification by stimulated emission of radiation (LASER) was realized by Theodore Maiman [6].

Ever since the introduction of the first laser, many groups set out to experiment with this 'new' type of technology; testing its abilities and attempting to enhance its performance. In 1960 and 1961, Bernard *et al*. [7] and Pankove *et al*. [8] reported the effects of radiative recombination in semiconductors, which was quickly followed by Nathan *et al*. and Hall *et al*. demonstrating the use of GaAs p-n junctions to create coherent light emission from semiconductors in 1962 [9]-[11]. From here on in, extensive work and research has been carried out in order to enhance and develop the laser diode design to enable the devices to be used in such a broad number of applications.

1.2 – The Semiconductor Laser Diode

In a conventional semiconductor laser, the amplifying element is the forward biased p-n junction. This has been formed in a direct-bandgap semiconductor, where there is an active layer sandwiched between two cladding layers. Optical gain is provided to the laser through the recombination of holes and electrons within the p-n junction, and when the semiconductor laser is forward biased, the electrons will be injected from the n side of the junction, whereas the holes will be injected from the p side of the junction. Current is injected into the p-n junction via a metal strip contact where population inversion will take place between the valence and conduction bands. A resonator will continually recirculate the light within the semiconductor, and is therefore responsible for the very coherent output that is inherent in semiconductor laser diodes. Generally, the resonator will include a waveguide that confines the light two dimensionally, it will hence travel back and forth along a mostly linear path. The resonator is bound by mirrors, formed in the simplest devices by cleaving facets at either end of the waveguide, and this is where the light from the laser is emitted. Such a laser is known as an edge-emitting laser, and most of which that contain a resonator composed of two plane-parallel mirrors are known as Fabry Pérot resonators; most conventional lasers are of this type. A schematic of an edge emitting laser can be found in figure 1.1.

In semiconductor lasers, there are two different ways of forming the active layer; either by using a single heterostructure, or double heterostructure (DH) scheme [12]. In a single heterostructure semiconductor laser, the active layer material will be different to that of the cladding layer, and the thickness of the layer is chosen to either produce so called bulk ($\sim$ 100nm), or quantum-well (5-10nm)

structures [13]. Quantum-well lasers will be analysed for part of the work in this thesis. An illustration of a heterostructure laser diode can be seen in figure 1.1.

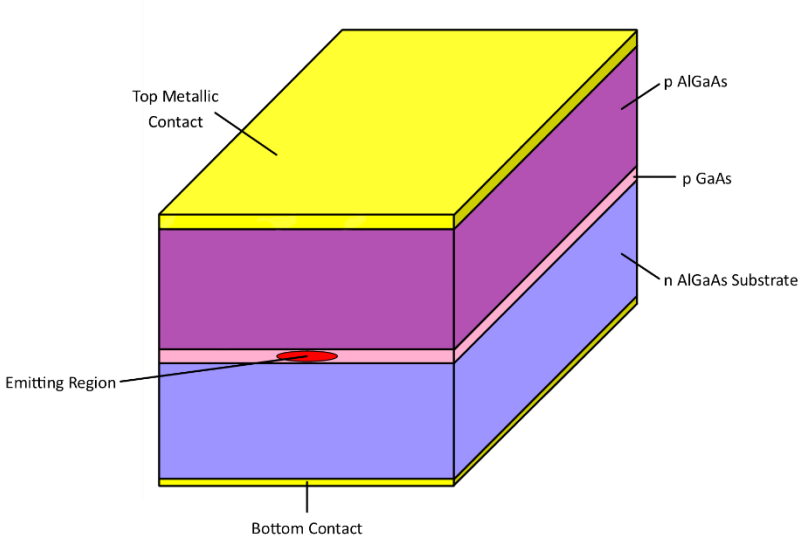

Figure 1.1: *Schematic layer structure of a Heterostructure laser diode.*

Room temperature operation of a DH laser was observed in 1970 by Hayashi *et al*. [14]. In a double heterostructure (DH) laser, a layer of low bandgap material is sandwiched between two high band gap layers. This creates two heterojunctions, as the actual materials are different and not just the same material with different types of doping. An example of a DH laser diode is illustrated in figure 1.2.

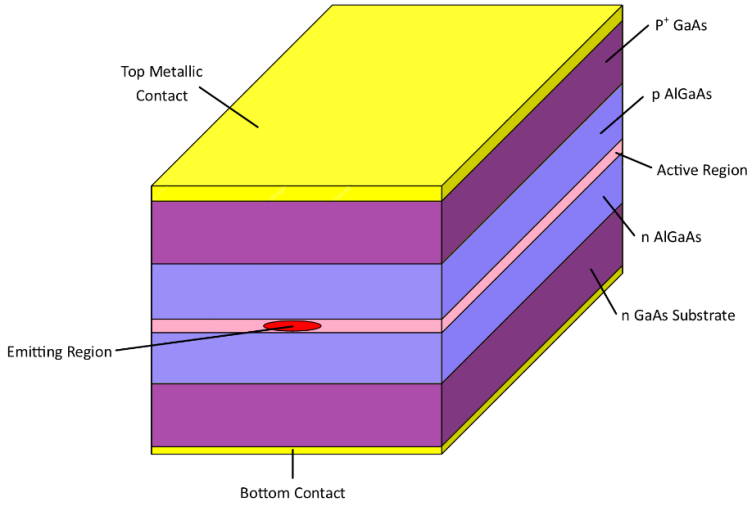

Figure 1.2: *Schematic layer structure of a conventional DH Fabry-Pérot laser diode.*

A commonly-used pair of materials is GaAs paired with AlGaAs [14]. The advantage of the DH laser diode is that the holes and the electrons will be confined to the middle layer, which acts as the active region. By confining the holes and the electrons to this region, there will be an increase in electron-

hole pairs that are available for the laser optical amplification process. Additionally, the change in the material at the heterojunction helps to contain the light within the active region, where the amplification takes place; hence the carriers and the light are confined to the same region.

Semiconductor lasers also share with other types of laser the properties of coherence, monochromaticity and threshold.

1.3 – Vertical-Cavity Surface-Emitting Laser (VCSEL) and the Vertical-External-Cavity Surface-Emitting Laser (VECSEL)

There are two main types of common semiconductor laser, those being the edge emitting, discussed in section 1.2, and the more recently developed vertical-cavity surface-emitting laser (VCSEL) which will now be discussed. Unlike the edge emitting semiconductor laser where the light emission is from the edge of the active layer, in a VCSEL the laser emission is perpendicular to the plane of the active layer. The first VCSEL was demonstrated by Soda *et al*. in 1979 [15], [16]. In their work, they designed a bulk DH surface emitting laser designed with a GaInAsP wafer active region containing a metallic mirror for the reflections. Typically, the cavity length of a surface emitting laser is much shorter than in an edge emitting laser (a few µm compared to ~ 300µm).

It wasn't until 1984 where Iga *et al*. (involved with the development of the first VCSEL [14]) successfully demonstrated the first room temperature electrically pumped VCSEL [17], and it wasn't until 1989 where the first room temperature, continuous-wave (CW) 895nm VCSEL was achieved by Koyama *et al*. [18]. This was followed by the first 1300nm room temperature, electrically pumped, CW VCSEL by Baba *et al*. in 1993 [19].

In a VCSEL structure, the active layer (or the light emitting layer) is sandwiched between two highly reflecting mirrors. Figure 1.3 illustrates a typical VCSEL structure.

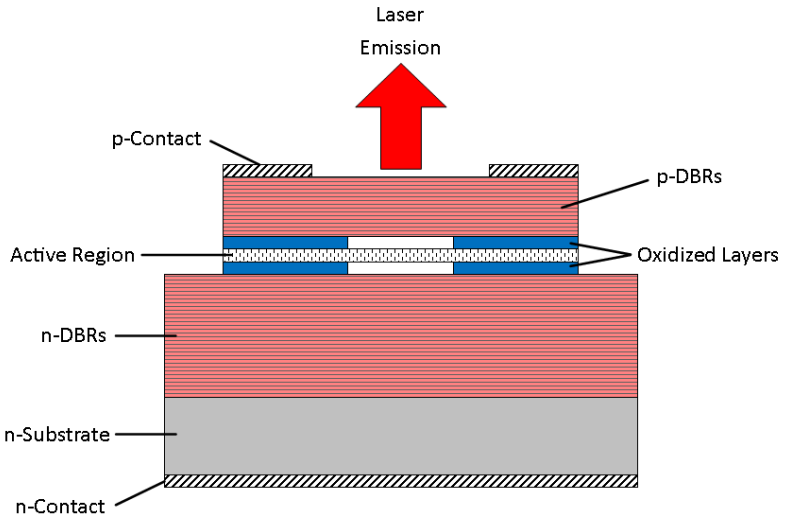

Figure 1.3: *Schematic layer structure of a conventional VCSEL.*

The mirrors are typically epitaxial growth mirrors, known as distributed Bragg reflectors (DBRs) [20]. The DBRs are made up of several quarter-wavelength-thick layers of semiconductors of multiple alternating periods of high and low refractive index layers. The reflectivity of these mirrors is typically greater than 99.9% [20]. As a result of the structure, the light will oscillate perpendicular to the layers and will hence emit from the top of the device.

Due to the compact size of VCSELs (typically 400 X 400μm^2), more devices per wafer are able to be manufactured [20], [21], hence making VCSELs low cost and manufacturable in high quantities. Such laser devices yield many promising advantages, including their low power consumption, narrow beam divergence, high modulation bandwidth and easy polarization control [20]. These make them very attractive laser light sources. They can also be used in applications such as optical storage, laser printers, barcode scanners, digital displays, optical sensors, spatial light modulators, backplanes and smart pixels, and microscopes [20], [22]-[25].

In a VCSEL, as illustrated in figure 1.3, the two highly reflecting mirrors are embodied into the laser structure in order to form the optical cavity. However, in a VECSEL, as illustrated in figure 1.4 one of these two mirrors is external to the laser structure. As a result, the cavity of the laser includes a free-space region. Part of this thesis is based upon a new design of the current state of the art dual-wavelength VECSEL (vertical-external-cavity surface-emitting laser) for the generation of terahertz radiation [26].

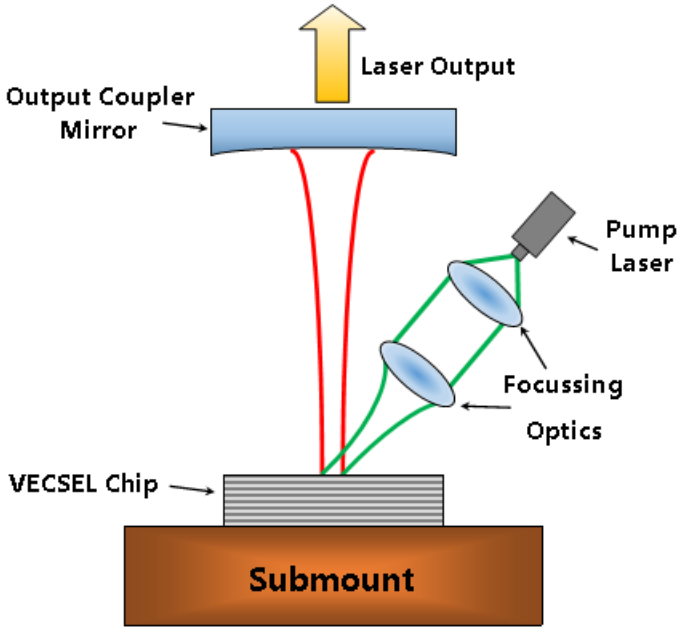

***Figure 1.4**: Schematic structure of an optically pumped VECSEL with a semiconductor gain chip and an external laser resonator.*

1.4 – Laser Theory

Section 1.4 is going to review fundamental laser theory based on the textbook 'Diode Lasers and Photonic Integrated Circuits' by Larry A. Coldren and Scott W. Corzine [27]. The topics under discussion will include the generation of carriers and photons, and rate equations for both the density of carriers and photons. Threshold gain and steady-state gain in lasers will also be discussed, as well as the power out vs. current in characteristics of a typical laser diode. The section will conclude with a discussion of relaxation resonance frequency.

1.4.1 – Carrier Generation

A common analogy for the processes within a laser that establish a carrier density steady-state level within the active region of a laser diode is by comparing the processes to that of filling and draining a water reservoir simultaneously. This is illustrated in figure 1.4. The generation terms can be represented by the filling of the reservoir, and the recombination terms may be represented by the draining of the reservoir. These will be discussed in more detail later. From figure 1.4, a current leakage term is apparent, and this contributes to reducing the internal quantum efficiency, η_i. The internal quantum efficiency is the fraction of terminal current that generates carriers within the active region [27]. Coldren and Corzine believe that this current leakage term may originate from possible shunt paths around the active region [27]. From figure 1.5, the carriers 'splashing out' of the reservoir are defined as carrier leakage, R_l. These are carriers that 'leak' out of the active region of the laser before recombining. This carrier leakage, as illustrated in figure 1.4, contributes to a loss of carriers in the active region which could otherwise be used usefully to generate light [27].

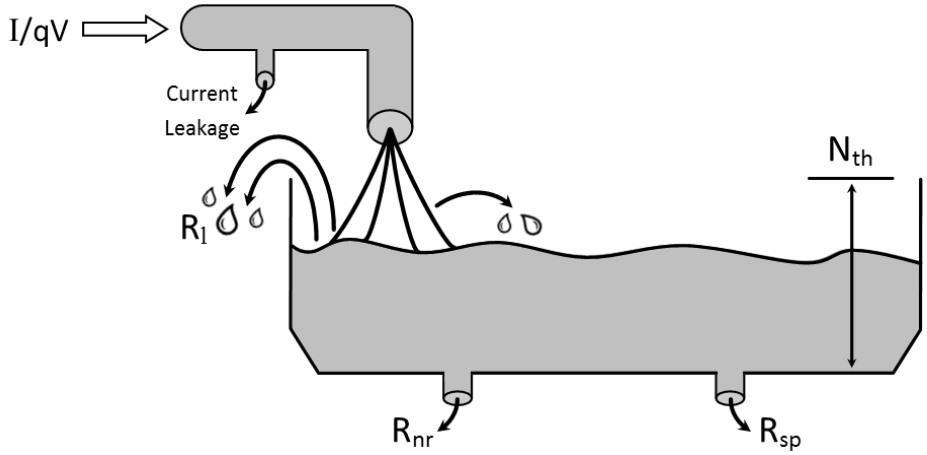

Figure 1.5: *Comparing the process of establishing a carrier density steady-state level in the active region of a laser to that of filling and draining a water reservoir simultaneously [27].*

In a DH active region, the injected current, I, provides the generation term, G_{gen}. In addition, the recombination terms, R_{rec}, are provided by various radiative and nonradiative processes, together with the carrier leakage term. Through combining the generation and recombination terms, a carrier density rate equation, N, may be expressed as [27]:

$$\frac{dN}{dt} = G_{gen} - R_{rec} \tag{1.1}$$

where G_{gen} is the rate of injected electrons, and R_{rec} is the rate of recombining electrons per unit volume in the active region. There will be $\eta_i I/q$ electrons per second injected into the active region, hence, the generation term will become [27]:

$$G_{gen} = \frac{\eta_i I}{qV} \tag{1.2}$$

where q is the charge of electrons, V is the volume of the active region, and I is the injected current. Included within the recombination term, R_{rec}, are the spontaneous recombination (spontaneous emission) term, R_{sp}, a nonradiative recombination rate, R_{nr}, and a carrier leakage rate, R_l, all illustrated in figure 1.4. In addition, a net stimulated recombination term, R_{st}, must also be included, which contains both the stimulated emission and absorption terms. As a result, R_{rec}, may be expressed as [27]:

$$R_{rec} = R_{sp} + R_{nr} + R_l + R_{st} \tag{1.3}$$

From equation (1.3), R_{sp}, R_{nr} and R_l are the terms referring to the natural, or unstimulated, carrier decay processes. However, the stimulated recombination term, R_{st}, requires the presence of photons. The natural decay process is commonly represented by a carrier lifetime, represented by τ, and with the absence of photons, or a generation term, the carrier decay may be expressed by [27]:

$$\frac{dN}{dt} = \frac{N}{\tau} \tag{1.4}$$

where

$$\frac{N}{\tau} \equiv R_{sp} + R_{nr} + R_l \tag{1.5}$$

Each of the terms in equation (1.5) are dependent upon the presence of carriers. Consequently, R_{rec} may be expressed as [27]:

$$R_{rec} = \frac{N}{\tau} + R_{st} \tag{1.6}$$

Through combining equations (1.4)-(1.6), the carrier rate equation may be expressed as [27]:

$$\frac{dN}{dt} = \frac{\eta_i I}{qV} - \frac{N}{\tau} - R_{st} \tag{1.7}$$

When the laser is operating below threshold (or in the case of most LEDs), there is a deficiency of a large amount of photons and so the stimulated emission term, R_{st}, may be neglected.

1.4.2 – Photon Generation

As mentioned in the previous section, R_{st} may be neglected below threshold, however, above threshold, R_{st} becomes the dominant term. A photon is generated each time an electron-hole pair recombines, however, typically in laser cavities, the volume of the cavity that is occupied by photons, V_p, is larger than the active region occupied by electrons, V. As a result, the photon density generation rate will become [27]:

$$\left[\frac{V}{V_p}\right] R_{st} \tag{1.8}$$

The V/V_p term is known as the electron-photon overlap factor, and this is more commonly referred to as the confinement factor, represented by Γ [27].

In laser cavities, photon losses will be apparent; these losses are as a result of optical absorption and scattering out of the laser mode. These losses occur at the output of the coupling mirror where a portion of the resonant mode is usefully coupled to some output medium. Similarly, where the natural decay process is commonly represented by a carrier lifetime, represented by τ, the net loss is commonly represented by a photon (or a cavity) lifetime, represented by τ_p. As a result, an initial version of the photon density rate equation, S, may be expressed as [27]:

$$\frac{dS}{dt} = \Gamma R_{st} + \Gamma \beta_{sp} R_{sp} - \frac{S}{\tau_p} \tag{1.9}$$

where β_{sp} is the spontaneous emission factor, which defines the amount of spontaneous emission that is coupled into a given mode. As can be seen from equation (1.9), with no generation terms present, the photons will simply decay exponentially with a decay constant of τ_p [27].

1.4.3 – Carrier and Photon Density Rate Equations

The previous two sections have explored the generation of both carriers and photons in a laser cavity, as derived by Coldren and Corzine. This section is going to look at their development of the carrier and photon density rate equations.

Firstly, equations (1.7) and (1.9) represent two coupled equations, and Coldren and Corzine state that these are able to be solved at the steady-state, and for dynamic responses, of diode lasers. These, however, need to be developed further in order to establish solutions at the steady-state, and so several terms must be included in terms of N and S.

Referring back to the stimulated recombination term, R_{st}; this terms represents the photon-stimulated net electron-hole recombination, and this term will generate more photons. This is hence known as the gain process for photons [27]. Included in R_{st} are the net effects of the upward and downward electronic transitions; these correspond to stimulated absorption and emission of photons,

respectively. Figure 1.6 illustrates that when passed through a small length, Δz, of active region the photon density will grow from an incoming value of S, to an exiting value of $S + \Delta S$ [27].

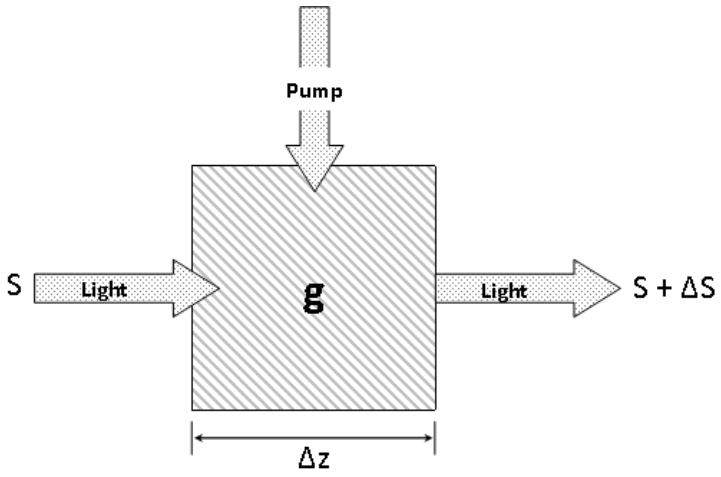

Figure 1.6: *The growth in photon density from an incoming value of S when passed through a small segment of gain material [27].*

In order to simplify the derivations, Coldren and Corzine assume that a full overlap exists between the active region and the photon field. As a result, $\Gamma = 1$, and hence the growth may be described in terms of the gain per unit length, g. This may be expressed as [27]:

$$S + \Delta S = Se^{g\Delta z} \tag{1.10}$$

If the active region length, Δz, were to be sufficiently small, then [27]:

$$e^{g\Delta z} \approx 1 + g\Delta z \tag{1.10}$$

Also:

$$\Delta z = v_g \Delta t \tag{1.11}$$

where v_g is the group velocity, then it can be shown that [27]:

$$\Delta \mathrm{S} = S \mathrm{g} v_g \Delta t \tag{1.12}$$

In other words, the generation term, G_{gen}, for dS/dt is given by [27]:

$$\left(\frac{dS}{dt}\right)_{gen} = R_{st} = \frac{\Delta S}{\Delta t} = v_g g S \tag{1.13}$$

As a result, the full carrier and photon density rate equations are expressed as [27]:

$$\frac{dN}{dt} = \frac{\eta_i I}{qV} - \frac{N}{\tau} - v_g g S \tag{1.14}$$

$$\frac{dS}{dt} = \Gamma v_g g S + \Gamma \beta_{sp} R_{sp} - \frac{S}{\tau_p} \tag{1.15}$$

1.4.4 – Threshold Gain in Lasers

Now that the rate equations for the density of carriers and photons have been established, the next stage is to establish an understanding of the threshold gain level in laser diodes. As the current injected into the cavity is increased, at some current value, the carrier density will equal the threshold carrier density, N_{th}. When the carrier density, N, equals the threshold carrier density, N_{th}, the gain, g, will equal the threshold gain, g_{th}, and the photon density, S, will become infinite. This is illustrated in figure 1.7. Below threshold, spontaneous emission is the dominant process, however above threshold, stimulated emission is the dominant process. As the gain increases, the stimulated emission rate will also increase and will reach the rate at which the photons are lost from the cavity; each photon in the cavity now has a chance to multiply before it is lost from the cavity.

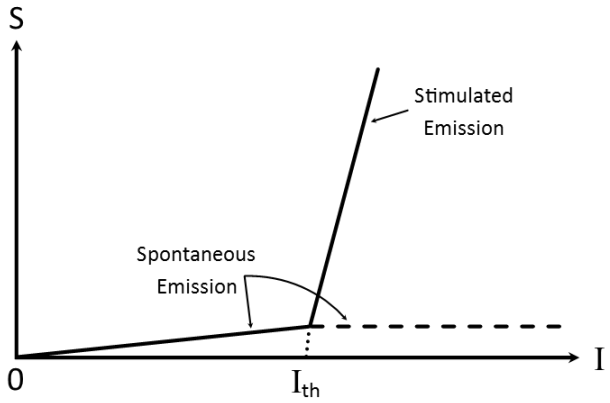

Figure 1.7: *The increase in photon density, S, above current threshold, I_{th}.*

As discussed in section 1.4.3, the cavity loss may be expressed by a photon decay lifetime, τ_p. In this section, as defined by Coldren and Corzine, the photon lifetime will be explicitly expressed in terms of the losses associated with optical propagation along the cavity as well as the cavity mirrors. It also needs to be shown that the net loss of some mode gives the value of the net gain that is required in order to reach the lasing threshold [27].

Laser cavities may be divided into two general sections; the active section length, defined as L_a, and the passive section length, L_p. It should also be noted that the gain, g, and the loss, α_i, will clearly be different in these two sections; in the passive section, the gain will be zero, and the loss will be designated a subscript, depending on the section of interest. The propagating mode will be reflected by two end mirrors, each of which will have amplitude reflection coefficients, r_1 and r_2; these provide the resonant cavity [27].

In order for a laser mode to reach threshold, the following condition must be met, whereby the gain in the active region must be increased to the point where all of the propagation and mirror losses are compensated for [27].

As previously mentioned, the photon lifetime, τ_p, is determined by the cavity loss, and this comprises the laser emission, and Coldren and Corzine define the gain at threshold as [27]:

$$g_{th} = \Gamma g_{th} = \langle \alpha_i \rangle + \frac{1}{L} ln\left(\frac{1}{R}\right) \tag{1.16}$$

where g_{th} is the gain at threshold, $\langle \alpha_i \rangle$ is the average internal loss, L is the total cavity length, and R is the laser facet reflectivity, which is equal to $r_1 r_2$.

For simplicity, Coldren and Corzine abbreviate the mirror loss to [27]:

$$\alpha_m \equiv \left(\frac{1}{L}\right) ln\left(\frac{1}{R}\right) \tag{1.17}$$

Also, by noting that the photon decay rate is [27]:

$$\frac{1}{\tau_p} = v_g(\langle \alpha_i \rangle + \alpha_m) \tag{1.18}$$

then it is also possible to write:

$$\Gamma g_{th} = \langle \alpha_i \rangle + \alpha_m = \frac{1}{v_g \tau_p} \tag{1.19}$$

1.4.5 – Steady-State Gain in Lasers

Now that an understanding of threshold gain in lasers has been established, this section will investigate the above threshold steady-state gain in diode lasers. In this case, the steady-state gain must clamp at its threshold value provided by equation (1.16). As a result, the gain, where the injected current is above its threshold value, is given by [27]:

$$g(I > I_{th}) = g_{th}\ (steady\ state) \tag{1.20}$$

If the gain were to be higher than its threshold value, then the amplitude would just simply continue to increase without any boundary. This, of course, cannot exist at the steady-state. Additionally, as the gain is monotonically related to the carrier density, this gives the impression that the carrier density must also clamp at its threshold value. As such, the carriers, where the injected current is above threshold, is given by [27]:

$$N(I > I_{th}) = N_{th}\ (steady\ state) \tag{1.21}$$

In this situation, what actually happens is that as the injected current is increased above its threshold value, the carrier density and the gain, initially (for an order of a nanosecond), will increase to values above their threshold values. Similarly, the photon density will also increase. At the same time, the stimulated recombination term, R_{st}, also increases, and consequently, the carrier density and gain will reduce until a new steady-state dynamic balance will be reached, where again, equations (1.20) and (1.21) are satisfied [27].

This may be illustrated, referring back to the reservoir analogy from figure 1.5, whereby the stimulated recombination term in equation (1.14) will use up all of the additional carrier injection above

threshold. From the reservoir analogy, the water has now reached the top of the reservoir, and any further increase in the input will simply flow out of the sides of the reservoir, without increasing the depth of water. The top of the reservoir depicts stimulated recombination, as illustrated in figure 1.8.

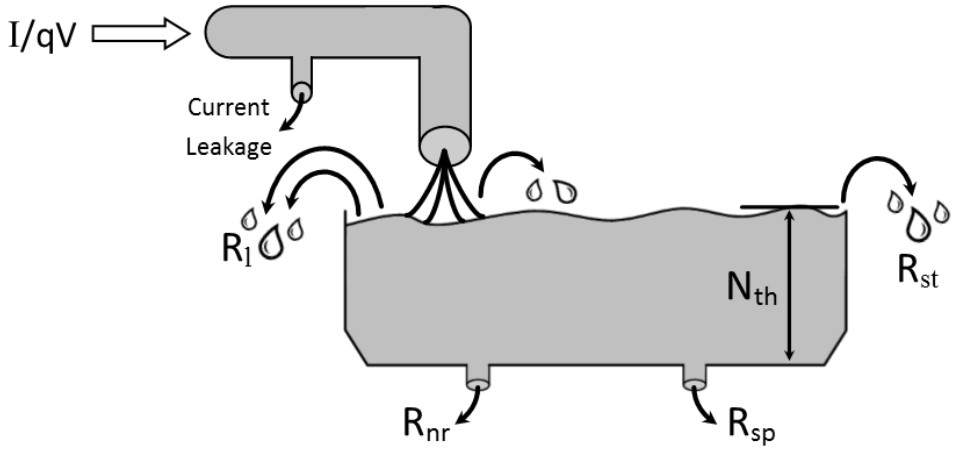

Figure 1.8: *The reservoir analogy above threshold where the water level has increased to the top of the reservoir, and an increased input will result in an increased output, R_{st}, but no increase in carrier density. The R_{nr} and R_{sp} levels do not change above threshold [27].*

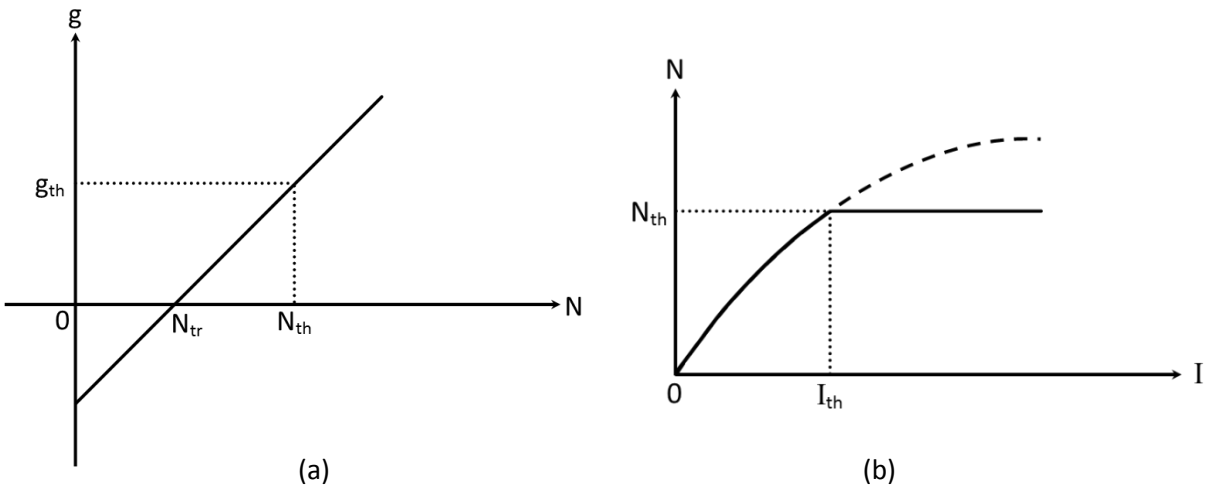

Figure 1.9: *The gain vs. carrier density in (a) and the carrier density vs. input current in (b). The carrier density clamps at threshold causing the gain also to clamp [27].*

Figures 1.9 (a) and (b) represent the carrier clamping effect in a laser cavity (as derived in equations (1.20) and (1.21)), depicting the gain vs. carrier density in (a) and carriers vs. injected current in (b). In a laser cavity, the physics of the g vs. N curve will never change. The feedback effect will cause the carrier density to clamp, in order to keep the gain at its threshold value [27].

1.4.6 – Power Out Vs. Current In

The penultimate section of laser theory to be discussed here is the power out vs. current in characteristic for a laser diode, and the first thing to note here are that the rate equations defined in equations (1.14) and (1.15) are valid for both below and above threshold. In this section, a below threshold LED characteristic will be introduced, together with an above threshold laser characteristic in order to establish the power out vs. current in characteristic for a diode laser.

Coldren and Corzine define the power an LED emits into some receiving aperture as [27]:

$$P_{LED} = \eta_c \eta_i \eta_r \frac{h\nu}{q} I = \eta_{ex} \frac{h\nu}{q} I \tag{1.22}$$

where η_c is defined as the net collection efficiency (the fraction of carriers injected into the active region), $h\nu$ is the energy per photon and η_{ex} is the external LED quantum efficiency, defined as the fraction of carriers injected into the active region, the fraction of these recombining radiatively, and the fraction of those usefully coupled out; i.e. the number of photons coupled to the receiving aperture per electron flowing into the LED. η_r is the radiative efficiency, and may be defined as [27]:

$$\eta_r = \frac{R_{sp}}{R_{sp} + R_{nr} + R_l} \tag{1.23}$$

Next, the above threshold equation shall be considered. The first process here is to consider the below threshold steady-state carrier rate equation, defined by Coldren and Corzine as [27]:

$$\frac{\eta_i I}{qV} = R_{sp} + R_{nr} + R_l \tag{1.24}$$

Now, by considering equation (1.24) almost at threshold, i.e. [27]:

$$\frac{\eta_i I}{qV} = \left(R_{sp} + R_{nr} + R_l\right)_{th} = \frac{N_{th}}{\tau} \tag{1.25}$$

then, from equation (1.21), Coldren and Corzine observed that above threshold, $\left(R_{sp} + R_{nr} + R_l\right)$ will also clamp at its threshold value given by equation (1.25). As a result, equation (1.25) may be substituted into equation (1.14) in order to obtain a new, above threshold, carrier density rate equation, expressed as [27]:

$$\frac{dN}{dt} = \eta_i \frac{(I - I_{th})}{qV} - v_g g S \qquad (I > I_{th}) \tag{1.26}$$

In equation (1.26), Coldren and Corzine have assumed η_i not to be a function of current below threshold. Now, from equation (1.26), a steady-state photon density above threshold can be established, where $g = g_{th}$. This may be expressed as [27]:

$$S = \frac{\eta_i (I - I_{th})}{q v_g g_{th} V} \qquad (steady\ state) \tag{1.27}$$

All of the equations are now present in order to establish an equation for the power out. Coldren and Corzine state that this must be proportional to the photon density, S. Before defining the power out,

Coldren and Corzine note that it is first necessary to define the stored optical energy in the cavity, E_{os}, through multiplying the photon density, S, the energy per photon, $h\nu$, and the cavity volume, V_p, such that [27]:

$$E_{os} = ShvV_p \tag{1.28}$$

Coldren and Corzine then multiply equation (1.28) by the energy loss rate through the mirrors, expressed as [27]:

$$v_g\alpha_m = \frac{1}{\tau_m} \tag{1.29}$$

From this, the optical power output from the mirrors is then established [27]:

$$P_o = v_g\alpha_m ShvV_p \tag{1.30}$$

Through then substituting from equations (1.27) and (1.19), and by using $\Gamma = V/V_p$ into equation (1.30), the output power from a laser diode may be expressed as [27]:

$$P_o = \eta_i\left(\frac{\alpha_m}{\langle\alpha_i\rangle + \alpha_m}\right)\frac{h\nu}{q}(I - I_{th}) \qquad (I > I_{th}) \tag{1.31}$$

and through defining the differential quantum efficiency, η_d, as [27]:

$$\eta_d = \frac{\eta_i\alpha_m}{\langle\alpha_i\rangle + \alpha_m} \tag{1.32}$$

then equation (1.31) for power output may be simplified to [27]:

$$P_o = \eta_d\frac{h\nu}{q}(I - I_{th}) \qquad (I > I_{th}) \tag{1.33}$$

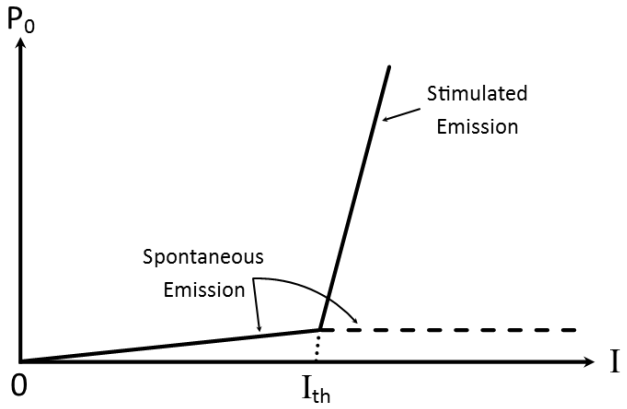

Figure 1.10: *The output power vs. current in for a typical laser diode [27].*

A typical output power vs. current in for a typical diode laser is illustrated in figure 1.10. Below threshold, only spontaneous emission is important, whereas above threshold the stimulated emission power increases, while the spontaneous emission is clamped at its threshold value.

1.4.7 – Relaxation Resonance Frequency

The final section to be considered for fundamental laser theory is the relaxation resonance frequency. Here, equations (1.14) and (1.15) will be utilized in order to briefly outline the derivation for relaxation resonance frequency, defined by Coldren and Corzine.

The first stage is to consider the application of an above threshold DC current, I_0, superimposed with a small AC current, I_1, to a diode laser. By then considering the steady-state conditions, the laser's carrier and photon densities would respond very similarly, with a drive frequency, ω. By utilising complex frequency domain notation, the injected current, I, the carrier density, N, and the photon density, S, may be defined as [27]:

$$I = I_0 + I_1 e^{j\omega t} \tag{1.34}$$

$$N = N_0 + N_1 e^{j\omega t} \tag{1.35}$$

$$S = S_0 + S_1 e^{j\omega t} \tag{1.36}$$

Before these equations can be applied to the carrier and photon density equations of (1.14) and (1.15), Coldren and Corzine state that they must first be re-written, taking into account the gain as a function of carrier density. This can be approximated by a straight line, at least under small-signal conditions, such that [27]:

$$g \approx a(N - N_{tr}) \tag{1.37}$$

where a is the differential gain defined as $\partial g/\partial N$, and N_{tr} is the transparency carrier density. Coldren and Corzine are able to re-write the rate equations, utilising equation (1.37) for the gain, as they assume small-signal conditions. As a result, the gain can be well approximated as a straight line over some distance, provided the local slope is used [27].

Another assumption Coldren and Corzine make here is that the DC current is sufficiently far above threshold, that the spontaneous emission term can be neglected. Through their assumption, Coldren and Corzine are able to express the carrier and photon density rate equations as [27]:

$$\frac{dN}{dt} = \frac{\eta_i I}{qV} - \frac{N}{\tau} - v_g a(N - N_{tr})S \tag{1.38}$$

$$\frac{dS}{dt} = \Gamma v_g a(N - N_{tr})S - \frac{S}{\tau_p} \tag{1.39}$$

By now substituting equations (1.34), (1.35) and (1.36) for I, N and S, in equations (1.38) and (1.39), it can be seen that the DC components satisfy the steady-state versions of equations (1.38) and (1.39), whereby dN/dt and $dS/dt \to 0$. These can hence be grouped together, and set to zero. Next, Coldren and Corzine state that it can be seen that the steady-state gain factors, $a(N_0 - N_{tr})$ are simply equal to g_{th} and are able to be replaced by $\left[\Gamma v_g \tau_p\right]^{-1}$ according to equation (1.16). Finally, Coldren and Corzine delete the second harmonic that involve $e^{j2\omega t}$ and divide out an $e^{j\omega t}$ common factor, such that [27]:

$$j\omega N_1 = \frac{\eta_i I_1}{qV} - \frac{N_1}{\tau} - \frac{S_1}{\Gamma\tau_p} - v_g a N_1 S_0 \quad (1.40)$$

$$j\omega S_1 = \Gamma v_g a N_1 S_0 \quad (1.41)$$

To finalise this analysis, the coupling between the small-signal photon density, S_1, and the small-signal carrier density, N_1, will be examined. The carrier density depends upon S_1 through the third term in equation (1.40), while at the same time, the photon density depends upon N_1 from equation (1.41). Coldren and Corzine note that by viewing the left hand side of these equations as time derivatives, then it can be observed from equation (1.41) that as N_1 increases and becomes positive, S_1 will increase in time as a result of an increased gain in the laser. However, Coldren and Corzine note that by looking at the third term in equation (1.40), once S_1 becomes positive, it will consequently cause a decrease in N_1 as a result of an increase in stimulated emission. Now, as N_1 decreases and becomes negative, S_1 begins to fall, and once it becomes negative it will consequently cause N_1 to increase once more. From this point onwards, the pattern will repeat itself until a steady-state value has been established. This phenomenon produces a natural resonance in the laser cavity which shows up as a ringing in the output power of the laser in response to sudden changes in the input current. Coldren and Corzine show that it is possible to find this natural frequency of oscillation associated with the mutual dependence between N_1 and S_1 by multiplying equations (1.40) and (1.41) together, ignoring all but the third term on the right hand side of the first equation. In doing so yields [27]:

$$\omega_R{}^2 = \frac{v_g a S_0}{\tau_p} \quad (1.42)$$

This natural resonance frequency is more commonly referred to as the relaxation resonance frequency, ω_R (where the relaxation refers to an attempt by the photons and the carriers to relax to their steady-state values). It is directly proportional to the square root of the differential gain and average photon density in the cavity (the output power), and is also inversely proportional to the square root of the photon lifetime within the cavity [27].

1.5 – Terahertz (THz) Radiation

The interest in terahertz (THz) technology and millimetre waves (mm-waves) has grown significantly over the last few years, due to the availability of sources and detectors that are capable of emitting efficiently within this frequency range [28]-[32]. The THz frequency range may be defined as the frequencies between 300GHz-10THz, which translates to approximately 1mm to 30µm in wavelength [33] [34]. As can be seen from figure 1.11, THz waves sit in-between infrared and microwaves. THz waves are able to interact with all types of matter, including liquids, solids and gasses, and also have a significant penetration in some materials, including some plastics and ceramics, fabrics, wood and paper [33]. This makes them very attractive sources for applications in medical imaging, or security

purposes [35]-[38]. They are also highly desirable sources for applications including spectroscopy [39], biosensing [40], and quality inspection in different industrial industries [41]-[43]. They also have applications within the world of astronomy [44], however THz waves suffer from poor atmospheric transmission, and hence any astrophysical experiments would have to be conducted outside of the earth's atmosphere [33]. Another potential field of application is in heterodyne receivers, also for the study of astronomy, where they may be used as high powered sources at key frequencies including 1.4, 1.9 and 2.7THz [38]. These frequencies are used for the detection of far-infrared (FIR) atomic fine structure lines in space, such as the atomic fine structure lines of singly ionized nitrogen (NII) at 1.4THz, singly ionized carbon (CII) at 1.9THz [44], and the 1-0 transition of deuterated molecular hydrogen, HD, at 2.7THz [45].

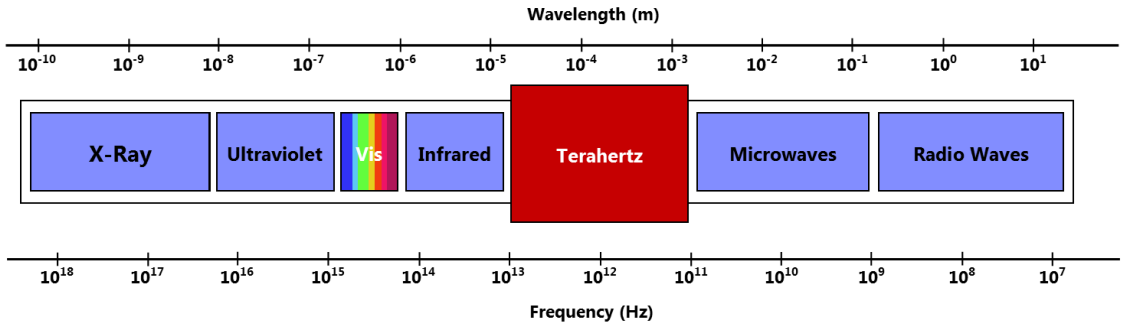

Figure 1.11: *Electromagnetic spectrum indicating the location of Terahertz waves.*

As THz waves have significant penetration in some materials, this means that it is possible to see through them in this particular frequency range much better than in the infrared (IR) or optical regime. This is particularly useful in THz imaging, notably for security screening. Another advantage of THz waves are that they have natural frequencies for femtosecond probing [33]. This is particularly useful when very fast reactions are present, and measuring these reactions is required; for example, to measure moving molecules, or charge motion within a structure. THz waves would be able to actually measure how things move at the femtosecond scale. THz apertures also have advantages over millimetre apertures [33]; when compared directly to millimetre wavelengths, it would be possible to just scale up the frequency for the same antenna diameter, and also scale the resolution (or the pixel size) down linearly with aperture diameter. This would give a real portability advantage for some applications. Other advantages include its non-ionizing nature, unlike x-ray radiation [33].

There are also numerous drawbacks to THz technologies, including very poor atmospheric transmission [33] as mentioned previously. Due to the heavily absorbing nature of water and oxygen in the Earth's atmosphere it is not possible to transmit distances of more than ~1-2km at the low end

of the THz band, and as low as meters (or tens of meters) at the high end of the THz band before a significant amount of power has been absorbed in the atmosphere [33]. THz waves also suffer from poor contrast and a high speckle ratio, especially in THz imaging. The thermal differences in the environment under measurement using a passive sensor, or even the differences apparent with an active sensor, suffer very heavily from speckle and very large reflections from objects that would normally have a very minimal contrast in the passive environment. In active work, there can be quite a big reflection from materials such as paper or even cardboard which will swamp the background signal, hence care must be taken imaging within this wavelength range [33]. Such a technology also requires large apertures; for example, when trying to imitate an optical system in the THz band, the diameter of lenses or mirrors would need to be ~x1000 more than what would be needed in the optical regime when a spot size of ~1mm is required [33], and the cost for such components and instruments is high [33].

When considering the efficient generation of THz radiation within the THz frequency range of 300GHz-10THz (also known as the 'terahertz-gap'), there is a problem [46]. The problem is the difficulty in generating THz waves due to the fact that the frequency is too high for conventional radio transmitters, and too low for optical transmitters [47]. Additionally, although THz radiation has the ability to penetrate certain materials (as mentioned previously), it is absorbed by water, and hence limits the use of THz devices within the Earth's atmosphere to short distances [47]. This problem has drawn a prominent amount of attention and research over the last decade or so. It has drawn so much attention due to the large number of promising applications which can be realised with THz technologies, some of which have been noted previously.

This thesis is going to look at two different means of potentially realising THz radiation; those being the dual-wavelength VECSEL, whereby the wavelength spacing between the two lies within the THz frequency range, and the four-wave mixing (FWM) scheme, which will utilize the injection-locking phenomenon, in order to produce a non-zero frequency separation between the lasers frequencies while operating in the locked condition. Again, the aim is to have a frequency separation which lies in the THz frequency range.

1.6 – Realizing Terahertz Radiation

A number of different approaches have been employed to generate high-power radiation in the THz frequency range, some of which are going to be explored within this thesis. These include the dual-wavelength VECSEL [26], utilising photoconductive (PC) emitters, fabricated as either emitters or switches [46], and the four-wave mixing (FWM) phenomenon [48].

A potential method for realising efficient terahertz radiation is via a multilayer dielectric slab waveguide structure [49] and this is illustrated in figure 1.12 which shows a five-layer optical waveguide structure where $n_1 > n_3 > n_2 = n_4$.

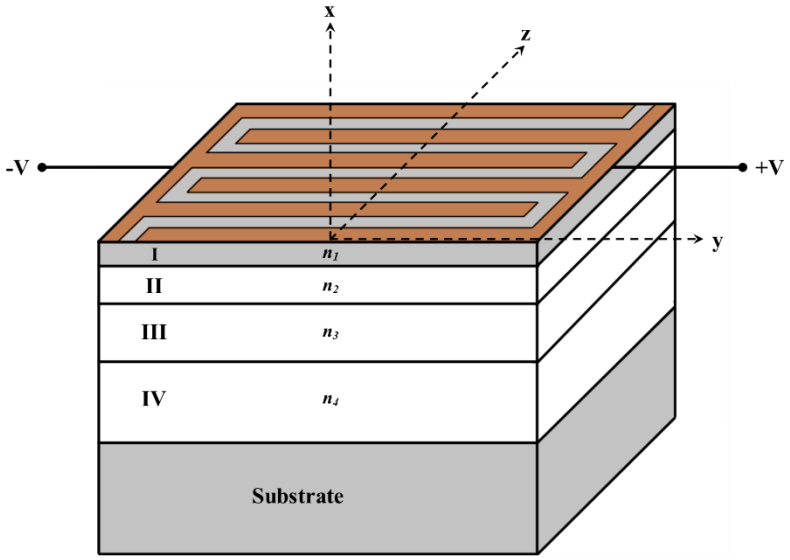

Figure 1.12: *Schematic of a five-layer dielectric slab waveguide proposed by Saeedkia et al. for terahertz edge-coupled photomixer applications [49].*

In this scheme, Saeedkia *et al*. state that the structure guides the beams of two interfering lasers, where their central frequency difference falls into the terahertz spectrum. In such a scheme, the two frequency-detuned interfering laser beams will uniformly shine on the whole of the x-y facet; this will excite guided modes travelling along the x-axis. In the dielectric waveguide structure, the top layer is constructed from an ultra-fast photo-absorbing material, such as low-temperature grown GaAs (LT-GaAs), wherein the power of the guided modes is being absorbed and converted into a terahertz signal [49]. Regions II, III and IV are epitaxially grown over an appropriate substrate, and these are transparent at the operating optical wavelengths [49].

Another promising method for harnessing the distinctive features of terahertz waves is the use of photoconductive antennas (PCA) [50]. These are extensively used to generate THz broadband pulses and THz narrowband CW signals. In the CW mode, two CW laser beams, whose frequency difference lies within the THz range, combined either inside an optical fiber or properly overlapped in space will be mixed in a photo-absorbing medium (photomixer) and will generate a beat frequency signal [50]. Figure 1.13 illustrates a DC biased aperture THz PCA which is illuminated by a laser beam (pulsed or CW). With the applied DC bias and the incident laser beam, an induced current is generated, which will radiate a THz wave into free space [50].

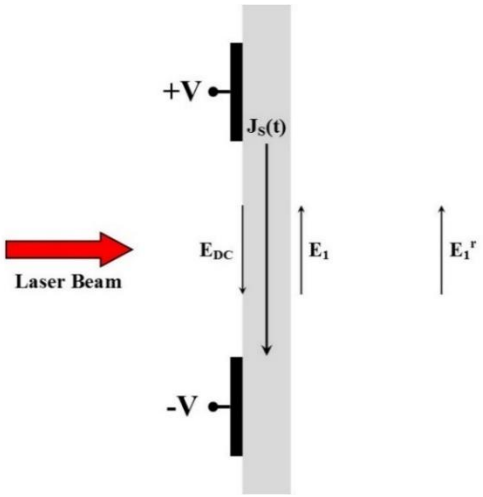

Figure 1.13: *An aperture THz PCA illuminated by a laser beam where E_{DC} is the applied DC bias, $J_S(t)$ is the induced surface current, and E_1 and $E_1{}^r$ are the THz electric near and far fields respectively. The thickness of the photoconductor is assumed to be much less than the THz wavelength [50].*

A way of utilising PCAs is through utilizing the photomixing method. Photomixing is the generation of continuous wave THz radiation from two lasers. A THz Photomixer works by mixing the light from two laser beams together in a nonlinear medium, where the frequency of the generated signal will be equal to the frequency difference between the two individual laser beams by employing the optical heterodyning scheme [51] [52]. The two laser beams with a difference frequency lying in the THz range, illuminate a DC-biased photoconductive film, or a PCA, where a CW THz signal is generated. This is illustrated in figure 1.14. Photomixers are an attractive source for generating terahertz radiation as they are potentially compact, low-power consuming, coherent, and have low manufacturing costs [35].

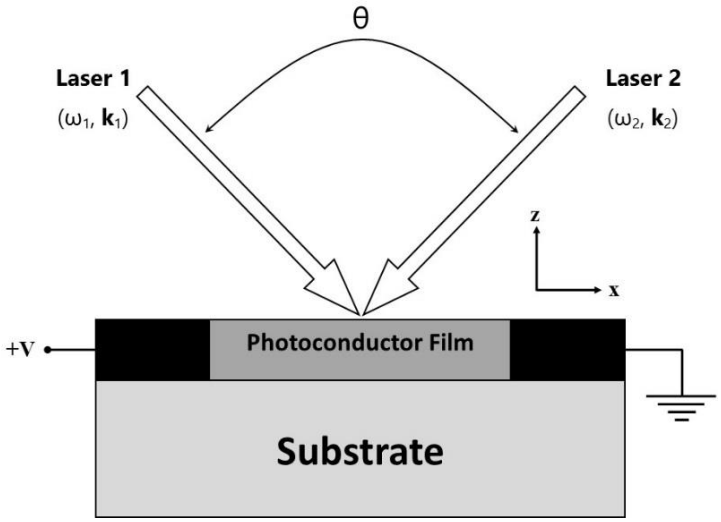

Figure 1.14: *Photoconductive photomixer configuration [50].*

Another attractive method for generating efficient terahertz radiation within the terahertz gap is through four-wave mixing (FWM) in semiconductor laser diodes. Four-wave mixing represents one of the most general, but very important, phenomena in nonlinear optics [53]. When considering FWM, two or more waves are interacting in a nonlinear medium, resulting in outputs at assorted sum or difference frequencies [53]. It is the notion of three separate electromagnetic fields interacting in order to produce a fourth field that is fundamental to the description of all four-wave mixing processes [54].

1.7 – Thesis Outline and Contribution

This thesis is devoted to exploring a number of potential approaches to generate terahertz radiation. There are three main approaches employed within this thesis;

1. Designing a new dual-wavelength VECSEL, inspired by pre-existing literature [26] with a significantly reduced wavelength spacing between the wavelengths, and improved positioning of the QWs to potentially improve the performance of the structure;
2. Investigating in detail the scheme of injection locking, thoroughly studying the different behaviours the scheme exhibits under both unidirectional and bidirectional injection locking. Under this scheme, there is a zero frequency spacing between the lasers' frequencies in the locked condition;
3. Using injection locking as a building block for the four-wave mixing (FWM) scheme, whereby a system is modelled, based on the FWM approach, utilizing the injection locking scheme, in order to model a system with a nonzero frequency spacing between the lasers' frequencies in the locked condition.

The thesis will begin with an analysis and a contribution made to designing a new dual-wavelength laser based on the work of Leinonen *et al*. [26]. During the course of the design, the wavelength separation between the two wavelengths has been significantly reduced, with the aim of having a 5nm (1.54THz) spacing between the two wavelengths. The quantum-wells (QW) have also been re-positioned to potentially improve the performance of the laser. The thesis will also consider the effect of linewidth broadening which could be a limiting factor in significantly reducing the wavelength separation between two wavelengths in a dual-wavelength laser. As a result, the thesis will consider the Schawlow-Townes [5] linewidth for both structures.

The next method employed in this thesis as a potential method for generating THz radiation is the injection locking scheme. Here, the thesis will look at the work undertaken to model an injection locking system based on a two-laser system. Both unidirectional and bidirectional injection locking will be explored, whereby the different behaviours of both systems within the locking region will be

investigated. In the locked condition, there will be a zero frequency separation between the two lasers, and as a result, the work here will provide the building blocks for the final approach employed within this thesis; four-wave mixing (FWM).

The FWM scheme employed here is based on the approach of Zanola *et al*. [28], where two distributed feedback lasers, emitting at the frequencies ν_1 and ν_2, respectively, are phase-locked via mutual injection, assisted by the four-wave mixing process that takes place in the third, auxiliary, laser, with fixed wavelength separation, emitting at the frequency of ν_3. This is a novel and compact scheme which has the potential to substantially improve the spectral purity of photomixing signals [28]. In such a scheme, the frequency stability of the RF signal will be enhanced through the introduction of a feedback effect on the instantaneous emission frequencies of the two semiconductor lasers that generate the beating signal; this is achieved through the third laser, emitting at ν_3 [28]. In their work, they designed and fabricated a monolithic optoelectronic device for the generation of tunable and narrow linewidth millimetre wave signals. They investigate two and three laser locking, studying the levels of optical injection required to lock the lasers, and the dependence of the locking range on the mutually injected power.

Here, a contribution is made to modelling a three laser system, utilising the FWM scheme, based on the injection locking approach, as a potential method for realizing THz radiation. As with the injection locking scheme, a detailed analysis of the different behaviours of the system within the locking region will be explored for the first time, together with an investigation into the resilience of the system to introduced perturbations, with the aim of defining an optimal locking region within the system.

This thesis is laid out in eight chapters. Chapter two will look at the first potential method employed for realising THz radiation; the dual-wavelength VECSEL proposed by Leinonen *et al*. [48]. This chapter will pay particular attention to the design of their VECSEL structure, and the conclusions they made on the performance of the laser. The chapter will begin with a review of the proposed structure by Leinonen *et al*. before making a contribution, namely designing a new dual-wavelength VECSEL structure inspired by Leinonen *et al*. This is done for two reasons; firstly, to significantly reduce the wavelength separation between the two wavelengths, and secondly, to re-position the QWs in the active regions in order to improve the performance of the VECSEL structure.

Chapter three is a continuation from chapter two and will look at the potential constraints to significantly reducing the wavelength spacing between two wavelengths in a dual-wavelength laser, paying particular attention to linewidth broadening. The work here will provide a review of the linewidth equation derived by Schawlow and Townes [5], and how the equation derived here was modified by Melvin Lax [55] and then by Charles Henry [56], to include the linewidth enhancement

factor, α, (also known as the Henry Alpha factor). The chapter will then look at how the same modified Schawlow-Townes equation may be applied to both VCSEL and VECSEL type lasers.

Chapter four will then make a further contribution to the dual-wavelength VECSEL design, applying the Schawlow-Townes equation to both the structures by Leinonen *et al*. and the newly designed VECSEL structure in order to establish whether or not linewidth broadening would be a limiting factor when designing dual-wavelength lasers.

Chapter five then provides a review of the laser injection locking scheme, whereby a system is built based on a two laser approach. The chapter will include two injection locking approaches; unidirectional and bidirectional injection locking. The chapter will first investigate the unidirectional injection locking scheme, whereby a fraction of light from the first laser is injected into the cavity of the second laser. The chapter will then look at bidirectional injection locking, whereby a fraction of light from the first laser will be injected into the cavity of the second laser, at the same time that a fraction of light from the second laser is injected into the cavity of the first laser. For both schemes, a detailed investigation will be made into the different behaviours present within the locking regions. In this scheme, in the locked condition, there is a zero frequency separation between the two lasers frequencies while operating in the locked condition, and as a result, this chapter provides the building blocks for the three laser FWM scheme presented in chapter six.

Chapter six will make a contribution to modelling a three laser system based on the FWM scheme, utilising the injection locking approach, as a potential means for generating THz radiation. The scheme is simulated based on the device by Zanola *et al*. [28]. For the first time, the different locking regions are studied in detail for varying detuning frequency values and injection rates, together with varying modulation frequencies. The varying behaviours of the system within the locking regions are thoroughly investigated, and a comparison is drawn with that of the injection locking scheme. The three laser FWM scheme is employed as a method for generating a nonzero frequency spacing between the lasers while operating in the locked condition, with this difference lying within the THz frequency range.

Chapter seven is a continuation from chapter six, making a further contribution to the three laser FWM system, whereby a perturbation is introduced to one of the lasers in order to establish how this effects the overall performance of the system, and whether the three laser FWM scheme provides an improvement in performance over the uncoupled laser, i.e. does the three laser FWM system supress any of the introduced perturbations, and if so, by how much. This is done by calculating the phasor difference between the lasers in order to find one resultant wave, where the amplitude of the resulting wave will be either worse, the same, or improved over the uncoupled laser. This is conducted

with the overall aim of trying to find an optimal locking region in the three laser FWM scheme where the perturbations are significantly supressed.

Finally, chapter eight outlines the main conclusions from each of the three approaches considered within this thesis. Proposals for potential future work are also considered in chapter eight.

Appendix A includes a list of journal papers (accepted for publication by the journals), and conference papers (presented and accepted) that have arisen from the work in this thesis.

REFERENCES

[1] **J. P. Gordon**, H. J. Zeiger, C. H. Townes, "Molecular microwave oscillator and new hyperfine structure in the microwave spectrum of NH_3", Phys. Rev., vol. 95, no. 1, pp. 282-284, May. 1954.

[2] **J. P. Gordon**, H. J. Zeiger, C. H. Townes, "The maser – new type of microwave amplifier, frequency standard, and spectrometer", Phys. Rev., vol. 99, no. 4, pp. 1264-1274, Aug. 1955.

[3] **D. Lindley**, "Invention of the maser and laser", Phys. Rev. Focus., vol. 15, no.4, Jan. 2005.

[4] **W. E. Lamb Jr**, R. C. Retherford, "Fine structure of the hydrogen atom by a microwave method", Phys. Rev., vol. 72, no. 3, pp. 241-243, Aug. 1947.

[5] **A. L. Schawlow**, C. H. Townes, "Infrared and optical masers", Phys. Rev., vol. 112, no. 6, pp. 1940-1949, Dec. 1958.

[6] **T. H. Maiman**, "Stimulated optical radiation in ruby", Nature., vol. 187, pp. 493-494, Aug. 1960.

[7] **J. I. Pankove**, "Influence of degeneracy on recombination radiation in germanium", Phys. Rev., vol. 4, no. 1, pp. 20-21, Jan. 1960.

[8] **M. G. A. Bernard**, G. Duraffoug, "Laser condition in semiconductors", Phys. Status Solidi., vol. 1, no. 7, pp. 699-673, 1961.

[9] **M. I. Nathan**, W. P. Dumke, G. Burns, F. H. Hill, G. Lasher, "Stimulated emission of radiation from GaAs p-n junctions", Appl. Phys. Lett., vol. 1, no. 3, pp. 62-64, Nov. 1962.

[10] **R. N. Hall**, G. E. Fenner, J. D. Kingsley, R. O. Carlson, "Coherent light emission from GaAs junctions", Phys. Rev. Lett., vol. 9, no. 9, pp. 366-368, Nov. 1962.

[11] **M. I. Nathan**, "Invention of the injection laser at IBM", IEEE J. Quantum Electron., vol. QE-23, no. 6, pp. 679-683, Jun. 1987.

[12] **Z. Alferov**, "Double heterostructure lasers: Early days and future perspectives", IEEE Select. Topics Quantum Electron., vol. 6, no. 6, pp. 832-840, Dec. 2000.

[13] **A. A. Qader**, "Polarisation properties of externally driven vertical cavity surface emitting lasers", Ph. D. thesis, Dept. Elect. Eng., Bangor Univ., Bangor, North Wales, 2013.

[14] **I. Hayashi**, M. B. Panish, P. W. Foy, S. Sumski, "Junction lasers which operate continuously at room temperature", Appl. Phys. Lett., vol. 17, no. 3, pp. 109-111, Aug. 1970.

[15] **H. Soda**, K. Iga, C. Kitahara, Y. Suematsu, "GaInAsP/InP surface emitting semiconductor lasers", JPN. J. Apply. Phys., vol. 18, no. 12, pp. 2329-2330, 1979.

[16] **K. Iga**, "Surface-emitting laser – Its birth and generation of new optoelectronics field", IEEE J. Select. Topics Quantum Electron., vol. 6, no. 6, pp. 1201-1215, Nov. 2000.

[17] **K. Iga**, S. Ishikawa, S. Ohkouchi, T. Nishimura, "Room temperature pulsed oscillation of GaAlAs/GaAs surface emitting injection laser," Appl. Phys. Lett., vol. 45, no. 4, pp. 348-350, Aug. 1984.

[18] **F. Koyama**, S. Kinoshita, K. Iga, "Room temperature continuous wave vertical cavity surface emitting laser and high-power 2D laser arrays", Tech. Digest, Conf. Lasers and Electro-Optics, paper FC1, pp. 380-381, 1989.

[19] **T. Baba**, Y. Yogo, K .Suzuki, F. Koyama, K. Iga, "Near room temperature continuous wave lasing characteristics of GaInAsP/InP surface emitting laser", Electron. Lett., vol. 29, no. 10, pp. 913-914, May. 1993.

[20] **S. F. Yu**, Chapter 1 in "Analysis and Design of Vertical Cavity Surface Emitting Lasers", Wiley, New Jersey, p. 1, 2003.

[21] **G. J. Fokken**, W. L. Walters, L. E. Mattson, B. K. Gilbert, "Low cost, multi GHz electrical packaging for serial optoelectronics links utilizing vertical cavity surface emitting lasers", IEEE Trans. Adv. Pack., vol. 23, no. 1, pp. 42-54, Feb. 2000.

[22] **J. A. Hudging**, S. F. Lim, G. S. Li. W. Yuen, K. Y. Lau, C. J. Chang-Hasnain, "Compact, integrated optical disk readout head using a novel bistable vertical cavity surface emitting lasers", IEEE Photon. Technol. Lett., vol. 11, no. 2, pp. 245-247, Feb. 1999.

[23] **J. Geske**, V. Jayaraman, T. Goodwin, M. Culick, M. MacDougal, T. Goodmough, D. Welch, J. Bower, "2.5 Gb/s transmission over 50 km with a 1.3 μm vertical-cavity surface-emitting laser", IEEE Photon. Technol. Lett., vol. 12, no. 12, pp. 1707-1709, Dec. 2000.

[24] **H. Kosaka**, "Smart integration and packaging of 2D VCSEL's of high speed parallel links", IEEE. Select. Topics Quantum Electron., vol. 5, no. 2, pp. 184-192, Mar/Apr. 1999.

[25] **K. Nasahara**, "VSTEP based smart pixels", IEEE J. Quantum Electron., vol. 29, no. 2, pp. 757-768, Feb. 1993.

[26] **T. Leinonen**, Y. A. Morozov, A. Härkönen, M. Pessa, "Vertical external-cavity surface-emitting laser for dual-wavelength generation", IEEE Photon. Technol. Lett., vol. 17, no. 12, pp. 2508-2510, Dec. 2005.

[27] **L. A. Coldren**, S. W. Corzine, Chapter 2 in Diode Lasers and Photonic Integrated Circuits, Wiley, Ney York, pp. 28-50, 1995.

[28] **M. Zanola**, M. J. Strain, G. Giuliani, M. Sorel, "Monolithically integrated DFB lasers for tunable and narrow linewidth millimeter-wave generation", IEEE J. Quantum Electron., vol. 19, no. 4, Paper ID. 1500406, Jul/Aug. 2013.

[29] **H. Sun**, Y. J. Ding, I. B. Zotova, "THz spectroscopy by frequency-tuning monochromatic THz source: From single species to gas mixtures", IEEE Sensors J., vol. 10, no. 3, pp. 621-629, Mar. 2010.

[30] **S. Wang**, B. Ferguson, D. Abbott, X.-C. Zhang, "T-ray imaging and tomography", J. Biol. Phys., vol. 29, no. 2-3, pp. 247-256, 2003.

[31] **D. Mittleman**, R. Jacobsen, R. Neelamani, R. Baraniuk, M. Nuss, "Gas sensing using terahertz time-domain spectroscopy", Apply. Phys. B: Lasers Opt., vol. 67, pp. 379-390, Feb. 1998.

[32] **C. Baker**, T. Lo, W. R. Tribe, B. E. Cole, M. R. Hogbin, M. C. Kemp, "Detection of concealed explosives at a distance using THz technology", Proc. IEEE, vol. 95, no. 8, pp. 1559-1565, Aug. 2007.

[33] **P. H. Siegel**, "Introduction to terahertz (THz): Technology and applications", IEEE. MTT-S Webinars, California Institute of Technology and THz Global, Pasadena, CA, USA., Presented on Jan. 12, 2016.

[34] **C. M. Armstrong**, "The truth about terahertz", IEEE Spectrum., Available: http://spectrum.ieee.org/aerospace/military/the-truth-about-terahertz. [Accessed on: Jun. 10, 2016].

[35] **D. Saeedkia**, R. R. Mansour, S. Safavi-Naeini, "Analysis and design of a continuous-wave terahertz photoconductive photomixer array source", IEEE Trans, Ant and Prop., vol. 53, no. 12, pp. 4044-4050, Dec. 2005.

[36] **A. J. Fitzgerald**, B. E. Cole, P. F. Taday, "Nondestructive analysis of tablet coating thickness using terahertz pulsed imaging", J. Pharm. Sci., vol. 94, no. 1, pp. 177-183, Jan. 2005.

[37] **P. H. Siegel**, "Terahertz technology in biology and medicine", IEEE Trans. Microw. Theory Tech., vol. 52, no. 10, pp. 2438-2447, Oct. 2004.

[38] **M. Scheller**, J. M. Yarborough, J. V. Moloney, M. Fallahi, M. Koch, S. W. Koch, "Room temperature continuous wave milliwatt terahertz source", Optics Express., vol. 18, no. 26, pp. 27112-27117, Dec. 2010.

[39] **D. Grinschkowsky**, S. Keiding, M. Exter, C. Fattinger, "Far-infrared time-domain spectroscopy with terahertz beams of dielectrics and semiconductors", J. Opt. Soc. Am. B., vol. 7, no. 10, pp. 2006-2015, Oct. 1990.

[40] **C. Debus**, P. H. Bolivar, "Frequency selective surfaces for high sensitivity terahertz sensing", Appl. Phys. Lett., vol. 91, no. 18, pp. 184102-1 – 184102-3, Oct. 2007.

[41] **T. Yasui**, T. Yasuda, K. Sawanaka, T. Araki, "Terahertz paintmeter for noncontact monitoring of thickness and drying progress in paint film", Appl. Opt., vol. 44, no. 32, pp. 6849-6856, 2005.

[42] **C. D. Stoik**, M. J. Bohn, J. L. Blackshire, "Nondestructive evaluation of aircraft composites using transmissive terahertz time domain spectroscopy", Opt. Express., vol. 16, no. 21, pp. 17039-17051, 2008.

[43] **C. Jördens**, M. Koch, "Detection of foreign bodies in chocolate with pulsed terahertz spectroscopy", Opt. Eng., vol. 47, no. 3, Mar. 2008.

[44] **P. H. Siegel**, "THz instruments for space", IEEE Trans. Antenn. Propag., vol. 55, no. 11, pp. 2957-2965, Nov. 2007.

[45] **H-W. Hübers**, "Terahertz heterodyne receivers", IEEE J. Select. Topics Quantum Electron., vol. 14, no. 2, pp. 378-391, Mar/Apr. 2008.

[46] **G. Kh. Kitaeva**, "Terahertz generation by means of optical lasers", Laser Phys. Lett., vol. 5, no. 8, pp. 559-576, May. 2008.

[47] **Asian Scientist Newsroom**, "Ultrashort laser bursts to bridge the terahertz gap", Asian Scientist., Available: http://www.asianscientist.com/2015/09/in-the-lab/oist-laser-ablation-terahertz-gap/ [Accessed on: Jun. 10, 2016].

[48] **Z. Wang**, H. Liu, N. Huang, Q. Sun, J. Wen, "Efficient terahertz-wave generation via four-wave mixing in silicon membrane waveguides", Optics Expr., vol. 20, no. 8, pp. 8920-8929, 2012.

[49] **D. Saeedkia**, M. Neshat, S. Safavi-Naeini, "Edge-coupled terahertz photomixer sources for on-chip sensing applications", IEEE Microwave Photon., pp. 187-190, Oct. 2007.

[50] **D. Saeedkia**, "Terahertz photoconductive antennas: Principles and applications", IEEE Proc. 5th Euro. Conf. Ant. Prog., pp. 3326-3328, Apr. 2011.

[51] **D. Saeedkia**, A. H. Majedi, S. Safavi-Naeini, R. R. Mansour, "Analysis and design of a photoconductive integrated photomixer / antenna for terahertz applications", IEEE J. Quantum Electron., vol. 41, no. 2, pp. 234-241, Feb. 2005.

[52] **E. F. Pliński**, "Terahertz photomixer", Bull Pol. Acad. Sci. Techn. Sci., vol. 58, no. 4, 2010.

[53] **D. Marciu**, "Optical limiting and degenerate four-wave mixing in novel fullerenes", Ph. D. thesis, Dept. Phys., Virginia Polytechnic Institute and State Univ., Blacksburg, Virginia, 1999.

[54] **C. W. Thiel**, “Four-Wave mixing and its applications”, Montana State Univ., Available: http://staff.mbi-berlin.de/bfreyer/fwmixing.pdf [Accessed on: Jun. 08, 2016].

[55] **M. Lax**, “Classical noise V. Noise in self-sustained oscillators”, Phys. Rev., vol. 160, no. 2 p. 290, Aug. 1967.

[56] **C. H. Henry**, “Theory of the linewidth of semiconductor lasers”, IEEE J. Quantum Electron., vol. 18, no. 2, pp. 259-264, Feb 1982.

CHAPTER TWO

DUAL-WAVELENGTH VECSEL DESIGNS

One approach for realizing terahertz radiation is utilizing a dual-wavelength laser, with the wavelength separation between them lying within the THz range. This chapter consists of two halves; the first will give a review of the pre-existing work on a dual-wavelength laser as proposed by Leinonen *et al*. [1], underlying the basic principles in their VECSEL design and paying particular attention to their conclusions, whereby their proposed VECSEL worked effectively up to 2.4W of pump power. Beyond this, their laser began showing signs of self-pulsation, where the sinusoidal components of the short and long wavelength pulse components were in strong phase correlation, riding on top of the CW components. They suggest that this occurs due to the Q-switching of the short wavelength component by residual absorption in the deep quantum-wells (QW) which are not located exactly at the nodes of the short wavelength standing wave pattern. The second half of the chapter will then discuss a new structure design inspired by Leinonen *et al*, optimising the new VECSEL structure in detail, to better improve the performance through repositioning the QWs in order to reduce the residual absorption, and through significantly reducing the wavelength spacing between the two wavelengths. This constituted an original contribution presented in this thesis.

The contents of this chapter are organised as follows:

In section 2.1, a general introduction to the dual-wavelength laser will be given, together with the different approaches that have been utilised to implement the dual-wavelength laser. Section 2.2 will then go on to discuss in detail the device proposed by Leinonen *et al*., and the limitations they faced with the device, and why they thought the limitations were apparent. Section 2.3 will then look in detail at the structure proposed by Leinonen *et al*, detailing the exact quantum-well (QW) locations and their alignment with the nodes and antinodes of the short and long wavelength standing wave patterns; hence, sections 2.1-2.3 are a review of the structure proposed by Leinonen *et al*.

Section 2.4 will then discuss the original work done to design a new VECSEL structure inspired by the work of Leinonen *et al*. with two objectives in mind. Firstly, the QWs have been repositioned in an attempt to reduce the residual absorption of the short wavelength component in the deep QWs. Secondly, the wavelength spacing compared to the original structure is significantly reduced. The section will then discuss the potential improvement in performance of the new VECSEL structure compared to the original. Section 2.5 will then discuss the cross-absorption constant between the long wavelength, short wavelength and the corresponding QWs, to quantify the misalignment of the QWs in the long wavelength active region, with respect to the nodes of the short wavelength standing wave

pattern and the antinodes of the long wavelength standing wave pattern. This will be calculated for both the Leinonen *et al*. structure and the newly designed structure, and a detailed comparison of the cross-absorption constant between both structures will be made. Section 2.6 gives a summary of the main conclusions derived from the analysis and design. Hence, sections 2.4-2.6 are the original contributions made to the new dual-wavelength VECSEL design.

2.1 – Introduction

Dual-wavelength lasers are an attractive source for realizing THz radiation as they are an attractive light source for subsequent nonlinear frequency down-conversion and two-wavelength interferometry [1]-[3]. A number of different approaches have been utilized to demonstrate a dual-wavelength laser, including an array of semiconductor lasers where the gain regions have been physically separated [4], external gratings [5], [6], or a coupled-cavity structure, which is either electrically or optically pumped [7]-[10]. From the previous mentioned approaches, the array of semiconductor lasers where the gain regions have been physically separated, and the external grating structures, are somewhat bulky, reducing the attractiveness of those sources, whereas the coupled-cavity structure is much more compact, reducing the size of the device significantly. The downside to this is that such a structure gives an undamped optical mode competition [8], whereby the device would only emit at dual-wavelengths for certain pump current, hence making the emission from this type of dual-wavelength laser unstable, and thus limiting the device to only operate efficiently at restricted intervals of pump currents [8].

The VECSEL (vertical-external-cavity surface-emitting laser) is judged to be a very flexible source of creating bright and coherent sources of radiation [11], [12], and the laser of this geometry can provide an exclusive set of features that are hardly accessible with any other types of laser [12]. These features include the ability of lasing at fundamental wavelengths ranging from 670nm through to 2.35μm, the ability to emit a nearly Gaussian beam profile, and providing a high enough level of output power [12], [13].

Leinonen *et al*. expanded these possibilities in 2005 after they experimentally demonstrated their dual-wavelength VECSEL [1]. A schematic structure of a conventional VECSEL can be seen in figure 2.1, which has been reproduced from chapter one for convenience. In a VCSEL (as illustrated in figure 1.3 of chapter one), the two highly reflecting mirrors are embodied into the laser structure in order to form the optical cavity. However, in a VECSEL, one of these two mirrors is external to the laser structure. As a result, the cavity of the laser includes a free-space region. The VECSEL proposed by Leinonen *et al*. is optically pumped, as illustrated in figure 2.1, and incorporates a series of non-identical quantum-wells (QW) placed in a single gain structure. The VECSEL structure by Leinonen *et*

al. is typical of any other VECSEL geometry, however their QW region has been specifically designed for dual-wavelength emission, which will be discussed in more detail later. Since they introduced their dual-wavelength VECSEL, a number of different modifications have been proposed for a VECSEL emitting at two different wavelengths simultaneously [12], [14].

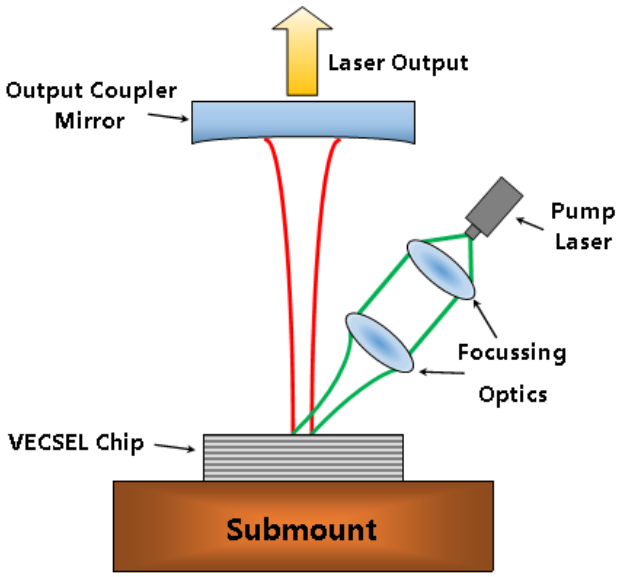

***Figure 2.1**: Schematic structure of an optically pumped VECSEL with a semiconductor gain chip and an external laser resonator.*

These include the introduction of an intracavity Fabry-Pérot (FP) étalon and a Brewster window where the proper free spectral range (FSR) of the tilted étalon allows the VECSEL to oscillate at two wavelengths simultaneously, as proposed by Fan *et al*. [15]. A Fabry-Pérot étalon, also known as a Fabry-Pérot interferometer, is made up of two parallel, flat, semi-transparent mirrors separated by a fixed distance; it is this arrangement that is known as an étalon [16], [17]. When an étalon is placed in the path of a laser beam, it will experience multiple reflections. As a result, interference occurs between the multiple reflections, and this interference will be either constructive, or destructive. The interference which is then outputted from the étalon will cause a modulation in the transmitted and reflected beams [16]. Constructive interference will arise if the transmitted beams are in phase; this correlates with a high-transmission peak of the étalon. Destructive interference occurs when the transmitted beams are out of phase, and this correlates with a transmission minimum [18]. Whether or not the multiple beams are in phase or not depends on the wavelength of the light, the angle at which the light is travelling through the étalon, the thickness of the étalon, and the refractive index of the material between the reflecting surfaces. The transmission spectrum of an étalon will have a series

of peaks in the spectrum, separated by the FSR. The FSR is the wavelength separation between two adjacent transmission peaks, and can be defined as [19]:

$$\Delta\nu_{FSR} = \frac{c}{2L} \tag{2.1}$$

where c is the speed of light and L is the round trip length of the cavity.

A Brewster window is an uncoated substrate which are utilized as polarizers. They are positioned in a laser beam at Brewster's angle, as an alternative to using external mirrors [20]. When positioned at Brewster's angle, the P-polarized component of the light will enter and exit the window without any reflection losses, whereas the S-polarized component of the light will be reflected [20].

Another proposal for modifying a VECSEL for dual-wavelength emission is a two chip co-linear T-cavity VECSEL capable of generating two continuously tunable orthogonally polarized lasing wavelengths [21].

It is believed by Kuznetsov [13] that one of the most important and promising applications of these lasers is the generation of difference-frequency (DF) radiation within the mid-IR up to the THz range through intracavity nonlinear frequency conversion [12]. In 2010, Scheller *et al*. [22] successfully demonstrated a continuous wave THz emission source via the generation of intracavity DF radiation in the dual-wavelength laser based on the proposal of Fan *et al*. [15]. As mentioned above, the work of Fan *et al*. incorporates an intracavity Fabry-Pérot (FP) étalon and a Brewster window in order to obtain dual-wavelength emission. In their work, the design of the active region did not differ from that of an ordinary VECSEL, and was able to oscillate at two wavelengths simultaneously due to the proper FSR of the tilted étalon. The VECSEL structure was designed for emission around the 975nm wavelength, and was grown using metal-organic vapour phase epitaxy on an undoped GaAs substrate. The active region consisted of 14 InGaAs compressive strained QWs, each of which was 8nm thick and surrounded by approximately 31nm thick GaAsP strain compensation layers and AlGaAs pump-absorbing barriers. In strained QWs, a material is used which has a different native lattice constant to that of the surrounding barrier material. If the native lattice constant of the QW is larger than the surrounding lattice constant, then the QW lattice will compress in the plane, and is hence said to be under compressive strain [23].

2.2 – VECSEL Device by Leinonen *et al*.: *An Overview*

The dual-wavelength laser proposed by Leinonen *et al*. [1] has been specifically designed for nonlinear-frequency generation within the mid-IR range. As a result, the active regions contain QWs of different molar compositions. The difference in these compositions provides the generation at two wavelengths; 984nm as the short wavelength and 1042nm for the long wavelength, giving a wide separation of 58nm between both wavelengths [1], [12]. This wavelength separation corresponds to

a frequency spacing of 16.97THz. As mentioned in the introduction, the device proposed by Leinonen *et al*. is typical of any other VECSEL structure, however the QW region has been specifically designed for two wavelength emission. The VECSEL structure proposed by Leinonen *et al*. is illustrated in figure 2.2. The active region, as can be seen in figure 2.2, consists of eight QWs, each 8nm thick, placed in three different regions, I, II and III. The QWs are separated by high potential-energy barriers produced from GaAs which act as absorbers for the pump radiation. Four of these QWs are produced from $In_{0.17}Ga_{0.83}As$ and emit at the short wavelength, λ_S (984nm). These are placed in regions I and III, with two QWs placed in each. Regions I and III are defined as the short wavelength active region. The four other QWs are produced from $In_{0.23}Ga_{0.77}As$ and emit at the long wavelength, λ_L (1042nm). These are placed in region II, and this region is known as the long wavelength active region.

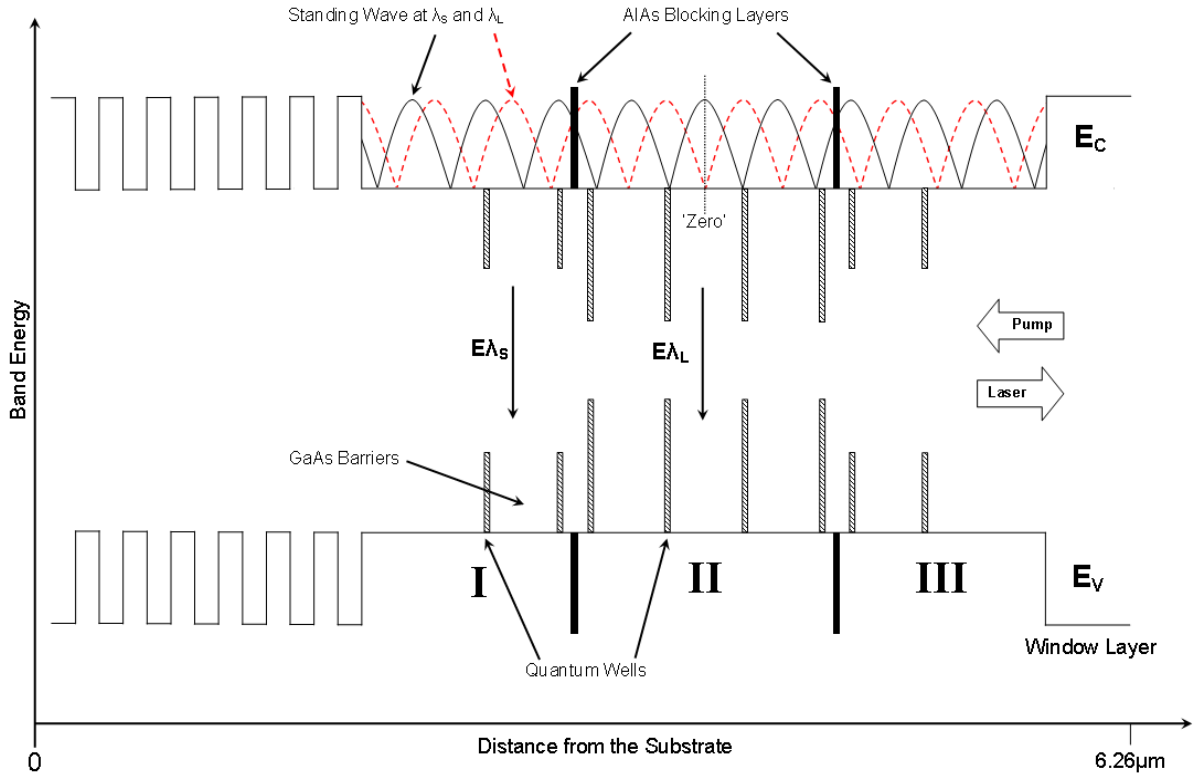

Figure 2.2: *Energy band diagram of a VECSEL as a function of distance from the substrate, showing the two Fabry-Pérot standing wave components, the conduction and valence bands, E_C and E_V, and the positions of the quantum-wells and carrier blocking layers [1].*

The QWs that are located in regions I and III are shallow, and this will provide the gain for the short wavelength, while the QWs in region II are deep, thus providing the gain for the long wavelength. One of the distinguishing features of this structure is that it is possible to separately optically pump all three QW regions at the same time. Blocking layers, produced from wide band-gap AlAs are placed between the regions (which are transparent to the pump wavelength; $\lambda_{pump} < \lambda_S$) which block the

carrier flow from the shallow QWs into the deeper QWs [24]. These barriers play an important part in providing nearly equal pumping of the QWs [1], [12].

In the structure by Leinonen *et al*., the deep QWs are positioned at the nodes of the short wavelength standing wave pattern, λ_S (solid black line from figure 2.2), as can be seen from the amplitude distribution of the fields in the long wavelength active region (region II) from figure 2.2. They are located here in order to minimize the optical absorption of λ_S in the deep QWs. The deep QWs are also located at the antinodes of the long wavelength standing wave pattern, λ_L (red dotted line), to enhance the gain coefficient, and to also provide the maximal use of the available gain. The shallow QWs are located at the antinodes of the short wavelength standing wave pattern, λ_S, in order to provide the maximal use of the available gain. It should be noted that λ_L cannot excite the shallow QWs [1], [12]. The reflection from the gain mirror is provided by a distributed Bragg mirror (DBR) in which a contrast between the refractive indices of the GaAs/AlAs layers is sufficient to ensure a high reflection at both of the generated wavelengths [12]. The total length of the structure is 6.26µm, as can be seen in figure 2.2.

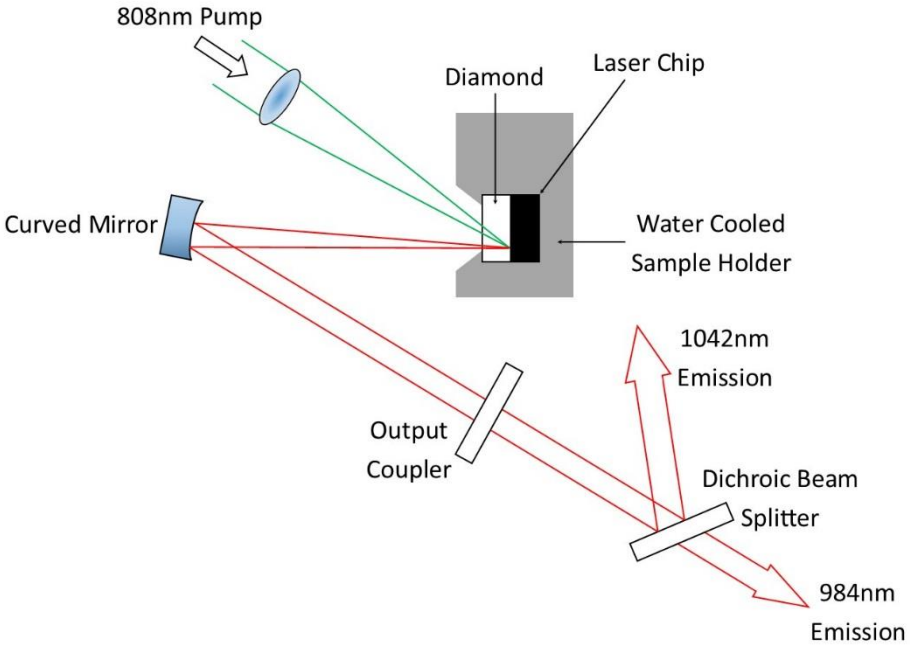

Figure 2.3: *Leinonen et al. experimental setup of a VECSEL [1].*

As previously mentioned, the structure by Leinonen *et al*. has been specifically designed to operate at a long wavelength, λ_L, of 1042nm, and the short wavelength, λ_S, of 984nm, giving a wide separation of 58nm (16.97THz) between the two wavelengths. In their work, Leinonen *et al*. reported that experimentally, the VECSEL structure would emit coherent, continuous wave light at both λ_L and λ_S up to a pump power of 2.4W, where several distinct lines were visible in the emission spectrum. It is

believed that the lines in the emission spectrum originate from the étalon formed by the intracavity diamond, and this effect was apparent even though the diamond was coated with an antireflective coating [1]. The experimental setup employed in their work can be seen in figure 2.3. Beyond pump powers of 2.4W, the VECSEL structure began to show signs of self-pulsation, where the sinusoidal component of the long and short wavelength pulse components were in strong phase correlation, riding on top of the CW components. They suggest that this may be originating from the effect of Q-switching of the short wavelength component by residual absorption in the deep QWs, which are not actually located exactly at the nodes of the short wavelength standing wave pattern [1]. This is where the review of the work by Leinonen *et al*. ends and sections 2.3 onwards give a detailed contribution of the investigation into a new dual-wavelength VECSEL design.

2.3 – VECSEL Device by Leinonen *et al*. – Device Analysis

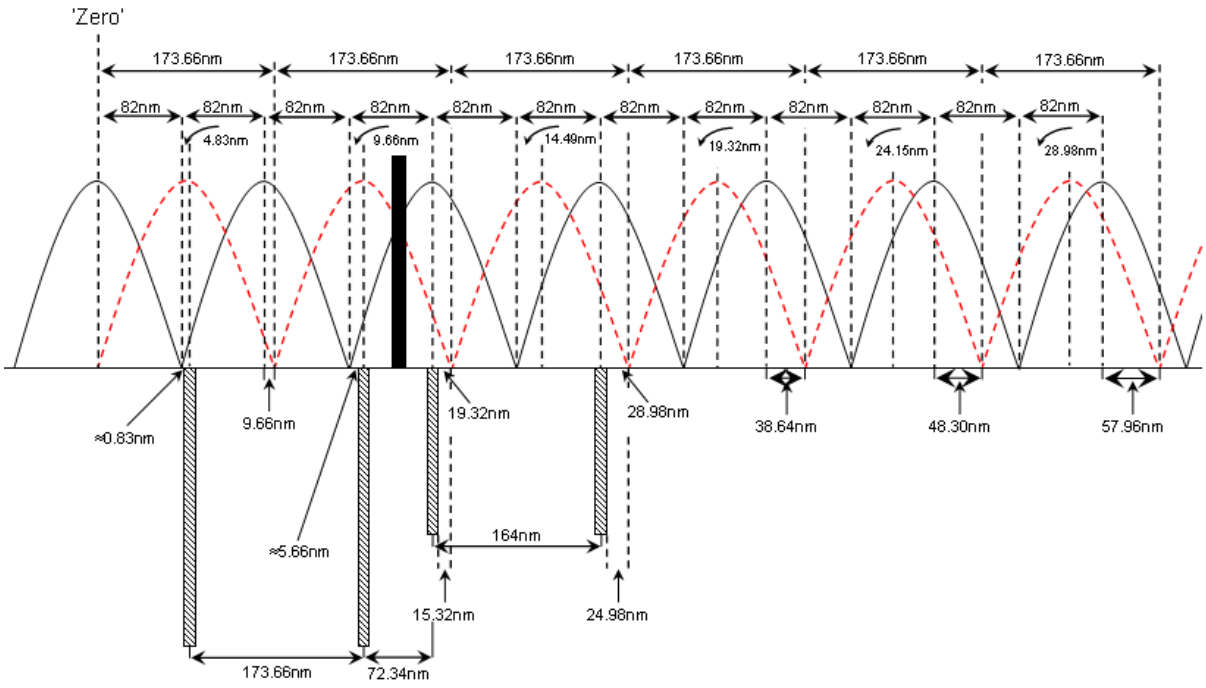

Figure 2.4: *Structure by Leinonen et al. detailing the locations of the quantum-wells in regions II and III compared to the nodes and antinodes of the short wavelength standing wave pattern (solid black line), and the nodes and antinodes of the long wavelength standing wave pattern (red dotted line), and the wide band-gap blocking layer [1].*

Figure 2.4 gives a detailed outline of the VECSEL structure by Leinonen *et al*. from figure 2.2, detailing the locations of the QWs in regions II and III in comparison to the nodes and antinodes of the short and long wavelength standing wave patterns. It also details the location of the wide band-gap blocking layer. In the following analysis, it should be noted that is has been assumed that there are no effects

due to carrier density, and as such there will be no effect of refractive index changes due to carrier density, and hence a so called 'cold cavity' response has been assumed. As such, the assumptions made here may give rise to limitations on the final utility of the results. It has also been assumed that the antinode of the short wavelength standing wave is coincident with the node of the long wavelength standing wave in the middle of the long wavelength active region, i.e. between the two deep QWs. This is consistent with the design proposed by Leinonen *et al*. [1], and this central point has been labelled with 'zero' in figures 2.2 and 2.4. Consequently, figure 2.4 only shows the right hand side of the VECSEL structure from this central point.

The values obtained from figure 2.4 have been calculated, first of all, by taking into account the central point, and from there calculating each wavelength, assuming a refractive index of 3. This gives a short wavelength of 328nm, and a long wavelength of 347.33nm. From there, the half wavelengths of each must be calculated, thus yielding 164nm for the short wavelength and 173.66nm for the long wavelength, as can be seen in figure 2.4. By then assuming that the first deep QW (furthest left in figure 2.4) is located exactly at the antinode of λ_L, then the node of λ_S is calculated to be located 0.83nm to the left of the corresponding deep QW. The remaining QWs are calculated in the same manner.

Further analysis of figure 2.4 gives a clear indication that the deep QWs are not aligned perfectly with the nodes of the short wavelength standing wave pattern. As noted above, examination of the first deep QW shows that the node of λ_S is approximately 0.83nm to the left of that QW, and hence not situated anywhere on that QW. Further analysis shows that the node of λ_S is even further from the edge of the second QW, at a distance of approximately 5.66nm from the left side of that QW. It is therefore clear that the nodes of the short wavelength standing wave pattern are entirely outside each of the deep QWs within the long wavelength active region of region II. Therefore, there is clearly more absorption of the short wavelength light in the deep QWs than intended.

It should also be noted that the deep QWs are 173.66nm away from each other in the long wavelength active region, and the shallow QWs are 164nm away from each other in the short wavelength active region, corresponding to the values calculated above. The QWs either side of the blocking layer are separated by 72.34nm.

It is clear from the analysis of the structure by Leinonen *et al*. that their suggestion that the deep QWs are not actually located exactly at the nodes of the short wavelength standing wave pattern is correct. As a result, there will be unwanted absorption of the short wavelength light into the deep QWs. Section 2.4 will now look at the significant contribution made to designing a new VECSEL structure inspired by Leinonen *et al*.

2.4 – New VECSEL Structure Design

The work conducted in section 2.3 led to the proposal of designing a new laser structure inspired by Leinonen *et al*. in order to achieve two things; firstly, to reduce the absorption of the short wavelength light in the deep QWs by improving the positions of the QWs, and secondly, significantly reducing the wavelength spacing between λ_S and λ_L. As a result, the effect of self-pulsation would be reduced through having reduced the residual absorption in the deep QWs. This is illustrated in figure 2.5. Similar to figure 2.4, figure 2.5 details the locations of the QWs in regions II and III compared to the nodes and antinodes of the short and long wavelength standing wave patterns. It also shows the location of the wide band-gap blocking layer.

For this VECSEL structure, the short wavelength is kept at 984nm, hence the molar composition will remain the same at $In_{0.17}Ga_{0.83}As$, whereas the long wavelength is significantly reduced to 989nm, hence reducing the molar composition of the deep QWs to approximately $In_{0.18}Ga_{0.82}As$. These values give a wavelength separation of only 5nm between the two wavelengths, compared with 58nm previously. This new wavelength spacing corresponds to a frequency spacing of 1.54THz, compared with a frequency spacing of 16.97THz in the original structure. It should also be noted that the length of the structure has been kept the same at 6.26µm.

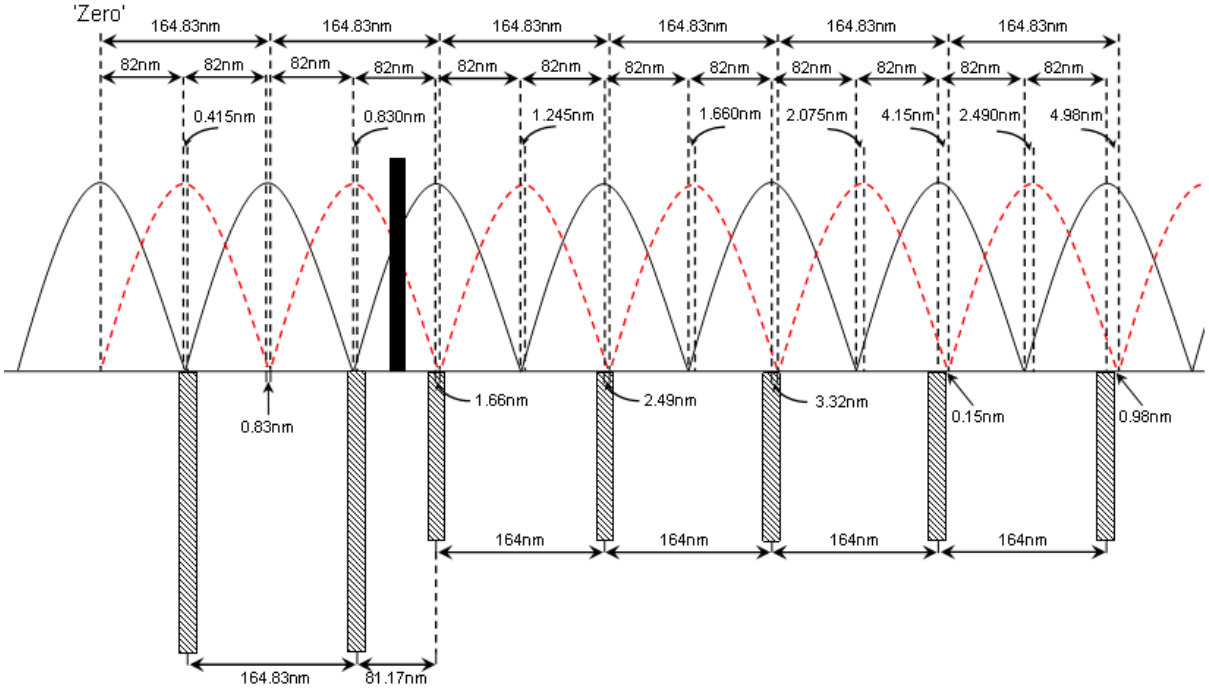

Figure 2.5: *Newly designed structure detailing the locations of the quantum-wells in regions II and III compared to the nodes and antinodes of the short wavelength standing wave pattern (solid black line), and the nodes and antinodes of the long wavelength standing wave (red dotted line), and the wide band-gap blocking layer.*

It has again been assumed that the antinode of the short wavelength standing wave is coincident with the node of the long wavelength standing wave in the middle of the long wavelength active region, thus defining the central point of the structure. This has been denoted with a 'zero' in figure 2.5. The values in figure 2.5 have been calculated using the same method as in section 2.3, also taking into account the reduction in the long wavelength to 989nm. The deep QWs have been located exactly at the antinodes of the long wavelength standing wave pattern, while also being located about the nodes of the short wavelength standing wave pattern.

Analysis of the first deep QW (furthest left in figure 2.5) shows that the node of λ_S, and the antinode of λ_L, align with the QW, with only a difference of 0.415nm between them. When compared to the structure by Leinonen *et al*. where the node of λ_S was 0.83nm away from the left side of the corresponding deep QW, a significant difference is apparent. Examination of the second deep QW yields that again, both the node of λ_S, and the antinode of λ_L, are aligned with the corresponding QW, now with a difference of 0.830nm between them. This again shows a significant difference from the structure by Leinonen *et al*. where the node of λ_S was 5.66nm away from the left edge of the second deep QW. In the short wavelength active region (region III), it can be noted that the nodes of λ_L are all coincident with each QW up until the fourth QW where the node of λ_L is only 0.15nm away from the left edge of that corresponding shallow QW.

The separation between the deep QWs in the long wavelength active region is 164.83nm, compared with 173.66nm previously, and the shallow QWs in the short wavelength active region are again 164nm apart. The separation of the QWs either side of the blocking layer is 81.17nm, increasing the distance by 8.83nm from the VECSEL structure by Leinonen *et al*.

2.5 – Cross-Absorption Constant

For both the structure by Leinonen *et al*. and the newly designed structure, it is important to know the cross-absorption constant between λ_S, λ_L and the corresponding QWs. What this means is that the phase angle (i.e. the phase difference) between the nodes and the antinodes of the standing wave patterns for both wavelengths must be known, and how these compare with the alignment of the deep QWs compared with λ_S in the long wavelength active region, and how these compare with the alignment of the shallow QWs compared with λ_L in the short wavelength active region. From this, a calculation of the overlap integral for each individual QW can then be made. This is an important aspect of the analysis in order to establish what percentage of the short wavelength light is being absorbed into the deep QWs, compared to 100% where the deep QWs are located exactly at the antinodes of the long wavelength standing wave pattern. Figure 2.6 shows the phase angle calculations for the structure by Leinonen *et al*.

The angles in figure 2.6 were calculated using the following formula:

$$f(x) = \sin(k_{S,L}x + \varphi) \tag{2.2}$$

where k is the propagation constant for the short and long wavelengths respectively, x is the horizontal position (in meters), and φ is the phase constant. In order to obtain the phase angle, equation (2.2) must be re-arranged for the phase angle, φ. The propagation constant, k, is defined as:

$$k = \frac{2\pi}{\lambda_{S,L}} rads/m^{-1} \tag{2.3}$$

where $\lambda_{S,L}$ are the short and long wavelengths, respectively.

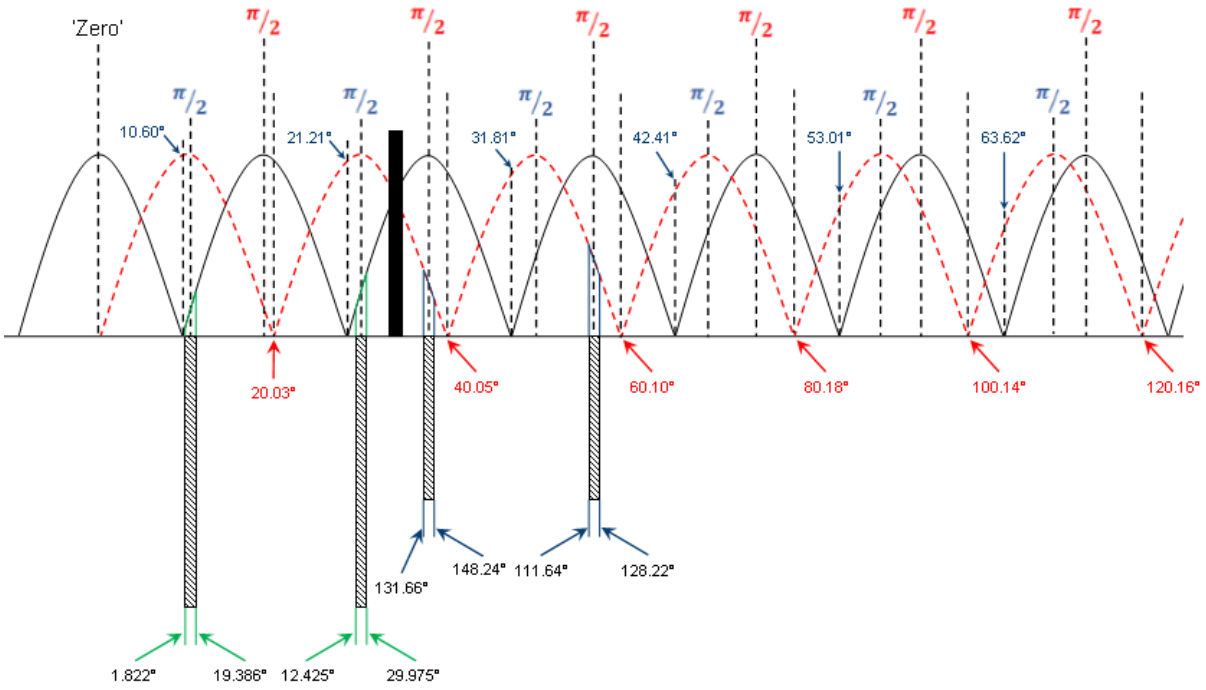

Figure 2.6: *Structure by Leinonen et al. showing the phase angles for the nodes and antinodes of the short wavelength standing wave pattern (solid black line), the long wavelength standing wave pattern (dotted red line), and the quantum-wells in regions II and III.*

For the deep QWs, the distance from the nodes of the short wavelength standing wave pattern to the edge of each corresponding QW must be known. For the first deep QW, (furthest left in figure 2.6), the left edge of the QW, defined as x_2, is calculated to be 0.83nm to the right of the node of λ_S (from figure 2.4), and as the QWs have been assumed to be 8nm thick, the right edge of that QW, defined as x_1, is calculated to be 8.83nm to the right of the node of the short wavelength standing wave.

By applying equations (2.2) and (2.3), the phase angle for x_2 is calculated as $\varphi_1 = -1.822^{\circ}$ and x_1 is calculated as $\varphi_2 = -19.386^{\circ}$. The angles for the shallow QWs were calculated by applying the same method, however the distances for the edges of the QWs were calculated from the nodes of the long wavelength standing wave pattern, as appose to the short wavelength standing wave pattern. The

value of k is also calculated taking into consideration the new, reduced, long wavelength value. Figure 2.7 shows the calculated angles for the new VECSEL structure design. Analysis of figure 2.7 shows that the angles for the newly designed VECSEL are significantly different to those of the structure by Leinonen *et al*.

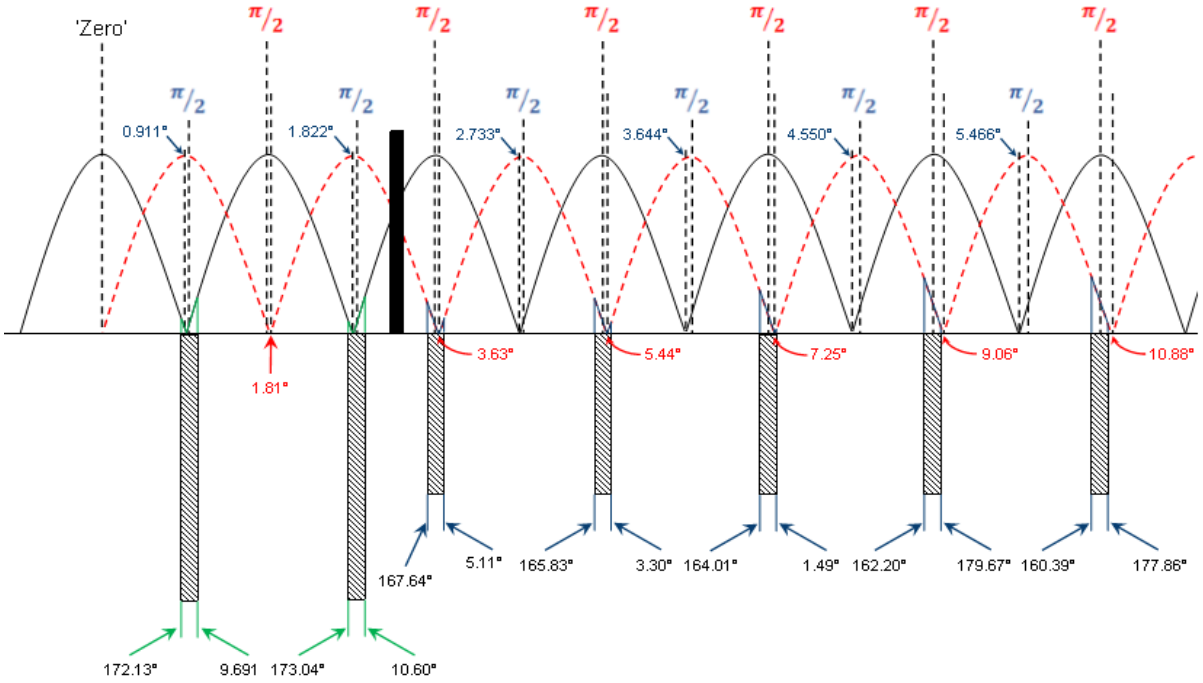

Figure 2.7: *Newly designed structure showing the phase angles for the nodes and antinodes of the short wavelength standing wave pattern (solid black line), the long wavelength standing wave pattern (dotted red line), and the quantum-wells in regions II and III.*

Calculation of the overlap integral between λ_S, λ_L and the corresponding QWs is an important aspect of this analysis, as previously discussed. The overlap integral is defined as the ratio of the absorption of λ_S in the deep QWs in the long wavelength active region (compared with the total overlap where the deep QWs are aligned exactly with the antinodes of the long wavelength standing wave pattern). It is also defined as the ratio of λ_L that aligns with the shallow QWs in the short wavelength active region (again, compared with the total overlap where the shallow QWs are aligned exactly with the antinodes of the short wavelength standing wave pattern). This overlap integral is defined as:

$$a = \frac{\int_{\varphi_2/k_S}^{\varphi_1/k_S} \cos(k_S x - \Phi) dx}{\int_{-\varphi/k_L}^{\varphi/k_L} \cos(k_L x)\, dx} \tag{2.3}$$

The overlap integrals for the original VECSEL structure were calculated to be 0.28840 for the deep QWs (corresponding to a value of 100%, as illustrated in figure 2.8, where the deep QWs are located exactly at the antinodes of λ_L) and 0.30530 for the shallow QWs (corresponding to a value of 100%, again as illustrated in figure 2.8, where the shallow QWs are located exactly at the antinodes of λ_S).

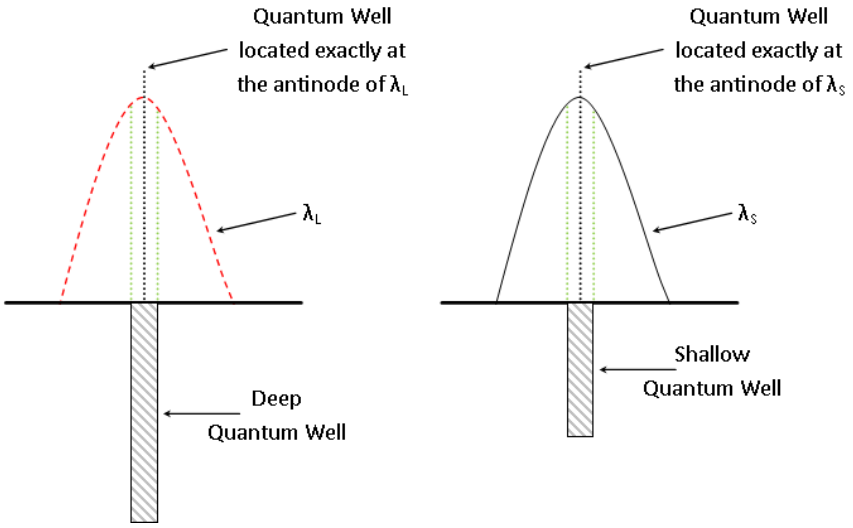

Figure 2.8: *Alignment of the deep and shallow QWs at the antinodes of λ_L and λ_S respectively.*

For the newly designed structure in figure 2.7, the overlap integral for the deep QWs will be different from the structure by Leinonen *et al*. due to the reduction in value for λ_L, from 1042nm down to 989nm. The overlap for the newly designed structure was calculated to be 0.30382 (corresponding to a value of 100%, again, where the deep QWs are located exactly at the antinodes of λ_L).

Quantum-Well	Overlap	As a Percentage
Deep 1	0.0561	19.45
Deep 2	0.1103	38.25
Shallow 1	0.1853	60.69
Shallow 2	0.2505	82.05

Table 2.1: *Table to show the overlap integral for both the deep and shallow QWs, and then as a percentage for the structure by Leinonen et al.*

Quantum-Well	Overlap	As a Percentage
Deep 1	0.0465	15.305
Deep 2	0.0465	15.305
Shallow 1	0.0492	16.115
Shallow 2	0.0492	16.115
Shallow 3	0.0492	16.115
Shallow 4	0.0478	15.657
Shallow 5	0.0573	18.768

Table 2.2: *Table to show the overlap integral for both the deep and shallow QWs, and then as a percentage for the newly designed structure.*

Tables 2.1 and 2.2 show the difference in overlap between each QW in the original and newly designed VECSEL structures. From the tables, it is clear that the overlaps for the QWs in the new structure design are much smaller, than in the original VECSEL structure. It can also be seen from the tables that the percentages in the newly designed structure are much smaller than those in the original VECSEL structure. The percentage are calculated utilising equation (2.4).

$$Overlap\ Percentage = \frac{Overlap}{A\ Value\ of\ 100\%} \times 100 \tag{2.4}$$

The minimum percentage in the original structure was 19.45%, compared to a maximum percentage in the newly designed structure of 18.768%. The percentages of interest are the ones corresponding to the deep QWs, as this is where the short wavelength component was being absorbed, thus causing the unwanted residual absorption. It is clear to see that the new structure design shows a significant percentage improvement in overlap values. The first deep QW shows an improvement of 21% in the newly designed structure compared to that by Leinonen *et al.*, thus suggesting a significant short wavelength absorption reduction. The second deep QW shows an improvement of 60% in the newly designed structure, thus suggesting an even greater reduction in short wavelength absorption than in the original VECSEL structure.

2.6 – Conclusion

A structure has been proposed to generate dual-wavelength emission with greatly reduced wavelength separation and much reduced cross-absorption to that reported by Leinonen *et al*. A new structure was designed in order to achieve two goals; firstly, to reduce the absorption of the short wavelength light in the deep QWs by improving the positions of the QWs, and secondly, significantly reducing the wavelength spacing between λ_S and λ_L, from 58nm (16.97THZ) down to 5nm (1.54THz). This would result in the effect of self-pulsation being reduced through having reduced the residual absorption in the deep QWs.

It is apparent from this analysis that the newly designed structure, where the long wavelength has been significantly reduced from 1042nm down to 989nm, shows evidence of containing much smaller overlap values between λ_S, λ_L and the corresponding QWs in both the long and short wavelength active regions. As a result, in the newly designed structure, the nodes of λ_S and the antinodes of λ_L both align with the deep QWs in the long wavelength active region. It is suggested that reducing this overlap would improve the performance of the VECSEL structure to allow the VECSEL to operate at higher pumping levels, and hence suggests a reduction in the effect of self-pulsation having reduced the residual absorption in the deep QWs.

The effect that must be carefully considered in a dual-wavelength VECSEL when the two wavelengths are close together (only 5nm apart in this case), is linewidth broadening. When the separation

between the two wavelengths is so close, it is possible that only one broad peak will appear in the spectrum of the laser, and this will be discussed in more detail in chapters three and four.

REFERENCES

[1] **T. Leinonen**, Y. A. Morozov, A. Härkönen, M. Pessa, "Vertical external-cavity surface-emitting laser for dual-wavelength generation", IEEE Photon. Technol. Lett., vol. 17, no. 12, pp. 2508-2510, Dec. 2005.

[2] **C. L. Wang**, C. L. Pan, "Tunable multiterahertz beat signal generation from a two-wavelength laser-diode array", Opt. Lett., vol. 20, no. 11, pp. 1292-1294, Jun. 1995.

[3] **C. L. Wang**, Y. H. Chuang, C. L. Pan, "Two-wavelength interferometer based on a two-colour laser-diode array and the second-order correlation technique", Opt. Lett., vol. 20, no. 9, pp. 1071-1073, May. 1995.

[4] **K. Poguntke**, J. B. D. Soole, A. Scherer, H. P. LeBlance, C. Caneau, R. Baht, M. A. Koza, "Simultaneous multiple wavelength operation of a multistripe array grating integrated cavity laser", Appl. Phys. Lett., vol. 62, no. 17, pp. 2024-2026, April. 1993.

[5] **C. F. Lin**, M. J. Chen, B. L Lee, "Wide-range tunable dual-wavelength semiconductor laser using asymmetric dual quantum wells," IEEE Photon. Technol. Lett., vol. 10, no. 9, pp. 1208-1210, Sept. 1998.

[6] **T. Hidaka**, Y. Hatano, "Simultaneous two wave oscillation LD using biperiodic binary grating", Electron. Lett., vol. 27, no. 12, pp. 1075-1076, Jun. 1991.

[7] **P. Pellandini**, R. P. Stanley, R. Houdre, U. Oesterle, M. Ilegems, "Dual-Wavelength laser emission from a coupled semiconductor micro-cavity", Appl. Phys. Lett., vol. 71, no. 7, pp. 864-866, Aug. 1997.

[8] **V. Badilita**, J. F. Carlin, M. Ilegems, K. Panajotov, "Rate-equation model for coupled-cavity surface-emitting lasers", IEEE J. Quantum Electron., vol. 40, no. 12, pp. 1646-1656, Dec. 2004.

[9] **J. F. Carlin**, R. P.Stanley, P. Pellandini, U. Oesterle, M. Ilegems, "The dual wavelength bi-vertical cavity surface emitting laser", Appl. Phys. Lett., vol. 75, no. 7, pp. 908-910, Aug. 1999.

[10] **D. M. Grasso**, K. D. Choquette, "Threshold and modal characteristics of composite-resonator vertical-cavity lasers", IEEE J. Quantum Electron., vol. 39, no. 12, pp. 1526-1530, Dec. 2003.

[11] **A. C. Trooper**, H. D. Foreman, A. Carnache, K. G. Wilcox, S. H. Hoogland, "Vertical-external-cavity semiconductor laser", J. Phys. D: Appl. Phys., vol. 37, no. 9, pp. R75-R85, Apr. 2004.

[12] **Y. A. Morozov**, M. Y. Morozov, "Intracavity Nonlinear Frequency Down-Conversion in a Continuous-Wave Operation Regime of a Dual-Wavelength Vertical-External-Cavity Surface-Emitting Laser", IEEE J. Quantum Electron., vol. 19, no. 5, Paper ID. 1702105, Sep/Oct. 2013.

[13] **M. Kuznetsov**, "VCSEL Semiconducot Lasers: A Path to High-Power, Quality Beam and UV to IR Wavelength by Design, 1st ed. Wiley-VCH, 2010.

[14] **V. Pal**, P. Trofimoff, B. X. Miranda, G. Baili, M. Alouini, L. Morvan, D. Dolfi, F. Goldfarb, I. Sagnes, R. Ghosh, F. Bretenaker, "Measurement of the coupling constant in a two-frequency VECSEL", Opt. Exp., vol. 18, no. 5, pp. 5008-5014, Feb. 2010.

[15] **L. Fan**, M .Fallahi, J. Hader, A. R. Zakharian, J. V. Moloney, W. Stolz, S. W. Koch, R. Bedford, J. T. Murray, "Linearly polarized dual-wavelength vertical-external-cavity surface-emitting laser", Appl. Phys. Lett., vol. 90, pp. 181124-1 – 181124-3, May. 2007.

[16] **Light Machinery**, "Designing and specifying Fabry-Pérot étalons", [Online]. Available: http://old.lightmachinery.com/Specifying-Fabry-Perot-Etalons.html. [Accessed on: Jun. 20, 2016].

[17] **R. Paschotta**, article on 'étalons' in the Encyclopaedia of Laser Physics and Technology, 1. edition, October 2008, Wiley-VCH, ISBN 978-3-527-40828-3.

[18] **R. A. Bacon**, "Fabry-Pérot interferometer", Dept. Phys., Surrey Univ., [Online]. Available: http://www.ph.surrey.ac.uk/UserFiles/File/Microsoft%20Word%20%20Two%20week%20exp_Fabry%20Perot%281%29.pdf. [Accessed on: Jun. 20, 2016].

[19] **R. Paschotta**, article on 'free spectral range' in the Encyclopaedia of Laser Physics and Technology, 1. edition, October 2008, Wiley-VCH, ISBN 978-3-527-40828-3.

[20] **AZO Optics**, "Brewster window – definition and applications", [Online]. Available: http://www.azooptics.com/Article.aspx?ArticleID=858. [Accessed on: Jun. 20, 2016].

[21] **C. Hessenius**, M. Lukowski, M. Fallahi, "High-power tunable two-wavelength generation in a two chip co-linear t-cavity vertical external cavity surface-emitting laser", Appl. Phys. Lett., vol. 101, pp. 121110-1 – 121110-3, Sept. 2012.

[22] **M. Scheller**, J. M. Yarborough, J. V. Moloney, M. Fallahi, M. Koch, S. W. Koch, "Room temperature continuous wave milliwatt terahertz source", Optics Express., vol. 18, no. 26, pp. 27112-27117, Dec. 2010.

[23] **L. A. Coldren**, S. W. Corzine, Chapter 4 in Diode Lasers and Photonic Integrated Circuits, Wiley, New York, p.161, 1995.

[24] **J. Geske**, K. –G. Gan. Y. L. Okuno, J. Piprek, J. E. Bowers, "Vertical-cavity surface-emitting laser active regions for enhanced performance with optical pumping", IEEE J. Quantum Electron., vol. 40, no. 9, pp. 1155-1162, Sep. 2004.

CHAPTER THREE

LINEWIDTH BROADENING

In chapter two, the notion of the dual-wavelength VECSEL was introduced as a potential way of realizing THz radiation. There, the work of Leinonen *et al*. [1] was presented, together with the limitations they discovered with their VECSEL structure when operating above 2.4W of pump power. This led to the proposal of designing a new VECSEL structure with a significantly reduced wavelength spacing (5nm compared to 58nm) and with reduced coupling between the short wavelength, long wavelength and the corresponding QWs by improving the positons of the QWs such that both the antinodes of the long wavelength standing wave pattern, and the nodes of the short wavelength standing wave pattern, both align with the deep QWs. This reduces the amount of residual absorption of the short wavelength light in the deep QWs. The effect that must be carefully considered when both wavelengths are so close together is linewidth broadening, and this will be discussed in this chapter. This chapter will recap the theory of the famous Schawlow-Townes linewidth equation [2], and how the Schawlow-Townes derivation was modified by Melvin Lax [3] and enhanced by Charles Henry [4] in order to obtain the full-width half-maximum (FWHM) linewidth for edge-emitting lasers. This chapter also investigates how the same Schawlow-Townes equation may be applied to both VCSELs and VECSELs [5].

The contents of this chapter are organised as follows:

Section 3.1 will give a brief introduction to the notion of linewidth broadening. Section 3.2 will then go on to review the famous Schawlow-Townes linewidth equation, and how they obtained their equation for the linewidth of a laser line through their work with masers. Section 3.3 will then go on to review that the same Schawlow-Townes linewidth equation may be applied to surface-emitting lasers, VCSELs, and external-cavity lasers, VECSELs. Section 3.4 will give a brief summary of the main conclusions from this chapter, and how the Schawlow-Townes linewidth equation will be applied to the dual-wavelength laser structure by Leinonen *et al*., and the newly designed VECSEL structure (presented in chapter two), which will be discussed in chapter four.

3.1 – Introduction

When a laser is operating under steady-state conditions, it can be assumed that the carrier and photon densities remain constant. Theoretically, this presumption is valid, however in practice, this is not the case, as random carrier and photon recombination and generation events are present. This in turn

leads to instantaneous variations in time in the carrier and photon densities. This effect is evident even when no current modulation is applied to the laser [6]. As a result, variations in the photon density apply, which lead to variations in the magnitude of the output power, which consequently provides a noise floor. Variations will also be evident in the carrier density, and will result in variations in the output wavelength. This all results in a finite spectral linewidth for the lasing mode [6]. When the laser is in operation, it will produce both intensity and frequency noise. Both of these effects can adversely affect the lasing spectrum of the laser. If great care is not taken, experiments will show that typical linewidths of laser didoes will be in excess of a megahertz. This would not be ideal for applications such as sensor or communications systems which use coherent detection, where linewidths of much less than a megahertz are desirable. As a result, a detailed understanding of the inherent linewidth of diode lasers is of great practical importance [7].

3.2 – Schawlow-Townes Linewidth

The finite linewidth of a laser line is a result of fluctuations in the phase at the output of the optical field. These fluctuations occur as a result of either spontaneous emission, or carrier density fluctuations [3], [6]-[9]. This will alter the phase and intensity of the lasing field, as illustrated in figure 3.1.

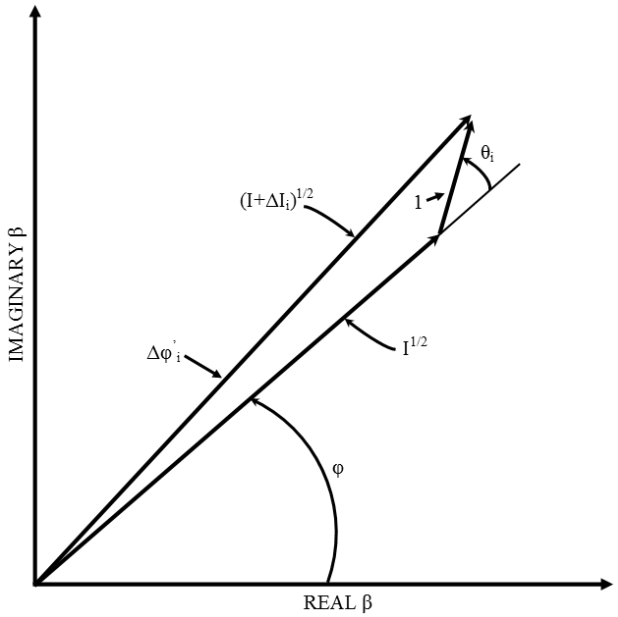

Figure 3.1: *The instantaneous changes of the phase, φ, and intensity, I, of the optical field caused by the ith spontaneous emission event. The field amplitude $\beta = I^{1/2}exp(i\varphi)$ increases by $\Delta\beta_i$ having an amplitude of unity and a phase $\varphi + \theta_i$, where θ_i is a random angle [4].*

Spontaneous emission is intrinsic in all lasers, and occurs as a result of the random addition of spontaneously emitted photons to the quasi-coherent resonant mode. Carrier density fluctuations are only considered to be of significant importance in diode lasers, and this effect occurs as a result of the proportionality between the carrier density, ΔN, and the linewidth, $\Delta \nu$, which are characterised by the frequency shift in response to changes in the carrier density [4], [7], which is defined as:

$$\Delta \nu = \frac{\alpha}{4\pi} \Gamma v_g a \Delta N \tag{3.1}$$

where Γ is the confinement factor, v_g is the group velocity and a is the differential gain. In equation (3.1), α is the *linewidth enhancement factor* (also known as the Henry Alpha factor, α_H) [4], [8], [11]. It is necessary to include the linewidth enhancement factor in the constant of proportionality because both the gain and the index of refraction depend directly upon the carrier density. The linewidth enhancement factor defines the relationship between how the real and imaginary indices are affected by the carrier density, and hence can be defined as [4], [8], [11]:

$$\alpha = \frac{\Delta n'}{\Delta n''} = -\frac{dn/dN}{dn_i/dN} = -\frac{4\pi}{\lambda}\frac{dn/dN}{dg/dN} = -\frac{4\pi}{\lambda a}\frac{dn}{dN} \tag{3.2}$$

where $\Delta n'$ is the deviation of the real part of the refractive index from its steady-state value, and $\Delta n''$ is the deviation of the imaginary part of the refractive index from it's steady-state value. The linewidth enhancement factor is a material parameter whose value is dependent upon the lasing frequency and on the threshold carrier concentration of the laser. Analysis of equation (3.2) shows that:

$$-\frac{4\pi}{\lambda}\frac{dn/dN}{dg/dN} \tag{3.3}$$

represent the differential refractive index and the gain, with respect to the carrier concentration within the laser cavity [8].

In semiconductor lasers, it is very desirable to reduce the linewidth enhancement factor, α, to zero, so that consequently, the subsequent linewidth of the lasing spectrum can be minimized. This is of primary importance in semiconductor lasers as α plays a critical role in determining the field linewidth, the chirping characteristics, and in any attempt to control these characteristics. It should also be noted that α has a strong wavelength dependence, and this reflects the spectral shape of the differential gain [8].

3.2.1 – Schawlow-Townes Linewidth: *A Brief History*

The first theoretical model for the linewidth of a laser was developed by Schawlow and Townes in 1958 before even the first laser was experimentally demonstrated [2]. Schawlow and Townes calculated the fundamental (quantum) limit for the linewidth in analogy to the linewidth of masers. The energy emitted from such a maser is usually an extremely monochromatic wave, and as a result, the energy produced by stimulated emission is much larger than that produced by spontaneous

emission, or to the normal background of thermal radiation. The frequency range over which appreciable energy is distributed is given by the following formula, and this is known as the *Schawlow-Townes* equation [2], [12].

$$\Delta\nu_{laser} = \frac{4\pi h\nu(\Delta\nu_c)^2}{P_{out}} \tag{3.4}$$

where $h\nu$ is the photon energy, $\Delta\nu_c$ is the half-width at half-maximum (HWHM) of the resonator bandwidth, and P_{out} is the output power. In the derivation of this equation, it has been assumed that there are no parasitic cavity losses [12]. In the development of the equation, Schawlow and Townes used the assumption of fluctuations in the phase of the optical field, and through this, they successfully explained the linewidth phenomena of gas lasers [13] such as the Lorentzian shape of the linewidth spectrum, and also the inverse relation between $\Delta\nu$ and the output power of such lasers [8].

3.2.2 – Schawlow-Townes Equation: *A Derivation*

In order to derive the Schawlow-Townes formula, it is first necessary to consider a simplified derivation of the spontaneous emission component of the laser linewidth. Even though this derivation is not entirely accurate for lasers operating above threshold, it does provide an instinctive sense of the origin of a finite laser linewidth [7].

In the derivation of the carrier and photon density rate equations, the cavity lifetime is characterized as the natural decay rate of photons in the resonant cavity when stimulated or spontaneous emission sources are not present. Through this concept, with the absence of sources, the photon density rate equation [14] may be defined as:

$$\frac{dN_p}{dt} = \left[\Gamma v_g g - \frac{1}{\tau_p}\right] N_p + \Gamma {R_{sp}}' \tag{3.5}$$

which will have the following solution [7]:

$$N_p(t) = N_{p0} e^{-t/\tau_p} \tag{3.6}$$

where N_p is the photon density, Γ is the confinement factor, v_g is the group velocity, g is the gain per unit length, τ_p is the photon lifetime and ${R_{sp}}'$ is the spontaneous emission rate per unit active volume into one optical mode [15]. The spontaneous emission rate per unit active volume, ${R_{sp}}'$, is defined as [16]:

$${R_{sp}}' = R_{sp}\beta_{sp} \tag{3.7}$$

where R_{sp} is the spontaneous emission term, and β_{sp} is the spontaneous emission factor.

From equation (3.6), the full-width half-maximum (FWHM) linewidth of the 'cold cavity' response (i.e. the undriven response) may be represented by $\Delta\omega = 1/\tau_p$, and hence corresponds to the filter bandwidth of a Fabry-Pérot resonator mode in which no active materials are present, hence being referred to as a 'cold cavity'. The pivotal point here is that the resonant width is linked with the photon

decay rate, and by re-including the stimulated emission term (which gives the gain in the cavity), from the photon density rate equation from equation (3.5), the same exponential solution in time is obtained, however it can now be identified by a new *effective* cavity lifetime [7]:

$$\frac{1}{\tau_p{}'} = \frac{1}{\tau_p} - \Gamma v_g g \tag{3.8}$$

As the gain in the cavity compensates for the losses in the cavity, the effective carrier lifetime will increase, and as a result, by including the gain terms, the FWHM linewidth will become $\Delta\omega = 1/\tau_p{}'$. Hence, as $\tau_p{}'$ increases, the resonance width will decrease, and consequently, the photon density rate equation from equation (3.5) can be solved in the steady-state for N_p [7]:

$$N_p = \frac{\Gamma R_{sp}{}'}{1/\tau_p - \Gamma v_g g} \tag{3.9}$$

Utilizing equation (3.9) to replace $\left[1/\tau_p - \Gamma v_g g\right]$ in equation (3.8), it is possible to express the driven FWHM linewidth as [7]:

$$\Delta v_{spon} = \frac{1}{2\pi\tau_p{}'} = \frac{\Gamma R_{sp}{}'}{2\pi N_p} \tag{3.10}$$

Equation (3.10) applies only for spontaneous emission effects, and is equivalent to the Schawlow-Townes equation [2], [12]. From equation (3.10), it can be concluded that the linewidth will vary inversely with the photon density, or with the output power. As the photon density within the laser cavity can grow very large, the linewidth can consequently collapse into a very narrow spectral line, and this, of course, is one of the distinctive features of a laser [7].

3.2.3 – Schawlow-Townes Equation: *Shortcomings*

The Schawlow-Townes equation does suffer from some shortcomings. Although it provides an accurate below threshold linewidth evaluation, and is thus correct for amplified spontaneous emission (ASE) problems, whereby the light that is produced by spontaneous emission, has been optically amplified by stimulated emission in the gain medium, when considering laser operation above threshold, the noise expressed in equation (3.10) is half 'in phase' (intensity) noise, and half 'in quadrature' noise [17]. This leads to a factor of two reduction in the linewidth derived by Schawlow and Townes, corrected by Melvin Lax in 1967 [3], [7], [12]. Through inclusion of a correction factor of $1/2$, and by converting the linewidth values in equation (3.4) to full-width half-maximum (FWHM) values (rather than half-width half-maximum), the modified Schawlow-Townes linewidth equation [7], [12] may be obtained:

$$\Delta v_{laser} = \frac{\pi\, hv\, (\Delta v_c)^2}{P_{out}} = \frac{\Gamma R_{sp}{}'}{4\pi N_p} \tag{3.11}$$

There are still some shortcomings with the modified Schawlow-Townes linewidth expression. Equation (3.11) only takes into account the spontaneous emission noise, and hence has neglected to include the carrier noise [7]. The Schawlow-Townes equation has also underestimated $\Delta\nu$ for semiconductor lasers by a factor of 30. This has occurred due to the disregard by Schawlow and Townes of the variation of the refractive index with the carrier concentration present inside the semiconductor materials [4], [8], [9]. The refractive index variation is as a result of the spontaneous-emission-induced phase and intensity change in the laser field. During laser operation, it must return to its steady-state condition, and in order for the laser to achieve this, it must undergo relaxation oscillations. Typically, these last approximately 1ns. During these relaxation oscillations, the laser will undergo a net gain change, equivalent to:

$$\Delta g(t) = (-2\omega/c)\Delta n''(t) \tag{3.12}$$

where $\Delta n''(t)$ is defined as the deviation of the imaginary part of the refractive index from it's steady-state value. The apparent change in n'' is as a result of a change in the carrier density, which will in turn alter the real part of the refractive index, n'. Hence, through the laser returning to its steady-state, it causes changes in the imaginary and real parts of the refractive index. The ratio of these changes is defined as the linewidth enhancement factor [4], [8], [18] as seen in equation (3.2). During a finite period of time, a change in $\Delta n'$ will result in an additional phase shift of the laser field, and as a result, an additional broadening of the laser line will be apparent [4].

To take into account the carriers that influence the induced index change, it is necessary to include the linewidth enhancement factor, α, in the expression for laser linewidth [8]. By referring back to the equation obtained for the linewidth enhancement factor in equation (3.2), it is clear that α is mainly dependent upon the physical properties of the laser material, and as a result, the modified equation for laser linewidth, $\Delta\nu$, may be expressed as [8], [19]:

$$\Delta\nu = \Delta\nu_{ST}(1+\alpha^2) = \frac{\Gamma {R_{sp}}'}{4\pi N_p}(1+\alpha^2) \tag{3.13}$$

where $\Delta\nu_{ST}$ is the modified Schawlow-Townes equation from equation (3.11) (a detailed derivation of $\Delta\nu$ was made by Charles Henry in 1982 [4]), and is thus *enhanced* by $1+\alpha^2$ in semiconductor lasers. This is where α obtains its identity as the linewidth enhancement factor [4], [18], [19]. In the enhancement of $1+\alpha^2$, the 1 represents the noise due to spontaneous emission, while α^2 represents the carrier noise contribution to linewidth [19].

3.3 – VCSEL and VECSEL Linewidth

3.3.1 – VCSEL Linewidth

The theoretical linewidth for VCSELs is provided by the same expression as for edge-emitting lasers. As discussed in section 3.2.3, the theoretical linewidth for edge-emitting lasers is provided by the modified Schawlow-Townes linewidth multiplied by a carrier noise enhancement factor of $(1+\alpha^2)$ defined in equation (3.13) [19]. This equation provides the FWHM linewidth for edge-emitting lasers, and the same equation may be applied to VCSELs [5]. For simplicity here, equation (3.7) may be substituted into equation (3.13) so that the full-width half-maximum (FWHM) linewidth may be written as [5]:

$$\Delta\nu = \Delta\nu_{ST}(1+\alpha^2) = \frac{\Gamma R_{sp}\beta_{sp}}{4\pi N_p}(1+\alpha^2) \tag{3.14}$$

The way in which equation (3.14) is defined suggests that the linewidth is directly proportional to the spontaneous emission factor, β_{sp}, however this is not the case. Firstly, account must be taken for the proportionality between the spontaneous emission and the gain given to the mode defined as [5]:

$$\beta_{sp}R_{sp}V = \Gamma g v_g n_{sp} \tag{3.15}$$

where n_{sp} is the population inversion factor.

Secondly, account must also be taken for the fact that the modal gain will clamp near the level of modal losses $(\beta_{sp} \ll 1)$ [5], which is typical for both edge-emitting and VCSEL type lasers.

Through careful consideration of these effects, equation (3.14) may be expressed in terms of the physical device parameters. The photon density rate equation must first be considered [5], which was defined in equation (3.5) [14], [20]. As previously discussed, in equation (3.5), the spontaneous emission rate per unit active volume, $R_{sp}{}'$, is defined as $R_{sp}\beta_{sp}$ where β_{sp} is the spontaneous emission factor, and R_{sp} is the spontaneous emission rate of carriers, which gives the generation rate of photons. It is possible to define the terms $g v_g N_p$ as the stimulated recombination of carriers (the generation rate of photons), where g is the incremental optical gain in the active material, and v_g is the group velocity in the axial direction of the mode under consideration. Γ is the confinement factor, and τ_p is the photon lifetime within the cavity [5].

A threshold modal gain value that equals the modal losses in the steady-state must be defined, hence [21]:

$$\Gamma g_{th} = \frac{1}{v_g \tau_p} = \langle\alpha_i\rangle + \alpha_m \tag{3.16}$$

where $\langle\alpha_i\rangle$ the incremental internal power loss, and α_m the facet loss (also known as the distributed mirror loss), which was given in chapter one through equation (1.26).

Through combinations of equations (3.5) and equation (1.28) from chapter one, which defines the gain at threshold, it is possible to obtain an expression for the linewidth of a laser line, which is, on the face of it, independent of the spontaneous emission factor, β_{sp} [5]:

$$\Delta\nu \approx \frac{n_{sp} v_g \alpha_m h\nu}{4\pi\tau_p P_0}(1+\alpha^2), \quad \beta_{sp} \ll 1 \tag{3.20}$$

The problem in the expression for the linewidth of a laser line is that it is an asymptotic value that is approached once the gain is effectively clamped and the 'P-I' characteristic becomes linear. However, for smaller drive currents, the linewidth can be much larger, as is provided by equation (3.14) [5].

From experimental evaluations, measured VCSEL linewidths have ranged from 20MHz to approximately 80MHz at output powers of approximately 1mW [22]-[25]. When considering powers in the milliwatts range in typical semiconductor lasers, the lasers produce linewidths in the tens-of-megahertz range [19].

3.3.2 – VECSEL Linewidth

This final section of chapter three will look at defining the linewidth broadening equation for the case of VECSELs. It is generally assumed [26] that the inherent linewidth in external cavity lasers is very small, around 10kHz or less [26]. The theoretical limit to the laser linewidth for such lasers can therefore also be represented by the same Schawlow-Townes equation, modified to include the linewidth enhancement factor, $(1+\alpha^2)$, as defined in equation (3.13) [26]-[28]. Typically, the Schawlow-Townes linewidth limit for distributed feedback (DFB) lasers are in the MHz range, whereas the Schawlow-Townes linewidth limit for VECSELs is around 6 orders of magnitude lower, typically less than the Hz level [27].

3.4 – Summary

This chapter has gone into detail on the derivation of the linewidth for laser lines, paying particular attention to the work of Schawlow and Townes [2], and how the equation derived here was corrected by Melvin Lax [3], and enhanced by Charles Henry [4].

Schawlow and Townes, and Henry, both discovered that the linewidth of a laser line results from fluctuations in the phase at the output of the optical field. These fluctuations occur as a result of either spontaneous emission, or carrier density fluctuations.

It has also been found in this chapter that the same Schawlow-Townes equation may be applied to both VCSEL and VECSEL type lasers. As a result, in the next chapter, the modified Schawlow-Townes equation will be applied to both the original and newly designed dual-wavelength lasers presented in chapter two in order to calculate appropriate linewidths for both structures. This will enable a

determination on whether there is a fundamental limit on how close two wavelengths may be together in a dual-wavelength VECSEL before only one broad peak will be apparent in the spectrum, rather than two narrow peaks defining the two individual wavelengths.

REFERENCES

[1] **T. Leinonen**, Y. A. Morozov, A. Härkönen, M. Pessa, "Vertical External-Cavity Surface-Emitting Laser for Dual-Wavelength Generation", IEEE Photon. Technol. Lett., Vol. 17, No. 12, pp. 2508-2510, Dec. 2005.

[2] **A. L. Schawlow**, C. H. Townes, "Infrared and optical masers", Phys. Rev., vol. 112, no. 6, pp. 1940-1949, Dec. 1958.

[3] **M. Lax**, "Classical noise V. Noise in self-sustained oscillators", Phys. Rev., vol. 160, no. 2 p. 290, Aug. 1967.

[4] **C. H. Henry**, "Theory of the linewidth of semiconductor lasers", IEEE J. Quantum Electron., vol. 18, no. 2, pp. 259-264, Feb 1982.

[5] **C. Wilmsen**, H. Temkin, L. A. Coldren, Chapter 2 in Vertical-Cavity Surface-Emitting Lasers – Design, Fabrication, Characterization and Applications, Cambridge University Press, Cambridge, p.64, 1999.

[6] **L. A. Coldren**, S. W. Corzine, Chapter 5 in Diode Lasers and Photonic Integrated Circuits, Wiley, New York, p.221, 1995.

[7] **L. A. Coldren**, S. W. Corzine, Chapter 5 in Diode Lasers and Photonic Integrated Circuits, Wiley, New York, pp.225-227, 1995.

[8] **S. F. Yu**, Chapter 8 in Analysis and Design of Vertical Cavity Surface Emitting Lasers, Wiley Series in Lasers and Applications, New Jersey, p.353, 2003.

[9] **M. Osinksi**, J. Buus, "Linewidth broadening factor in semiconductor lasers – an overview", IEEE J. Quantum Electron., vol. 23, no.1, pp. 9-29, Jan. 1987.

[10] **B. Zhao**, T. R. Chen, A. Yariv, "A comparison of amplitude-phase coupling and linewidth enhancement in semiconductor QW and bulk lasers", IEEE J. Quantum Electron., vol. 29, no. 4, pp. 1027-1030, Apr. 1993.

[11] **L. A. Coldren**, S. W. Corzine, Chapter 5 in Diode Lasers and Photonic Integrated Circuits, Wiley, New York, p.209, 1995.

[12] **R. Paschotta**, article on 'Schawlow-Townes linewidth' in the *Encyclopaedia of Laser Physics and Technology*, 1st ed. Oct. 2008, Wiley-VCH, ISBN 978-3-527-40828-3.

[13] **A. Yariv**, Quantum Electronics, 3rd ed., New York, Wiley, 1989, Appendix A.

[14] **L. A. Coldren**, S. W. Corzine, Chapter 5 in Diode Lasers and Photonic Integrated Circuits, Wiley, New York, p. 187, 1995.

[15] **L. A. Coldren**, S. W. Corzine, Chapter 4 in Diode Lasers and Photonic Integrated Circuits, Wiley, New York, p.139, 1995.

[16] **L. A. Coldren**, S. W. Corzine, Chapter 4 in Diode Lasers and Photonic Integrated Circuits, Wiley, New York, p.143, 1995.

[17] **K. Vahala**, "Optical Microcavities", World Scientific Publishing Co. Pte. Ltd, 2004

[18] **C. H. Henry**, "Theory of the phase noise and power spectrum, of a single mode injection laser", IEEE J. Quantum Electron., vol. 19, no. 9, pp. 1391-1397, Sep. 1983.

[19] **L. A. Coldren**, S. W. Corzine, Chapter 5 in Diode Lasers and Photonic Integrated Circuits, Wiley, New York, pp. 240-241, 1995.

[20] **C. Wilmsen**, H. Temkin, L. A. Coldren, Chapter 2 in Vertical-Cavity Surface-Emitting Lasers – Design, Fabrication, Characterization and Applications, Cambridge University Press, Cambridge, p.33, 1999.

[21] **C. Wilmsen**, H. Temkin, L. A. Coldren, Chapter 2 in Vertical-Cavity Surface-Emitting Lasers – Design, Fabrication, Characterization and Applications, Cambridge University Press, Cambridge, p.35, 1999.

[22] **R. S. Geels**, S. W. Corzine, L. A. Coldren, "InGaAs vertical-cavity surface-emitting lasers", IEEE J. Quantum Electron., vol. 27, no. 6, pp. 1359-67, Jun. 1991.

[23] **N. M. Margalit**, J. Piprek, S. Zhang, D. I. Babic, K. Streubel, R. P. Mirin, J. R. Wesselmann, J. E. Bowers, E. L. Hu, "64˚C continuous-wave operation of 1.5 μm vertical cavity laser", IEEE J. Selected Topics in Quantum Electron., vol. 3, no. 2, pp. 359-365, Apr. 1997.

[24] **H. Tanobe**, F. Koyama, K. Iga, "Spectral linewidth of AlGaAs/GaAs surface emitting laser", Electron. Lett., vol. 25, no. 21, pp. 1444-1446, Oct. 1989.

[25] **W. Schmid**, C. Jung, B. Weigl, G. Reiner, R. Michalzik, K. J. Ebeling, "Delayed self-heterodyne linewidth measurement of VCSEL's", Photon. Technol. Lett., vol. 8, no. 10, pp. 1288-1290, Oct. 1996.

[26] **S. D. Saliba**, R. E. Scholten, "Linewidths below 100kHz with external cavity diode lasers", Appl. Opt., vol. 48, no. 36, pp.6961-6966, Dec. 2009.

[27] **M. Myara**, M. Sellahi, A. Laurain, A. Garnache, M. Michon, I. Sagnes, "Noise properties of NIR and MIR VECSELs", Proc. Noise and Fluctuations (ICNF), 2013 22nd International Conference, pp. 1-4, Jun. 2013.

[28] **J. Harrison**, A. Mooradian, “Linewidth and offset frequency locking of external cavity GaAlAs lasers”, IEEE J. Quantum Electron., vol. 25, no. 6, pp. 1152-1155, Jun. 1989.

CHAPTER FOUR

LIMITS ON DUAL-WAVELENGTH DEVICES DUE TO LINEWIDTH BROADENING

In chapter two, an original contribution was made whereby a new VECSEL structure was designed with a greatly reduced wavelength separation and much reduced cross-absorption to that reported by Leinonen *et al* [1]. The cross absorption of the short wavelength light in the deep QWs was reduced by improving the positons of the QWs in both the long wavelength and short wavelength active regions. The wavelength separation was also significantly reduced from 58nm (16.97THz), down to 5nm (1.54THz), through reducing λ_L from 1042nm down to 989nm.

Chapter two also gave a detailed analysis of the dual-wavelength VECSEL by Leinonen *et al*. [1], where their device had a long wavelength, λ_L, of 1042nm, and a short wavelength, λ_S, of 984nm, hence giving a large wavelength separation of 58nm, corresponding to a frequency spacing of 16.97THz. During the course of their work, they discovered that the VECSEL suffered from self-pulsation when operating at high pump powers. They theorized that this self-pulsation was as a result of the effects of Q-switching of the short wavelength component by residual absorption in the deep QWs which are not actually located exactly at the nodes of the short wavelength standing wave pattern.

Chapter three gave a detailed theoretical review of the effects of linewidth broadening derived by Schawlow and Townes [2] and enhanced by Henry [3]. This is an important consideration to make when the wavelength spacing in a dual-wavelength laser is very small (5nm / 1.54THz) in this case.

This chapter gives a further contribution to the work on designing a new dual-wavelength VECSEL by investigating the limits of linewidth broadening on both the structures by Leinonen *et al*. and the newly designed structure and concluding whether or not linewidth broadening would be a limiting factor in the design of dual-wavelength lasers.

The contents of this chapter are organised as follows:

Section 4.1 will determine a linewidth value for the VECSEL structure by Leinonen *et al*. through analysis of the lasing spectrum of the device from [1]. Section 4.2 will then make a contribution to a numerical analysis of both structures based on a FORTRAN laser rate equation simulation model, utilising evolutions of equations (1.14) and (1.15) from chapter one for the carrier and photon density rate equations, and the calculated overlap percentages from chapter two, in order to simulate the behaviour of a dual-wavelength laser. Section 4.3 will then procced to discuss the results from the simulation models and the values for the linewidths of both structures will be discussed. Section 4.4

will proceed to discuss whether or not there is a fundamental limit due to linewidth broadening as to how close the two wavelengths must be before only one broad peak will be visible in the lasing spectrum, before section 4.5 discusses the main conclusions from this section of the work.

4.1 – Linewidth of the Structure by Leinonen *et al*.

Now that a comprehensive understanding of the inherent linewidth of semiconductor edge-emitting lasers, VCSELs and VECSELs has been established in chapter three, the final stage of this part of the work is to calculate the linewidth for both the structures by Leinonen *et al*. and the newly designed structure. The linewidth for the VECSEL structure by Leinonen *et al*. may be calculated through examination of the lasing spectrum presented in their paper [1], which is reproduced in figure 4.1 for convenience.

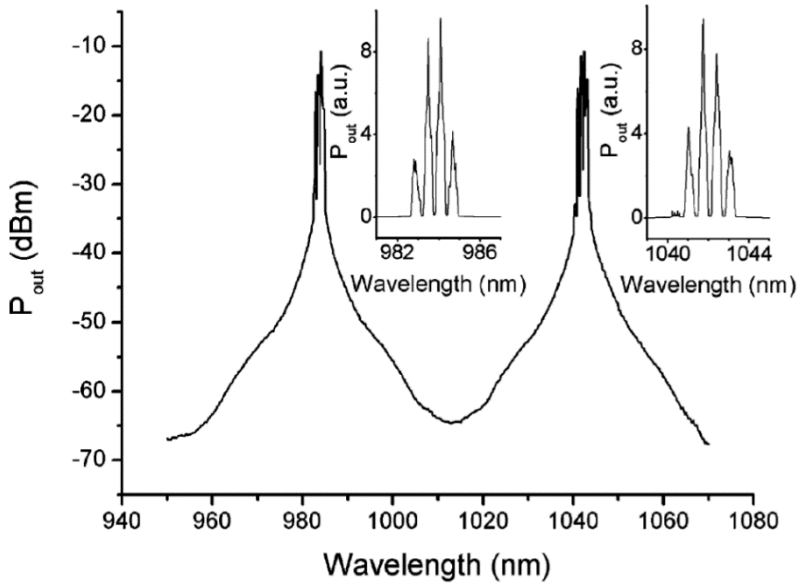

Figure 4.1: *Lasing spectrum of the structure by Leinonen et al. measured at a pump power of 2.4W. The insets show the spectra on a linear scale, with the multiple peaks indicating multimode operation [1].*

It is clear from figure 4.1 that the centre wavelengths are 984nm for λ_S and 1042nm for λ_L. Through examination of their lasing spectrum, λ_S was found to have a linewidth of approximately 440GHz, and λ_L was found to have a linewidth of approximately 470GHz. The insets of figure 4.1 also show the spectra on a linear scale, and through examination of these plots it was found that λ_S had a linewidth of approximately 52.67GHz, whereas λ_L was found to have a linewidth of approximately 49.7GHz. It has been assumed here that the linear scale spectra are the most accurate here, as the larger linewidths (440GHz and 470GHz) have been taken from a log scale plot, and are hence more difficult

to measure the -3dB point for accurate linewidth measurements. It is also apparent from the insets of figure 4.1 that multiple peaks are visible in the spectrum of both wavelengths, thus indicating multimode operation.

4.2 – Theoretical Analysis

For a numerical analysis of both structures, a model of a dual-wavelength laser was implemented in FORTRAN based on the carrier and photon density rate equations, which are defined as [4]:

$$\frac{dN_{(S,L)}}{dt} = \frac{\eta_i I}{qV} - \left(R_{sp} + R_{nr}\right) - v_g g S_{(S,L)} \tag{4.1}$$

$$\frac{dS_{(S,L)}}{dt} = \left[\Gamma \mathrm{g} v_g - \frac{1}{\tau_p}\right] S_{(S,L)} + \Gamma R_{sp}{}' \tag{4.2}$$

where $N_{(S,L)}$ are the carrier densities for λ_S and λ_L respectively, $S_{(S,L)}$ are the photon densities for λ_S and λ_L respectively, η_i is the internal quantum efficiency, I is the injected current, q is the charge of electrons, V is the volume of the active region, R_{sp} is the spontaneous recombination rate, R_{nr} is the nonradiative recombination rate, v_g is the group velocity, g is the gain, Γ is the confinement factor, τ_p is the photon lifetime, and $R_{sp}{}'$ is the spontaneous emission rate per unit active volume into one optical mode.

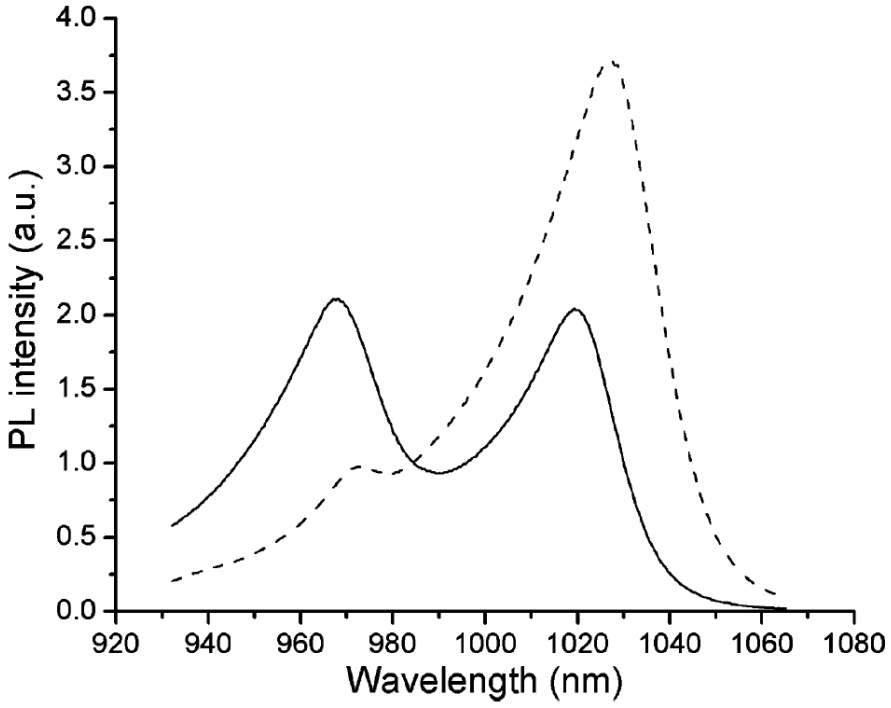

Figure 4.2: *Photoluminescence spectrum of the structure by Leinonen et al. fabricated with the blocking layers (solid line) and without the carrier blocking layers (dashed line) [1].*

It should be noted here that there are separate carrier density equations for the long and the short wavelengths in order to take into account the barrier layers between the short and long wavelength active regions. In this analysis, it is assumed that carrier leakage and diffusion between the reservoirs is negligible. This could be modelled with an additional term akin to $(N_L - N_S)/\tau$ in the carrier rate equations, where τ is defined as the diffusion time constant. The effectiveness of the carrier blocking layers is illustrated by the photoluminescence spectrum from the work of Leinonen *et al*. from [1], which have been reproduced in figure 4.2 for convenience, where the carrier depletion due to absorption has a much greater effect in the absence of the blocking layer, where a lasing threshold carrier density in the shallow QWs would not be achieved.

To emulate the behaviour of a dual-wavelength laser, light was coupled from λ_S into λ_L, by using the calculated overlap percentages, hence the equations (4.1) and (4.2) for λ_L become:

$$\frac{dN_{(L)}}{dt} = \frac{\eta_i I}{qV} - \left(R_{sp} + R_{nr}\right) - v_g g S_{(L)} - g S_{(S)} v_g \kappa_o \tag{4.3}$$

$$\frac{dS_{(L)}}{dt} = \left[\Gamma g v_g - \frac{1}{\tau_p}\right] S_{(L)} + \Gamma R_{sp}{}' + \Gamma g v_g S_{(L)} \kappa_o \tag{4.4}$$

where κ_o is the overlap percentage. It should be noted that the same confinement factor, Γ, is used throughout equation (4.4). The rate equations for λ_S remain unchanged.

The values for the parameters in the rate equations were based on the list of common parameters for laser structures from [5] and can be found in table 4.1.

For each simulation of the VECSEL structure by Leinonen *et al*. and the newly designed structure, the pumping level was kept at a constant 0.5mA for all overlap percentages, and the FORTRAN model used for these simulations can be found in Appendix B.

Parameter	Symbol	Value
Volume of the Active Region	V	$2.4 \times 10^{-12} cm^3$
Group Velocity	v_g	$3 \times 10^{10} cm/s$
Confinement Factor	Γ	0.05
Injected Current	I	$0.5mA$
Internal Quantum Efficiency	η_i	0.8
Photon Lifetime	τ_p	$2.20 \times 10^{-12} ps$
Spontaneous Emission Factor	β_{sp}	2×10^{-4}

Table 4.1: *Summary of the parameters used for the VCSEL models.*

4.3 – Simulation Results

4.3.1 – Leinonen *et al*. VECSEL Structure

The overlap percentages in the following work correspond to the calculated overlap percentages from chapter two, tables 2.1 and 2.2. The overlap percentages for the structure by Leinonen *et al*. are higher than for the new VECSEL structure design due to the increased residual absorption in the original structure. The results of the simulation for the VECSEL structure by Leinonen *et al*. showed that for λ_S, both the carrier and photon density steady-state values would remain the same for all overlap percentages used. This is to be expected as no light is being coupled into λ_S from λ_L. For λ_L, as the overlap percentages are increased, the photon density steady-state would steadily increase. As a direct consequence, the carrier density steady-state values would steadily decrease to take account for the increase in the photon densities. Table 4.2 summarizes these results.

Overlap Percentage (%)	λ_S		λ_L	
	Carrier Density	Photon Density	Carrier Density	Photon Density
19.45	2.537×10^{18}	6.653×10^{13}	2.425×10^{18}	7.261×10^{13}
38.25	2.537×10^{18}	6.653×10^{13}	2.353×10^{18}	7.643×10^{13}
60.69	2.537×10^{18}	6.653×10^{13}	2.289×10^{18}	7.969×10^{13}
82.05	2.537×10^{18}	6.653×10^{13}	2.242×10^{18}	8.201×10^{13}

Table 4.2: *A summary of the steady-state carrier and photon density steady-state values for both λ_S and λ_L for the overlap percentages of 19.45% through to 82.05% for the structure by Leinonen et al.*

With the steady-state values obtained, it was then possible to calculate the linewidth for each coupling constant by utilizing the modified Schawlow-Townes equation [6] (equation 3.13 from chapter three), the values for the VCSEL parameters from table 4.1, and the steady-state carrier and photon density values obtained from the simulation in table 4.2. The linewidth calculations in tables 4.3 and 4.5 have been conducted by assuming a value of 5 for α; this is consistent with the work presented in chapters five-seven.

Table 4.3 summarizes the Schawlow-Townes linewidth of the VECSEL structure by Leinonen *et al*. for each value of overlap percentage. From table 4.3, it is clear that, as expected, the linewidth for λ_S stays constant at 7.699MHz for increasing overlap percentages, however for λ_L, the linewidth gradually decreases from 6.45MHz to 4.88MHz as the overlap percentage increases. This occurs due to the fact that the steady-state photon density increases as the overlap percentage increases, whereas the carrier density steady-state values decrease. As can be seen from table 4.3, the linewidths obtained for the long and short wavelengths are much smaller than those obtained by Leinonen *et al*.

from figure 4.1. Some of this discrepancy may be attributed to the measurement equipment used by Leinonen *et al*. for their experiments. Also, the dual-wavelength model is based on the list of common parameters for laser structures from [5], and not on the parameters that were used by Leinonen *et al*.

Overlap Percentage (%)	$\Delta\lambda_S$	$\Delta\lambda_S(1+\alpha^2)$	$\Delta\lambda_L$	$\Delta\lambda_L(1+\alpha^2)$
19.45	7.669MHz	199.39MHz	6.45MHz	167.70MHz
38.25	7.669MHz	199.39MHz	5.76MHz	149.76MHz
60.69	7.669MHz	199.39MHz	5.23MHz	135.98MHz
82.05	7.669MHz	199.39MHz	4.88MHz	126.88MHz

Table 4.3: *Summary of the Schawlow-Townes linewidths for the structure by Leinonen et al. for the overlap percentages of 19.45% through to 82.05%.*

4.3.2 – New VECSEL Structure Design

The newly designed VECSEL structure was analysed in the same way, utilizing the same FORTRAN model and parameter values from table 4.1. Again, as with the previous VECSEL structure, the steady-state carrier and photon densities would not change for λ_S as no light is being coupled into this wavelength from λ_L. For λ_L, the same pattern is apparent as the previous VECSEL structure where the photon density steady-state would gradually increase as the overlap percentage increased, and as a result the carrier density steady-state would decrease to compensate for this effect. These results are summarized in table 4.4.

As expected, the maximum photon density steady-state values in the newly designed structure are significantly smaller than those in the original VECSEL structure, and this is to be expected due to the smaller values in coupling constants.

Again, from the values in table 4.4, it is possible to calculate values for the Schawlow-Townes linewidth for both λ_S and λ_L. The calculated values for the linewidths can be found in table 4.5.

Overlap Percentage (%)	λ_S		λ_L	
	Carrier Density	Photon Density	Carrier Density	Photon Density
15.305	2.537×10^{18}	6.653×10^{13}	2.445×10^{18}	7.157×10^{13}
15.657	2.537×10^{18}	6.653×10^{13}	2.443×10^{18}	7.166×10^{13}
16.115	2.537×10^{18}	6.653×10^{13}	2.441×10^{18}	7.179×10^{13}
18.768	2.537×10^{18}	6.653×10^{13}	2.429×10^{18}	8.245×10^{13}

Table 4.4: *A summary of the steady-state carrier and photon density steady-state values for both λ_S and λ_L for the overlap percentages of 15.305% through to 18.768% for the newly designed structure.*

Overlap Percentage (%)	$\Delta\lambda_S$	$\Delta\lambda_S(1+\alpha^2)$	$\Delta\lambda_L$	$\Delta\lambda_L(1+\alpha^2)$
15.305	7.669MHz	199.39MHz	6.65MHz	172.90MHz
15.657	7.669MHz	199.39MHz	6.63MHz	172.38MHz
16.115	7.669MHz	199.39MHz	6.61MHz	171.86MHz
18.768	7.669MHz	199.39MHz	6.48MHz	168.48MHz

Table 4.5: *Summary of the Schawlow-Townes linewidths for the newly designed structure for the overlap percentages of 15.305% through to 18.768%.*

The same pattern is apparent where the linewidth for λ_S would remain the same for all values of the overlap percentage, whereas the linewidth for λ_L would gradually decrease as the overlap percentage increased. This again is due to the fact that the photon density steady-state values are increasing for increasing overlap percentages, whereas the carrier density steady-state values are decreasing.

A comparison of the linewidths for both structures shows that the linewidth for λ_S always remains constant at 7.669MHz, whereas the linewidth for λ_L is larger in the newly designed structure. The maximum linewidth for the original and the newly designed VECSEL structures are 6.45MHz and 6.65MHz respectively. Comparing the linewidth with the maximum overlap percentage for both structures, it can be noted that the structure by Leinonen *et al*. has a linewidth of 4.88MHz, whereas the newly designed structure has a linewidth of 6.48MHz. It is also noted that the difference between $\Delta\lambda_S$ and $\Delta\lambda_L$ is shorter in the newly designed structure than in the structure by Leinonen *et al*. owing to the significant reduction in wavelength separation between λ_S and λ_L in the newly designed structure.

4.4 – Fundamental Limit on Wavelength Separation

In order to analyse the linewidths in more detail, it is necessary to convert the frequency linewidths from frequency values (MHz) into wavelength values (nm). It is essential to do this in order to establish the minimal limit for the wavelength separation where it would not be possible to see two resolved lines in the lasing spectrum. The conversion is applied via the following equation:

$$\Delta f = \frac{c}{\lambda_{(S,L)}^{\,2}}\Delta\lambda \tag{4.5}$$

where Δf is the frequency linewidth (Hz), c is the speed of light, $\lambda_{(S,L)}$ are the centre wavelengths for the short and long wavelengths respectively, and $\Delta\lambda$ is the wavelength linewidth (nm). Tables 4.6 and 4.7 show the calculated values for the wavelength linewidth for the original VECSEL structure and the

newly designed VECSEL structure respectively. It should be noted that the wavelength linewidths have been calculated for the maximum overlap percentages (82.05% and 18.768% respectively).

Linewidth	λ_S	λ_L
Frequency Linewidth	7.669MHz	4.88MHz
Wavelength Linewidth	0.02pm	0.017pm

Table 4.6: *Summary of the frequency linewidth and wavelength linewidth for the structure by Leinonen et al. for the maximum overlap percentage of 82.05%.*

Linewidth	λ_S	λ_L
Frequency Linewidth	7.669MHz	6.48MHz
Wavelength Linewidth	0.02pm	0.021pm

Table 4.7: *Summary of the frequency linewidth and wavelength linewidth for the newly designed structure for the maximum overlap percentage of 18.768%.*

For the original VECSEL structure, the linewidth is found to be 0.02pm for λ_S, and 0.017pm for λ_L. For the new VECSEL structure design, λ_S is again found to be 0.02pm, whereas λ_L is found to be 0.021pm. As these values are so close to zero, it would seem apparent that linewidth broadening would not be a limiting factor in significantly reducing the wavelength separation between the two wavelength values in a dual-wavelength VECSEL where it would not be possible to see two resolved lines in the spectrum.

A possible limiting factor arises in the molar compositions for the deep and shallow QWs. For the newly designed structure, these have been estimated to be approximately $In_{0.17}Ga_{0.83}As$ for the shallow QWs, and $In_{0.18}Ga_{0.82}As$ for the deep QWs (compared to $In_{0.23}Ga_{0.77}As$ in the original structure). As the new wavelength separation (5nm) is approximately 8.6% of the original wavelength separation (58nm), then 8.6% of In composition is added to the deep QW composition with respect to the shallow QW composition, i.e. $(0.17 \times 8.6\%) + 0.17 = 0.18$. Having molar compositions so close together may be a cause for concern in the design of dual-wavelength VECSELs.

4.5 – Conclusion

To conclude this chapter, a new dual-wavelength VECSEL structure has been proposed, with the possibility of realizing terahertz radiation. The original structure proposed by Leinonen *et al*. had a wavelength spacing of 58nm (16.97THz), where λ_S had a wavelength of 984nm and λ_L had a wavelength of 1042nm. In their work, Leinonen *et al*. reported that their VECSEL structure would work efficiently with high pump powers, however with increased pumping powers, the laser indicated signs of self-pulsation. These were believed to originate from the effects of Q-switching of the short wavelength component by residual absorption in the deep QWs, which are not exactly aligned with the nodes of the short wavelength standing wave pattern.

A new VECSEL structure design has been proposed to generate dual-wavelength emission with greatly reduced wavelength separation and a much reduced cross-absorption to that reported by Leinonen *et al*. This was achieved by significantly reducing the wavelength separation between λ_S and λ_L from 58nm (16.97THz), down to 5nm (1.54THz), and by re-positioning the deep QWs in order to reduce the cross-absorption of the short wavelength light in the deep QWs. The deep QWs were re-positioned at the antinodes of the long wavelength standing wave pattern, while at the same time, positioned about the nodes of the short wavelength standing wave pattern. This was done in order to align the antinodes of λ_L and the nodes of λ_S with the deep QWs (in the structure by Leinonen *et al*. the nodes of λ_S were entirely outside the deep QWs, thus contributing to the effect of cross-absorption of the short wavelength light in the deep QWs).

In reducing the wavelength separation, and by improving the positions of the QWs, the newly designed structure shows evidence of containing much smaller overlap values between λ_S, λ_L and the corresponding QWs in both the long and short wavelength active regions. Hence, the nodes of λ_S and the antinodes of λ_L are both aligned with the deep QWs in the long wavelength active region. This suggests a significant reduction would be observed in cross-absorption of the short wavelength light in the deep QWs in the newly designed structure compared with the original.

A reduction in this overlap suggests an overall performance benefit of the new VECSEL structure to allow the VECSEL to operate at higher pumping levels, in excess of the 2.4W reported. This therefore suggests that the effect of self-pulsation would be reduced as the effect of residual absorption in the deep QWs would no longer be apparent, as they are now aligned with the nodes of the short wavelength standing wave pattern.

A detailed analysis on the linewidth broadening effects was also conducted, which is of great importance when the wavelength spacing is significantly reduced. This was undertaken in order to establish a fundamental limit on how close the two wavelengths may be together where it would not be possible to see two resolved lines in the lasing spectrum of the laser.

The results of the Schawlow-Townes linewidth calculations for both VECSEL structures show that even though the linewidth for λ_L is smaller in the original VECSEL than in the new VECSEL structure design, it does not seem apparent that the Schawlow-Townes linewidth would be a limiting factor in significantly reducing the separation between two wavelengths in a dual-wavelength VECSEL.

The potential here would be to shine the output of the dual-wavelength laser onto a photoconductive antenna (PCA) [7]-[12] in order to realise THz radiation.

The results of the work in chapters two through to four will allow the design of a dual-wavelength laser with a minimum separation of 5nm (1.54THz) between the two wavelengths.

REFERENCES

[1] **T. Leinonen**, Y. A. Morozov, A. Härkönen, M. Pessa, "Vertical External-Cavity Surface-Emitting Laser for Dual-Wavelength Generation", IEEE Photon. Technol. Lett., Vol. 17, No. 12, pp. 2508-2510, Dec. 2005.

[2] **A. L. Schawlow**, C. H. Townes, "Infrared and optical masers", Phys. Rev., vol. 112, no. 6, pp. 1940-1949, Dec. 1958.

[3] **C. H. Henry**, "Theory of the linewidth of semiconductor lasers", IEEE J. Quantum Electron., vol. 18, no. 2, pp. 259-264, Feb 1982.

[4] **L. A. Coldren**, S. W. Corzine, Chapter 5 in Diode Lasers and Photonic Integrated Circuits, Wiley, New York, p. 187, 1995.

[5] **L. A. Coldren**, S. W. Corzine, Chapter 5 in Diode Lasers and Photonic Integrated Circuits, Wiley, New York, pp. 198-199, 1995.

[6] **L. A. Coldren**, S. W. Corzine, Chapter 5 in Diode Lasers and Photonic Integrated Circuits, Wiley, New York, pp. 240-241, 1995.

[7] **D. Saeedkia**, R. R. Mansour, S. Safavi-Naeini, "The interaction of laser and photoconductor in a continuous-wave terahertz photomixer", IEEE J. Quantum Electron., vol. 41, no. 9, pp. 1188-1196, Sept. 2005.

[8] **D. Saeedkia**, R. R. Mansour, S. Safavi-Naeini, "Analysis and design of a continuous-wave terahertz photoconductive photomixer array source", IEEE Trans. Ant and Prop., vol. 53, no. 12, pp. 4044-4050, Dec. 2005.

[9] **D. Saeedkia**, A. H. Majedi, S. Safavi-Naeini, R. R. Mansour, "Analysis and design of a photoconductive integrated photomixer/antenna for terahertz applications", IEEE J. Quantum Electron., vol. 41, no. 2, pp. 234-241, Feb. 2005.

[10] **D. Saeedkia**, A. H. Majedi, S. Safavi-Naeini, “CW photoconductive photomixer/antenna array source for THz applications”, Proc. IEEE Micro. Photon. Conf., Oct. 2004, pp. 317-320.

[11] **D. Saeedkia**, S. Safavi-Naeoni, “A comprehensive model for photomixing in ultrafast photoconductors”, IEEE Photon Technol Lett., vol. 18, no. 13, pp. 1457-1459, Jul. 2006.

[12] **D. Saeedkia**, A. H. Majedi, S. Safavi-Naeini, R. R. Mansour, “High-temperature superconductive photomixer patch antenna: Theory and design”, IEICE Trans. Electron., vol. E86-C, no. 7, pp. 1318-1327, Jul. 2003.

CHAPTER FIVE

LASER INJECTION LOCKING

In chapters two to four, a detailed investigation and design of a new dual-wavelength VECSEL structure was undertaken as a potential method for realizing THz radiation.

This chapter is going to look at a different method for realising THz radiation, as discussed in chapter one; laser injection locking. An injection locking scheme, utilised through means of a two laser system, will be modelled and investigated, where the effects of injecting light from one laser into the second laser cavity will be explored (unidirectional injection locking) as well as, at the same time, injecting light from the second laser cavity into the first laser cavity (bidirectional injection locking). A detailed analysis of the different locking regions that are apparent between the two lasers, with different frequency detuning values and varying injection rates for both schemes will be made. In addition, the various behaviours observed at varying detuning frequency values and injection rates will be investigated in detail. With the scheme of injection locking, there will be a zero frequency separation between the lasers frequencies while operating in the locked condition.

The work on injection locking is an important phenomenon to consider, and because there is a zero frequency separation between the lasers frequencies in the locked condition, it will lay the foundation for the work in chapters six and seven, whereby the effect of injection locking will be built on in order to develop a three laser system based on the four-wave mixing (FWM) scheme for realising THz radiation in order to obtain a nonzero wavelength separation between the lasers in the locked condition.

The contents of this chapter are organised as follows:

In section 5.1, an introduction to the injection locking scheme will be given, whereby the scheme is utilised through means of a two laser system, whereby the light from the first laser is injected into the second laser cavity. Section 5.2 will then outline a brief history of injection locking, observed as early at the 17^{th} century. In section 5.3, the different techniques employed in optical injection locking in semiconductor lasers will be considered, looking at the experimental setups for a typical edge-emitting laser, and surface emitting laser, employed as the slave laser. Section 5.4 will then explore unidirectional injection locking, and the work undertaken to model a system whereby the light from the first laser is injected into the second laser cavity. A detailed analysis of the locking regions and different behaviours of the system will be discussed in section 5.5. Section 5.6 will then look at the work undertaken to model a bidirectional injection locking system, whereby the light from the

first laser is injected into the cavity of the second laser, but at the same time, the light from the second laser is also injected into the cavity of the first laser. Again, the locking regions and varying behaviours will be discussed and explored. Finally, section 5.7 will include a summary and the main conclusions from this work, and how this work is important for laying the groundwork for chapters six and seven whereby the FWM scheme is employed in order to generate a system with a nonzero frequency separation between the lasers frequencies in the locked condition.

5.1 – Introduction

Injection locking has proved to be of great interest in the world of optics for more than two and a half decades. It has been demonstrated as a durable and systematic approach to improve the spectral and dynamic performance of directly modulated laser diodes. The approach of injection locking is where the frequency and the phase of an oscillator, referred to as the slave oscillator, are locked via direct coupling from another oscillator, known as the master oscillator. This notion not only applies to mechanical oscillators, but also to electronic and optical oscillators [1].

The technique of locking laser frequencies is mainly applied to continuous-wave (CW), single-frequency, laser sources. This technique is used when a high output power is required with a very low intensity noise and phase noise. Low-noise performance, and even single-frequency operation, is notoriously more difficult to achieve in high power lasers [2]. This occurs as a result of the susceptibility of such lasers to mechanical vibrations, they are unable to utilize very low-noise pump sources, and are also prone to significant thermal influences. In addition, inserting optical filters into the laser resonator is highly undesirable, as such filters could degrade the power efficiency, and may be unable to tolerate the high power levels [2]. Optical filters are generally inserted into the laser resonator to selectively transmit or reject a wavelength, or a range of wavelengths.

Principally, construction of low-noise, low-power lasers is a possibility, and then just simply amplify the output signal using a high-power fiber amplifier. Such a scheme is known as a master oscillator power amplifier [2]. This method is however plagued with various practical drawbacks. Such drawbacks include amplifier noise (which to some extent can be avoided) which will raise the noise level. In addition to amplifying the input signal, optical amplifiers will also add some excess noise to the output. Additionally, multiple amplifier stages are often required (such as an amplifier chain) if the desired overall amplification factor is large, hence increasing the number of components required in the scheme.

A method of producing high power, narrow linewidth light is known as injection locking. Using such an approach achieves the required high output power using a high power laser, rather than an amplifier, and is termed the ‘slave’ laser. The noise level of this laser is significantly reduced by

injecting the output of a low-noise, low-power 'master' laser (sometimes termed a seed laser), through a partially transparent resonator mirror, into the cavity of the 'slave' laser. On the condition that the frequencies of the master laser and the free-running slave laser are adequately close, the injection will force the slave laser to operate exactly on the injected frequency. The higher the injected power, the larger the allowable frequency offset between the master and slave lasers' resonance [2]. The work in this chapter will investigate the injection locking characteristics of a two laser system, beginning with injecting light from the first laser into the cavity of the second laser (unidirectional injection locking). The chapter will then investigate injecting light from the first laser into the cavity of the second laser, at the same time as injecting light from the second laser into the cavity of the first laser (bidirectional injection locking).

5.2 – A Brief History of Optical Injection Locking

Systems that are oscillatory in nature tend to have injection locking, or pulling, characteristics [5]. The phenomenon of injection locking was first observed as early as the 17th century by the Dutch scientist Christiaan Huygens [1], [3], [4]. He discovered, while confined to bed with illness, that the pendulums of two clocks (mechanical oscillators) would swing in unison if they were hung close to each other on the wall [3], [4]. He made the assumption that the pendulums synchronized together through the coupling of the mechanical vibrations through the wall. It has also been observed that humans also exhibit injection locking phenomena. When left in an isolated bunker for a period of time, they revealed a 'free-running' sleep-wake pattern of around 25 hours, [3] however, when they were brought back into the natural world, they were injection locked to the Earth's cycle [5].

Another example of a natural locking phenomena would be that of so called 'crowd synchrony' [6], whereby crowds of people walking in unison can cause structures, such as bridges, to fail. In April of 1831, a brigade of British soldiers was marching in step across the Broughton Suspension bridge, England, and according to reports from the time, the bridge broke apart beneath their feet, with many of the soldiers ending up in the water below [7]. Even though structures, such as bridges and buildings, appear structurally sound, they have a certain natural frequency of vibration, and if a force is applied to them of the same frequency as the natural frequency, it will amplify the vibration of the structure causing a phenomena known as mechanical resonance [7]. As such, when the soldiers marched in unison across the Broughton Suspension Bridge, their frequency was closely matched to the bridge's natural frequency, which consequently caused an amplification of the bridge's mechanical resonance, causing the bridge to fail as a result of the amplified force. After this event, the British Army sent new orders to all regiments, stating that soldiers crossing a bridge must 'break stride', or not march in unison, to stop such a situation from re-occurring in the future [7].

Such a phenomena was observed again on June the 10th 2000, with the opening of the Millennium Bride in London [6], [8]-[10]. On the opening day, thousands of people swarmed over it, with the bridge initially staying still; then the bridge began to sway from side to side [8], [10]. Many of the people walking along the bridge had spontaneously fallen into step with the bridge's natural frequency, casing the bridge's resonance to amplify [10]. The difference in this example to the one of soldiers walking in step, is that the pedestrians were not trying to walk in step with each other, they were only doing so to compensate for the bridge's movement under their feet [8]. The bridge had inadvertently been designed with a natural frequency close to that of human walking, and as a result, only a small crowd of people was required to initiate the 'wobble' [8], [10]. With a certain critical number of pedestrians walking in sync, this was enough to amplify the wobbling, consequently forcing everyone to walk in stride with each other, thus amplifying the problem [8]. In a paper by Strogatz *et al*. in 2005 [10], he derived that the critical number of pedestrians was as low as 160. It was estimated that around 80,000 people crossed the Millennium Bridge on June the 10th 2000, with as many as 2,000 people on it at any one time [8]. The Millennium Bridge reopened in 2002, after engineers fitted the bridge with 91 dampers to absorb both lateral and vertical oscillations [8].

Van der Pol [1], [11] later used the phenomenon discovered by Huygens to develop forced oscillator circuits (electronic oscillators) in 1927. This technique was then further developed by Robert Adler in 1946 [1], [12]. In his work, he developed a differential equation for the oscillator phase as a function of time [12] in order for the technique of injection locking to be used in electronics and communications [1]. After Maiman's invention of the first laser (optical oscillators) on May the 16th, 1960, Stover and Steier [1], [13] studied the effects of injection locking He-Ne filled lasers in 1966. They succeeded in phase locking one laser to another by direct injection of the first laser beam into the cavity of the second laser [13]. The results from their work were found to be in qualitative agreement with Adler's classical frequency locking analysis [12], [14], and their work is widely believed to be the first to demonstrate optical injection locking (OIL) [1], [14]. The analysis of Adler's work was further developed by Paciorek in 1965 [15] to include the injection of large signals.

From the discovery of injection locking by Huygens in the 17th century, up until the first demonstration of optical injection locking by Stover and Steier, no matter what kind of locking was being observed (mechanical, electronic or optical), the underlying principle of the work was to investigate the locking, or synchronization, of the oscillators' phase and frequency. A paper by Buczek *et al*. in 1973 [16] gave a review of the basic principles of laser injection locking.

With the development of semiconductor laser diodes in the following years, this revolutionised the changes that are seen today in the telecommunications technology, and hence additional properties of lasers were found to be strongly dependent upon external light injection [1]. Such applications

include frequency division [3], [17], quadrature generation [3], [18], [19] and oscillators with finer phase separations [3], [20]. Of particular interest are the dynamic modulation characteristics, which prove essential for communication applications [1].

5.3 – Optical Injection Locking in Semiconductor Lasers

When the technology of semiconductor lasers first came to fruition in the 1970s, numerous investigations were undertaken by various groups to enhance the performance of injection locking in lasers. Kobayashi and Kimura [21] were the first group to demonstrate optical injection locking of a double heterostructure (DH) AlGaAs laser in 1980. This was further developed by Iwashita and Nakagawa in 1982 [22] who demonstrated side mode suppression of a Fabry-Pérot laser diode through the injection locking technique. By doing this, they obtained single-mode operation from a multimode laser with reduced mode partition noise [1]. It was a paper by Roy Lang in 1982 [23] who published the first fundamental theory paper on injection locking of semiconductor lasers [1]. His work provided a theoretical framework, which would then go on to become the foundation of numerous theoretical predictions and studies over the following years [1].

Optical injection locking (OIL) was initially studied on Fabry-Pérot lasers in the early 1980s; it was first theoretically and experimentally demonstrated in 1982 by Kobayashi and Kimura [24], whereby two DH AlGaAs semiconductor lasers of identical cavity length, operating continuously in a single longitudinal mode at 840nm, were injection locked. The technique was used as a method for obtaining single-longitudinal-mode lasers in order to improve the transmission performance in single-mode fibres (SMF) [1]. As time progressed, advancements were made in laser technology where single-mode lasers were becoming commercially available, namely distributed feedback (DFB) lasers. As a result, the technique of OIL was revisited as a method of improving the performance of these lasers, rather than just being used simply for frequency selection and stabilization [1].

In the OIL scheme, the master laser is usually kept under continuous wave (CW) operation. To obtain unidirectional locking, an isolation component is placed in the optical path between the master and the slave lasers. The isolation component may be either an optical isolator or an optical circulator. An optical isolator, as illustrated in figure 5.1 (a), will only allow light to travel in one direction; they are used to stop back reflections that may arise after the isolator, hence, for unidirectional injection locking, the isolator would stop the slave laser light reflecting back into the master laser cavity. The isolator is made up of an input polarizer, a Faraday rotator, and an output polarizer. The input polarizer will only allow linearly polarized light into the Faraday rotator. The Faraday rotator will then rotate the input polarization light by 45° and will then exit the isolator via the second linear polarizer; the output light is now rotated by 45° with respect to the input light. For any backward reflections that

may occur, the light will enter the polarizer via the second linear polarizer and then pass through the Faraday rotator, whereby the polarization of the light is again rotated by 45°; the polarization of the light is now rotated 90° with respect to the input light. The plane of polarization is now perpendicular to the transmission axis of the input polarizer, and as a result, the light will be either reflected or absorbed [25], [26]. The transmission of light through an optical isolator is polarization dependent (because of the polarizers) [26]. They are commonly used to protect polarization dependent lasers from back reflections [26].

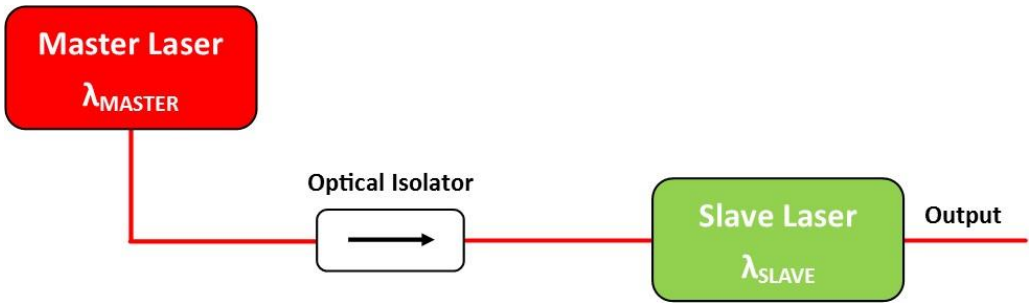

Figure 5.1 (a): *Typical experimental setup for an edge-emitting laser as a slave laser [1].*

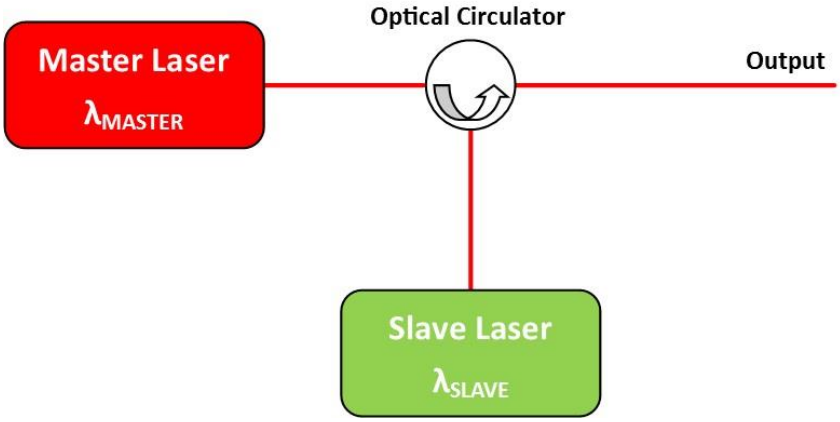

Figure 5.1 (b): *Typical experimental setup for a surface-emitting laser as a slave laser [1].*

The second type of isolation component is an optical circulator. A common type of optical circulator contains three ports; similar to optical isolators, they only allow the light to travel in one direction only, but unlike optical isolators, they are polarization independent [26]. In a 3-port circulator, as illustrated in figure 5.1 (b), the input light will pass from port 1 into port 2, and the input light at port 2 will pass to port 3 (no light will travel from port 2 to port 1, and similarly, no light will pass from port 3 to port 2). Practically, one or two of the ports are utilised as inputs, and one port is utilised as an output (as per the configuration in figure 5.1 (b)).

If bidirectional injection were desirable, the master laser light would be injected into the slave laser cavity, and similarly, the slave laser light would be injected into the master laser cavity. Figure 5.1 (a)

& (b) shows the typical experimental setup for OIL using either an edge-emitting laser or a surface-emitting laser as the slave laser. An optical isolator, or a circulator will be used depending on the slave laser used (polarization dependent or independent).

5.4 – Self-Injection Locking

This section will give a brief introduction to another type of injection locking scheme, self-injection locking, otherwise known as optical feedback [27]-[31]. It is possible to introduce optical feedback to a diode laser by returning a portion of the output light back into the cavity of the device from a reflecting surface external to it [29], [30]; doing so introduces an external cavity, as illustrated in figure 5.2.

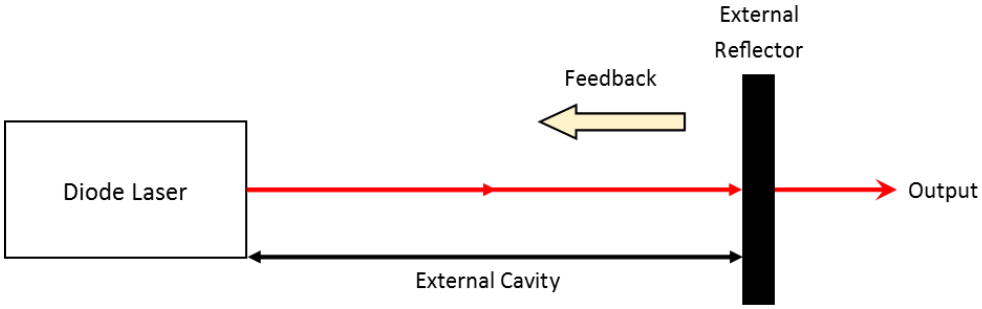

Figure 5.2: *Schematic showing a diode laser subjected to optical feedback, provided by an external reflector, which consequently generates an external cavity.*

Introducing feedback effects to a diode laser can have varying effects on the operating characteristics of the laser. In 1980, Lang and Kobayashi [29] investigated the effects of optical feedback on the operating characteristics of semiconductor diode lasers, and the paper observed multistable behaviour and hysteresis in the output of a diode laser which was subjected to optical feedback [29], [30]. Optical feedback can be deemed disadvantageous, especially as it may cause unwanted instabilities in the laser output, however, optical feedback may also be advantageous, under certain conditions, as it can improve various features of the solitary laser, such as narrowing the linewidth, and increasing the side mode suppression [30]-[32].

In 1986, Tkach and Chraplyvy [28] identified five distinct regimes of operation, and for 30 years, has been the reference for describing and classifying feedback effects in a semiconductor laser [27]. The T-C diagram identifies five regimes of feedback [27] which depend on three main factors [33]; the ratio of the feedback power to the emitted power, the distance to the feedback reflector, and the phase of the incoming power. The five regimes can be mapped depending upon the first two factors, as illustrated in figure 5.3. According to the original description of feedback-induced regimes [27], [28], regime 1 is that of the lowest feedback level, where the laser linewidth is either broadened or narrowed; the spectrum of the laser would show that the laser linewidth is broadened or narrowed

based on the distance from the external reflector which determines the phase of the feedback signal [27], [33], [34]. In regime 2, the laser would be conditionally stable, where the larger the distance from the external feedback reflector, the more sensitive the laser become to lower levels of feedback. While operating in this regime, changes in the phase of the optical feedback will give rise to mode hopping in the spectrum of the laser [27], [33], [34]. The third regime is a very narrow regime, operating from feedback levels of -39dB to -45dB. This regime causes the linewidth of the laser to narrow, and the laser will operate in a single mode [27], [33], [34]. In regime 4, the laser will operate in an unstable manner, where the spectrum will develop side modes which are separated by the main mode by the relaxation oscillation frequency. As the level of feedback is increased, the laser will enter into 'coherence collapse' where the laser line will broaden to several 10's of GHz with several peaks. In this regime, the laser is insensitive to changes in the feedback phase, and is independent of the distance from the external feedback reflector [27], [33], [34]. In regime 5, the laser shows a stable operation, with a significant linewidth reduction. This regime typically requires an anti-reflective coating on the laser output facet, and is again independent of the distance from the external feedback reflector. In this regime, the laser will return to a single-mode oscillation, which now uses the external reflector as the cavity mirror [27], [33], [34].

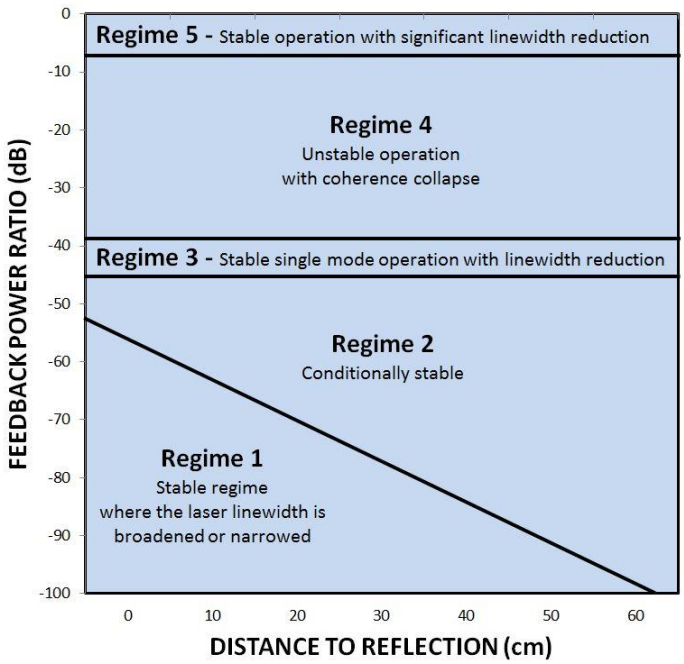

Figure 5.3: *Diagram of coupling strength, in decibel, versus external cavity length. According to the original description by Tkach and Chraplyvy [28], regime 1 corresponds to linewidth narrowing or broadening, regime 2 to line splitting and mode hopping, regime 3 returns the laser to single-mode narrow-line operation, regime 4 causes coherence collapse, and regime 5 oscillated on the external cavity [27], [28], [33], [34].*

5.5 – Unidirectional Injection Locking

This section will investigate the phenomenon of unidirectional injection locking, consisting of a two laser configuration. Being setup with unidirectional injection, a fraction of the light from the first laser will be injected into the second laser cavity. The dynamics of the semiconductor laser with optical feedback are modelled using the single-mode laser diode rate equations from the paper by Peters-Flynn *et al*. [35], [36], however the rate equations are related to those initially developed by Lang and Kobayashi [29]. There are two equations each for both of the lasers; one represents the slowly varying complex electric field amplitude $A(t)$ in the laser cavity (either the first, $A_1(t)$, or the second, $A_2(t)$), and one for the number of charge carriers $N(t)$ in the gain medium (again for either the first, $N_1(t)$, or the second, $N_2(t)$). These are represented by equations (5.1)-(5.3). The coefficient κ_c represents the injection rate of the coupling field into the second laser. The gain in the medium is represented by equation (5.4), and applied to both the first and second lasers respectively.

$$\frac{dA_1(t)}{dt} = \frac{1}{2}(1+i\alpha)\left[G_1 - \frac{1}{\tau_p}\right]A_1(t) \tag{5.1}$$

$$\frac{dA_2(t)}{dt} = \frac{1}{2}(1+i\alpha)\left[G_2 - \frac{1}{\tau_p}\right]A_2(t) + \kappa_c A_1(t)e^{i\Delta\omega t} \tag{5.2}$$

$$\frac{dN_{1,2}(t)}{dt} = \frac{J}{e} - \frac{N_{1,2}(t)}{\tau_n} - G_{1,2}\left|A_{1,2}(t)\right|^2 \tag{5.3}$$

$$G_{1,2} = \frac{g\left(N_{1,2}(t) - N_0\right)}{1 + \epsilon\left|A_{1,2}(t)\right|^2} \tag{5.4}$$

The frequencies of the optical fields that are emitted by both the free-running (with no coupling) are ω_1 and ω_2 respectively, and hence the detuning may be defined as $\Delta\omega = \omega_1 - \omega_2 = 2\pi\Delta f$ which controls the phase of the coupling term. It should be noted here that everything in the model is kept identical, except for the wavelength. This is justifiable for this work as it serves as a 'building-block' for the work presented in chapters six and seven, where the work in this chapter is built upon. In practice, the gains etc. would not be identical in both lasers, but the work here wishes to control the thought process behind the system as much as possible.

Figure 5.4 shows a schematic configuration of this setup. By implementing the beam splitter (BS), the output from the first laser is coupled to the second laser via the optical isolator (ISO) and the variable attenuator. The variable attenuator is used to control the injection rate, κ_c. Table 5.1 gives a list of all of the parameters used within this model, together with their values.

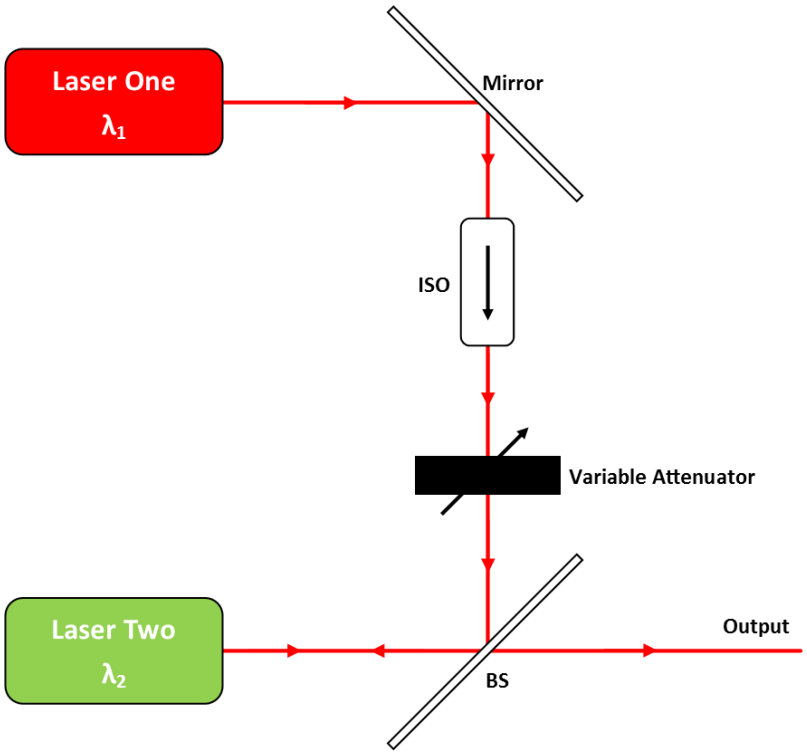

Figure 5.4: *Schematic representation of the unidirectionally coupled external cavity lasers [36].*

Parameter	Symbol	Value
Linewidth Enhancement Factor	α	5
Carrier Lifetime	τ_n	$2\ ns$
Photon Lifetime	τ_p	$2\ ps$
Gain Coefficient	g	$15 \times 10^3\ s^{-1}$
Gain Saturation Coefficient	ϵ	1.5×10^{-17}
Carrier Number at Transparency	N_0	1.5×10^8

Table 5.1: *Laser parameters used in the investigation [35], [36].*

5.6 – Unidirectional Injection Locking Model Simulation

The model was simulated in FORTRAN (the code for which can be found in Appendix C) using the parameter values listed in table 5.1. The model was simulated with detuning values, Δf, ranging from -55GHz to 26GHz and the injection rate, κ_c, ranges from $5ns^{-1}$ to $90ns^{-1}$ to get a full range of results. The results can be seen in figure 5.5. From the figure, the black crosses are where the laser's carrier and photon number output are oscillating periodically (figure 5.6, (a)-(d)), the blue squares are where the laser's carrier and photon number output seems to exhibit a chaotic behaviour (figure 5.7), which potentially may represent period doubling route to chaos, and the red circles represent the locking

condition between the first and the second laser (figure 5.8). The blank areas in the plot are areas that have not been studied for this part of the work. Outside of the 'locking region', the second lasers' carrier number, photon number and electric field will simply oscillate at a beat frequency equal to the detuning frequency, as can be seen in figure 5.7.

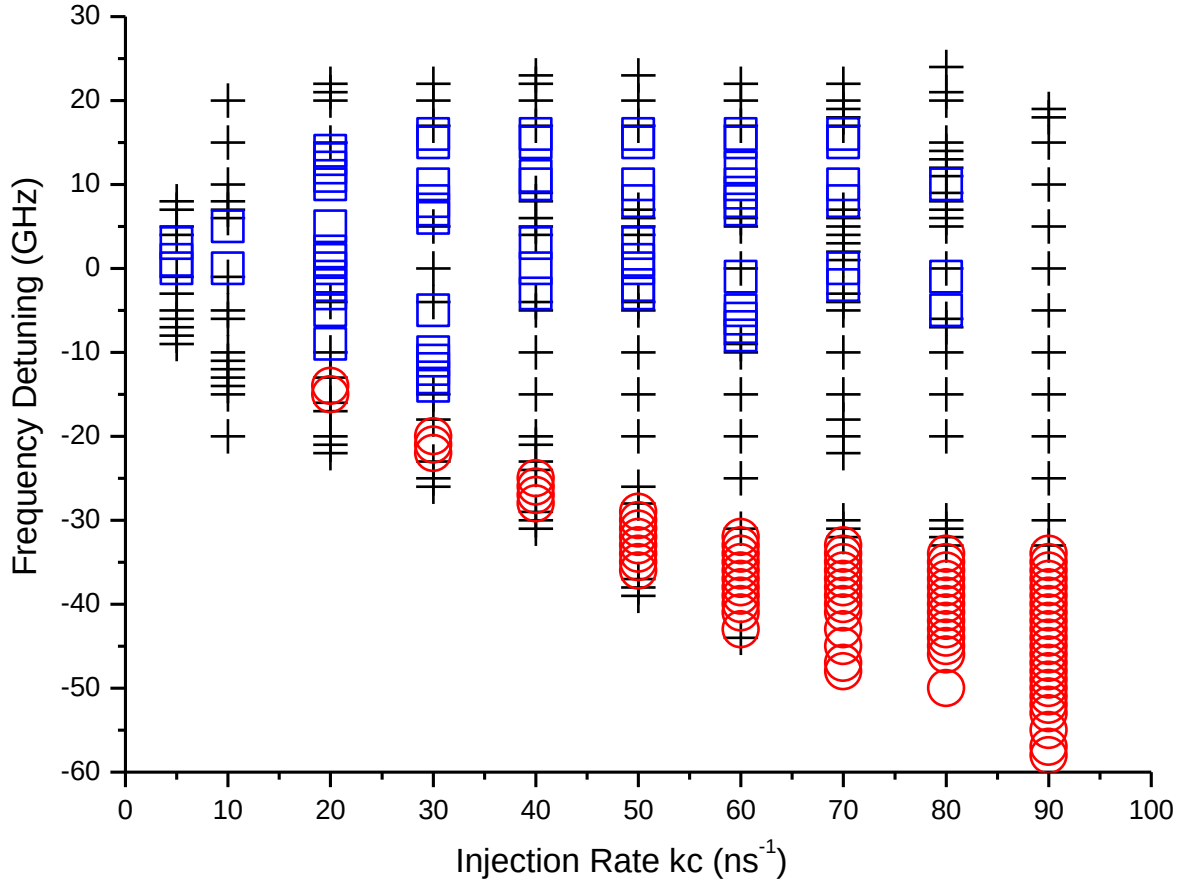

Figure 5.5: *Behavioural plot for the case of unidirectional injection with detuning values, Δf, ranging from -55GHz to 26GHz, with injection rates, κ_c, ranging from 5ns^{-1} to 90ns^{-1}. The black crosses represent the lasers' carrier and photon number output oscillating periodically, the blue squares represent the carrier and photon number output potentially exhibiting a chaotic behaviour, and the red circles represent the locking condition between the first and second lasers'. The blank areas within the locking regions are areas that have not been studied for this part of the work. (Data for the plot can be found in Appendix D).*

From the graph (figure 5.5), the locking region closely follows a typical 'V' shape as shown by Peters-Flynn *et al*. in [35] and [36]. This gives some assurance that the model is behaving as expected. It is clear to see that the locking range is asymmetric in shape, and this closely follows what was also seen in [1] and [23]. The asymmetry is a result of the linewidth enhancement factor, α. The external light injection from the first laser will reduce the carrier number, and this will in turn reduce the gain in the

second laser. The linewidth enhancement factor couples the gain and the phase of the laser field, and as a result the gain variation will result in the second laser cavity shifting to a longer wavelength (red-shift) through the linewidth enhancement factor. As a result, the second laser tends to be locked to a longer wavelength than its lasing wavelength [1]. As can be seen in figure 5.5, the stronger the injection rate is, the wider the locking range is. From looking at the injection rate of $90ns^{-1}$, it can be seen that this is by far the widest locking range observed. It can be assumed that this pattern would continue for even higher injection rates.

Figures 5.6, (a)-(d) show a clear periodic pattern, and in all cases (with the exception of the carrier number plot in figure 5.6 (a)) appear to contain more than one harmonic, with photon number of figure 5.6 (b) appearing to show the most amount of harmonics. In all cases, it is clear to see that these harmonics are oscillating at frequencies that do not appear to be related to the frequency of the detuning frequency set in the model. Clear examples of this can be seen in figures 5.6 (b) & (c) where the harmonics are oscillating periodically at a fundamental frequency of approximately 4.99GHz and approximately 6.56GHz respectively, whereas the detuning frequencies are set to -37GHz and -20GHz respectively. Similarly, in figure 5.6 (d), although the frequency detuning is set to 10GHz, the carriers and photons are oscillating, with apparent multiple harmonics, at a fundamental frequency of approximately 13.45GHz.

In order to confirm the multiple harmonics assumption noted above, Fast-Fourier-Transform (FFT) plots, with a Hamming Window setting, have been made from the photon number in order to examine the power spectrum in each case. These can be seen in the lower plots from figures 5.6 (a)-(d). It should be noted here that the DC components of the spectrum have been removed for clarity. It is clear from the FFT plots that the outputs from the photon numbers do contain more than the one fundamental harmonic, thus emphasising the additional harmonics seen in figure 5.6 (a)-(d).

Figure 5.6 (a) show the carriers oscillating periodically at a fundamental frequency of approximately 10.14GHz with a frequency detuning of -20GHz. The difference between the frequency detuning value and the measured oscillations gives an indication that the system is still operating within the locking region (when operating outside the locking region, the second lasers' carriers and photons would simply oscillate at a beat frequency of the same value as the detuning frequency, as illustrated in figure 5.7). It is this similar pattern that is apparent where all the black crosses can be seen in figure 5.5.

As can be seen in figure 5.7, when outside of this locking region, the system oscillates at the same frequency as the detuning frequency; for an injection rate of $10ns^{-1}$, and a frequency detuning of -21GHz, it is clear from the plot that the second lasers' carriers and photons are oscillating periodically at a beat frequency of approximately 21GHz, which is the same frequency as the detuning frequency, thus giving a clear indication that the system is no longer operating within the locking region.

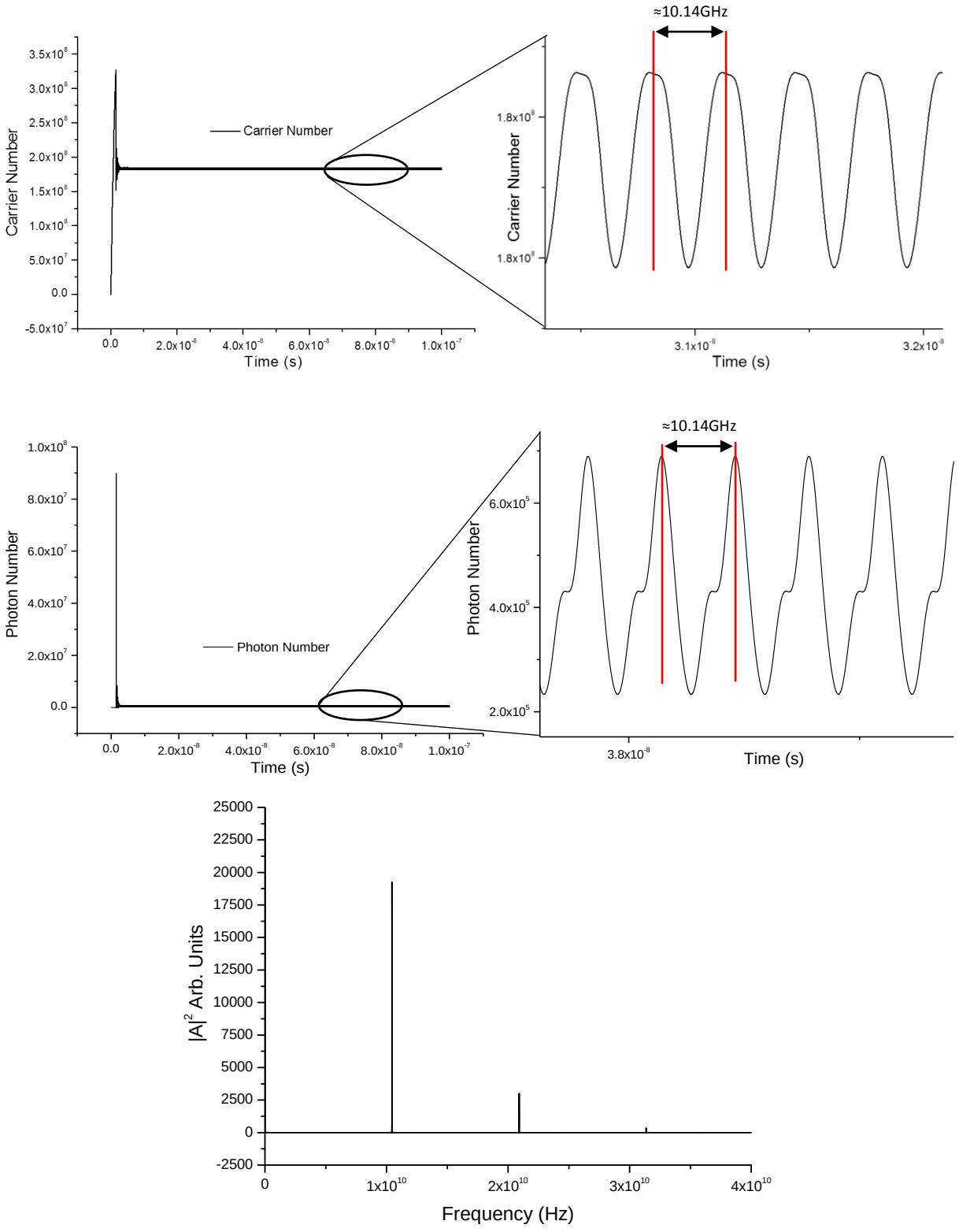

Figure 5.6 (a): *Carrier (top figure) and photon (middle figure) number output with an injection rate, κ_c, of 10ns^{-1} with Δf = -20GHz. The carrier and photon numbers are oscillating periodically at a fundamental frequency of ≈10.14GHz. The bottom graph shows the photon number plotted on an FFT, and this confirms the multiple harmonics seen in the photon number plot.*

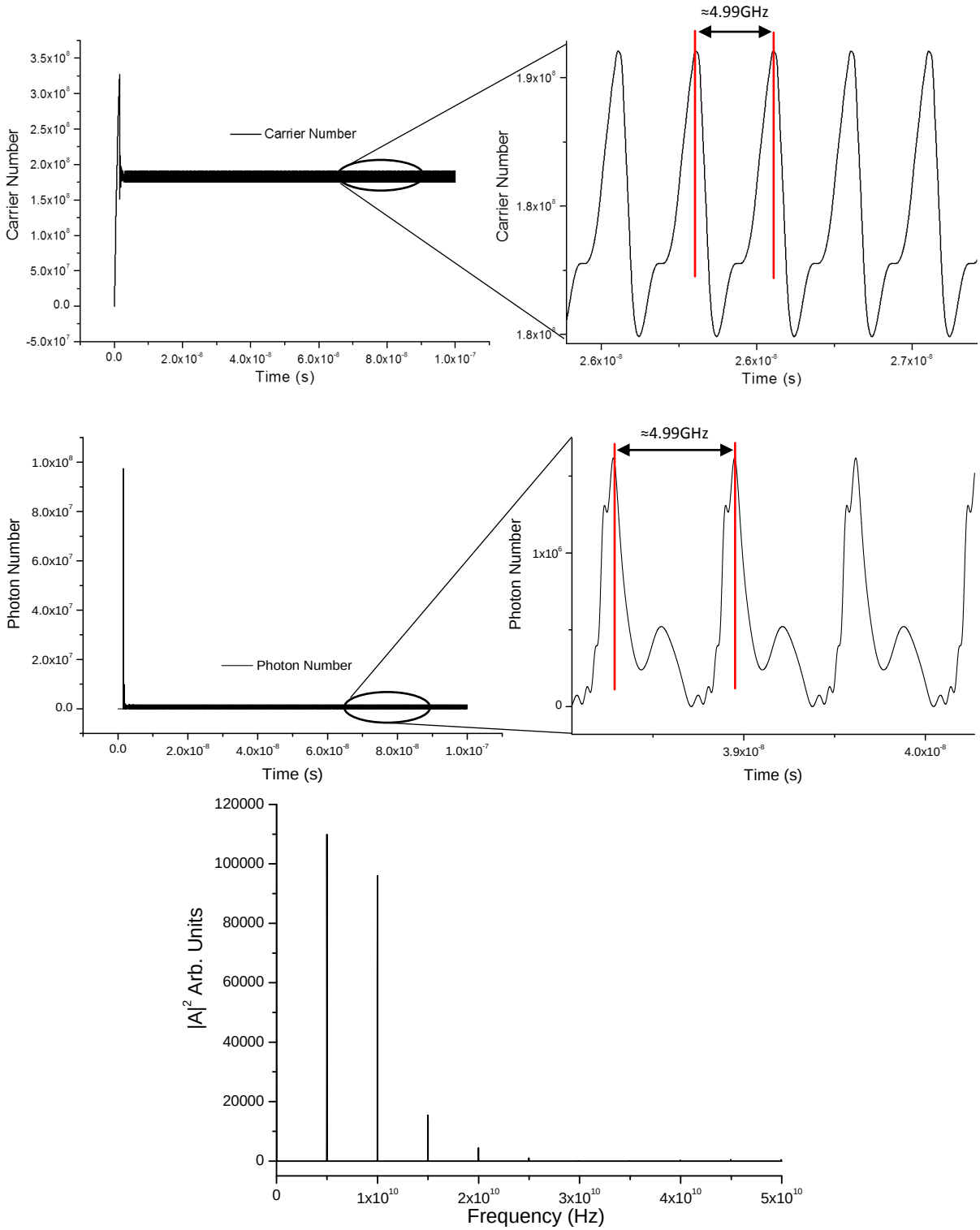

Figure 5.6 (b): *Carrier (top figure) and photon (middle figure) number output with an injection rate, κ_c, of 50ns^{-1} with Δf = -37GHz. The carrier and photon numbers are oscillating periodically, where the waveform appears to include multiple harmonics oscillating with a fundamental frequency of ≈4.99GHz. The bottom graph shows the photon number plotted on an FFT, and this confirms the multiple harmonics seen in the photon number plot.*

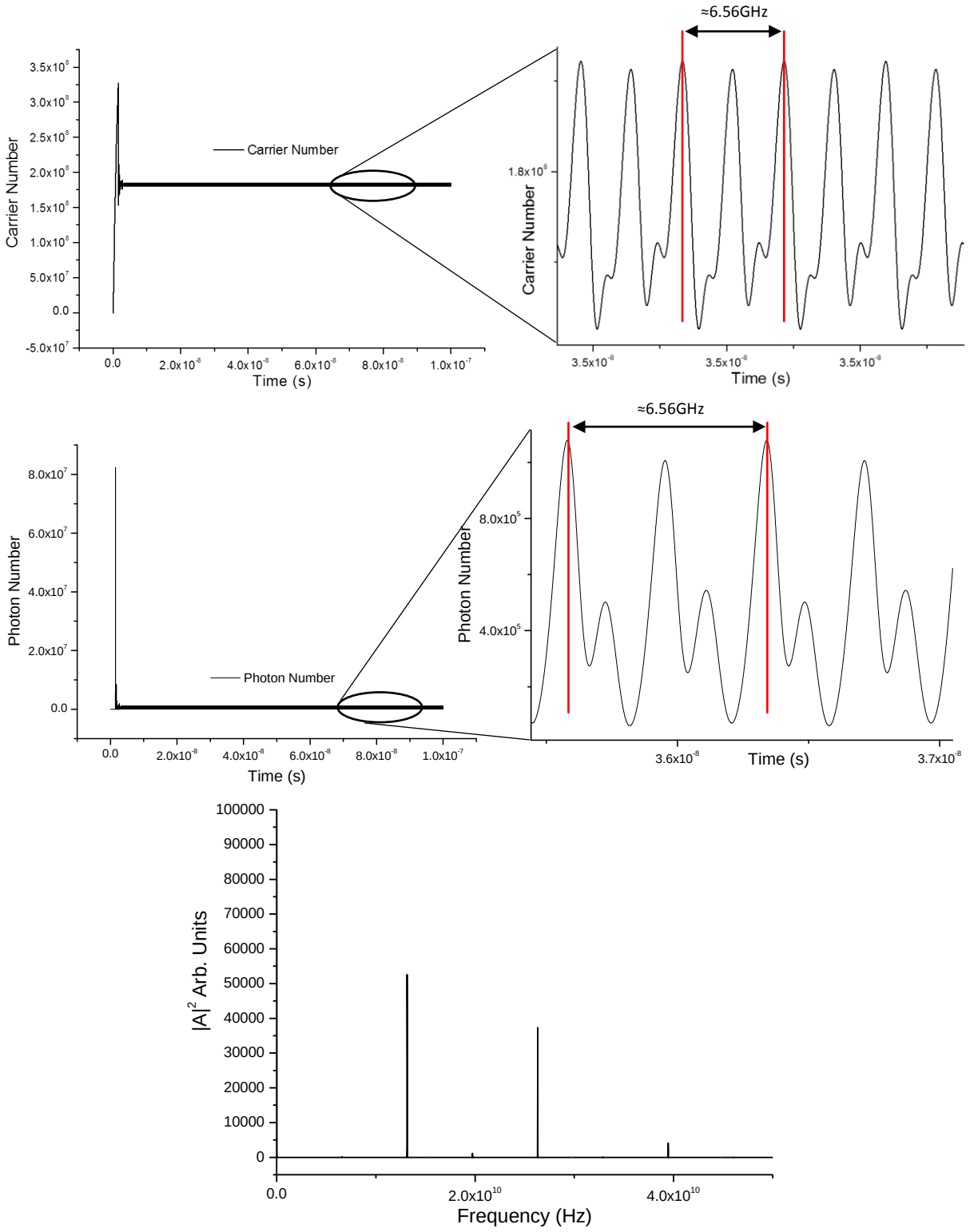

Figure 5.6 (c): *Carrier (top figure) and photon (middle figure) number output with an injection rate, κ_c, of 50ns^{-1} with Δf = 20GHz. The carrier and photon numbers are oscillating periodically, where the waveform appears to include multiple harmonics oscillating with a fundamental frequency of ≈6.56GHz. The bottom graph shows the photon number plotted on an FFT, and this confirms the multiple harmonics seen in the photon number plot.*

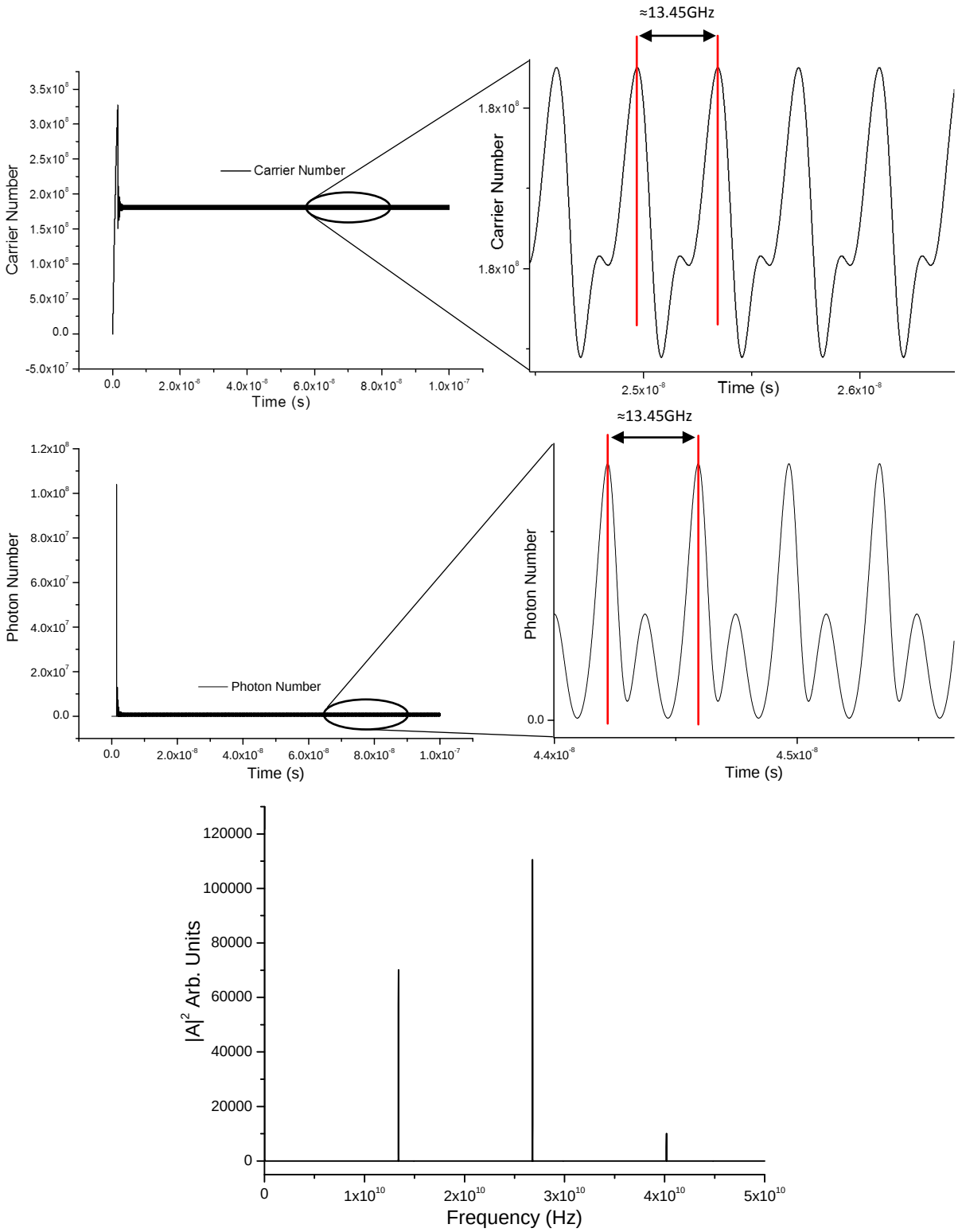

Figure 5.6 (d): *Carrier (top figure) and photon (middle figure) number output with an injection rate, κ_c, of 90ns^{-1} with Δf = 10GHz. The carrier and photon numbers are oscillating periodically, where the waveform appears to include multiple harmonics oscillating with a fundamental frequency of ≈13.45GHz. The bottom graph shows the photon number plotted on an FFT, and this confirms the multiple harmonics seen in the photon number plot.*

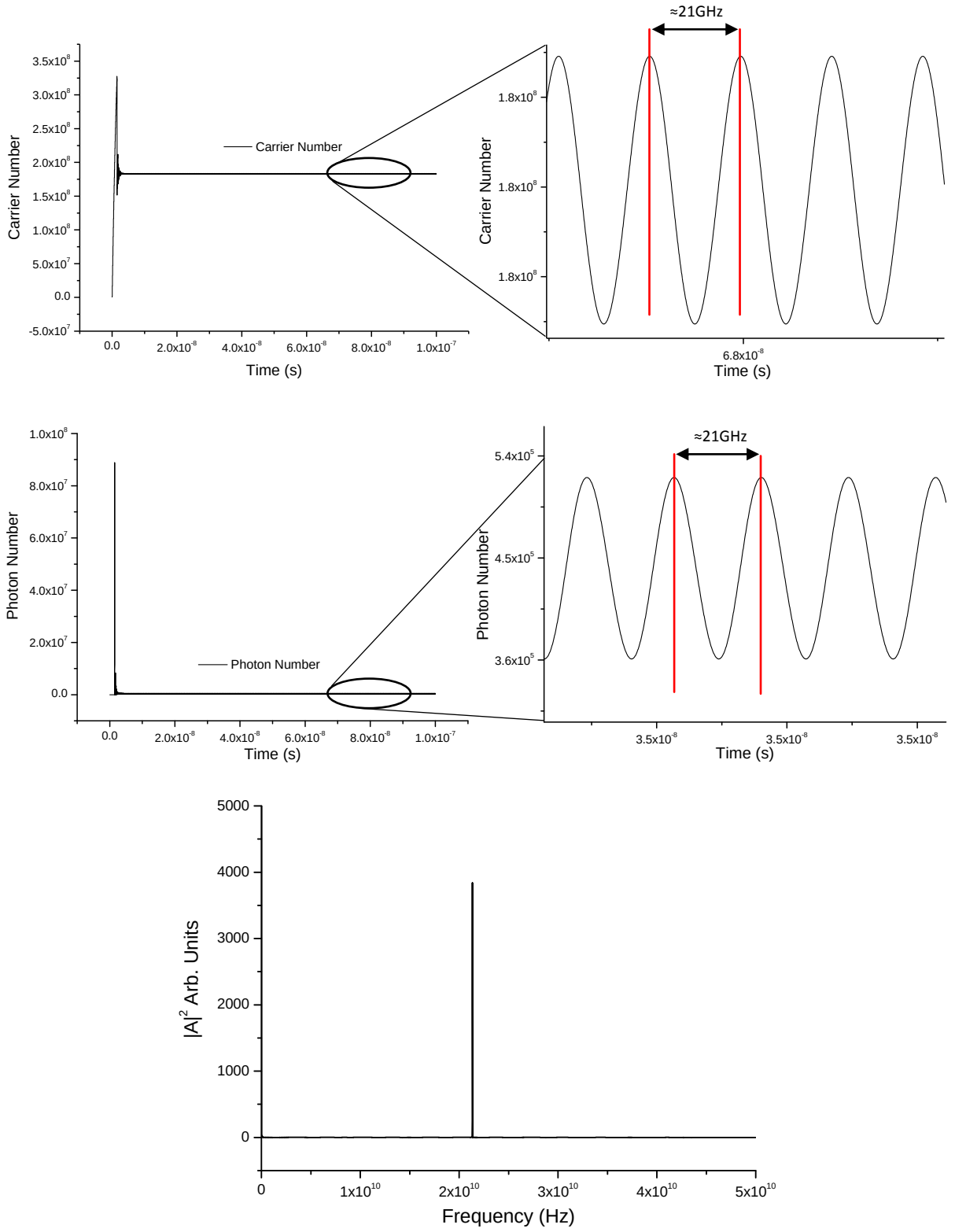

Figure 5.7: Carrier (top figure) and photon (middle figure) number output with an injection rate, κ_c, of 10ns^{-1} with a frequency detuning, Δf, of -21GHz – The carrier and photon numbers are oscillating periodically with a fundamental frequency of ≈21.37GHz. *The bottom graph shows the photon number plotted on an FFT, which clearly shows the single harmonic in the spectrum.*

As previously discussed, when operating inside the locking region, the second lasers' carriers would oscillate, often with multiple harmonics, similar to the behaviours seen in figures 5.6, (a)-(d), where the second lasers' carriers and photons would oscillate at a frequency unrelated to the detuning frequency. Considering the data in Appendix D, there is a clear transition from where the system is not oscillating at the detuning frequency, to where it is. There are, however, a couple of interesting discrepancies in the data where, although the system is outside the locking region, the system is oscillating at a higher frequency than the detuning frequency (this was only apparent for higher injection rates and positive values of detuning). For example, with an injection rate of $60ns^{-1}$, and a frequency detuning of +23GHz, the system would oscillate with a frequency of approximately 28.58GHz. Similarly, with an injection rate of $70ns^{-1}$, $80ns^{-1}$ and $90ns^{-1}$ and a frequency detuning of +23GHz in each case, the system would oscillate at approximately 29.04GHz, 29.77GHz and 30.89GHz respectively. This is a clear increase in frequency compared to the detuning frequency, and compared to lower injection rates.

The case will now be considered where chaos is potentially apparent in the behaviour of the system (blue squares in figure 5.5). There are smaller regions of chaos than there were of the periodic behaviour. An example of the potential chaos observed can be seen in figure 5.8. From the figure, there appears to be some periodicity, and this seems to have a frequency of approximately 9.12GHz. There appears to be multiple harmonics visible in the plot, and this could indicate a sign of period doubling route to chaos [37]-[39]. The assumption of period doubling route to chaos is made here as this is consistent with the multiple harmonic response as seen in figure 5.6 (b)-(d). In order to confirm the potential chaotic behaviour of the system, the photon numbers are plotted on an FFT in order to examine the power spectrum; this is shown in the lowest plot from figure 5.8. From the figure, it is not easy to see the individual peaks in the spectrum, thus indicating the potential chaotic behaviour of the system. It should again be noted that the DC component has been removed for clarity.

This is a potentially very interesting region of behaviour of the system, however, for the work conducted here, this behaviour is to be avoided.

From figure 5.5, there are two potential chaotic regions for each injection rate, with the exception of $5ns^{-1}$ and $10ns^{-1}$ where only a single potential chaotic region is observed, and no potential chaotic region at all for an injection rate of $90ns^{-1}$. From analysis, it can also be seen that the potential chaotic regions vary in width, with the widest region apparent with an injection rate of $20ns^{-1}$. Here, the chaotic region ranges from -3GHz up to +14GHz, thus giving a width of 18GHz, whereas the smallest chaotic region observed, of just a single point, is with an injection rate of $80ns^{-1}$ and a frequency detuning of +10GHz.

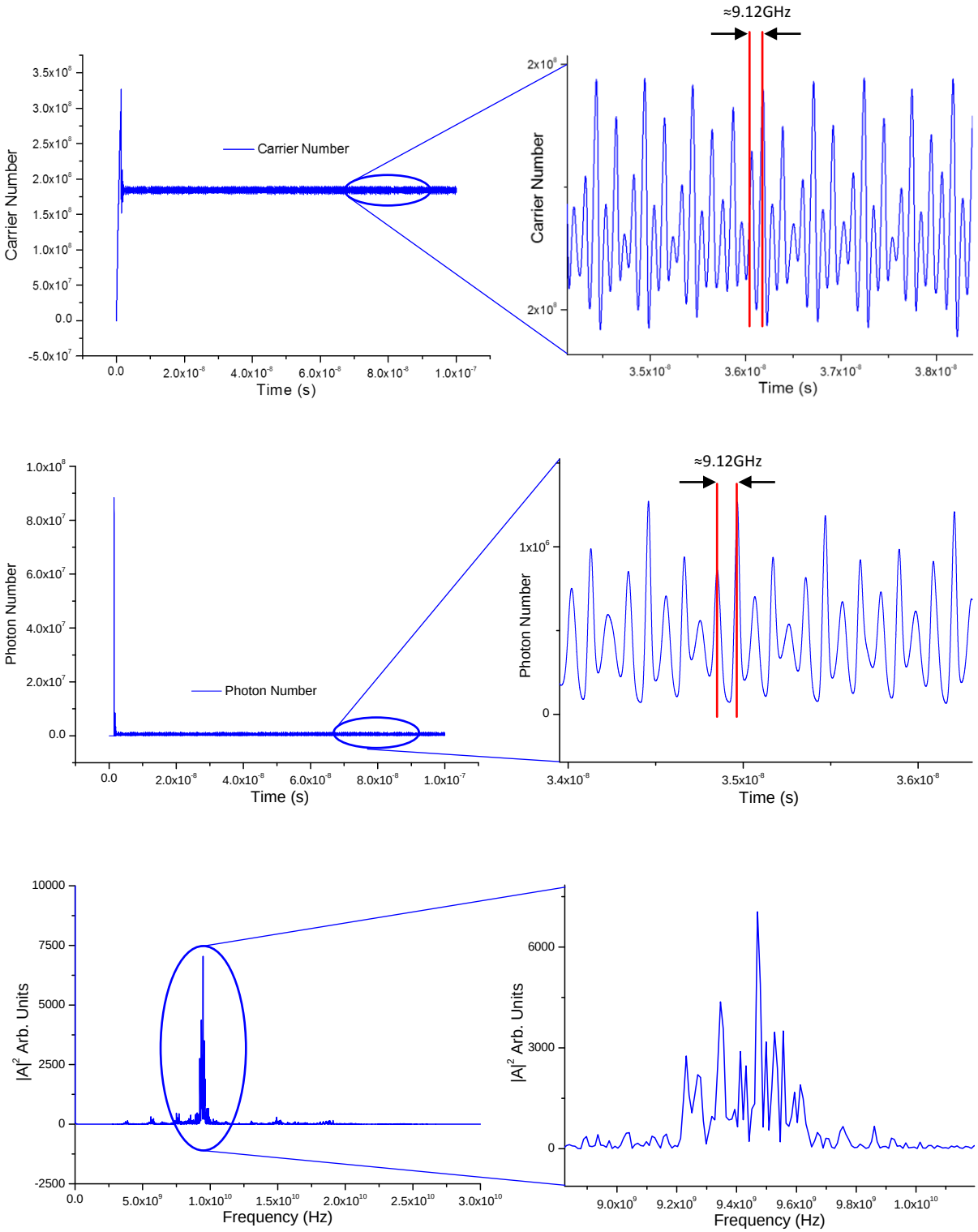

Figure 5.8: *Carrier (top figure) and photon (middle figure) number output with an injection rate, κ_c, of 10ns^{-1} with a frequency detuning, Δf, of 0GHz – The carrier and numbers are clearly oscillating in a potentially chaotic manner with a periodicity of ≈9.12GHz. The bottom figure shows the photon number plotted on an FFT, which clearly confirms the potential chaotic behaviour of the system.*

The final region of interest from figure 5.5 is where injection locking (red circles) is present between the two lasers, as can be seen in figure 5.9. From the figure, it can clearly be seen that there are no oscillations apparent in the carrier or photon output response of the system, and both the first and second lasers' carriers and photons have settled to a constant steady-state value, albeit that the first has settled to a higher value than the second. This behaviour is to be expected; because the light from the first laser is being injected into the cavity of the second laser, this will cause the photons in the second laser cavity to increase (similar to the behaviour that was observed in the dual-wavelength laser simulations). As a direct consequence, the number of carriers in the second laser cavity will decrease to take account for the increase in photons. This is further emphasised in the plot of the photons where the steady-state photon number for the second laser is higher than the steady-state photon number for the first laser.

In order to emphasis the fact that the carrier and photon numbers for both lasers are operating on a single frequency, the photon numbers are plotted on FFT plots (bottom plots from figure 5.9), and as can be seen here, we only have the one harmonic in the spectrum for both lasers, thus indicating a single frequency operation.

As previously mentioned, the stronger the injection rate, the wider the locking range appears to be. The narrowest locking range is with an injection rate of $20ns^{-1}$, where the second laser locks to the frequency of the first laser, with a detuning frequency of -14GHz to -15GHz. The widest locking range by far is when the system is operating with an injection rate of $90ns^{-1}$, where the lasers are injection locked from -34GHz to -55GHz, with a couple of anomalies which will be discussed. When operating at the edge of the locking range, the system will either return to periodic oscillations (as per figure 5.6 (a)-(d)), or the system will oscillate at the same frequency as the detuning frequency. As previously mentioned, it can be assumed that the width of the locking range will continue to increase if the injection rate is increased. As previously mentioned, there are a couple of anomalies in the locking range, particularly at higher injection rates. The first is apparent at an injection rate of $60ns^{-1}$, where there is injection locking at -41GHz, the system will then oscillate at approximately 43.43GHz, with a detuning frequency of -42GHz, and then with a detuning frequency of -43GHz, the system will return to being injection locked. With a frequency detuning of -44GHz, periodic oscillations are apparent of approximately 4.10GHz, before the system returns to oscillating at approximately 45.82GHz with a frequency detuning of -45GHz. A similar pattern is observed with an injection rate of $70ns^{-1}$, $80ns^{-1}$ and $90ns^{-1}$ where the system will 'jump' from being injection locked, to either periodic oscillations or oscillating at the same frequency as the detuning frequency.

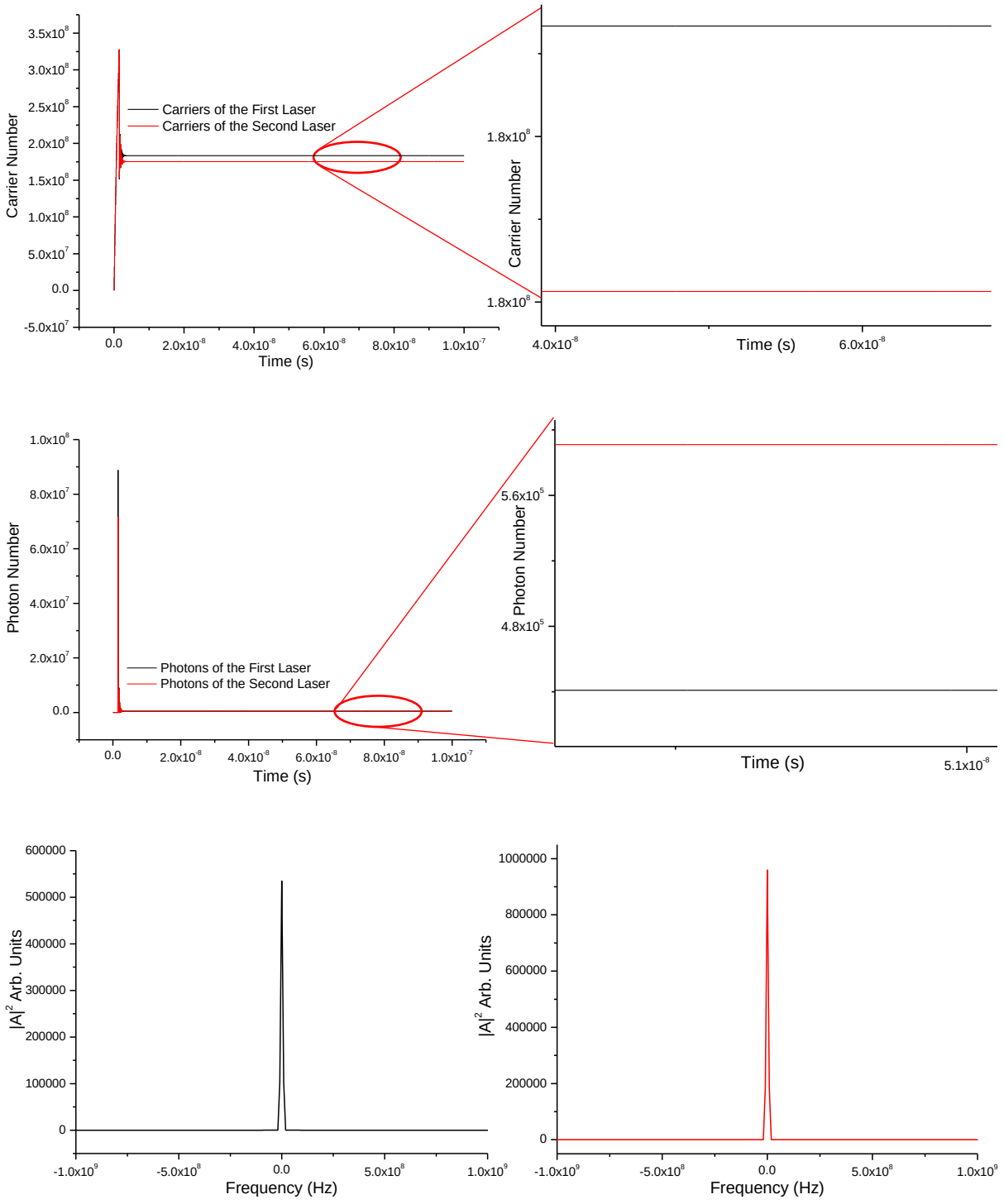

Figure 5.9: *Carrier (top figure) and photon (middle figure) number output for the two lasers with an injection rate, κ_c, of 90ns^{-1} with a frequency detuning, Δf, of -40GHz. The carrier and photon numbers have clearly settled to a constant steady-state value, thus indicating a single frequency operation. This is emphasised in the FFT plot (bottom figure) where only a single harmonic is present in the system.*

5.7 – Bidirectional Injection Locking Model Simulation

The next stage is to analyse the difference in behaviour seen in the system when the system is operating with bidirectional injection, again using the FORTRAN model (the code for which is an evolution of the code in Appendix C), and again implementing equations (5.1)-(5.4), and the parameter values from table 5.1. It is the work here that will build a foundation for the work on FWM presented in chapters six and seven. In order to implement the effect of bidirectional injection, the injection rate term must be included in the first laser equation (equation (5.1)) as well as the second laser equation (equation (5.2)) in order to simulate the effects of the first laser injecting light into the second laser cavity, and the second laser injecting light into the first laser cavity. Hence, equation (5.1) becomes:

$$\frac{dA_1(t)}{dt} = \frac{1}{2}(1 + i\alpha)\left[G_1 - \frac{1}{\tau_p}\right]A_1(t) + \kappa_c A_2(t)e^{-i\Delta\omega t} \tag{5.6}$$

From equation (5.6), it must be noted that the detuning frequency, $\Delta\omega$, is negative for the first laser as a consequence of the relative frequencies of the lasers. It should again be noted here that everything in the model is kept identical, except for the wavelength. This is again justifiable for this work as it serves as a 'building-block' for the work presented in chapters six and seven, where the work in this chapter is built upon.

The results of this model can be seen in figure 5.10. In this case, the model was simulated with detuning values, Δf, ranging from -40GHz to 40GHz, and the injection rate ranges from 10ns^{-1} to 90ns^{-1}. As with the case in figure 5.5, the black crosses represent the laser's carrier and photon numbers oscillating periodically, the blue squares represent a potential chaotic behaviour, and the red circles represent the injection locking region between the two lasers.

From figure 5.10, it is clear to see the symmetry in the locking region compared to the system that was only operating under unidirectional injection locking, however, similarly to the case of unidirectional injection, the width of the locking range increases the stronger the injection rate is. The symmetry of the locking range is apparent due to the opposing signs of detuning frequencies as seen in equations (5.2) and (5.6).

From the results, it is apparent that there are only two regions where a potential chaotic behaviour was observed, those being at an injection rate of 30ns^{-1} and 80ns^{-1}, with detuning frequencies of +10GHz and +25GHz respectively. This is contrary to the case of unidirectional injection where many more potential chaotic regions were apparent, in addition to much wider regions of potential chaotic behaviour. An example of the observed chaotic region can be seen in figure 5.11. It should be noted here that only the carrier and photon response of the first laser are shown in all the following figures, as both the first and the second laser show the exact same responses.

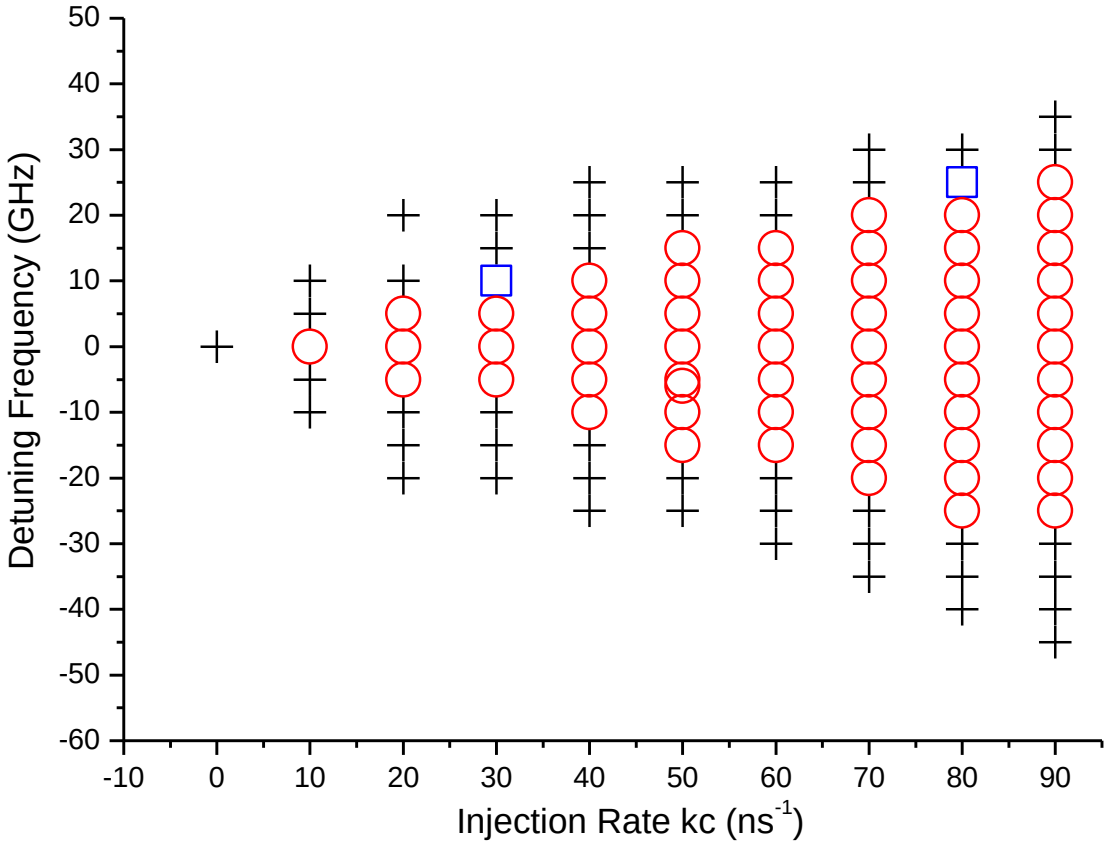

Figure 5.10: *Behavioural plot for the case of bidirectional injection with detuning values, Δf, ranging from -40GHz to 40GHz, with injection rates, κ_c, ranging from 10ns^{-1} to 90ns^{-1}. The black crosses represent the lasers' carrier and photon number output oscillating periodically, the blue squares represent the carrier and photon number output potentially exhibiting a chaotic behaviour, and the red circles represent the locking condition between the first and second lasers'. The blank areas within the locking regions are areas that have not been studied for this part of the work. (Data for the plot can be found in Appendix E).*

As mentioned previously, the first regions to be examined here are the regions of potential chaotic behaviour, as represented in figure 5.11. The example of potential chaotic behaviour is for an injection rate of 30ns^{-1} and a frequency detuning of +10GHz. From the figure, there are clearly multiple harmonics in the responses of the carrier and photon numbers, which also appear to show some periodicity; however, the period is slightly reduced to approximately 6.98GHz for the carrier oscillations, and approximately 14.05GHz for the photon oscillations, as appose to approximately 9.12GHz for unidirectional injection locking. In order to confirm the potential chaotic behaviour, the photon number has been plotted on an FFT (lowest plot in figure 5.11), and from the FFT it is again not easy to see the individual peaks in the spectrum, thus indicating the potential chaotic behaviour of the system.

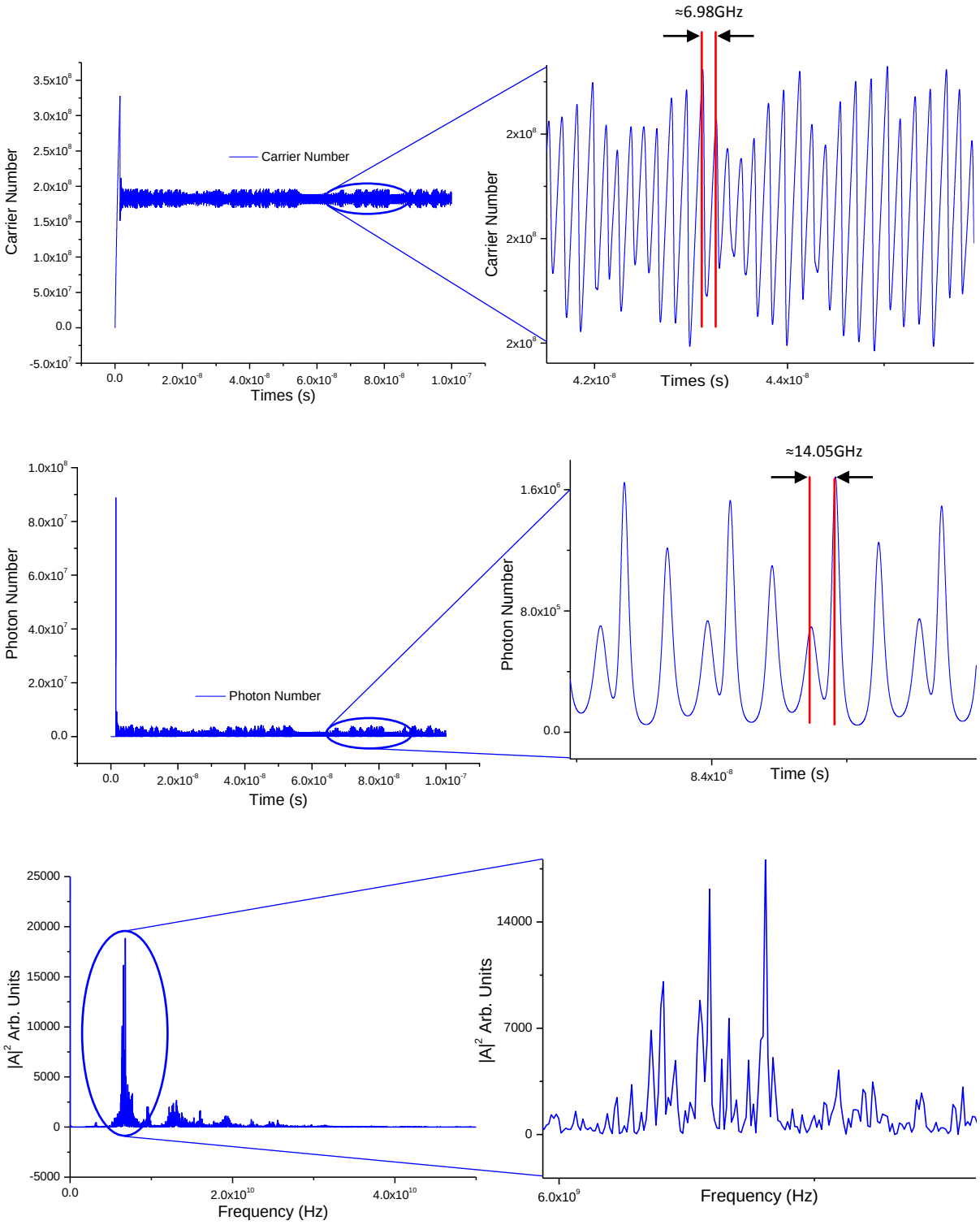

Figure 5.11: *Carrier (top figure) and photon (middle figure) number output with an injection rate, κ_c, of 30ns^{-1} with a frequency detuning, Δf, of 10GHz – The carrier and numbers are clearly oscillating in a potentially chaotic manner with a periodicity of ≈6.98GHz for the carriers, and ≈14.05GHz for the photons. The bottom figure shows the photon number plotted on an FFT, which clearly confirms the potential chaotic behaviour of the system.*

Similarly, for the case of unidirectional injection locking, the black crosses in figure 5.10 are where the carrier and photon number output are oscillating periodically, as illustrated in figure 5.12, (a)-(c). Unlike the case for unidirectional injection locking, whereby multiple harmonics were visible in the carriers' and photons' output response, for bidirectional injection locking, only one harmonic is apparently visible in each case, with the exception of the photon number output plot from figure 5.12 (b). However, similarly to the case of unidirectional injection locking, the harmonics seem to be oscillating at frequencies that seem unrelated to the detuning frequency in any way. By first considering figure 5.12 (a), it is possible to see a periodic pattern, whereby the carriers and photons are oscillating at approximately 7.64GHz (whereas the detuning frequency is set to -20GHz). What is also apparent from figure 5.12 (a) is that the carriers are oscillating in an almost triangular fashion, as appose to more of a sine wave, whereas the photon numbers are oscillating with apparent positive excursions, with the same frequency as the carriers. From looking at figure 5.12 (b), it can be seen again that the carriers and photons are oscillating periodically, however this time with a slightly higher frequency of approximately 9.74GHz. The response almost seems triangular in fashion again, however with a slight 'kink' each time the carriers are increasing. The photons are again oscillating with positive excursions, however there are additional humps at the troughs of these excursions. Again, the periodic frequency of approximately 9.74GHz seems entirely unrelated to the detuning frequency, seeing as the detuning frequency is set to -30GHz. Figure 5.12 (c) is more closely related to figure 5.6 (a), whereby the carriers' response closely represents a sine wave, oscillating at approximately 11GHz. It can be assumed here, as was the case for unidirectional injection locking, that the two lasers are still operating within the locking region here as the oscillations of the carriers are unrelated to the detuning frequency (oscillating at approximately 11GHz as appose to a detuning frequency of +30GHz).

In order to examine the potential for multiple harmonics in the response of the system, the photon numbers are again plotted on an FFT, and what is interesting is that each FFT plot appears to show multiple harmonics in the response of the system, which do not appear in the response of the carrier and photon number outputs (with the exception of the photon number output plot from figure 5.12 (b)).

At each point in figure 5.10 where a black cross is apparent, the two lasers' carrier and photon responses would show behaviours similar to figures 5.12 (a)-(c).

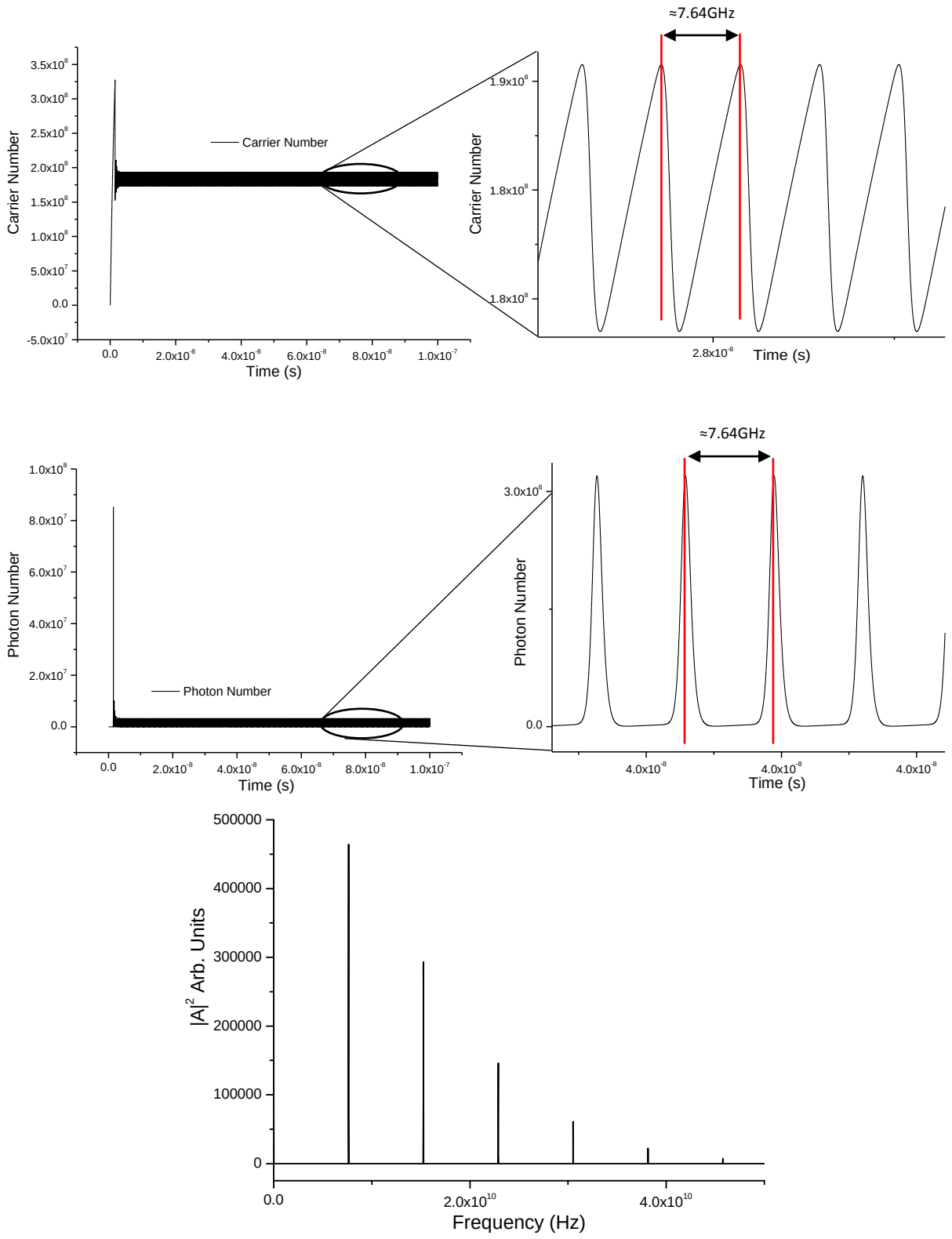

Figure 5.12 (a): *Carrier (top figure) and photon (middle figure) number output with an injection rate, κ_c, of 40ns^{-1} with Δf = -20GHz. The carrier and photon numbers are oscillating periodically at a fundamental frequency of ≈7.64GHz. The bottom graph shows the photon number plotted on an FFT, and this shows the apparent presence of multiple harmonics in the system.*

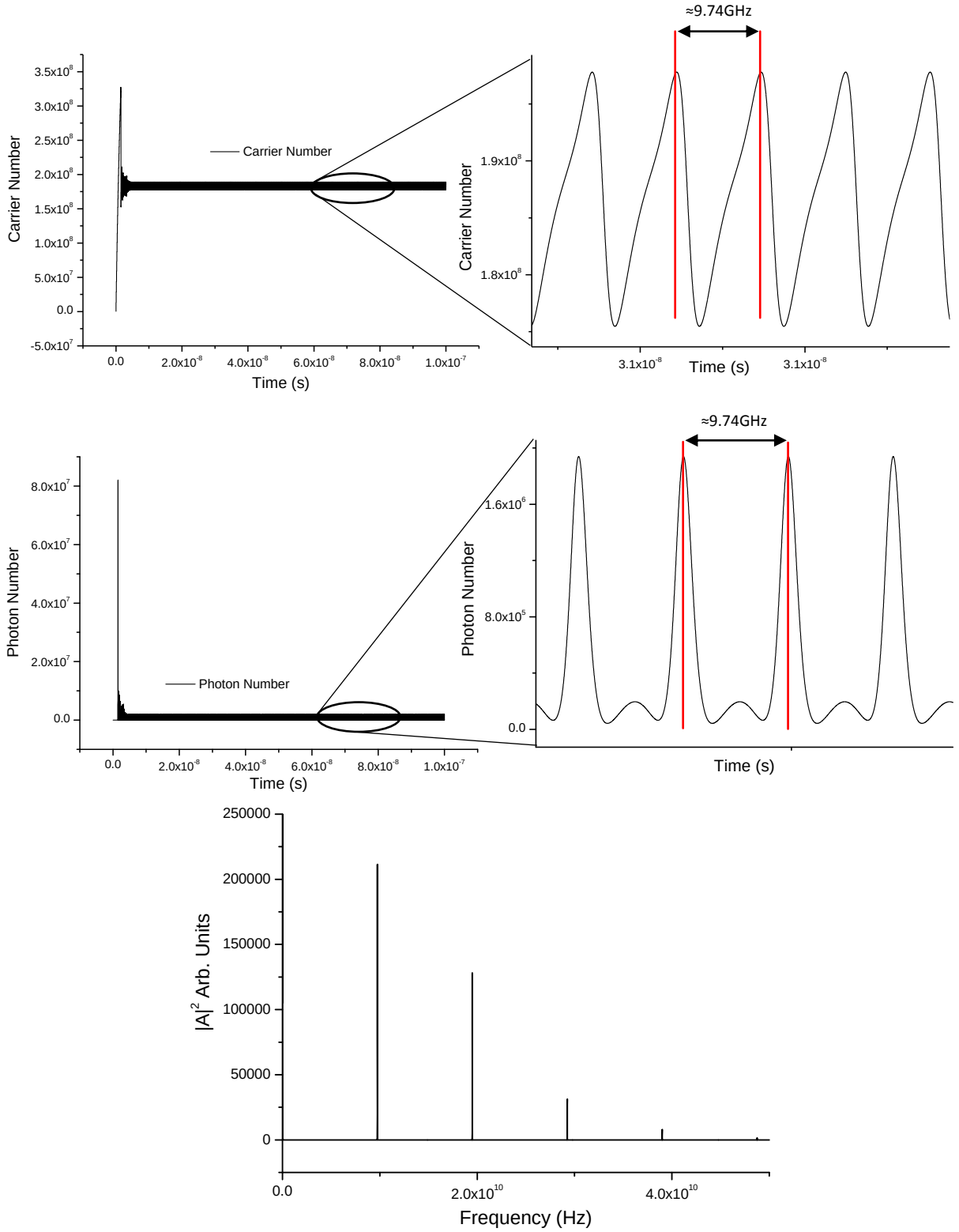

Figure 5.12 (b): *Carrier (top figure) and photon (middle figure) number output with an injection rate, κ_c, of 70ns^{-1} with Δf = -30GHz. The carrier and photon numbers are oscillating periodically at a fundamental frequency of ≈9.74GHz, with multiple harmonics present in the photon output response. The bottom graph shows the photon number plotted on an FFT, and this confirms the presence of multiple harmonics in the system.*

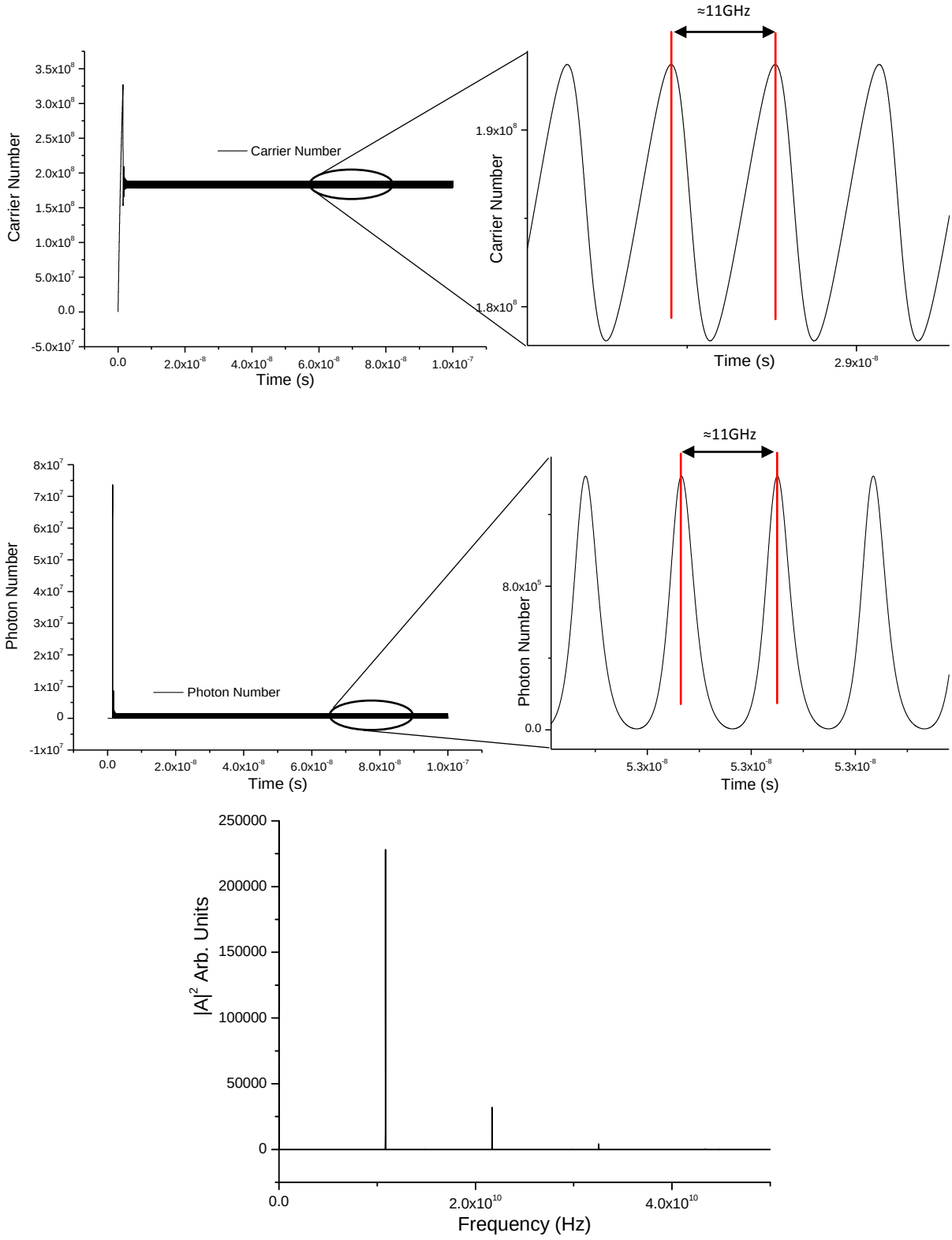

Figure 5.12 (c): *Carrier (top figure) and photon (middle figure) number output with an injection rate, κ_c, of 90ns^{-1} with Δf = 30GHz. The carrier and photon numbers are oscillating periodically at a fundamental frequency of ≈11GHz. The bottom graph shows the photon number plotted on an FFT, and this shows the apparent presence of multiple harmonics in the system.*

As previously discussed, when operating inside the locking region, the carriers and photons for both the first and second lasers' would oscillate at frequencies unrelated to the detuning frequency value, however, when operating outside the locking region, as illustrated in figure 5.13, the two laser's carriers and photons would simply oscillate at a beat frequency of the same value as the detuning frequency. The example shown here is for an injection rate of $30ns^{-1}$ and a frequency detuning of -30GHz, and it is clear from the figure that the first lasers' (as well as the second lasers') carriers and photons are oscillating at approximately the same frequency as the detuning frequency.

The final region of interest are the red circles in figure 5.10, and this is of course where the two lasers' have locked together in frequency. This is illustrated in figure 5.14 whereby the injection rate is set to $50ns^{-1}$ with a frequency detuning of -10GHz. Here, it is clear to see that the carriers and photons response for the first and the second lasers have settled to a constant value after the relaxation oscillations, however, unlike the case for unidirectional injection locking where they both settled to different values (owing to the singular direction of injection from the first laser into the cavity of the second laser), in this case, both the first and second lasers' carrier and photon outputs have settled to exactly the same value (both are shown individually in figure 5.14). This is to be expected as there is not only injection of light from the first laser into the cavity of the second laser, but also an injection of light from the second laser into the cavity of the first laser. As was the case with unidirectional injection locking, the stronger the injection rate, the wider the locking range appears to be. The narrowest locking range is with an injection rate of $10ns^{-1}$ and a frequency detuning of 0GHz, and the widest locking region is again with an injection rate of $90ns^{-1}$, where the lasers are injection locked from -25GHz to +25GHz. As was the case with unidirectional injection locking, it can be assumed that a further increase in injection rate would further broaden the locking range. It should also be noted here that each time the lasers injection locked together, the carriers (and also the field) would always settle to the same value as each other. As a result, the bidirectional injection locking scheme would always give a zero frequency separation between the two locked lasers.

Finally, when considering the case of unidirectional injection, and when operating outside of the locking range, particularly for higher injection rates, the system oscillates at slightly higher frequencies than the detuning frequency, however, when considering bidirectional injection, the opposite is true, where the system oscillates at a slightly lower frequency than the detuning frequency when operating outside of the locking range. Considering an injection rate of $60ns^{-1}$ with a frequency detuning of +30GHz as an example, it is possible to see that the system is actually oscillating at a frequency of approximately 23.36GHz, almost 7GHz lower than the frequency detuning value. It can be assumed that the system is outside of the locking region in these cases as an undistorted sine wave is observed in the output response of the system (similar to figures 5.7 and 5.13).

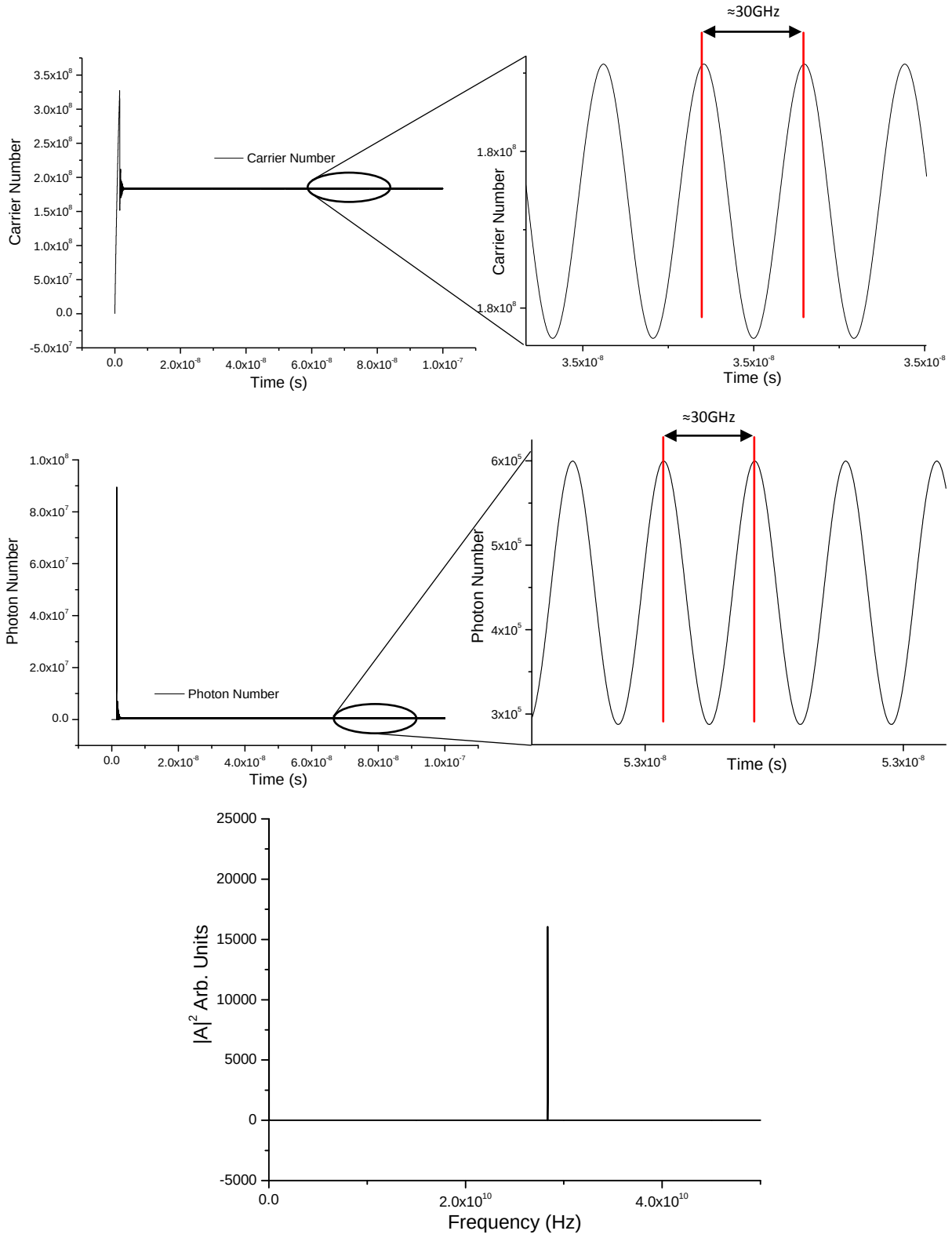

Figure 5.13: Carrier (top figure) and photon (middle figure) number output with an injection rate, κ_c, of 30ns^{-1} with a frequency detuning, Δf, of -30GHz – The carrier and photon numbers are oscillating periodically with a fundamental frequency of ≈30GHz. *The bottom graph shows the photon number plotted on an FFT, which clearly shows the single harmonic in the spectrum.*

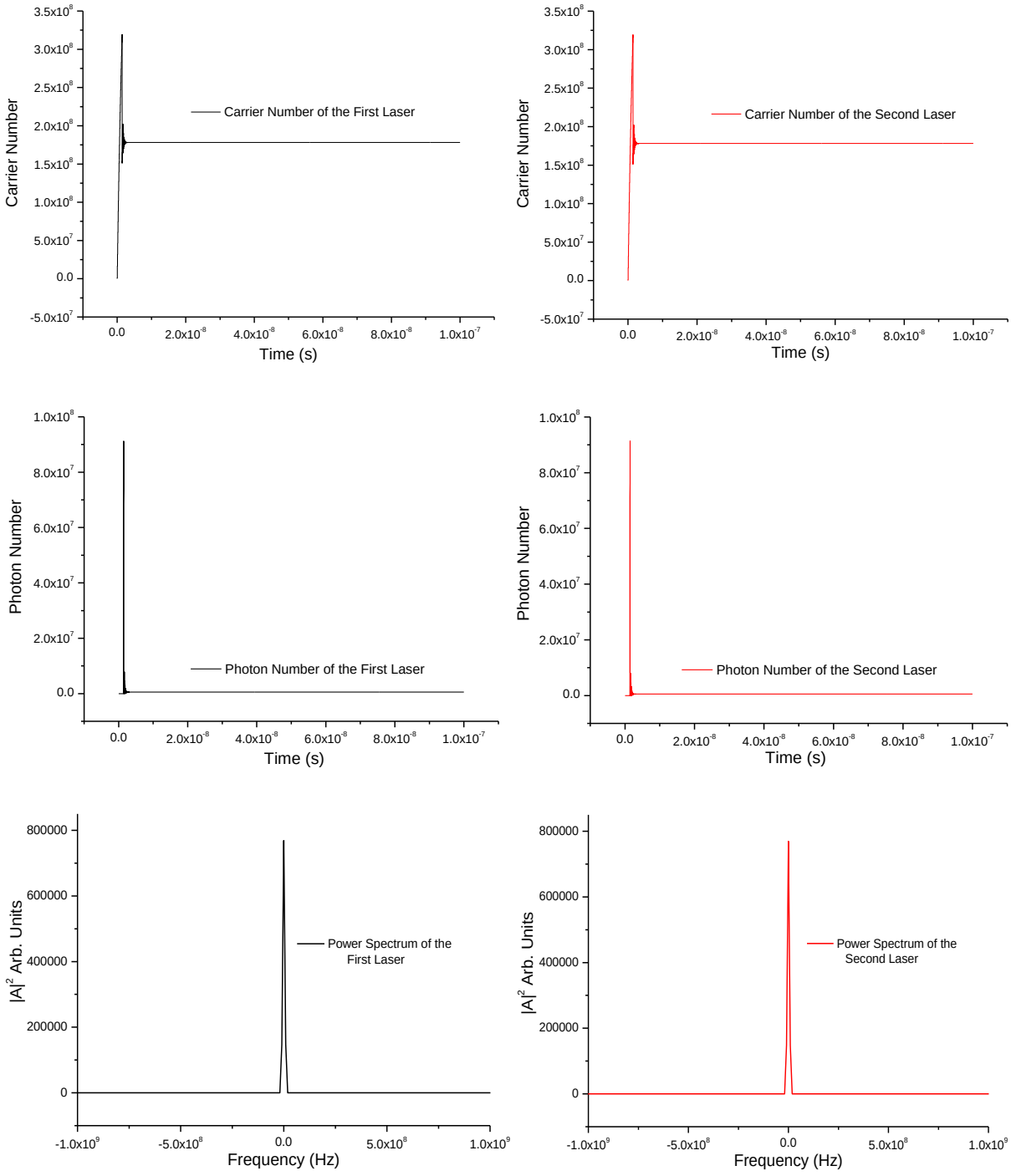

Figure 5.14: *Carrier (top figure) and photon (middle figure) number output for the two lasers with an injection rate, κ_c, of 50ns^{-1} with a frequency detuning, Δf, of -10GHz. The carrier and photon numbers have clearly settled to a constant steady-state value, thus indicating a single frequency operation. This is emphasised in the FFT plot (bottom figure) where only a single harmonic is present in the system.*

In order to confirm the locking condition, and hence emphasise the singular frequency operation of the system in the locked condition, FFT plots are made of the photon numbers (bottom plots in figure 5.14), and from these, it is possible to see the singular harmonic that is present in the spectrum from both lasers, thus indicating a singular frequency operation of the system.

5.8 – Summary and Conclusion

This chapter has looked in detail at both unidirectional and bidirectional injection locking, putting particular emphasis on the various locking regions and behaviours present in both schemes. In both schemes, four distinct behavioural regions are present; firstly, regions where either scheme would exhibit periodic responses in the carrier and photon output responses, a potential chaotic behaviour in the carrier output response, a locked condition where both the first and second lasers' carriers and photons would settle to a constant value, and finally, the unlocked condition whereby the carriers and photons would simply oscillate at a beat frequency of the same value as the detuning frequency.

There are clear differences in the locking regions when operating with either unidirectional, or bidirectional, injection locking. Under the unidirectional injection locking scheme, the locking region was highly asymmetrical, as a result of the linewidth enhancement factor, α, and the singular direction of detuning frequency (only applied to the second laser in this case). Under the bidirectional scheme, the locking region was highly symmetrical, as a result of the relative detuning frequencies ($+\Delta\omega$ in the second laser and $-\Delta\omega$ in the first laser).

Another clear difference between the unidirectional and bidirectional locking schemes are the areas where periodicity was apparent (black crosses from figures 5.5 and 5.10). In the unidirectional scheme, these areas often exhibit more than one harmonic in the carriers' and photons output oscillation response; these harmonics oscillated at frequencies unrelated to the detuning frequency value. To confirm these multiple harmonics, FFT plots were made of the photon numbers, which clearly showed multiple harmonics operating within the system. For the bidirectional scheme, the regions of periodicity would only exhibit a single harmonic in the carriers' and photons output oscillation response each time, with the exception of the photons' output oscillation with an injection rate of $70ns^{-1}$ and a frequency detuning of -30GHz, where additional 'humps' were visible at the troughs of the main peaks. Similarly to the unidirectional case, they would again oscillate at a frequency unrelated to the detuning frequency. What was interesting in these plots is that although the carriers and photons seemed to exhibit a single harmonic operation, the FFT plots of the photons clearly showed multiple harmonics oscillating in each case.

Similarly, in both schemes, when operating outside the locking regions, the second lasers' carriers and photons (for the case of unidirectional injection locking) and the first laser and second lasers' carriers

and photons (for the case of bidirectional injection locking) simply oscillated at a beat frequency of the same value as the detuning frequency, thus indicating an outside locking region operation.

Both schemes also exhibit a potential chaotic behaviour, whereby the carriers' and photons output response oscillated in an apparent chaotic manner, with multiple harmonics apparent in the response; these would be oscillating at a frequency unrelated to the detuning frequency value. The potential chaotic regions were far fewer in the bidirectional scheme, with only two separate regions observed at injection rates of $30ns^{-1}$ and $80ns^{-1}$ respectively, compared to the unidirectional scheme where multiple potential chaotic regions were observed at all injection rates, excluding $90ns^{-1}$.

The locking condition was apparent in both schemes whereby the second lasers' carriers and photons (for the case of unidirectional injection locking) and the first laser and second lasers' carriers and photons (for the case of bidirectional injection locking) would settle to a constant steady-state value after the relaxation oscillations. In the unidirectional scheme, the carriers and photons in the second laser would have a different steady-state value than those in the first laser; this is due to the fact that the light from the first laser is being injected into the cavity of the second laser, causing an increase in photons in the cavity. As a result, this will cause a decrease in the number of carriers in the second laser cavity. In the bidirectional scheme, the two lasers would settle to the exact same number of steady-state carriers and steady-state photons (due to the fact that the light from the first laser is being injected into the cavity of the second laser, and vice-versa). As a result of the two lasers settling to the same number of carriers, and the same number of photons, in the locked condition, the two lasers will always lock to the same value in frequency, hence there will always be a zero frequency separation between the two locked lasers, whereas the goal here is to obtain a nonzero frequency spacing between the two locked lasers', with the frequency spacing lying in the THz frequency range. This is confirmed in the FFT plot of the photon numbers where there is clearly only a single frequency present within the system. As a result, the work presented in this chapter provides the building blocks for the work presented in chapters six and seven, whereby a three laser system based on the four-wave mixing (FWM) scheme will be investigated as a means for providing a frequency separation between the two locked lasers.

In chapters six and seven the three laser FWM system will be investigated, whereby the locking regions will again be studied, and the optimum locking region in the '$\Delta\omega/\kappa$' parameter space will be found.

REFERENCES

[1] **X. Zhao**, "Optical injection locking on vertical-cavity surface-emitting lasers (VCSELs): Physics and applications", Ph.D thesis, Dept. Elect. Eng. and Comp. Sci., California Univ., Berkeley, USA, 2008.

[2] **R. Paschotta**, article on 'laser injection locking' in the Encyclopaedia of Laser Physics and Technology, 1. edition, October 2008, Wiley-VCH, ISBN 978-3-527-40828-3.

[3] **B. Razavi**, "A study of injection locking and pulling in oscillators", IEEE J. Solid-State Circuits., vol. 39, no. 9, pp.1415-1424, Sept. 2004.

[4] **R. H. Pantell**, "The laser oscillator with an external signal", Proc. IEEE., vol. 53, no. 5, pp. 474-477, Mar. 1965.

[5] **R. R. Ward**, The living Clocks, 1st ed. New York, Random House, 1971.

[6] **C. Cookson**, "Millennium Bridge wobble explained", Financial Times [Online]. Available: http://www.ft.com/cms/s/0/b758d1d2-4cd7-11da-89df-0000779e2340.html?ft_site=falcon&desktop=true. [Accessed on: Nov. 24, 2016].

[7] **E. Howell**, "Why do soldiers break stride on a bridge?", Live Science [Online]. Available: http://www.livescience.com/34608-break-stride-frequency-of-vibration.html. [Accessed on: Nov. 24, 2016].

[8] **Cornell University**, "Explaining why the Millennium Bridge wobbled", Science Daily [Online]. Available: https://www.sciencedaily.com/releases/2005/11/051103080801.htm. [Accessed on: Nov. 24, 2016].

[9] **K. Sanderson**, "Millennium Bridge wobble explained", Nature International Weekly Journal of Science [Online]. Available: http://www.nature.com/news/2008/081217/full/news.2008.1311.html. [Accessed on: Nov. 24, 2016].

[10] **S. H. Strogatz**, D. M. Abrams, A. McRbie, B. Eckhardt, E. Ott, "Crowd synchrony on the millennium bridge", Nature., vol. 438, pp. 43-44, Nov. 2005.

[11] **B. Van der Pol**, "Forced oscillations in a circuit with non-linear resistance", The Lon, Edin, and Dubl. Philos. Mag and J. of Sci., vol. 3, no. 13, pp. 65-80, 1927.

[12] **R. Adler**, "A study of locking phenomena in oscillators", Proc. IRE., vol. 34, pp. 351-357, Jun. 1946.

[13] **H. L. Stover**, W. H. Steier, "Locking of laser oscillators by light injection", Appl. Phys. Lett., vol. 8, no. 4, pp. 91-93, Feb. 1966.

[14] **S. Kobayashi**, T. Kimura, "Injection locking in AlGaAs semiconductor laser", IEEE J. Quantum Electron., vol. QE-17, no. 5, pp. 681-689, May. 1981.

[15] **L. J. Paciorek**, "Injection locking of oscillators", Proc. IEEE., vol. 53, no. 11, pp. 1723-1727, Nov. 1965.

[16] **C. J. Buczek**, R. J. Freiberg, M. L. Skolnick, "Laser injection locking", Proc. IEEE., vol. 61, no. 10, pp. 1411-1431, Oct. 1973.

[17] **E. Normann**, "The inductance-capacitance oscillator as a frequency divider", Proc. IRE., vol. 24, pp. 799-803, Oct. 1946.

[18] **C. J. M. Verhoeven**, "A high-frequency electronically tunable quadrature oscillator", IEEE J. Solid-State Circuits., vol. 27, pp. 1097-1100, Jul. 1992.

[19] **A. Rofougaran**, J. Rael, M. Rofougaran, A. Abidi, "A 900 MHz CMOS LC oscillator with quadrature outputs", IEEE ISSCC Dig. Tech. Papers., pp. 392-393, Feb 1996.

[20] **J. Kim**, B. Kim, "A low phase noise CMOS LC oscillator with a ring structure", IEEE ISSCC Dig. Tech. Papers., pp.430-431, Feb 2000.

[21] **S. Kobayashi**, T. Kimura, "Coherence of injection phase-locked AlGaAs semiconductor laser", Electron. Lett., vol. 16, no. 17, pp. 668-670, Aug. 1980.

[22] **K. Iwashita**, K. Nakagawa, "Suppression of mode partition noise by laser diode light injection", IEEE J. Qunatum Electorn., vol. QE-18, no. 10, pp. 1669-1674, Jun. 1982.

[23] **R. Lang**, "Injection locking properties of a semiconductor laser", IEEE Quantum Electron., vol. QE-18, no. 6, pp.976-983, Jun. 1982.

[24] **S. Kobayashi**, T. Kimura, "Optical phase modulation in an injection locked AlGaAs semiconductor laser", IEEE J. Quantum Electron., vol. QE-18, no. 10, pp. 1662-1669, Oct. 1982.

[25] **Seong Kyeong Photonics**, "Free-space optical isolators", Seong Kyeong Photonics [Online]. Available: http://www.skphotonics.com/pdf/la_pdf/Isolator.pdf. [Accessed on: Jun. 21, 2016].

[26] **M. O. van Deventer**, Fundamentals of Bidirectional Transmission over a Single Optical Fibre, 1st ed. Springer, 1996. pp. 61-62.

[27] **S. Donati**, R-H. Horng, "The diagram of feedback regimes revisited", IEEE J. Sel. Top. Quantum Electron., vol. 19, no. 4, pp. 1500309-1500309, Jul/Aug. 2013.

[28] **R. W. Tkach**, A. R. Chraplyvy, "Regimes of feedback effects in 1.5-um distributed feedback laser", IEEE J. Lightw. Technol., vol. JLT-4, no. 11, pp. 1655-1661, Nov. 1986.

[29] **R. Lang**, K. Kobayashi, "External optical feedback effects on semiconductor injection laser properties", IEEE J. Quantum Electron., vol. QE-16, no. 3, pp. 347-355, Mar. 1980.

[30] **J. S. Lawrence**, "Diode lasers with optical-feedback, optical injection, and phase-conjugate feedback", Ph.D. thesis, Dept. Phys., Macquarie Univ., Sydney, Australia, 2000.

[31] **K. Petermann**, “External Optical Feedback Phenomena in Semiconductor Lasers”, IEEE J. Sel. Top. Quantum Electron., vol. 1, pp. 480-489, 1995.

[32] **G. H. M. van Tartwijk**, D. Lenstra, “Semiconductor lasers with optical injection and feedback”, Quantum Semiclass. Opt., vol. 7, pp. 87-143, 1995.

[33] **Photodigm Application Notes**, “Optical feedback in laser diodes”, Photodigm [Online]. Available: http://www.photodigm.com/literature/applications-notes/optical-feedback-in-laser-diodes. [Accessed on: Nov. 24, 2016].

[34] **É. Hardy**, “optical feedback in lasers”, My Laser Spectrum [Online]. Available: http://mylaserspectrum.com/2016/09/optical-feedback-lasers/ [Accessed on: Nov. 24, 2016].

[35] **S. Peters-Flynn**, P. S. Spencer, S. Sivaprakasam, I. Pierce, K. A. Shore, “Identification of the optimum time-delay for chaos synchronization regimes of semiconductor lasers”, IEEE J. Quantum Electron., vol. 42, no. 4, pp. 427-434, Apr. 2006.

[36] **S. Peters-Flynn**, I. Pierce, P. S. Spencer, P. Rees, “Synchronisation recovery in unidirectionally coupled semiconductor lasers”, IEE Proc. Optoelectron., vol. 153, no. 1, pp. 8-12, Feb. 2006.

[37] **B. Thédrez**, J. G. Provost, “Nearly degenerate four-wave mixing investigation of period doubling in semiconductor lasers”, Optics Lett., vol. 14, no. 17, pp. 958-960, Sept. 1989.

[38] **J. Ye**, H. Li, J. G. McInerney, “Period-doubling route to chaos in a semiconductor laser with weak optical feedback”, Phys. Rev A., vol. 47, no. 3, pp.2249-2252, Mar. 1993.

[39] **T. B. Simpson**, J. M. Liu, A. Gavrielides, V. Kovanis, P. M. Alsing, “Period-doubling route to chaos in a semiconductor laser subject to optical injection”, Appl. Phys. Lett., vol. 64, no. 26, Jun. 1994.

CHAPTER SIX

FOUR-WAVE MIXING

Throughout this thesis, emphasis has been put on potential methods and schemes for realising terahertz radiation, and chapter five gave a fundamental introduction into the injection locking scheme, paying particular attention to the locking regions and behaviour patterns of both unidirectional and bidirectional injection locking. This will serve as a building block for chapter six, where the final method for potentially realising THz will be investigated; four-wave mixing (FWM). Four-wave mixing is where two or more waves interact in a nonlinear medium which results in an output at assorted sum or difference frequencies. As mentioned in the conclusion of chapter five, the disadvantage of injection locking is the fact that when the two lasers are operating in the locked condition, there is a zero frequency separation between them. The aim here is to utilise the FWM scheme to build a three laser system, utilising injection locking, that maintains a nonzero separation of the lasers' frequency, where the frequency separation lies within the THz range.

The work of this chapter will be based on the monolithic FWM scheme employed by Zanola *et al*. [1] whereby they utilised three separate semiconductor lasers. In the scheme proposed by Zanola *et al*., two distributed feedback (DFB) lasers, emitting at the frequencies ν_1 and ν_2, respectively, are phase-locked via mutual injection, assisted by the four-wave mixing process that takes place in the third, auxiliary laser, emitting at the frequency of ν_3. This is shown in figure 6.1. Laser 1 and laser 2 are injected into laser 3 (AUX) where the process of FWM takes place. During this process, FWM will generate two new conjugate FWM signals that are 'clones' of the signals from laser 1 and laser 2, and they have the idler frequencies of ${\nu_1}' = 2\nu_3 - \nu_1$ and ${\nu_2}' = 2\nu_3 - \nu_2$. This clone signal, ${\nu_1}'$, is then injected back into laser 2, and the clone signal ${\nu_2}'$ is injected back into laser 1, and if these clone signals are operating on the frequencies of ${\nu_1}' = 2\nu_3 - \nu_1$ and ${\nu_2}' = 2\nu_3 - \nu_2$, then under these conditions, lasers 1 and 2 will be unlocked. This is depicted in figure 6.2 (a). When the third laser is operating at the frequency of $\nu_3 = (\nu_2 + \nu_1)/2$, the conjugate FWM signals (i.e., where the resulting fields have a reversed propagation direction) will have the frequencies of ${\nu_1}' = \nu_2$ and ${\nu_2}' = \nu_1$. When these conditions are met, the clones will fall on top of the original signals, and hence laser 1 is potentially injection-locked by the 'clone' signal of laser 2, and laser 2 is potentially injection-locked by the 'clone' signal of laser 1. Under these conditions, laser 1 and laser 2 are mutually coupled via their conjugate four-wave mixing signals, and are hence phase-locked with a nonzero frequency spacing between the lasers while operating in the locked condition. This is illustrated in figure 6.2 (b). It should also be

noted that not only do the lasers lock when the frequencies of the clone signals coincide exactly, but also if they are different but sufficiently close to the frequencies of laser 1 and laser 2 respectively. The beat signal that would be generated by lasers 1 and 2 through the process of photomixing, is a potentially spectrally pure RF signal [1], [2].

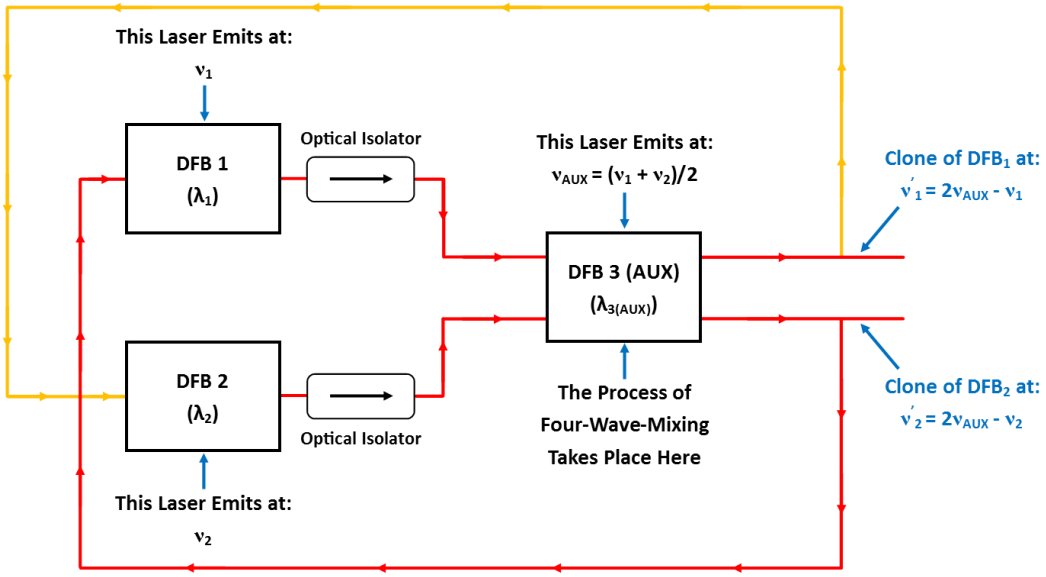

Figure 6.1: *Laser configuration for the photomixing assisted by mutual injection locking and the FWM technique. DFB 1 and DFB 2, emitting at the frequencies ν_1 and ν_2, are injected into DFB 3, emitting at the frequency of ν_{AUX}, where the process of FWM takes place. This generates two new conjugate FWM signals that are 'clones' of DFB1 and DFB 2 which have the idler frequencies of $\nu_1' = 2\nu_3 - \nu_1$ and $\nu_2' = 2\nu_3 - \nu_2$. The clone signal ν_1' is then injected back into DFB 2, and the clone signal ν_2' is injected back into DFB 1.*

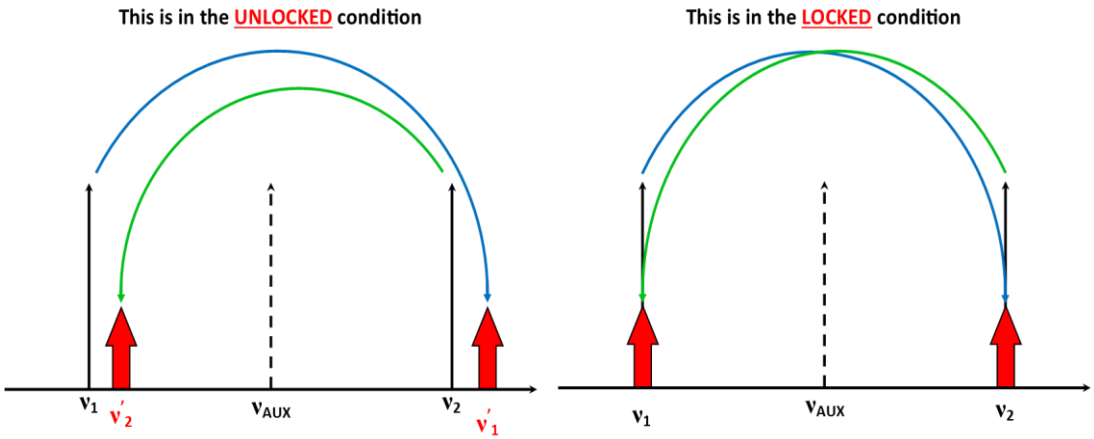

Figure 6.2: *Lasers 1 and 2 operating in the unlocked condition (a), where the clone signals of ν_1' and ν_2' have the frequencies of $\nu_1' = 2\nu_3 - \nu_1$ and $\nu_2' = 2\nu_3 - \nu_2$. When operating in the locked condition (b), ν_{AUX} must have the frequency $\nu_{AUX} = (\nu_2 + \nu_1)/2$, where the clone signals will have frequencies of $\nu_1' = \nu_2$ and $\nu_2' = \nu_1$, thus causing the system to lock.*

In the system proposed here, it is possible to treat the interactions happening inside the third laser as two separate FWM processes; one where the frequency from laser 1, ν_1, interacts with the frequency from laser 3, ν_3, in order to generate the conjugate signal $\nu_1{}' = 2\nu_3 - \nu_1$, and the second where the frequency from laser 2, ν_2, interacts with the frequency from laser 3, ν_3, in order to generate the conjugate signal $\nu_2{}' = 2\nu_3 - \nu_2$. This can be described by two energy-level descriptions [3], [4], as illustrated in figure 6.3 (a) and (b). In this description, $\nu_1 = \omega_1$, $\nu_2 = \omega_2$, $\nu_3 = \omega_3$, $\nu_1{}' = \omega_4$ and $\nu_2{}' = \omega_5$.

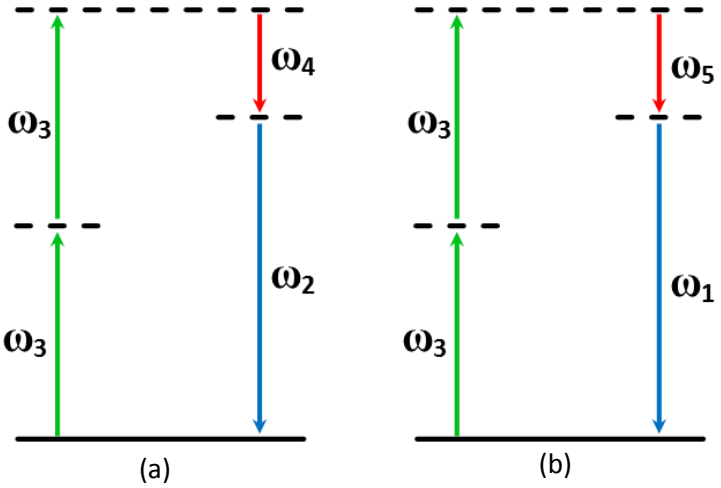

Figure 6.3: *Energy-level descriptions of the two FWM processes taking place, with (a) illustrating the generation of the idler frequency, $\nu_1{}' = 2\nu_3 - \nu_1$, and (b) illustrating the generation of the idler frequency, $\nu_2{}' = 2\nu_3 - \nu_2$.*

It is also possible to represent the FWM system under consideration mathematically. A nonlinear polarization may be defined as [3]:

$$\tilde{P}^3(t) = \epsilon_0 \chi^{(3)} \tilde{E}^3(t) \tag{6.1}$$

where $\tilde{P}(t)$ is the polarization of the material, ϵ_0 is the permittivity of free space, $\chi^{(3)}$ is the third-order nonlinear optical susceptibility, and $\tilde{E}(t)$ is the strength of the applied optical field.

This polarization may be induced by an applied field that consists of three frequency components [3], as per the FWM system under consideration:

$$\tilde{E}(t) = E_1 e^{-i(\omega_1)t} + E_2 e^{-i(\omega_2)t} E_3 e^{-i(\omega_3)t} + c.c \tag{6.2}$$

By then calculating $\tilde{E}^3(t)$, the resulting expression will contain 44 different frequency components, if the positive and negative frequencies are considered to be distinct [3] (which have been calculated in Appendix F). These frequencies are defined as [3] (and the negative of each):

$$\begin{gathered}\omega_1, \omega_2, \omega_3, 3\omega_1, 3\omega_2, 3\omega_3, (\omega_1 + \omega_2 + \omega_3), (\omega_1 + \omega_2 - \omega_3), (\omega_1 + \omega_3 - \omega_1), \\ (\omega_2 + \omega_3 - \omega_1), (2\omega_1 \pm \omega_2), (2\omega_1 \pm \omega_3), (2\omega_2 \pm \omega_1), (2\omega_2 \pm \omega_3), (2\omega_2 \pm \omega_1), \\ (2\omega_3 \pm \omega_2)\end{gathered} \tag{6.3}$$

The contents of this chapter are organised as follows:

Section 6.1 will give a brief introduction to the FWM scheme and the processes involved in its operation. Section 6.2 will then go on to discuss the process of phase conjugate injection, through which the scheme of FWM operates, and will then proceed to discuss the original contribution made to modelling a three laser FWM system, including the rate equations utilised in the construction of the system. Section 6.3 will then for the first time make an in-depth analysis of the locking regions and behaviour patterns observed (similar to what was seen in chapter five), and how they compare to those observed in chapter five. Section 6.4 will then give a summary of the main conclusions, and how they will be applied to the work in chapter seven where perturbations will be introduced to the first laser, and will investigate the resilience of the three laser FWM system to these perturbations.

6.1 – Introduction

FWM is one of the most general, but very important, phenomena in nonlinear optics [5]. In such a scheme, as discussed previously, two or more waves are interacting in a nonlinear medium, resulting in an output at assorted sum or difference frequencies [5]. It is the notion of three separate electromagnetic fields interacting in order to produce a fourth field that is fundamental to the description of all FWM processes [6]. To understand this process, it is possible to consider the individual interactions of the fields within a dielectric medium. Considering the first field being inputted into the medium, this will cause an oscillating polarization within the dielectric, and this will re-radiate with a phase shift that is determined by the damping of the individual dipoles [6]. This is just the conventional Rayleigh scattering taking place, which can be described by linear optics [6]. Rayleigh scattering is simply the scattering of light by particles of much smaller wavelength than that of the radiation. Through considering that a second field is now also being inputted into the medium, then this will also drive the polarization of the dielectric. It will be possible to see interference between the two inputting beams, and this will cause harmonics in the polarization at the sum and difference frequencies [6]. This is described by equation (6.4):

$$\begin{aligned} P_{NL} &= P_{NL}(\omega_1)e^{j\omega_1 t} + P_{NL}(\omega_2)e^{j\omega_2 t} \\ &+P_{NL}(2\omega_1 - \omega_2)e^{j(2\omega_1-\omega_2)t} + P_{NL}(2\omega_2 - \omega_1)e^{j(2\omega_2-\omega_1)t} \end{aligned} \tag{6.4}$$

where P_{NL} are the nonlinear polarizations, and $\omega_{1,2}$ are the frequencies of the two inputting beams. By inputting a third field into the medium, this will also drive the polarization, and this field will beat with both the other input fields, and also with the sum and difference frequencies. It is this beating at the sum and difference frequencies that generates the fourth field in the FWM scheme [6]. As all of the produced beat frequencies can also act as new source fields, a perplexing number of interactions and fields may be produced from this elemental process [6].

As previously mentioned, FWM is a nonlinear effect, which arises from the third-order nonlinearity, with arises from the third-order optical susceptibility, which can be described by the $\chi^{(3)}$ coefficient [7]. It can occur if at least two different frequency components are propagating together in a nonlinear medium, such as an optical fibre. Through simplifying the above analogy to just two input frequency components, defined as ν_1 and ν_2, where $\nu_2 > \nu_1$, then a refractive index modulation at the difference frequency will occur, and this will generate two additional frequency components, ν_3 and ν_4, as can be seen in figure 6.4.

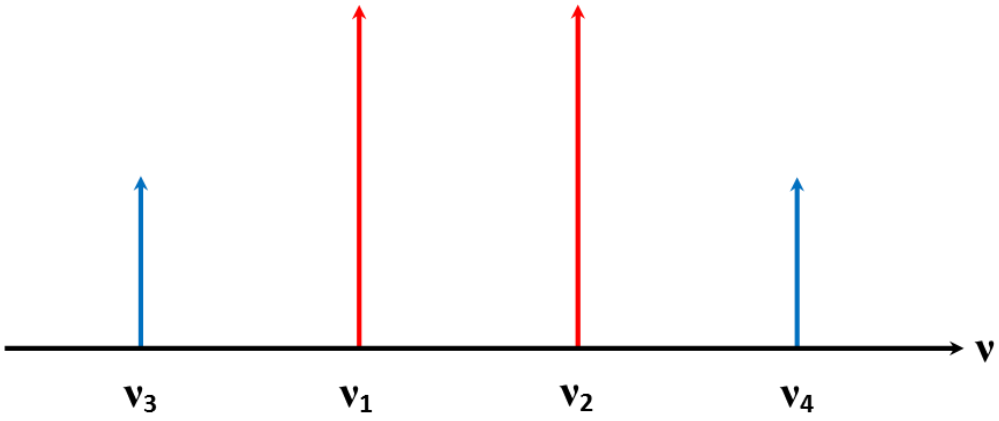

Figure 6.4: *Generation of new frequency components, ν_3 and ν_4, via FWM [7].*

Generally speaking, two new frequency components are generated, and these are defined as $\nu_3 = \nu_1 - (\nu_2 - \nu_1) = 2\nu_1 - \nu_2$ and $\nu_4 = \nu_2 + (\nu_2 - \nu_1) = 2\nu_2 - \nu_1$. In addition, a pre-existing wave at the frequencies of ν_3 or ν_4 can be amplified. In other words, they experience parametric amplification [7], [8]. In the above description, it has been assumed that four *different* frequency components are interacting via FWM. This is called *non-degenerate* FWM [7]. When all of the waves are of the *same* frequency, or when two of the four frequencies coincide, this process is known as *degenerate* four-wave mixing [5], [7]. Even though their frequencies are the same, the waves will have different wavevectors (i.e., they will be propagating in different directions), and this process arises from the nonlinear index of refraction [5]. An example of degenerate FWM would be a single pump wave which provides amplification for a neighbouring frequency component (a signal). Each time a photon is added to the signal wave, two photons will be taken away from the pump wave, and another will be put into an idler wave with a frequency present on the other side of the pump [7]. The three laser FWM system under consideration here will be a non-degenerate FWM system.

It should be noted that FWM is a phase-sensitive process. In other words, the interactions depend on the relative phases of all of the beams. This means that the effects of FWM can be efficiently achieved over longer distances, such as in fibre optics, but only if the phase-matching condition is satisfied.

What this means is that a proper phase relationship between the interacting waves must be maintained along the direction of propagation (this is to ensure optimum nonlinear frequency conversion). It can be said that this is generally the case if the frequencies involved are close together [7]. On the other hand, if there is a strong phase mismatch between the interacting waves, the effect of FWM is effectively supressed [7].

As discussed at the beginning of this chapter, the aim here is to generate THz radiation through utilising the FWM scheme in order to build a three laser system, based on injection locking, which maintains a nonzero separation of the lasers' frequency. This work extends on the work of Zanola *et al*. whereby they utilised three, separate (but monolithically integrated), semiconductor lasers. They injected light from laser 1 and laser 2 into laser 3, where FWM takes place. This creates two new conjugate FWM signals that are 'copies' of the light from lasers 1 and 2. They then inject these clone signals back into lasers 1 and 2, where the frequencies of lasers' one and two will potentially lock. Such a scheme is based on photomixing assisted by mutual injection locking via four-wave mixing [1], [2].

6.2 – Four-Wave Mixing Model

For the work presented here, phase conjugate injection (feedback) [9]-[16] is going to be implemented, rather than the conventional injection seen in chapter five, in order to model a similar system to that implemented by Zanola *et al*. [1]. They designed and implemented a monolithic optoelectronic device for the generation of tunable and narrow linewidth millimetre-wave signals based on the FWM technique.

Optical phase conjugation is a technique used in nonlinear optics whereby the direction of propagation of a beam of light is accurately reversed thus causing the return beam to exactly retrace the path of the incident beam. Such a method is also known as time-reversal reflection, or wavefront reversal [17].

The three laser FWM model presented here will be broadly based around the laser rate equations from the work of Peters-Flynn *et al*. [18], [19], where the rate equations were originally developed by Lang and Kobayashi [20], however the rate equations as seen in chapter five will be modified in order to accommodate optical phase conjugate feedback to simulate the dynamics of the system implemented by Zanola *et al*., [1], whereby lasers 1 and 2 are injected into laser 3, where the process of FWM takes place. The generated clone signals are then injected back into lasers 1 and 2; this was represented previously in figure 6.1. As previously, there will be two equations each for both the lasers; one represents the slowly varying complex electric field amplitude $A(t)$ in the laser cavity (either the first, $A_1(t)$, or the second laser, $A_2(t)$), and one equation for the number of charge carriers

$N(t)$ in the gain medium (again for either the first laser, $N_1(t)$, or the second laser, $N_2(t)$). The scheme implemented here is similar to that implemented for bidirectional injection locking, as seen in chapter five, whereby light from the first laser will be injected into the cavity of the second laser, and similarly, the light from the second laser will also be injected into the cavity of the first laser. To model the FWM process correctly, both of the electric fields must be conjugated, before being multiplied by the injection rate coefficient, κ_c, including the frequency detuning terms. It should be noted here that the frequency detuning terms for both the first and the second lasers are positive for this scheme (whereas the first laser had a negative detuning value when conducting bidirectional injection previously). The frequency detuning, $\Delta\nu$, in this case has a different meaning to that presented in chapter five; here, the detuning frequency defines the deviation of the 'clone' signals, $\nu_1{}'$ and $\nu_2{}'$ from the frequencies of ν_2 and ν_1 respectively, as depicted in figure 6.2 (a)-(b). For positive detuning, the 'clone' signals will move to the right of ν_1 and ν_2 (figure 6.5 (a)), and as a result, there will be an equal frequency spacing between $\nu_1 \rightarrow \nu_3$ and $\nu_3 \rightarrow \nu_1{}'$, and also between $\nu_2{}' \rightarrow \nu_3$ and $\nu_3 \rightarrow \nu_2$. For negative detuning, the 'clone' signals will move to the left of ν_1 and ν_2 (figure 6.5 (b)), and as a result, there will be equal frequency spacing between $\nu_2{}' \rightarrow \nu_3$ and $\nu_3 \rightarrow \nu_2$, and also between $\nu_1 \rightarrow \nu_3$ and $\nu_3 \rightarrow \nu_1{}'$. It should be noted that the deviation of ν_3 from the centre frequency will be half that of the detuning frequency. It is of course the deviation of ν_3 from its central frequency value that causes the system to operate in either the locked or unlocked condition, however it is the deviation of the 'clone' signals that have been modelled in this work, and this is what will be referred to as the detuning frequency, $\Delta\nu$, in the following work. The equations representing this system are represented by equations (6.5)-(6.8), where $\overline{A_{1,2}(t)}$ represent the conjugated terms, and the detuning frequency, $\Delta\omega = 2\pi\Delta\nu$. As in chapter five, the gain in the medium is represented by equation (6.8), and is again applied to both the first and the second lasers respectively. The model was simulated using the same parameter values as those in chapter five, table 5.1.

$$\frac{dA_1(t)}{dt} = \frac{1}{2}(1+i\alpha)\left[G_1 - \frac{1}{\tau_p}\right]A_1(t) + \kappa_c\overline{A_2(t)}e^{i\Delta\omega t} \tag{6.5}$$

$$\frac{dA_2(t)}{dt} = \frac{1}{2}(1+i\alpha)\left[G_2 - \frac{1}{\tau_p}\right]A_2(t) + \kappa_c\overline{A_1(t)}e^{i\Delta\omega t} \tag{6.6}$$

$$\frac{dN_{1,2}(t)}{dt} = \frac{J}{e} - \frac{N_{1,2}(t)}{\tau_n} - G_{1,2}\left|A_{1,2}(t)\right|^2 \tag{6.7}$$

$$G_{1,2} = \frac{g\left(N_{1,2}(t) - N_0\right)}{1 + \epsilon\left|A_{1,2}(t)\right|^2} \tag{6.8}$$

Here it is emphasised that the time of flight in the model is assumed to be zero. Further work might profitably examine a finite time of flight, thus modifying the coupling terms to be:

$$\frac{dA_1(t)}{dt} = \frac{1}{2}(1+i\alpha)\left[G_1 - \frac{1}{\tau_p}\right]A_1(t) + \kappa_c\overline{A_2(t)}e^{i\Delta\omega t} - \tau_f A_2(t) \quad (6.9)$$

$$\frac{dA_2(t)}{dt} = \frac{1}{2}(1+i\alpha)\left[G_2 - \frac{1}{\tau_p}\right]A_2(t) + \kappa_c\overline{A_1(t)}e^{i\Delta\omega t} - \tau_f A_1(t) \quad (6.10)$$

where τ_f is defined as the time of flight.

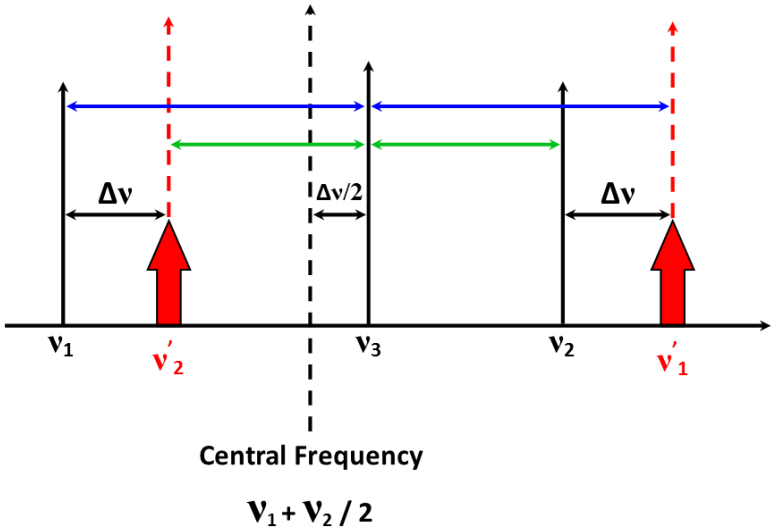

Figure 6.5 (a): *Illustration of the detuning frequency, Δν, as a function of the deviation of the 'clone' signals from ν_1 and ν_2 for positive detuning.*

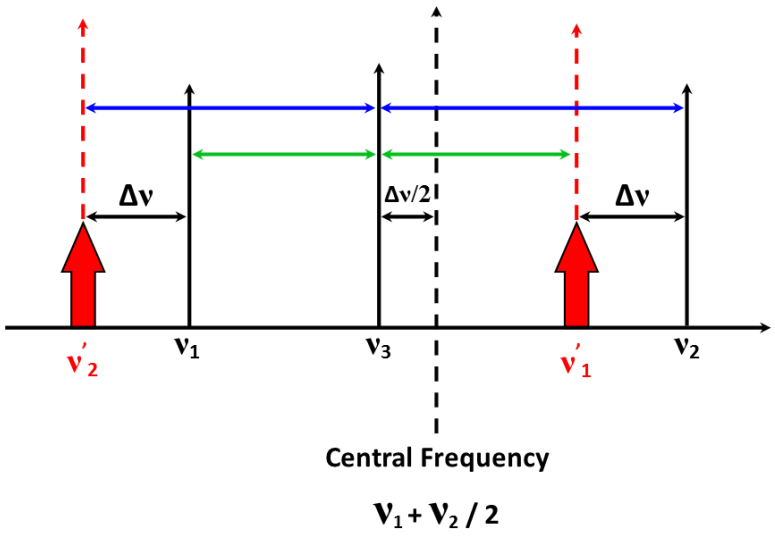

Figure 6.5 (b): *Illustration of the detuning frequency, Δν, as a function of the deviation of the 'clone' signals from ν_1 and ν_2 for negative detuning.*

6.3 – Four-Wave Mixing Model: *Locking Region Analysis*

The model was simulated using FORTRAN (the code for which is an evolution of the model used for bidirectional injection locking in chapter five (which can be found in Appendix C)), using the parameters listed in table 5.1. The model was simulated with detuning values, $\Delta\omega$, ranging from -10GHz to 1GHz, and the injection rate, κ_c, ranges from 0.1ns^{-1} to 8.0ns^{-1}, as shown in figure 6.6. In figure 6.6, the black crosses correspond to where the lasers' carrier and photon number output are oscillating periodically (figure 6.8, (a)-(e)), the blue squares correspond to where the laser's carrier and photon number output seems to potentially exhibit a chaotic behaviour (figure 6.10), which may represent period doubling route to chaos, the green stars correspond to a periodic, yet somewhat distorted waveform (figure 6.11 (a)-(b)), and finally the red circles (figure 6.13) correspond to the locking condition between the lasers (as was seen in chapter five).

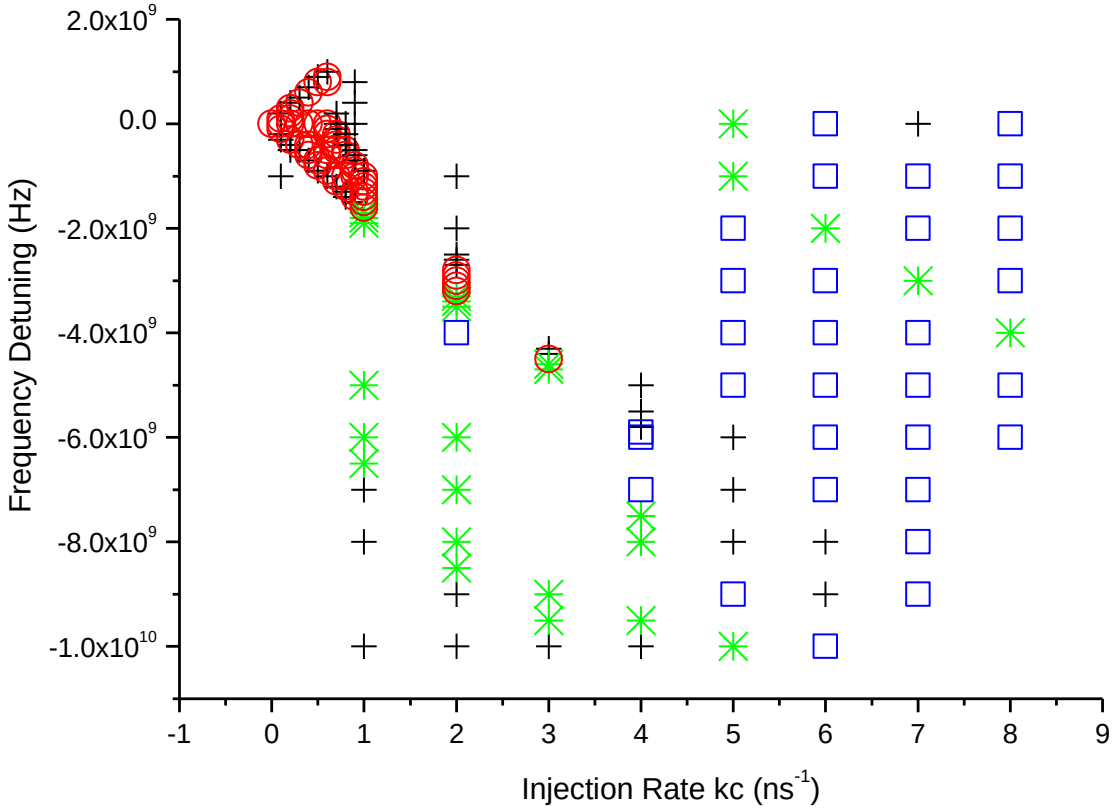

Figure 6.6: *Behavioural plot for the case of bidirectional phase conjugate injection, with frequency detuning values, $\Delta\omega$, ranging from -10GHz to 1GHz and injection rates, κ_c, ranging from 0.1ns^{-1} to 8.0ns^{-1}. The black crosses represent the lasers' carrier and photon number output oscillating periodically, the blue squares represent the carrier and photon number output potentially exhibiting a chaotic behaviour, the green stars correspond to a periodic, yet distorted wave, and the red circles represent the locking condition between the first and second lasers'. The blank areas within the locking regions are areas that have not been studied for this part of the work. (Data for the plot can be found in Appendix G).*

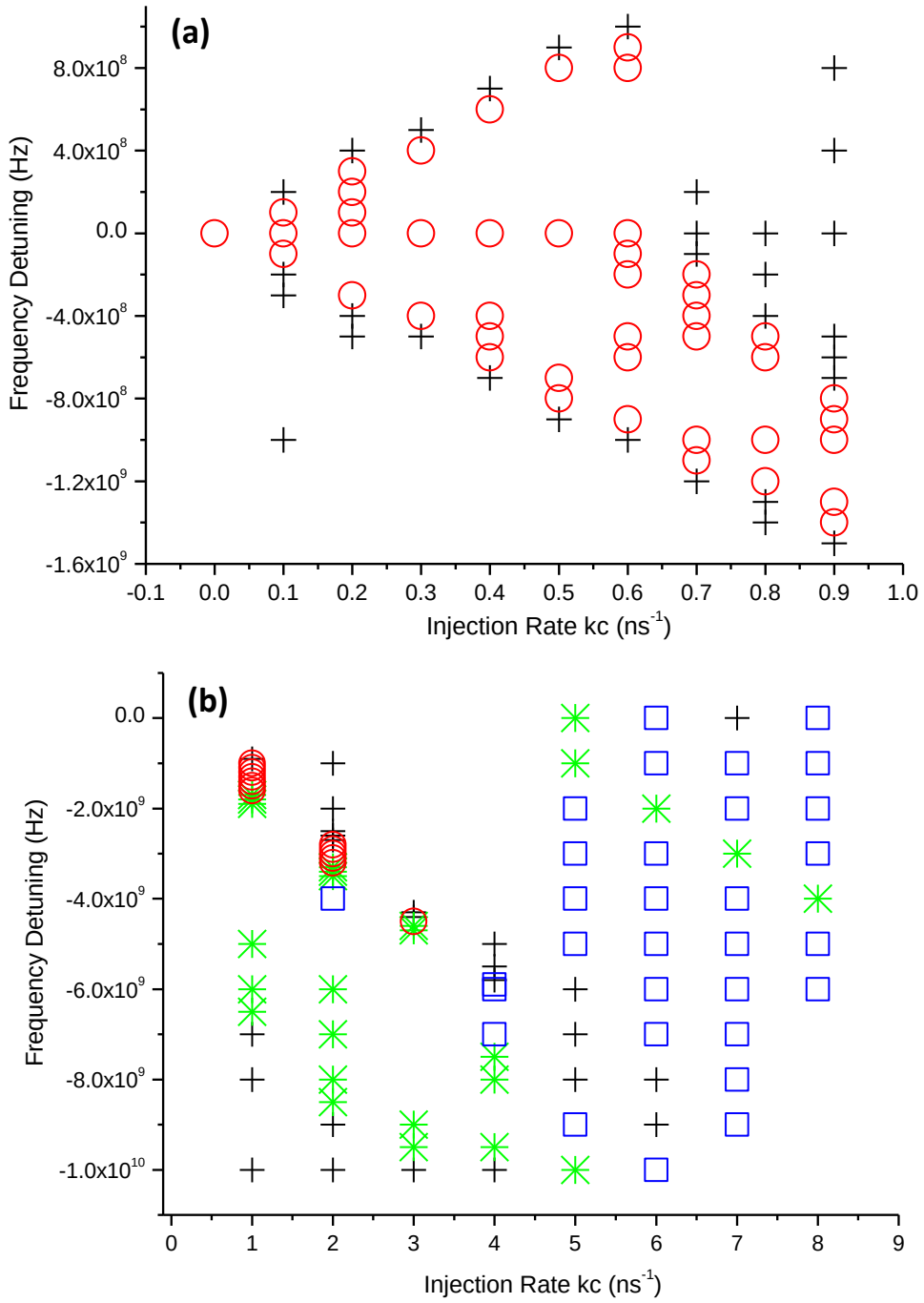

Figure 6.7: *Behavioural plots for the case of bidirectional phase conjugate injection, with frequency detuning values, $\Delta\omega$, ranging from -1.6GHz to 1GHz and injection rates, κ_c, ranging from 0.1ns^{-1} to 0.9ns^{-1} (figure (a)), and frequency detuning values, $\Delta\omega$, ranging from -10GHz to 0GHz and injection rates, κ_c, ranging from 1.0ns^{-1} to 8.0ns^{-1} (figure (b)). The black crosses represent the lasers' carrier and photon number output oscillating periodically, the blue squares represent the carrier and photon number output potentially exhibiting a chaotic behaviour, the green stars correspond to a periodic, yet distorted wave, and the red circles represent the locking condition between the first and second lasers'. (Data for the plots can be found in Appendix G).*

It is clear here that both the detuning ranges and injection rates used in this model are a lot smaller than those used for the injection locking model (when higher injection rates were simulated in the three laser FWM model, no injection locking regions were observed). The results of the simulations can be seen in figures 6.6 and 6.7. Figure 6.6 shows the locking region between -10GHz and 1GHz, with injection rates between $0.1ns^{-1}$ and $8.0ns^{-1}$, figure 6.7 (a) shows the locking region between -1.6GHz and 1GHz, with injection rates between $0.1ns^{-1}$ and $0.9ns^{-1}$, and figure 6.7 (b) shows the locking region between -10GHz and 0GHz for injection rates between $1.0ns^{-1}$ and $8.0ns^{-1}$.

Analysis of figures 6.6 and 6.7 show a variation of behaviours similar to what was seen in chapter five, where both unidirectional and bidirectional injection locking was analysed. For injection rates between $0.1ns^{-1}$ and $0.6ns^{-1}$, the behaviour of the system is very similar to that of a bidirectional injection locked system, where the locking region is symmetrical for both positive and negative detuning, whereas when looking at injection rates between $0.7ns^{-1}$ and $3ns^{-1}$, the system shows behaviours of a unidirectional injection locked system, where the locking region becomes very asymmetrical, where the system would only lock for negative values of detuning. It is also interesting to note that the width of the locking region increases for increasing injection rates between $0.1ns^{-1}$ and $0.6ns^{-1}$, similar to what was seen in chapter five, however, for injection rates between $0.7ns^{-1}$ and $3ns^{-1}$, the locking region gradually tapers off to become just a single point at an injection rate of $3ns^{-1}$ with a detuning of -4.5GHz. With any higher injection rate values, the system does not appear to lock with any value of frequency detuning. It should also be noted here that the injection rates are much smaller than what was seen in the case of conventional injection locking. With phase conjugation, the system locks with an injection rate as low as $0.1ns^{-1}$, whereas for conventional injection locking, an injection rate of at least $20ns^{-1}$ was required before any kind of injection locking was observed.

In figure 6.8, (a)-(e), a clear periodic pattern is apparent, and they all appear to show a single harmonic, with the exception of the carrier and photon numbers in figure 6.8 (d) and (e). Figure 6.8, (a)-(c) show an undistorted waveform, whereas in figure 6.8 (d) & (e), additional oscillations at the trough of the carriers' main oscillation are observed, and at the peak of the photons main oscillations.

From analysis of figure 6.8 (a), when an injection rate of $0.1ns^{-1}$ and a frequency detuning of -200MHz is applied to the system, rather than the oscillations following a clear sine wave pattern, periodic peaks in the carrier number output are visible, and these appear to be oscillating at approximately 116MHz. In direct comparison, the photon number output are oscillating with negative peaks, at the same frequency of approximately 116MHz. A similar pattern is apparent in figure 6.8 (c), when the injection rate is increased to $0.5ns^{-1}$ and the frequency detuning is increased to -900MHz, however the frequency of the oscillations in the carriers and photons also appear to have increased to approximately 388MHz. This pattern is apparent throughout the behaviour plot, where the greater

the injection rate and frequency detuning, the higher the frequency of these oscillations become. This is clear in the table of data in Appendix G; at an injection rate of $0.8ns^{-1}$ and a frequency detuning of -1.3GHz, the oscillations have a frequency of approximately 631.7MHz, with an injection rate of $1.0ns^{-1}$ and a frequency detuning of -1.9GHz, the oscillations seem to have a frequency of approximately 1.83GHz (figure 6.8 (e)), giving an increase of 1.7GHz between injection rates $0.1ns^{-1}$ and $1.0ns^{-1}$.

Figure 6.8 (d) & (e) also show periodicity, however, as previously mentioned, additional oscillations at the trough of the carriers, and at the peaks of the photons are visible. These oscillations appear to increase in amplitude the more the injection rate is increased; at an injection rate of $0.8ns^{-1}$, there appears to be three additional, smaller oscillations, at the trough of the carrier number output, and four additional, smaller oscillations, at the peaks of the photon number output, however with an injection rate of $1.0ns^{-1}$, it appears that there are six additional, smaller oscillations, apparent in the trough of the carrier and photon number output, doubling the amount of additional oscillations seen with an injection rate of $0.8ns^{-1}$.

Figure 6.8 (b) shows the response of the system with an injection rate of $0.1ns^{-1}$ and a frequency detuning of +200MHz. From the figure, it is clear that it shows a similar pattern to that seen in figure 6.8, (a) & (c), however the oscillations of the carriers are now negative excursions relative to the DC offset (this appears to be as a result of the positive frequency detuning; for negative frequency detuning, these oscillations are positive relative to the DC offset as sown in figure 6.8, (a) & (c)). These oscillations are also oscillating at a very similar frequency to those seen in figure 6.8 (a), with a frequency of approximately 117MHz.

In order to establish whether or not the additional, smaller oscillations, in the response of the carrier and photon outputs are additional harmonics, the photon numbers for each case are plotted on FFT plots, similar to what was seen in chapter five. Again, the hamming window setting is employed, with the DC component removed for clarity. These can be seen in the lowest plot in figure 6.8 (a)-(e). It is clear from these plots that the additional oscillations are not multiple harmonics, as only one fundamental frequency is apparent in the FFT spectrum of each.

Behaviours similar to those seen in figure 6.8, (a)-(e) were apparent at various values of frequency detuning for injection rates of $0.1ns^{-1}$ through to $2ns^{-1}$. Beyond this range, different behaviours were observed, which will be described and analysed later.

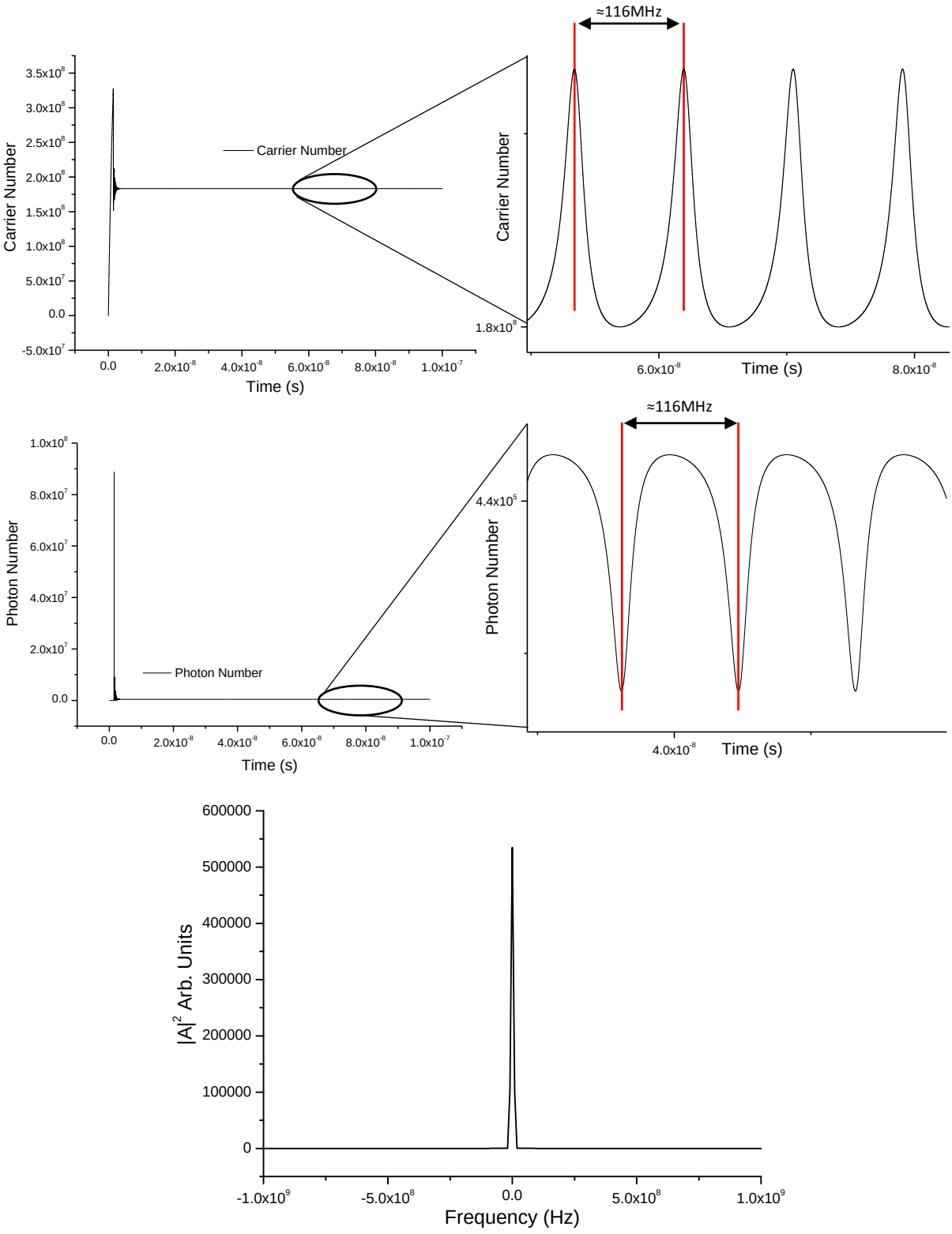

Figure 6.8 (a): *Carrier (top figure) and photon (middle figure) number output with an injection rate, κ_c, of 0.1ns^{-1} with Δf = -200MHz. The carrier and photon numbers are oscillating periodically with positive and negative excursions respectively at a fundamental frequency of ≈116MHz. The bottom graph shows the photon number plotted on an FFT, which shows only one fundamental frequency.*

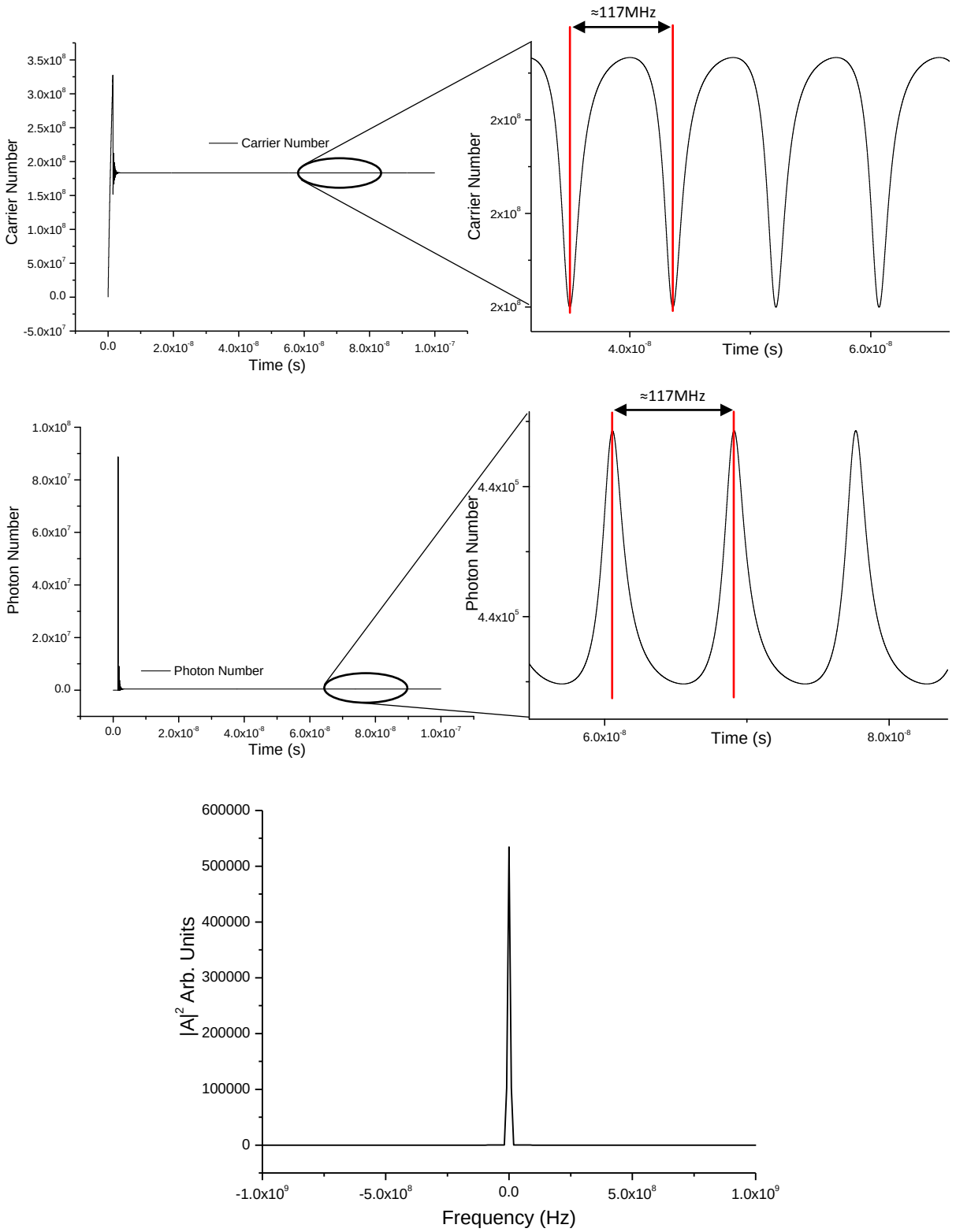

Figure 6.8 (b): *Carrier (top figure) and photon (middle figure) number output with an injection rate, κ_c, of 0.1ns^{-1} with Δf = +200MHz. The carrier and photon numbers are oscillating periodically with negative and positive excursions respectively at a fundamental frequency of ≈117MHz. The bottom graph shows the photon number plotted on an FFT, which shows only one fundamental frequency.*

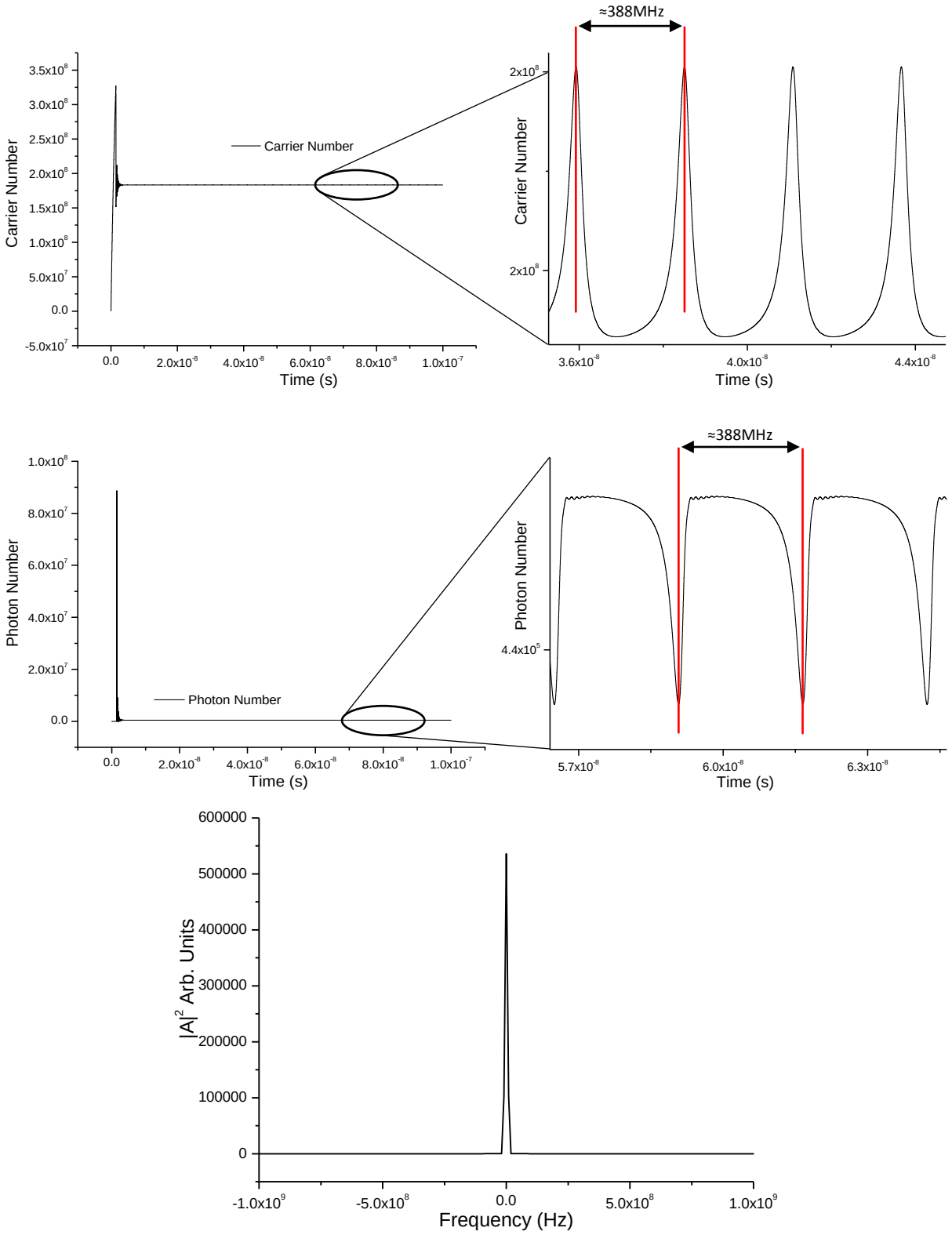

Figure 6.8 (c): *Carrier (top figure) and photon (middle figure) number output with an injection rate, κ_c, of 0.5ns^{-1} with Δf = -900MHz. The carrier and photon numbers are oscillating periodically with positive and negative excursions respectively at a fundamental frequency of ≈388MHz. The bottom graph shows the photon number plotted on an FFT, which shows only one fundamental frequency.*

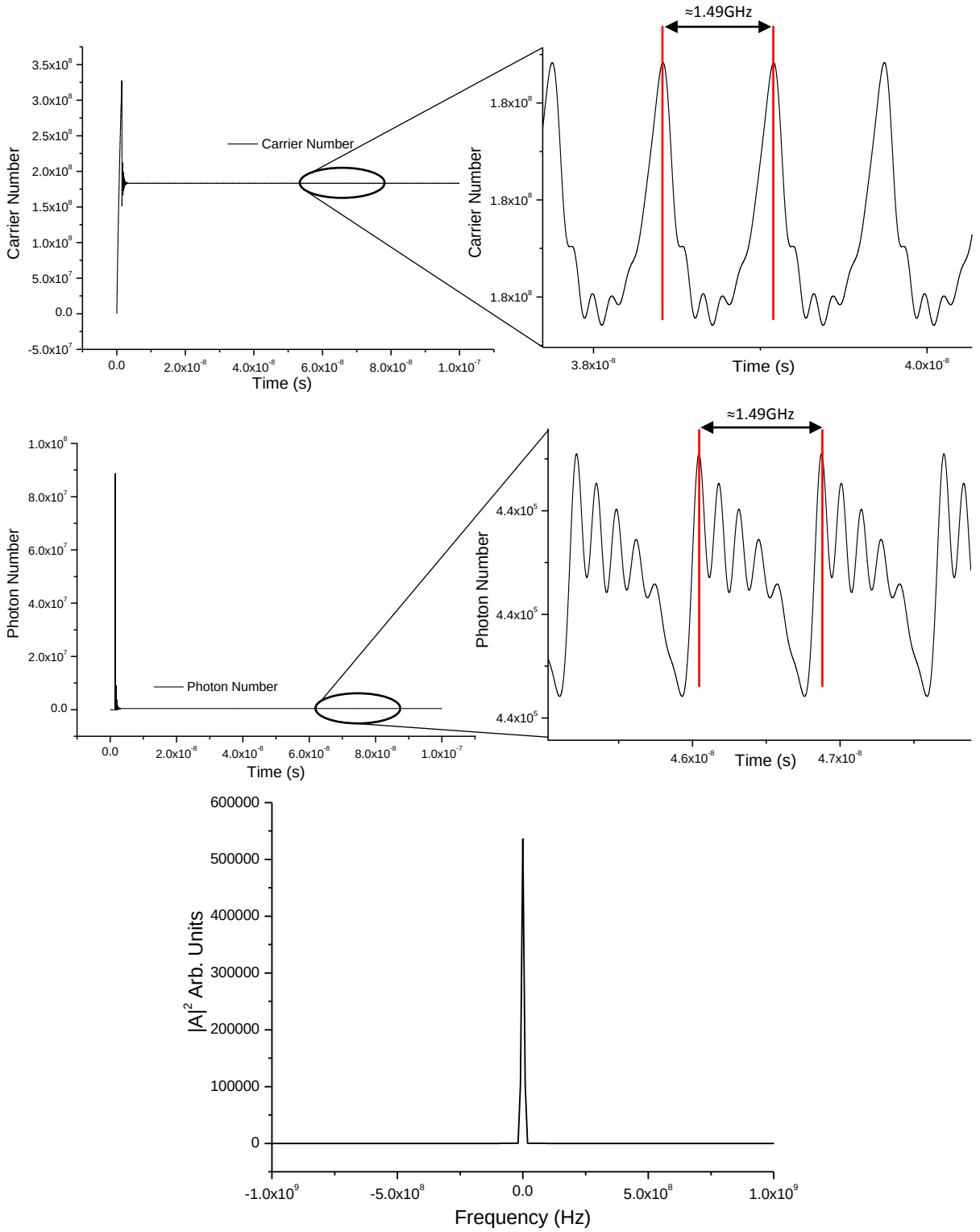

Figure 6.8 (d): *Carrier (top figure) and photon (middle figure) number output with an injection rate, κ_c, of 0.8ns^{-1} with Δf = -2GHz. The carrier and photon numbers are oscillating periodically with additional oscillations at the trough of the carriers' primary oscillations, and additional oscillations at the peaks of the photons primary oscillations at a frequency of ≈1.49GHz. The bottom graph shows the photon number plotted on an FFT, which shows only one fundamental frequency.*

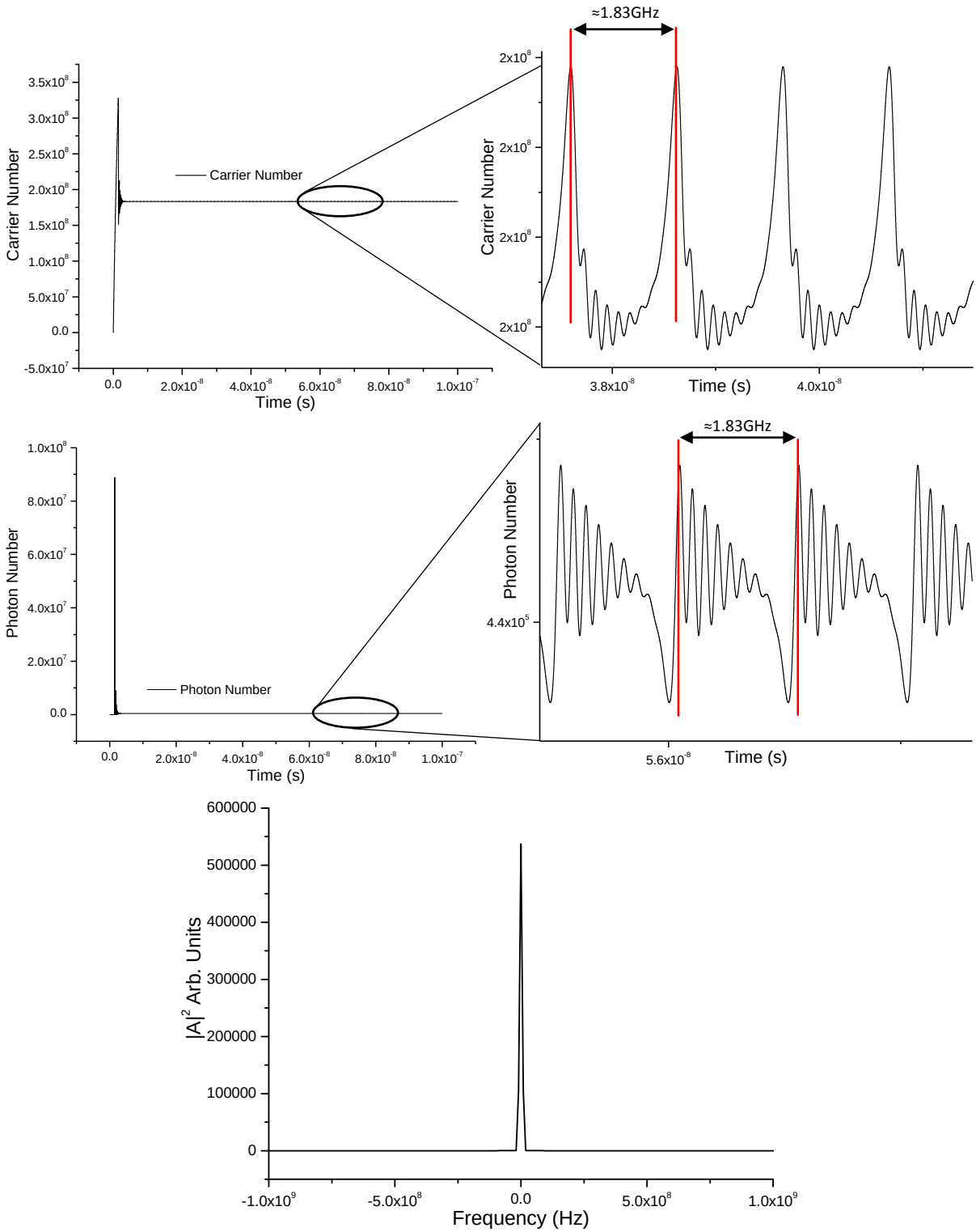

Figure 6.8 (e): *Carrier (top figure) and photon (middle figure) number output with an injection rate, κ_c, of 1.0ns^{-1} with Δf = -1.9GHz. The carrier and photon numbers are oscillating periodically with additional oscillations at the trough of the carriers' primary oscillations, and additional oscillations at the peaks of the photons primary oscillations at a frequency of ≈1.83GHz. The bottom graph shows the photon number plotted on an FFT, which shows only one fundamental frequency.*

Similarly to what was observed in chapter five where unidirectional injection locking was discussed, there were regions where the system would oscillate with an undistorted sine wave, as can be seen in figure 6.9. However, unlike the case for unidirectional injection locking where, when this happened, the system oscillates at approximately the same frequency as the detuning frequency; in this case, the system oscillates at approximately 9.2GHz each time, irrespective of the detuning frequency value. Analysis of the relaxation oscillation frequency shows it to have a frequency of approximately 8.8GHz, similar to the value obtained for the system's oscillations. It also seems apparent from figure 6.9 that these oscillations are undamped oscillations. It seems that when operating outside of the locking region, the system oscillates at the same frequency as the relaxation oscillation frequency of the system (approximately 9.2GHz), irrespective of the value of frequency detuning. An interesting observation here, from figures 6.6 and 6.7, and from the data in Appendix G, this relaxation oscillation frequency is only apparent when the locking region of the system starts to become asymmetrical in behaviour (from injection rates of $0.7ns^{-1}$ upwards), and only happens for lower detuning values before the system locks (red circles). It should be noted, however, that no frequencies of approximately 9.2GHz were observed for the lower injection rates (between $0.1ns^{-1}$ to $0.6ns^{-1}$, where symmetrical locking behaviour was observed).

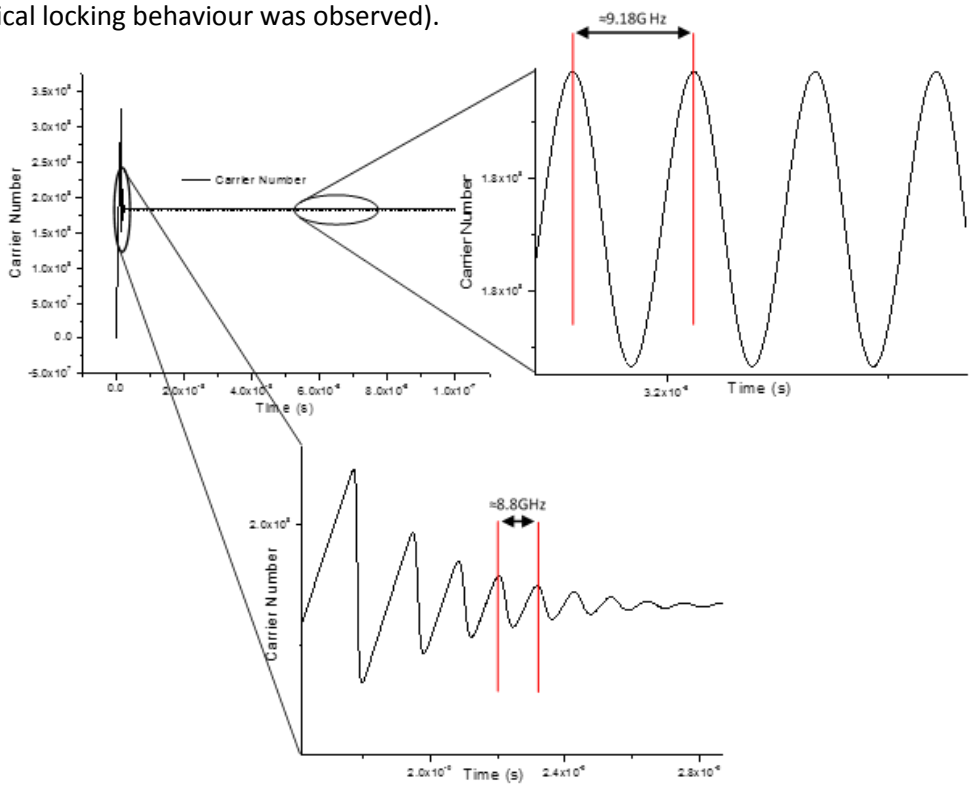

Figure 6.9: *Carrier number output with an injection rate, κ_c, of $0.8ns^{-1}$ with a frequency detuning, $\Delta\omega$, of 0GHz – The carrier numbers are oscillating periodically in a perfect sine wave with a frequency of ≈9.18GHz; This frequency is very similar in value to that of the relaxation oscillation frequency of ≈8.8GHz.*

The case will now be considered where potential chaos is apparent in the behaviour of the system (blue squares in figures 6.6 & 6.7). Unlike the case for injection locking in the unidirectional injection locking system shown in chapter five where there were one or two clear regions of the system exhibiting a potential chaotic behaviour (depending on the injection rate and detuning frequency), here, the regions appear to be a lot more randomly distributed, and do not appear until there is an injection rate of $2.0ns^{-1}$ and a frequency detuning of -4GHz. An example of the potential chaotic behaviour seen in this system can be seen in figure 6.10. From the figure, there are potentially multiple harmonics, similar to what was seen in chapter five, and these harmonics appear to have a periodicity of approximately 9.29GHz. It is again interesting to note that this frequency is approximately the same as the relaxation oscillation frequency. Such a response, as previously, could indicate period doubling route to chaos [21]-[23], and as was the case with unidirectional and bidirectional injection locking, these regions should be avoided for the work under consideration here.

The regions of potential chaotic behaviour become more apparent when increasing the injection rate of the system, with the region of potential chaotic behaviour increasing from a width of 4GHz at an injection rate of $5.0ns^{-1}$, to a width of 6GHz at $7.0ns^{-1}$. It can be assumed that the width is wider still for an injection rate of $8.0ns^{-1}$, following the same behavioural pattern as was seen for lower injection rates. It is also worth noting that the potential chaotic behaviour also appears to be asymmetrical with respect to the detuning frequency, with these regions creeping to the left with increasing injection rates. With injection rates between $5.0ns^{-1}$ and 8.0ns, two potential chaotic regions are apparent, similar to what was observed with unidirectional injection locking.

In order to confirm whether or not the carriers and the photons are truly exhibiting a chaotic behaviour, the photon numbers are plotted on FFT plots, again with the DC component removed for clarity. This is shown in the lowest plot of figure 6.10. From the FFT plot, as was the case in chapter five, it is not easy to see the individual peaks in the spectrum, thus giving a clear indication of the potential chaotic behaviour that the system exhibits in these regions.

Again, as was the case in chapter five, this is a potentially very interesting region of behaviour of the system, however, for the work conducted here, this behaviour is to be avoided.

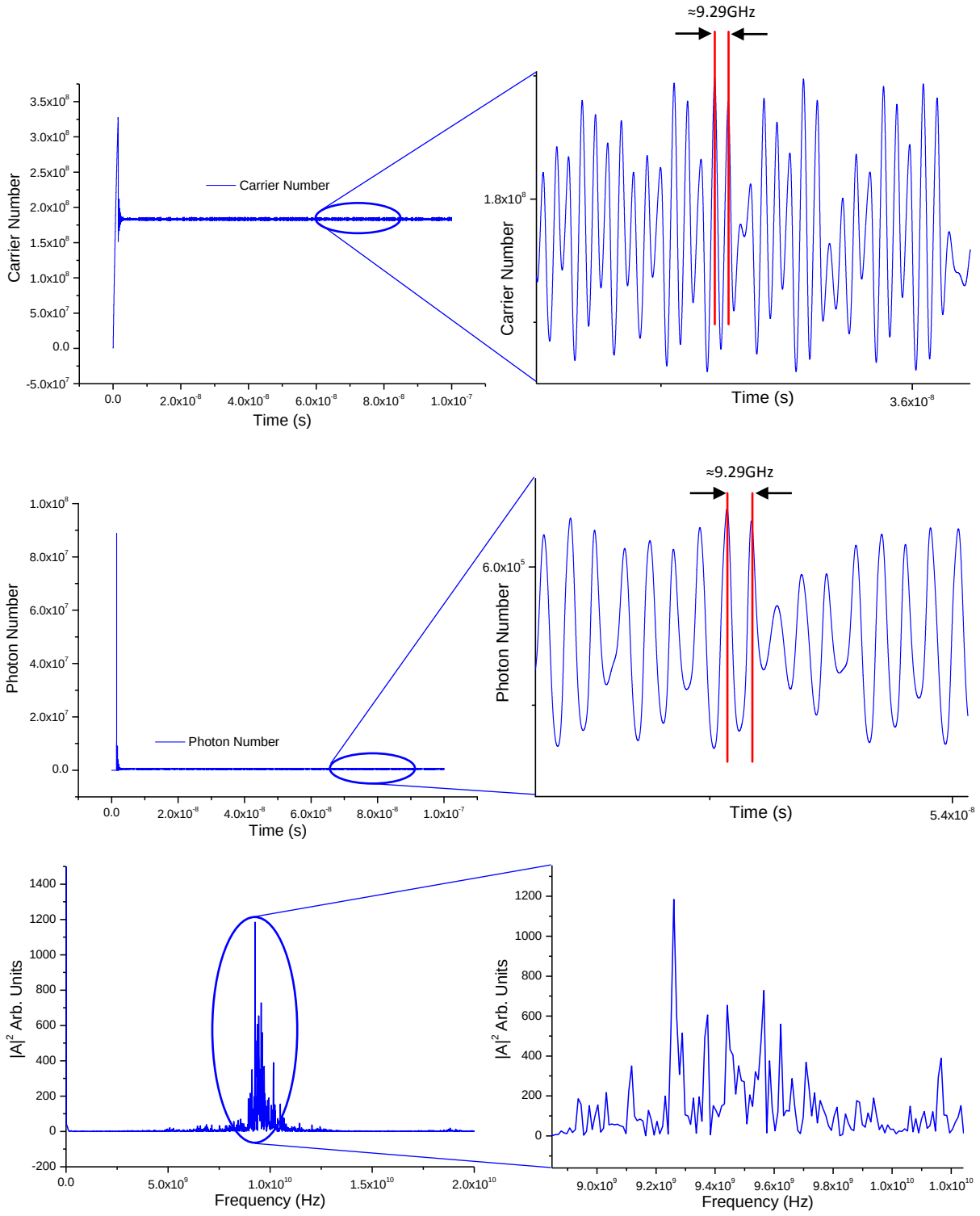

Figure 6.10: *Carrier (top figure) and photon (middle figure) number output with an injection rate, κ_c, of 5.0ns^{-1} with a frequency detuning, Δf, of -4GHz – The carrier and photon numbers are clearly oscillating in a potentially chaotic manner with a periodicity of ≈9.26GHz for the carriers and the photons. The bottom figure shows the photon number plotted on an FFT, which clearly confirms the potential chaotic behaviour of the system.*

The next region of interest in the response of the system is the region of green stars in figures 6.6 & 6.7. Here, a periodic response is apparent, however varying frequencies are present, ranging from approximately 3.11GHz at an injection rate of 5.0ns^{-1} with a frequency detuning of 0GHz (figure 6.11 (b)), to approximately 4.6GHz at an injection rate of 3.0ns^{-1} with a frequency detuning of -4.6GHz (figure 6.11 (c)). From looking at figure 6.11 (a) & (b), there are clearly multiple harmonics in the carriers' and photons response of the system. In the case of figure 6.11 (a), the oscillations appear to follow the same frequency as the detuning frequency, however when considering figure 6.11 (b), the detuning frequency is set to 0GHz, whereas the oscillations appear to have a frequency of approximately 3.11GHz. Considering the data in Appendix G, which presents the data obtained for figures 6.6 and 6.7, it is apparent that generally, wherever multiple harmonics are present in the response, the frequency of these oscillations is unrelated to the frequency detuning. Looking at an injection rate of 4.0ns^{-1} with frequency detuning values of -7.5GHz, -8GHz and -9.5GHz as examples, similar responses to what was seen in figure 6.11 (a) & (b) are observed, however the oscillations have frequencies of approximately 5.10GHz, 5.42GHz and 6.41GHz respectively, which do not appear to be simply related to the detuning frequency.

Again, in order to confirm these multiple harmonics, the photon number outputs have been plotted on FFT plots, which can be seen in the lowest plots in figure 6.11 (a) and (b), where the DC component has again been removed for clarity. From these figures, it is clear to see the additional harmonics present in the system for both of the cases under consideration.

Figure 6.11 (b) is of particular interest; it is clear here that the injection rate and detuning frequency have a significant impact on the behaviour of the system as a whole. Not only do the carriers and photons oscillate with multiple harmonics, but the peak carrier number at turn-on of the laser is much lower than what was seen in figure 6.11 (a). Comparing both responses, it can be seen from figure 6.11 (a) that the carrier number will reach a peak of approximately 3.27×10^8 as the laser is turning on before the relaxation oscillations commence, before settling to the regular oscillations of approximately 4.78GHz with an offset of approximately 1.8×10^8. These oscillations are approximately equal to the detuning frequency in this case.

Comparing this to figure 6.11 (b), it can be seen that the carrier numbers will only reach a peak of approximately 2.15×10^8 as the laser is turning on, which is significantly lower than what was seen in figure 6.11 (a). After the relaxation oscillations, the system will settle to the periodic response with oscillations at approximately 3.11GHz, with a similar offset of approximately 1.8×10^8. Wherever green crosses are apparent in figures 6.6 & 6.7, the system shows behaviours similar to those seen in either figure 6.11 (a) or in figure 6.11 (b).

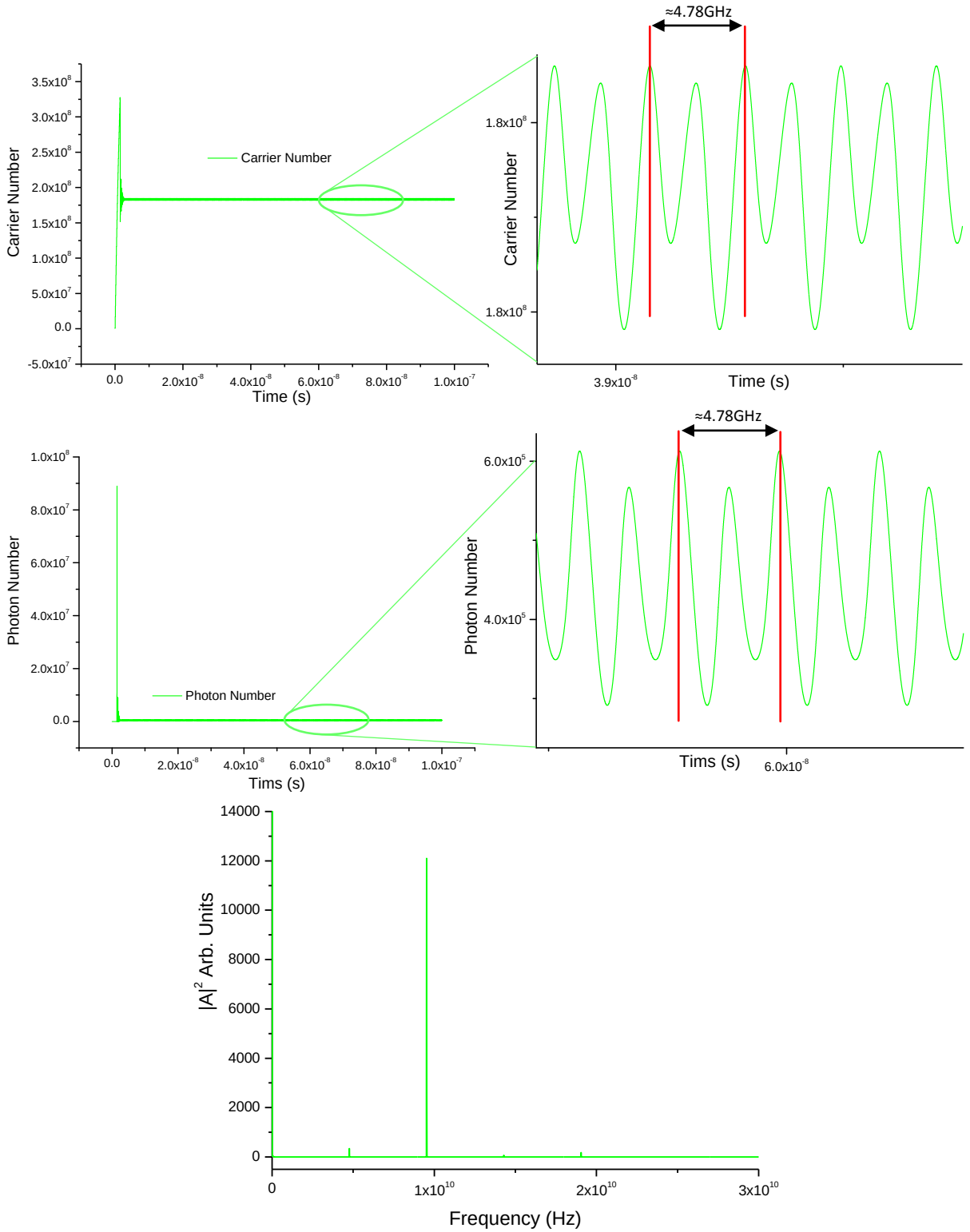

Figure 6.11 (a): *Carrier (top figure) and photon (middle figure) number output with an injection rate, κ_c, of 3.0ns^{-1} with a frequency detuning, Δf, of -4.6GHz – The carrier and photon number outputs are oscillating periodically, where the waveforms appear to contain two harmonics oscillating at ≈4.6GHz. The bottom graph shows the photon number plotted on an FFT, and this confirms the multiple harmonics seen in the photon number plot.*

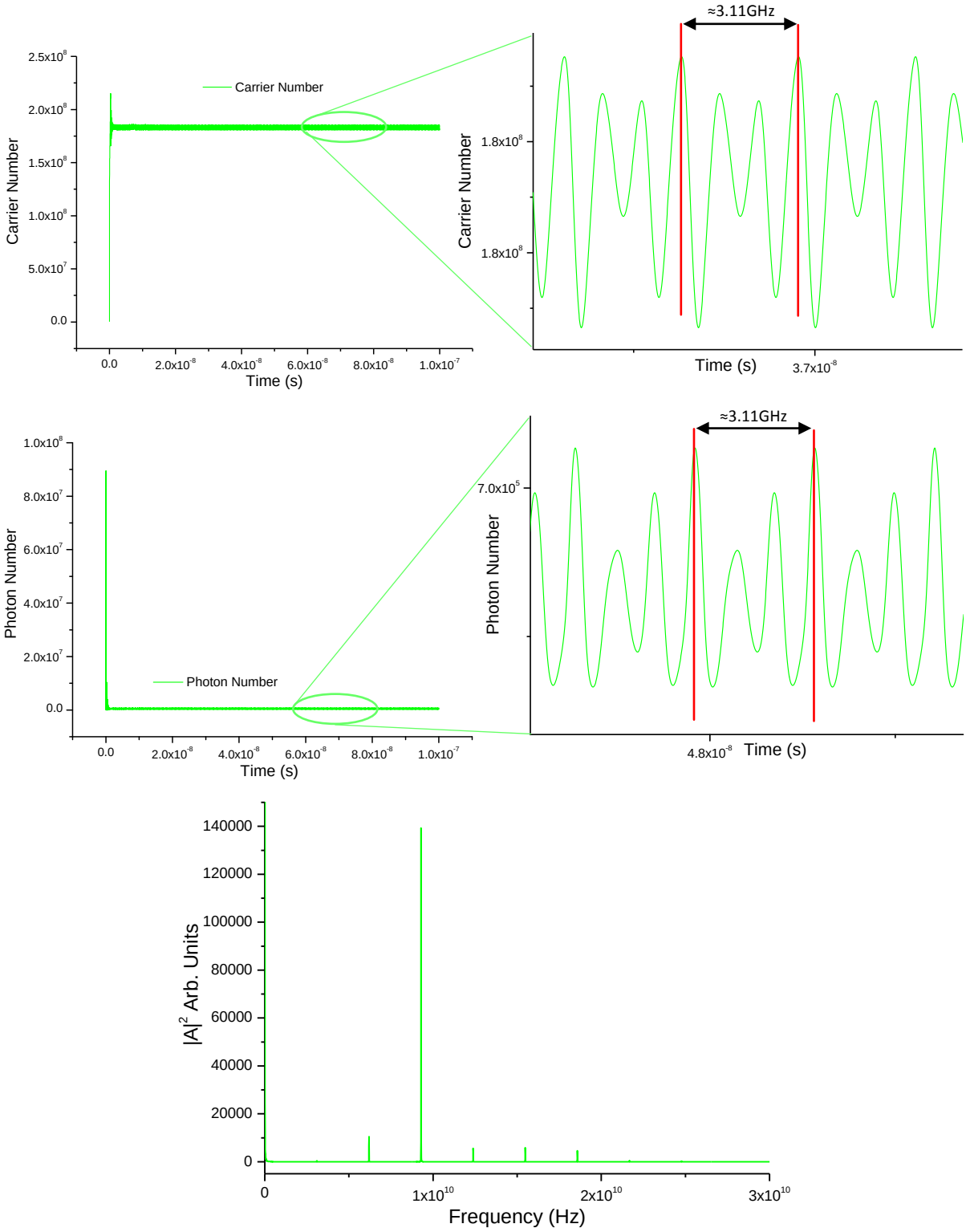

Figure 6.11 (b): *Carrier (top figure) and photon (middle figure) number output with an injection rate, κ_c, of 5.0ns^{-1} with a frequency detuning, Δf, of 0GHz – The carrier and photon number outputs are oscillating periodically, where the waveforms appear to contain two harmonics oscillating at ≈3.11GHz. The bottom graph shows the photon number plotted on an FFT, and this confirms the multiple harmonics seen in the photon number plot.*

Another response that is apparent in the system is where an almost undistorted sine wave is visible in the response of the carrier output, however there are unequal peaks and troughs, as shown in the top plot of figure 6.12. When comparing this to the photon output, this shows a much more distorted sine wave, as can be seen in the middle plot of figure 6.12.

Figure 6.12 shows the results for an injection rate of $7.0ns^{-1}$ with a frequency detuning of -3GHz. It is clear from the figure that there is an almost undistorted sine wave response, as was seen in figure 5.6 (a) from chapter five, and it is clear from the frequency of the oscillations that the system is oscillating very close to the relaxation oscillation frequency of 9.2GHz which was established earlier. What is interesting here is the apparent presence of multiple harmonics in the response of the system when the photon output is plotted on an FFT, even though the response of the photon output only appears to show a single harmonic. A similar response is apparent to that of figure 6.12 with injection rates of $7.0ns^{-1}$ and $8.0ns^{-1}$ with frequency detuning values of -10GHz and -4GHz respectively, and in each case, the system oscillates at frequencies of approximately 9.25GHz and 8.63GHz respectively. This is again clearly close to the relaxation oscillation frequency of approximately 9.2GHz. The only exception to this is with an injection rate of $2.0ns^{-1}$ and frequency detuning of -8.5GHz where the system oscillates at a slightly lower frequency of approximately 6.15GHz. This could be due to the injection rate being too low.

The final areas of interest in figures 6.6 and 6.7 is shown by the red circles, and this of course is where the locking condition between both the first and second lasers is observed, and this can be seen in figure 6.13. This figure shows the carriers (top figure), photons (middle figure) and the FFT (bottom figure) for an injection rate of $0.6ns^{-1}$ with a frequency detuning of -500MHz. In a similar manner to what was seen in chapter five, there are no oscillations present in the carrier or photon output response of the system, and both the first and the second laser settle to a very similar value of steady-state carriers and steady-state photons, however, unlike in chapter five where there was no frequency spacing between the two lasers in the locked condition, there is now a fixed frequency separation between the two.

From looking at the FFT plots for both the first and the second lasers, it is clear that there is only a single harmonic present in both the first and second lasers' while operating in the locked condition.

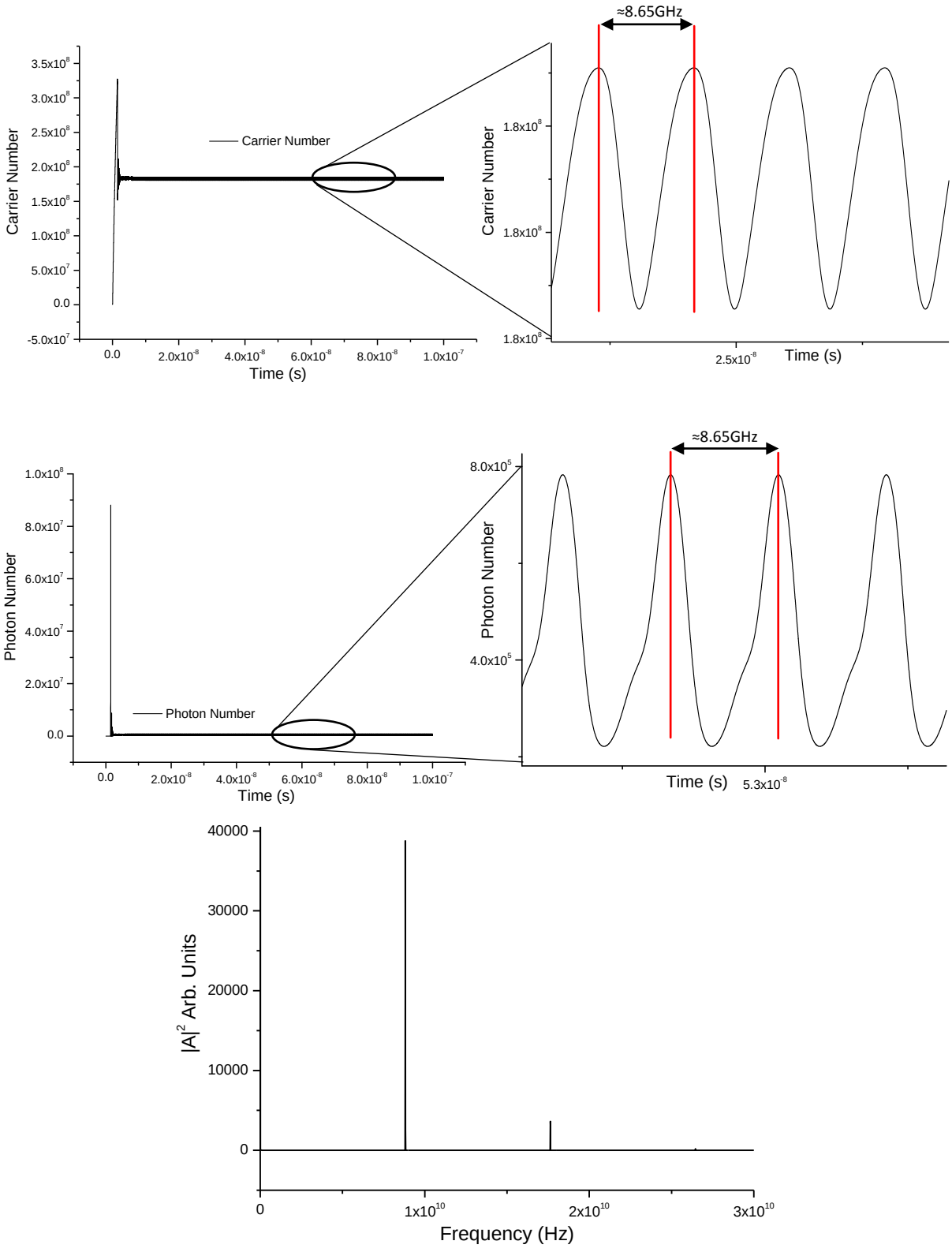

Figure 6.12: *Carrier (top figure) and photon (middle figure) number output with an injection rate, κ_c, of 7.0ns^{-1} with Δf = -3GHz. The carrier and photon numbers are oscillating periodically at a fundamental frequency of ≈8.65GHz. The bottom graph shows the photon number plotted on an FFT, and this shows the apparent presence of multiple harmonics in the system.*

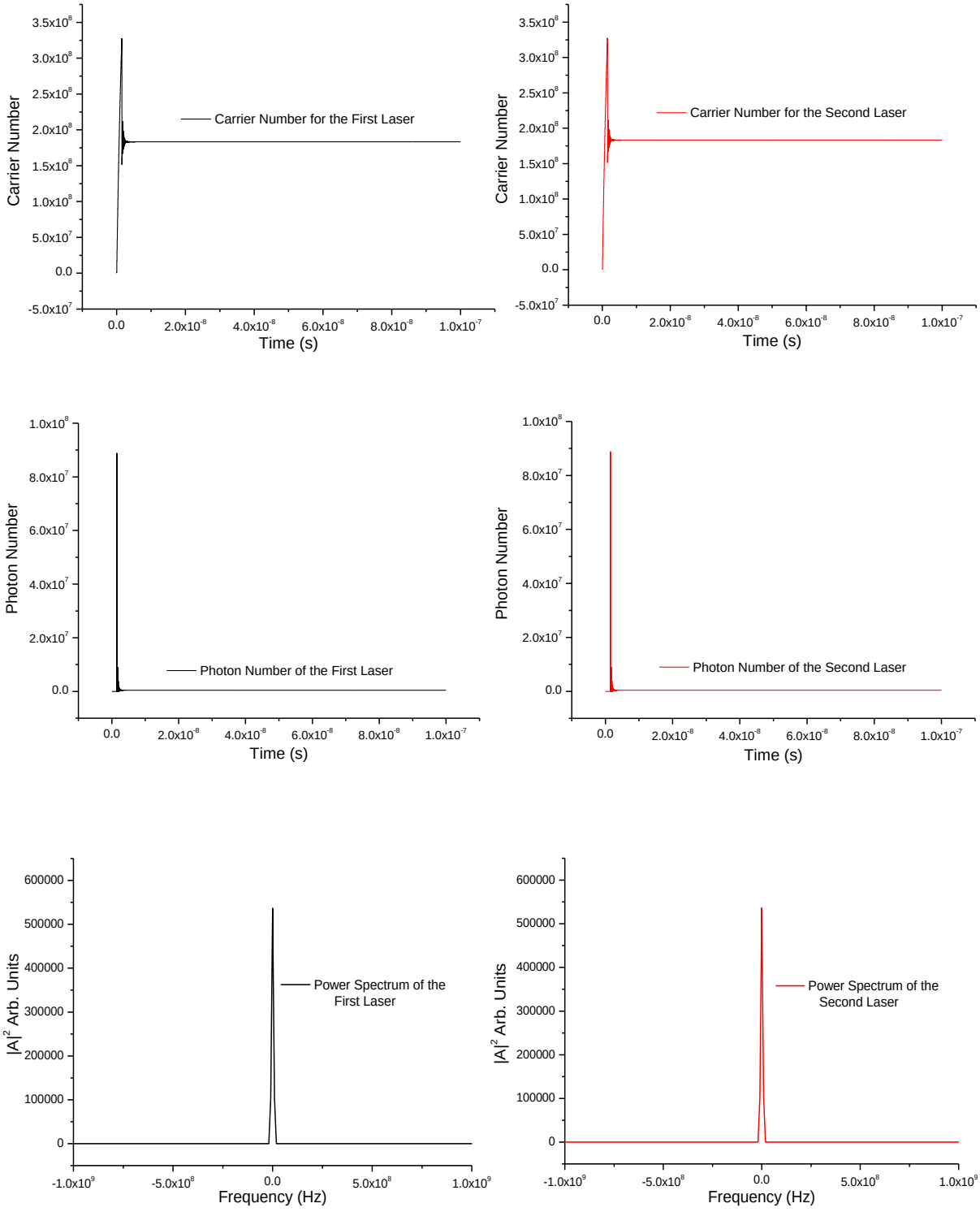

Figure 6.13: *Carrier (top figure) and photon (middle figure) number output for the two lasers with an injection rate, κ_c, of 0.6ns^{-1} with a frequency detuning, Δf, of -500MHz. The carrier and photon numbers have clearly settled to a constant steady-state value, thus indicating a single frequency operation. This is emphasised in the FFT plot (bottom figure) where only a single harmonic is present in the system.*

The table of data in Appendix G gives a comprehensive view of the behaviour of the system when injection locking is present. The table gives the number of photons in the system for both the first and the second laser at steady-state, and each time the system locks, it can be seen that the number of photons in both the lasers settle to the exact same number before the decimal point. After the decimal point, the number of photons settles to different numbers (yellow highlighted numbers), and in some cases, the seventh, eighth and ninth decimal places never settle at all (turquoise highlighted numbers). Because the difference in steady-state values are so small, when both the first and second laser's carrier responses are plotted on the same graph, it is not possible to see any difference in values between the two. Similarly, because it's only the seventh, eighth and ninth decimal places that never settle (sometimes it's only the ninth decimal place that doesn't settle, as is the case with an injection rate of $0.2ns^{-1}$ with frequency detuning values of +100MHz, +200MHz and +300MHz), it is also impossible to see when plotting the carrier number output.

From analysing the highlighted data from Appendix G, there is a clear 'curve' between the yellow and turquoise highlighted numbers when the lasers are operating in the locked condition, indicating that the system is going from the unlocked condition, into the locked condition, and then into the unlocked condition once more. In some of these instances, where the number of photons have settled to different numbers in both lasers, even though there is a slight drift in these numbers, they can be assumed to still be operating at the same wavelength. In addition, where the numbers do not settle at all, it would seem to appear a slight frequency drift in the lasers, however this is so small, it is impossible to see when plotted.

6.4 – Summary and Conclusion

This chapter has introduced a three laser FWM scheme, which has built upon the injection locking scheme presented in chapter five with a view of modelling a system with a nonzero frequency separation between the lasers while operating in the locked condition.

As discussed at the end of chapter five, the disadvantage of the bidirectional injection locking scheme is that there is a zero frequency difference between the first and the second lasers' while operating in the locked condition; hence, the aim of the work in this chapter was to utilise the FWM in a third laser to model a system, utilising injection locking, that maintains a nonzero separation of the lasers' frequency when the system is operating in the locked condition.

There are five distinct behaviour regions present in the response of the system. The first analysed region is where the system exhibits a periodic response in the carriers' and photons output, where at some points, this periodicity exhibits additional oscillations at the troughs and peaks of the waveforms. In order to establish whether or not these additional oscillations were additional

harmonics in the response of the system, the photon outputs were plotted on FFTs, and it was found that only a single frequency was present in the power spectrum for each case, thus indicating there was only a single harmonic present in the systems response.

The second area considered is where the carriers' and photons output oscillates as an undistorted sine wave, where the frequency of these oscillations was approximately the same as the relaxation oscillations.

The third behavioural region of interest is where the system exhibits a potential chaotic behaviour, similar to that observed in chapter five. Again, in order to confirm this potential chaotic behaviour, the photon output was again plotted on an FFT, and it was found that the photon output exhibited a potential chaotic behaviour as the spectrum appeared to show multiple, random peaks in the response.

The fourth area under study was where the carriers' and photons output oscillates with multiple harmonics in the response, and this was confirmed when plotting the photon output on an FFT as multiple peaks were present in the spectrum, thus indicating that more than one frequency was present in the system.

The final region of interest is where the two lasers' settle to a constant value, and are hence operating in the locked condition, with some cases exhibiting some residual frequency drifts. This is confirmed in the FFT plots where only a single frequency is apparent for each of the lasers spectrum.

In the three laser FWM scheme presented in this chapter, the locking regions (presented in figures 6.6 and 6.7) are highly symmetrical for injection rates between $0.1ns^{-1}$ and $0.6ns^{-1}$, and thereafter would become highly asymmetrical for injection rates between $0.7ns^{-1}$ and $8.0ns^{-1}$. As the injection rate increases above $0.6ns^{-1}$, the linewidth enhancement factor, α, will start to have more of an effect on the system, causing the asymmetry in the locking region, as seen with unidirectional injection locking.

Similarly to the case of injection locking in chapter five, when operating outside of the locking region, the carriers' and photons output simply oscillate with an undistorted sine wave; however, unlike the case for injection locking where these oscillations are approximately equal to the detuning frequency, in this case, these oscillations are approximately equal to the relaxation oscillation frequency. Here, the scheme is simply oscillating at the fundamental, preferred frequency, of the system.

Again, similarly to the case of injection locking, potential chaotic behaviour was observed for the three laser FWM system, however these regions were more randomly positioned than those seen previously; this area of behaviour should again be avoided during the course of this work.

The main region of interest here is where the system is operating within the locked condition (red circles from figures 6.6 and 6.7). Here, the first and the second lasers would settle to a constant steady-state value of carriers and photons after the relaxation oscillations, thus indicating a locked condition.

Although the carriers and photons settle to the same value in both the first and the second lasers, as was the case with bidirectional injection locking, there is a nonzero frequency spacing between the two lasers due to the nature of the frequency detuning.

Chapter seven will build further on the three laser FWM system, whereby the modulation response of the system will be investigated. It will also investigate the response of the locked system at various injection rates and detuning frequencies, and will consider an optimal locking region for the system.

REFERENCES

[1] **M. Zanola**, M. J. Strain, G. Giuliani, M. Sorel, "Monolithically integrated DFB lasers for tunable and narrow linewidth millimeter-wave generation", IEEE J. Quantum Electron., vol. 19, no. 4, Paper ID. 1500406, Jul/Aug. 2013.

[2] **M. Soldo**, N. Gibbons, G. Giuliani, "Generation of a narrow linewidth mm-wave signal from two phase-locked DFB lasers that are mutually coupled via four wave mixing", Proc. THz and Mid IR Rad: Basic Research and Practical Applications, 2009. TERA-MIR 2009. International Workshop., pp. 77-78, 2009.

[3] **R. Boyd**, Nonlinear Optics, 3rd ed. Academic Press, 2008.

[4] **D. Duchesne**, M. Ferrera, L. Razzari, R. Morandotti, B. Little, S. T. Chu, D. J. Moss, "Nonlinear optics in doped silica glass integrated waveguide structures", Frontiers in Guided Wave Optics and Optoelectronics, Bishnu Pa; (Ed.), InTech, 2010.

[5] **D. Marciu**, "Optical limiting and degenerate four-wave mixing in novel fullerenes", Ph. D. thesis, Dept. Phys., Virginia Polytechnic Institute and State Univ., Blacksburg, Virginia, 1999.

[6] **C. W. Thiel**, "Four-Wave mixing and its applications", Montana State Univ., Available: http://staff.mbi-berlin.de/bfreyer/fwmixing.pdf [Accessed on: Jun. 08, 2016].

[7] **R. Paschotta**, article on 'four-wave mixing' in the Encyclopaedia of Laser Physics and Technology, 1. edition, October 2008, Wiley-VCH, ISBN 978-3-527-40828-3.

[8] **R. H. Stolen**, J. E. Bjorkholm, "Parametric amplification and frequency conversion in optical fibers", IEEE J. Quantum Electron., vol. 18, no. 7, pp. 1062-1072, Jul. 1982.

[9] **G. P. Agrawal**, "Four-wave mixing and phase conjugation in semiconductor laser media", Optics Lett., vol. 12, no. 4, pp.260-262, Apr. 1987.

[10] **G. P. Agrawal**, J. T. Klaus, "Effect of phase-conjugate feedback on semiconductor laser dynamics", Optics Lett., vol. 16, no. 17, pp. 1325-1327, Apr. 1991.

[11] **M. W. Wright**, J. G. McInerney, C. Wu, "Injection locking characteristics of semiconductor lasers in double phase conjugate mirror geometry", Electronics Lett., vol. 29, no. 13, pp. 1183-1185, Jun. 1993.

[12] **M. W. Wright**, J. G. McInerney, "Injection locking semiconductor lasers with phase conjugate feedback", Optics Comms., vol. 110, no. 5-6, pp. 689-698, Sept. 1994.

[13] **H. Li**, T. L. Lucas, J. G. McInerney, M. W. Wright, R. A. Morgan, "Injection locking dynamics of vertical cavity semiconductor lasers under conventional and phase conjugate injection", IEEE J. Quantum. Electron., vol. 32, no. 2, pp. 227-235, Feb. 1996.

[14] **E. Bochove**, "Theory of a semiconductor laser with phase-conjugate optical feedback", Phys Rev A., vol. 55, no. 5, pp. 3891-3899, Nov. 1996.

[15] **Y. Hong**, J. M. Tang, K. A. Shore, "Optical phase conjugation in laser diodes subject to strong probe injection power", Electronics Lett., vol. 34, no. 15, pp. 1491-1492, Jul. 1998.

[16] **D. O'Brien**, G. Huyet, J. G. McInerney, "Low frequency fluctuations in a semiconductor laser with phase conjugate feedback", Proc. Lasers and Electro-Optics Soc. 2000 annual Meeting. LEOS 2000. 13th Annual Meeting., vol. 2, pp. 738-739, Nov. 2000.

[17] **McGraw-Hill Dictionary of Scientific & Technical Terms**, "Optical phase conjugation", [Online]. Available: http://encyclopedia2.thefreedictionary.com/optical+phase+conjugation [Accessed on: Jul. 06, 2016].

[18] **S. Peters-Flynn**, P. S. Spencer, S. Sivaprakasam, I. Pierce, K. A. Shore, "Identification of the optimum time-delay for chaos synchronization regimes of semiconductor lasers", IEEE J. Quantum Electron., vol. 42, no. 4, pp. 427-434, Apr. 2006.

[19] **S. Peters-Flynn**, I. Pierce, P. S. Spencer, P. Rees, "Synchronisation recovery in unidirectionally coupled semiconductor lasers", IEE Proc. Optoelectron., vol. 153, no. 1, pp. 8-12, Feb. 2006.

[20] **R. Lang**, K. Kobayashi, "External optical feedback effects on semiconductor injection laser properties", IEEE J. Quantum Electron., vol. QE-16, no. 3, pp. 347-355, Mar. 1980.

[21] **B. Thédrez**, J. G. Provost, "Nearly degenerate four-wave mixing investigation of period doubling in semiconductor lasers", Optics Lett., vol. 14, no. 17, pp. 958-960, Sept. 1989.

[22] **J. Ye**, H. Li, J. G. McInerney, "Period-doubling route to chaos in a semiconductor laser with weak optical feedback", Phys Rev A., vol. 47, no. 3, pp.2249-2252, Mar. 1993.

[23] **T. B. Simpson**, J. M. Liu, A. Gavrielides, V. Kovanis, P. M. Alsing, "Period-doubling route to chaos in a semiconductor laser subject to optical injection", Appl. Phys. Lett., vol. 64, no. 26, Jun. 1994.

CHAPTER SEVEN

MODULATION RESPONSE OF THE FWM SYSTEM AND OPTIMISATION

In chapter six, a three laser system was built based on the four-wave mixing (FWM) scheme from the work of Zanola *et al*. [1], utilising the injection locking method discussed in chapter five, as a potential means for realising THz radiation. As discussed, the disadvantage to the injection locking scheme is the fact that there is a zero frequency separation between the frequency of the first and second lasers. The advantage to the FWM scheme is that it will provide a frequency spacing between the two, with the aim of having this frequency spacing lie within the THz frequency range.

Chapter six looked in detail at the different behaviours present within the three laser FWM system with varying injection rates and detuning frequencies; it was found that the locking condition occurred at much lower injection rates than was seen with the conventional injection locking scheme. This chapter will look in detail at the modulation response of the same system to introduced perturbations, and whether or not the three laser FWM scheme provides a performance enhancement over the uncoupled laser. In order to establish this, an investigation will be made as to how well the three laser FWM system supresses the introduced perturbations. In addition, an optimal locking region will be considered, whereby the phasor difference between the two lasers will be calculated, and the amplitude of the resultant wave will be compared to that of the uncoupled laser. The optimal locking region will be classified as the point where the difference in amplitudes between the resultant wave and uncoupled laser is the greatest.

The contents of this chapter are organised as follows:

Section 7.1 will outline how the perturbations will be introduced to the system, including the modifications made to the rate equations from chapter six. This section will also look at the modulation response of the uncoupled laser. Section 7.2 will then go on to look in detail at the difference between the first and the second lasers' perturbations, and how increasing the modulation frequency of the system affects the phase difference between the first and the second lasers'. Section 7.3 will then establish whether or not there is a performance improvement in the three laser FWM system with the introduced perturbations, calculating the phasor difference between the first and the second lasers perturbations in order to find the resultant wave, and comparing the amplitude of this wave to the amplitude of the uncoupled laser. Section 7.4 will then discuss the percentage improvement in performance of the new system over the uncoupled laser, and will also suggest an

optimal locking region for the system. Finally, section 7.5 will give a summary and conclusions of the work presented in this chapter.

7.1 – Phase Conjugate Feedback with Introduced Perturbations

In order to establish a conclusion regarding the behaviour of this system, a small perturbation was introduced into the first laser's carrier equation to establish whether the second laser would follow the first laser's frequency in the locking region. This perturbation was introduced to the pumping term, hence equation (6.5) is modified to become equation (7.1) below. The second laser's charge carrier equation remains unchanged.

$$\frac{dN_1(t)}{dt} = \frac{J\left(1 + m\cos\left(\omega_m(t)\right)\right)}{e} - \frac{N_1(t)}{\tau_n} - G_1|A_1(t)|^2 \tag{7.1}$$

Here, m is the percentage of modulation introduced to the charge carrier equation, and for this analysis was kept unchanged at 1%, and ω_m is the modulation frequency, which was varied between 10MHz and 20GHz. The code for this model is again an evolution of that found in Appendix C. It should again be noted, as with chapter six, that the time of flight in the feedback term is assumed to be zero, and further work might profitably examine a finite time of flight.

The aim of this analysis is to establish whether the three laser FWM scheme provides improved performance over a singular uncoupled laser, i.e., the aim is to establish whether or not the three laser FWM system has reduced the effect of the introduced perturbations compared to the uncoupled laser, hence analysing the modulation response of the system. To do this, a single uncoupled laser model is run (which can be done by disabling one of the lasers from the model in Appendix C), and then the amplitude of the perturbations is measured for a range of modulation frequencies. This is then compared to the results for the phase conjugate feedback model with no perturbation, to establish whether this system has reduced the effect of the perturbations or not (i.e. improved the performance of the system). The results from the uncoupled laser can be seen in figure 7.1, where the modulation frequency is ranged from 10MHz to 20GHz.

It is clear from figure 7.1 that at low modulation frequencies (between 10MHz and 3GHz), the amplitude of the perturbations is very low. When the modulation frequency is increased above 3GHz, the amplitude of the perturbations begins to increase, until it reaches a peak at a modulation frequency of 9GHz, which is approximately the same frequency as the relaxation oscillation frequency of the system, as discussed in chapter six. When continuing to increase the modulation frequency beyond 9GHz, the amplitude of the perturbations decreases quite rapidly between frequencies of 9.5GHz and 12GHz and gradually start to settle again with modulation frequencies between 12GHz and 20GHz. The response observed here is consistent with the modulation response of a second order

system [2]. It should be noted that the same modulation response is observed for increasing injection rates and detuning frequencies, where the peak of the modulation response would always appear at a modulation frequency of 9GHz, which is approximately equal to the relaxation oscillation frequency, thus indicating that 9GHz is the fundamental frequency of the three laser FWM system.

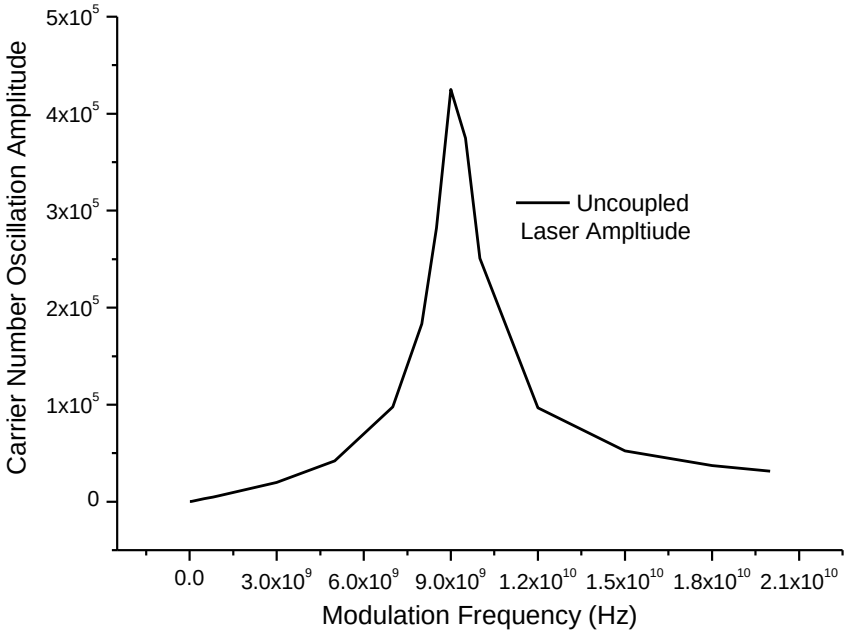

Figure 7.1: *Amplitude of oscillation in the carrier number of the uncoupled laser with modulation frequencies between 10MHz and 20GHz. The peak of the modulation response appears at 9GHz, which is approximately equal to the relaxation oscillation frequency.*

7.2 – First and Second Laser Perturbations

When running the model with the three laser FWM scheme employed (i.e. with bidirectional phase conjugate feedback), there are perturbations in both the first and second laser's output responses. An example can be seen in figure 7.2, where an injection rate, κ_c, of 0.6ns^{-1}, a detuning frequency of 0GHz and a modulation frequency of 1GHz has been used. The detuning frequencies are inside the locking regions of figures 6.6 and 6.7 from chapter six, and only the locking regions (red circles) have been analysed here. It is only these regions that have been analysed as it's in the locking condition between the first and the second laser that is important to this work. It is under these conditions that a nonzero frequency spacing will be apparent between the two lasers where THz radiation may be realised.

From figure 7.2, it is seen that there are clear perturbations in both the first and the second laser's carrier output response, clearly showing the influence the first laser has on the second laser. These perturbations are clearly out of phase (in this case by approximately 114°) with the second laser leading the first laser, and the first laser oscillation clearly has a higher amplitude than the second laser. When increasing the modulation frequency, both the first and second lasers' amplitudes

increase, but as in figure 7.2, the first laser generally has a higher amplitude than the second laser. The only exception to this is at low modulation frequencies (between 10MHz and 100MHZ) where both the first and second laser's amplitudes are approximately equal. Also, when the modulation frequency is increased, the first and the second lasers' perturbations become more and more in phase, and when increasing the modulation frequency beyond 9GHz, they become out of phase once more.

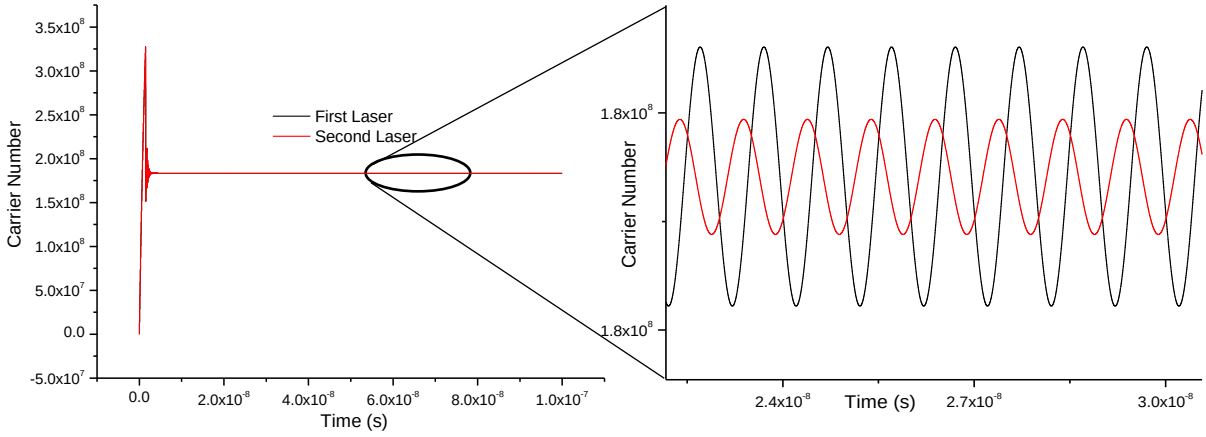

Figure 7.2: *The first and second laser perturbations with an injection rate, κ_c, of 0.6ns^{-1}, a frequency detuning of 0GHz and a modulation frequency of 1GHz. The first and the second laser's carrier output response are out of phase by approximately 114°.*

An example of this can be seen in figure 7.3 ((a)-(b)). Figure 7.3 (a) shows the carrier output response with an injection rate of 0.6ns^{-1}, a detuning frequency of 0GHz and a modulation frequency of 9GHz. It can clearly be seen from the figure that both the first laser and the second laser carrier responses are now much closer to being in phase, with only a difference of approximately 25° between them, compared to 114° at a modulation frequency of 1GHz. It can also be seen that the amplitude of the second laser has increased significantly relative to the first laser when compared to figure 7.2.

Through examination figure 7.3 (b), where the same injection rate and detuning frequency as figure 7.3 (a) are used, but the detuning frequency is increased to 12GHz, it can be seen that both the first and second lasers have gone beyond the point of being completely in phase, and are now approximately -81° out of phase, with the second laser now lagging the first laser. It can also be seen that the amplitude of the second laser is now much smaller relative to the first laser, and with further increases in modulation frequency, its amplitude becomes much smaller relative to the first laser, making it virtually impossible to measure any difference in phase between the two.

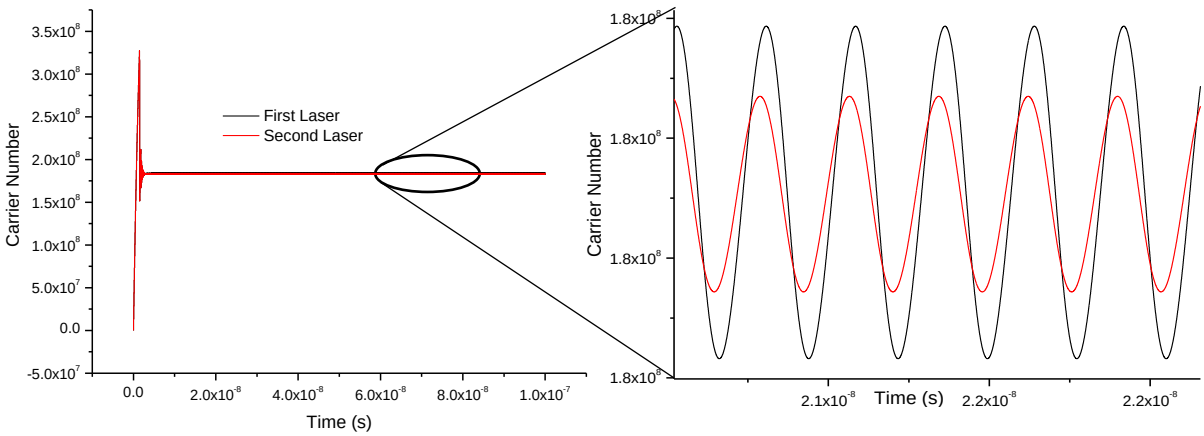

Figure 7.3 (a): *The first and second laser perturbations with an injection rate, κ_c, of 0.6ns^{-1}, a frequency detuning of 0GHz and a modulation frequency of 9GHz. The first and the second laser's carrier output response are out of phase by approximately 25°.*

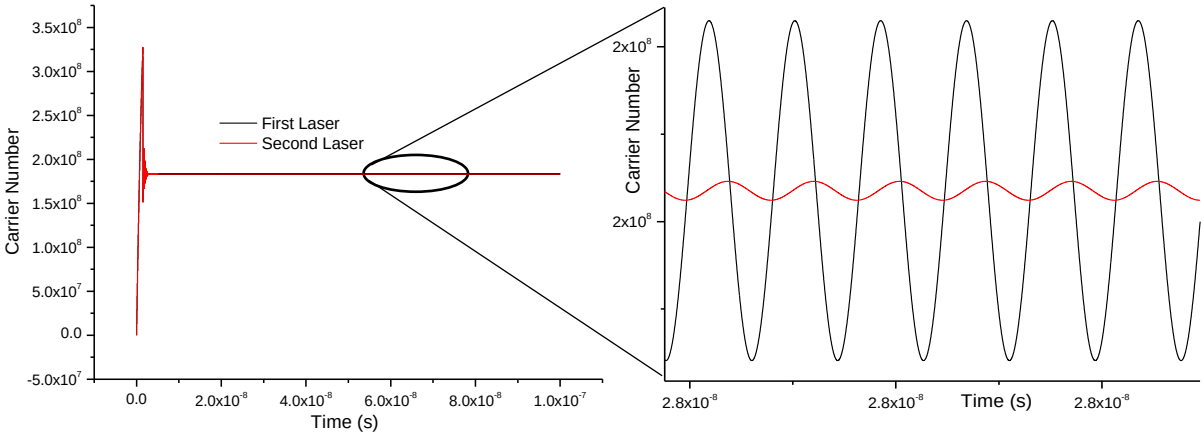

Figure 7.3 (b): *The first and second laser perturbations with an injection rate, κ_c, of 0.6ns^{-1}, a frequency detuning of 0GHz and a modulation frequency of 12GHz. The first and the second laser's carrier output response are out of phase by approximately -81°.*

From consideration of the difference in phase for modulation frequencies from 10MHz to 20GHz, it can be seen that the system goes through 270° of phase change, and this is shown in figure 7.4. This figure shows the change in phase for an injection rate of 0.6ns^{-1} with frequency detuning values of 0GHz and -900MHz, and an injection rate of 3.0ns^{-1} with a frequency detuning of -4.5GHz.

As can be seen in figure 7.4, there is a 180° phase shift in the system at low frequencies. This can be explained by looking at the response of the second lasers carriers and photons steady-state values for an increasing pumping level, and the results are summarized in table 7.1.

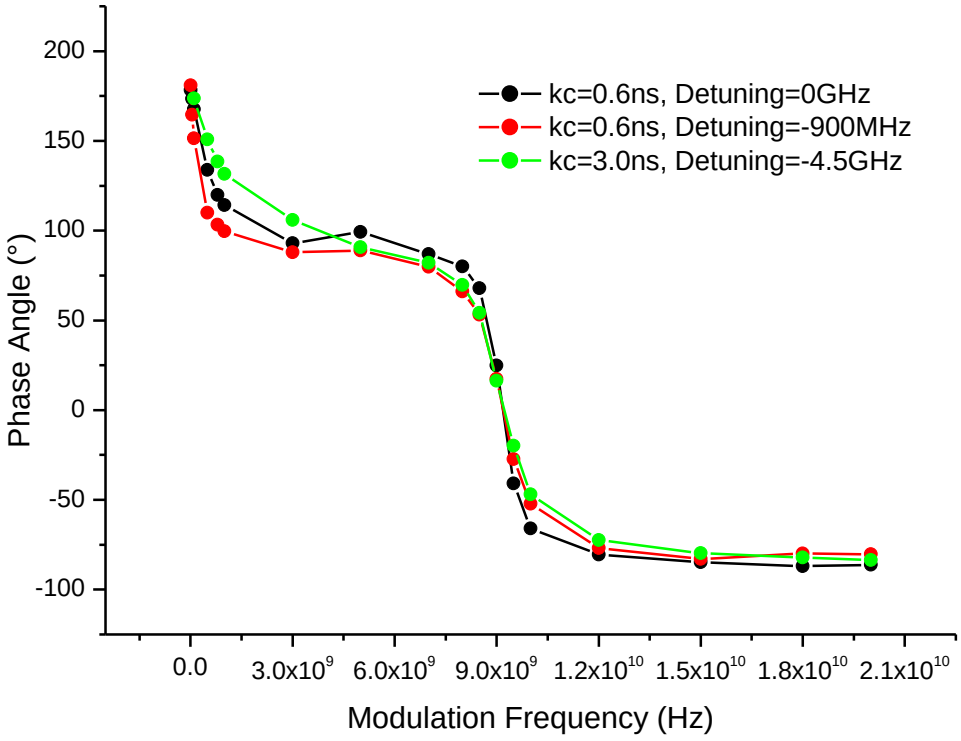

Figure 7.4: *Difference in phase for modulation frequencies between 10MHz and 20GHz for* $\kappa_c = 0.6ns^{-1}, \Delta F = 0GHz,\ \kappa_c = 0.6ns^{-1}, \Delta F = -900MHz$ *and* $\kappa_c = 3.0ns^{-1}, \Delta F = -4.5GHz.$

Pumping Level	Carrier Number	Photon Number
50mA	183341449	440797.342
60mA	183336608	566515.287
70mA	183332923	690636.956

Table 7.1: *Second lasers' carrier and photon numbers for an increasing pumping level.*

From table 7.1, it is clear to see that the more the pumping level is increased, the photon number (light generation) increases, and as a result, the carrier number decreases. This therefore explains the 180° phase shift at low modulation frequencies.

It is clear from figure 7.4 that there is a change in phase between modulation frequencies of 10MHz and 1GHz where the system goes through approximately 90° of phase shift. This is consistent with a first order system. The system then settles between 3GHz and 7GHz before the system then goes through a second region of phase changes between modulation frequencies of 8GHz and 12GHz, where the system now goes through approximately 180° of phase shift; double what was seen previously. This is now consistent with a second order system. The system then settles once more with a phase of approximately 270°. This pattern was apparent no matter what the injection rate and

frequency detuning. This therefore suggests that the system is behaving like a first order system in series with a second order system. To confirm this, the same data is plotted on a Bode plot. This can be seen in figure 7.5. Is it clear from the figure that there is a change in phase angle at a modulation of 10, where the phase angle changes through 180°, from 90° to 270°. This correlates with the result of figure 7.4.

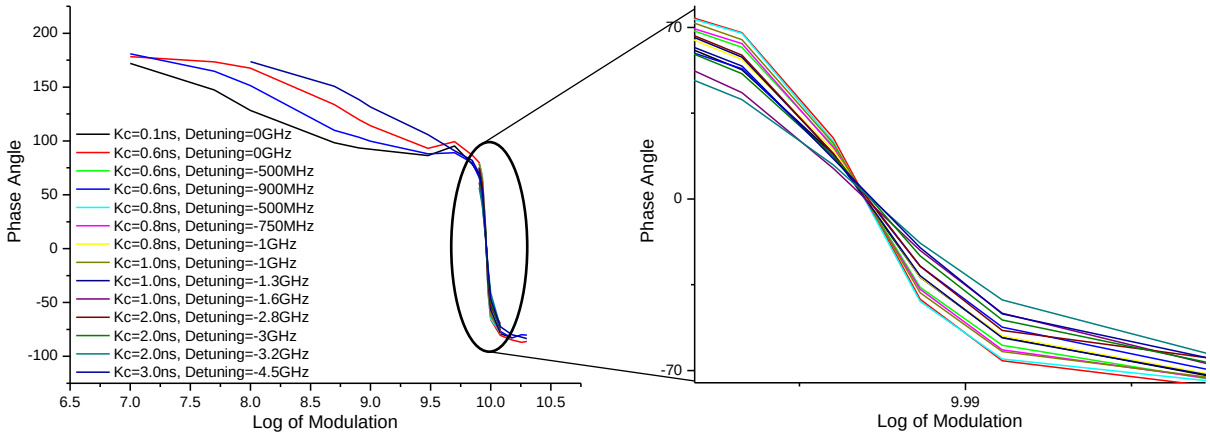

Figure 7.5: *Bode plot of the modulation frequency against the phase angle for injection rates of 0.1ns^{-1}, 0.6ns^{-1}, 1.0ns^{-1}, 2.0ns^{-1} and 3.0ns^{-1} and detuning frequencies between 0GHz and -4.5GHz.*

A first order system is assumed here for modulation frequencies between 10MHz and 1GHz as the system goes through 90° of phase shift; in a first order system, the phase would start at 0° at low frequencies, and then go through -90° of phase shift at high frequencies. The corner frequency (cut-off frequency) is at a phase of -45°, and this is consistent with what can be seen in figure 7.5. If the frequency response was plotted in terms of gain (in dB), then the slope after the corner frequency would have a slope of -20dB/decade. A second order system is assumed here for modulation frequencies between 8GHz and 12GHz as the system goes through 180° of phase shift; in a second order system, the phase would start at 0° for low frequencies, and then go through -180° of phase shift for high frequencies. The corner frequency (cut-off frequency) is at a phase of -90°, and this is again consistent with what is seen in figure 7.5. If the frequency response was plotted in terms of gain (in dB), then the slope after the corner frequency would have a slope of -40dB/decade.

It can also be seen from figure 7.5, that the lower the injection rates, the steeper the response in phase of the system is to changes in modulation frequency, hence suggesting an underdamped system. For higher injection rates, the slope becomes less steep, thus suggesting an overdamped system.

In such a system, between the modulation response of the injected current and the carriers in the first laser, N_1, it can be assumed that there will be a pair of complex conjugate poles in series with a single

pole. If the modulation response between the injected current and the carriers in the second laser, N_2, looks like a double pole, then this will cancel out the effect of the single pole in N_1. This partial pole zero cancellation would result in a total response that looks like a single pole in cascade with a double pole. However, as this is of course a coupled system, the response will be more complex than this.

7.3 – Difference in First and Second Laser Perturbations

This section will establish whether there is any improvement in response in the three laser FWM system for the coupled lasers with phase conjugate coupling, compared with the uncoupled laser; i.e. whether the three laser FWM system suppress any of the introduced perturbations, and if so, by how much, and if there is an optimum injection rate and detuning frequency within the locking range where this is achieved. In order to achieve this, a calculation to establish the difference in amplitude for the carriers between the first and the second laser must be done, while at the same time taking into account the phase difference between them; i.e. calculating the phasor difference between the two waves in order to find one resultant wave, where the amplitude of the resulting wave will be either worse, the same, or improved over the uncoupled laser. This is illustrated in figure 7.6 for an injection rate of 0.8ns^{-1} and detuning frequency of -750MHz, where the second laser is leading the first laser by approximately 76°.

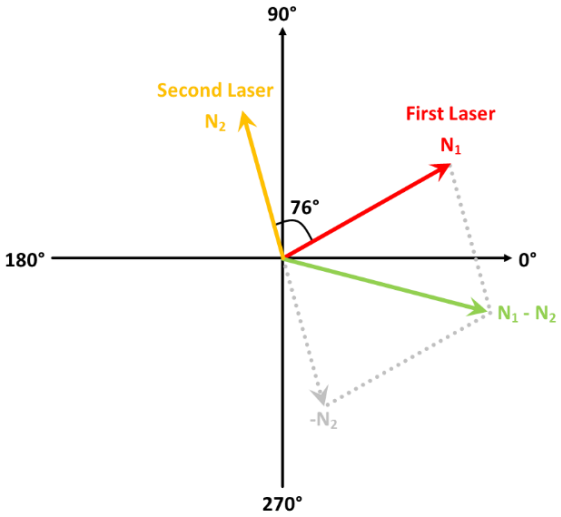

Figure 7.6: *Illustration of the calculation of the phasor difference between the first and the second laser.*

The system was simulated for injection rates of 0.1ns^{-1}, 0.6ns^{-1}, 1.0ns^{-1}, 2.0ns^{-1} and 3.0ns^{-1}, the results of which can be seen in figure 7.7. It should also be noted here, that for an injection rate of 3.0ns^{-1} and a frequency detuning of -4.5GHz, when the modulation frequency is below 50MHz, there is a response very similar to what was seen in figure 6.11 (a) from chapter six, where both the first and the second lasers are perfectly in phase. This can be seen in figure 7.8.

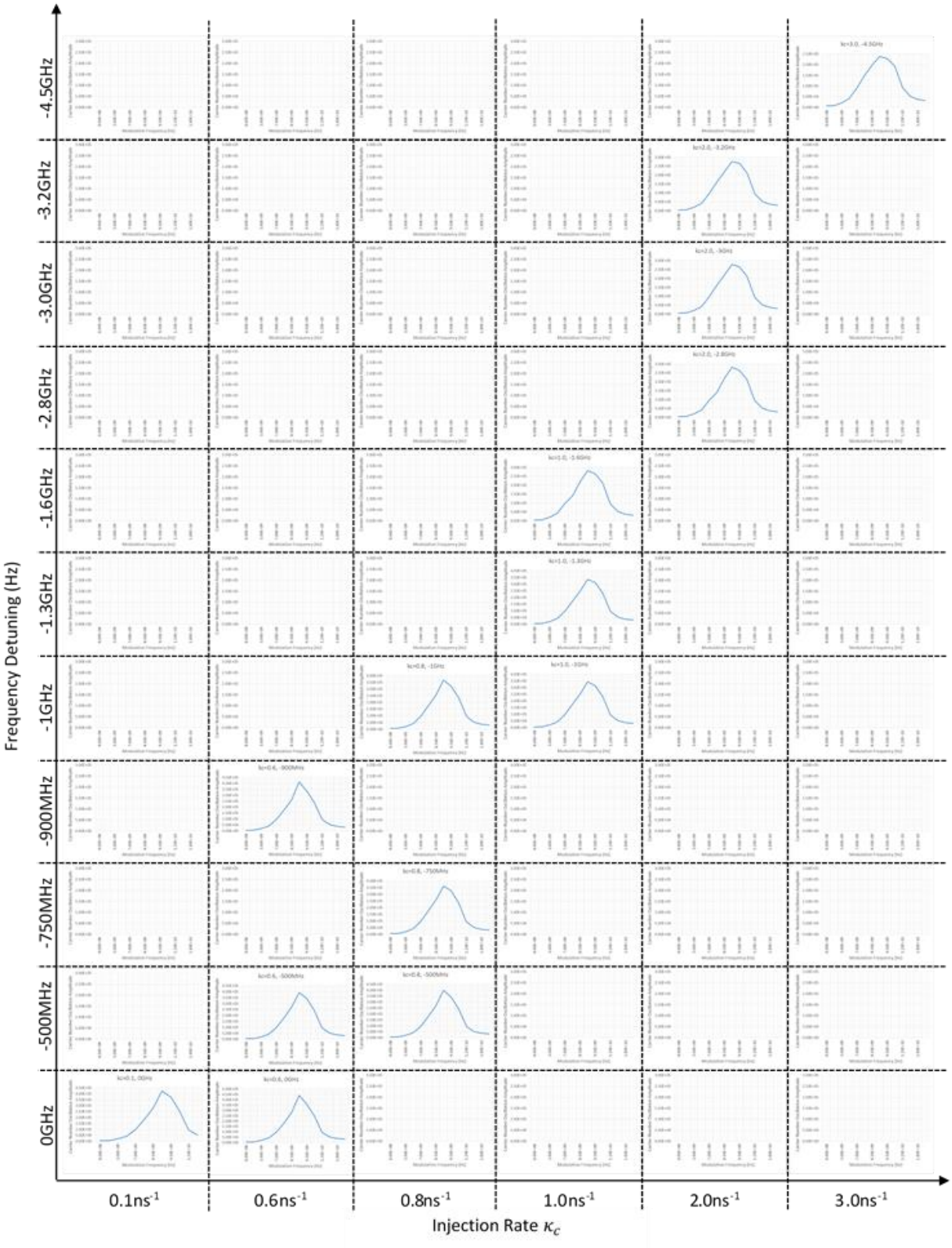

Figure 7.7: *Mesh plot of the amplitude of the uncoupled laser and resulting waves with modulation frequencies between 10MHz and 20GHz for injection rates of 0.1ns^{-1}, 0.6ns^{-1}, 1.0ns^{-1}, 2.0ns^{-1} and 3.0ns^{-1} and detuning frequencies between 0GHz and -4.5GHz. It can be seen that the higher the injection rate and frequency detuning value, the lower the amplitude of the carrier oscillations.*

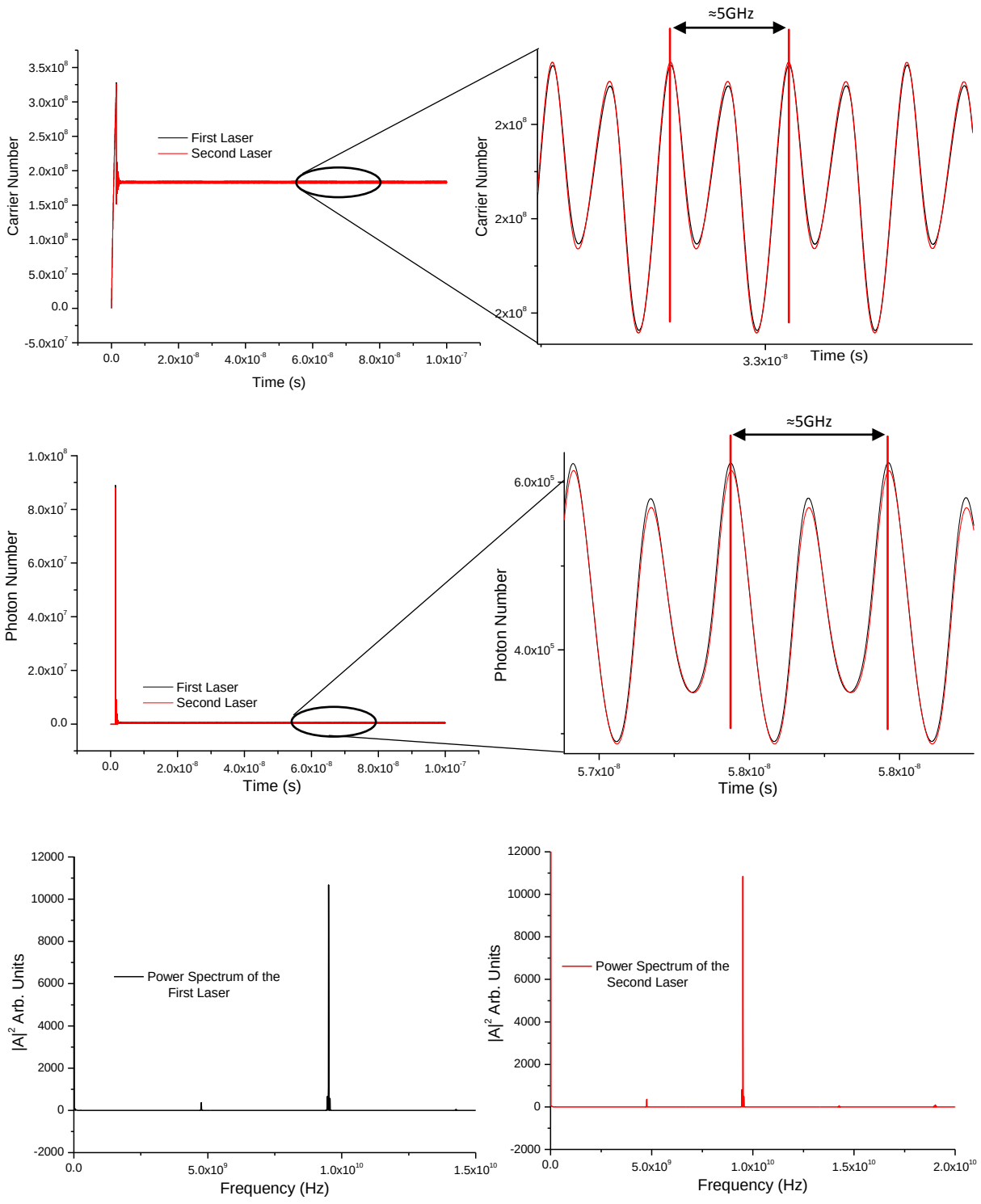

Figure 7.8: *Carrier (top figure) and photon (middle figure) number output with an injection rate, κ_c, of 3.0ns^{-1} with a frequency detuning, Δf, of -4.6GHz and a modulation frequency of 50MHz – The carrier and photon number outputs are oscillating periodically, where the waveforms appear to contain two harmonics oscillating at ≈5GHz. The bottom graph shows the photon number plotted on an FFT, and this confirms the multiple harmonics seen in the photon number plot.*

It can be seen here that the oscillations are periodic (oscillating at approximately 5GHz; very similar in frequency to that of figure 6.11 (a)) and clearly have potentially more than one harmonic, just like was seen in figure 6.11 (a). It should be noted that this only happened at an injection rate of $3.0ns^{-1}$, with modulation frequencies of less than 50MHz. In order to confirm the potential multiple harmonics, the photon outputs for both lasers were plotted on FFT plots, using the hamming window setting, with the DC component removed for clarity. It is clear to see the additional harmonics present in the spectrum while operating in this condition.

It is clear from the results of figure 7.7, that the more the injection rate and detuning frequency of the system are increased, the more the system will suppress the introduced perturbations, hence improving the performance of the system. It can be seen that the system significantly suppresses the perturbations with an injection rate of $3.0ns^{-1}$ and a frequency detuning of -4.5GHz, and this point is the final point that locking was observed in figures 6.6 and 6.7 from chapter six (as mentioned previously, outside of this locking region, no other locking points were observed).

It generally appears as though the system shows a gradual improvement in performance over the uncoupled laser the more the injection rate and detuning frequency are increased, however there is an exception to this case. From figure 7.7, it can be seen that with an injection rate of $0.6ns^{-1}$ and a detuning frequency of 0GHz, the response of the system is slightly worse compared to the uncoupled laser, hence suggesting that the system increases the amplitude of the perturbations, rather than suppressing them. This appears to be the only case where the response of the three laser FWM scheme is worse than the uncoupled case for the observed injection rates and detuning frequencies.

To see a more accurate response, the results of figure 7.7 are plotted on Bode plots, and these can be seen in figure 7.9 (a)-(c). From the Bode plots, it can be seen that when there is an injection rate of $0.1ns^{-1}$ and a frequency detuning of 0GHz, the response seems identical to that of the uncoupled laser, thus suggesting very little, or no improvement in performance with the three laser FWM scheme. When the injection rate is increased to $3.0ns^{-1}$ with a frequency detuning of -4.5GHz however, there is a slight reduction in the response in the frequency range, thus suggesting an improvement in the response of the system. Figure 7.10 shows the Bode plots for all the injection rates and frequency detuning values used to give a broader view of how the system changes with an increase in injection rate values. The uncoupled laser has been included in this plot for comparison.

Again, as was seen in figure 7.7, it can clearly be seen that the more the injection rate is increased, the more the system suppresses the response, thus suggesting an overall performance improvement compared to the uncoupled laser. It can again be seen that at an injection rate of $3.0ns^{-1}$ and a frequency detuning of -4.5GHz gives the best overall performance, just as was seen in figure 7.7.

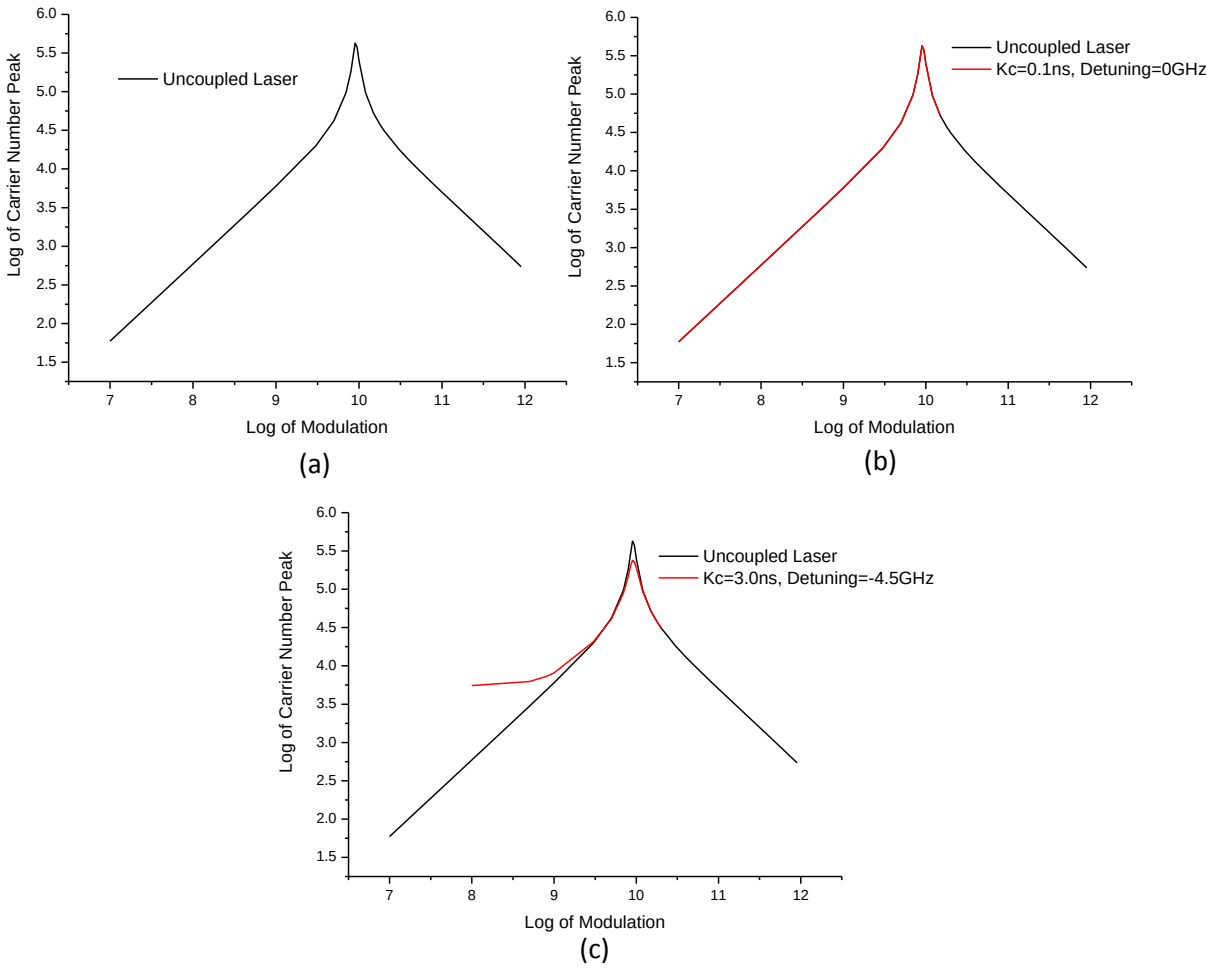

Figure 7.9: *Bode plots of the carrier output amplitude and modulation frequency for (a): The uncoupled laser; (b): The uncoupled laser plotted with an injection rate of 0.1ns^{-1} and a frequency detuning of 0GHz; and (c): The uncoupled laser plotted with an injection rate of 3.0ns^{-1} and a frequency detuning of -4.5GHz.*

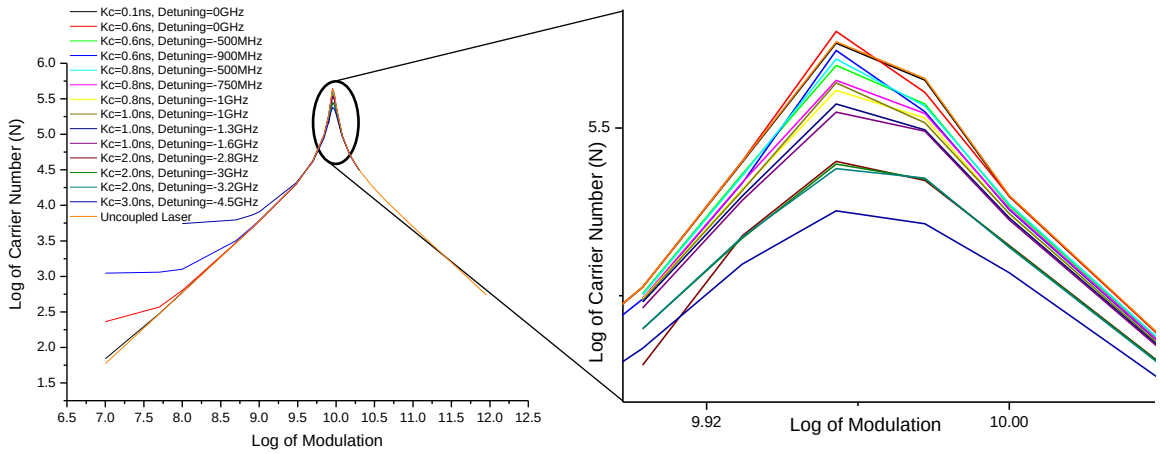

Figure 7.10: *Bode plots of the carrier output amplitude and modulation frequency for the uncoupled laser and for injection rates of 0.1ns^{-1}, 0.6ns^{-1}, 1.0ns^{-1}, 2.0ns^{-1} and 3.0ns^{-1} and detuning frequencies between 0GHz and -4.5GHz.*

7.4 – Percentage Improvement over the Uncoupled Laser

The improvement in the response of the system to an increasing injection rate over the uncoupled laser will now be quantified. To do this, the percentage improvement of the resulting phasor amplitude relative to the uncoupled laser is compared. This is defined by equation 7.2 and a table of the results can be found in table 7.2.

$$\%\ Improvement = \frac{(Uncoupled\ Amplitude) - (N_1 - N_2\ Amplitude)}{Uncoupled\ Laser\ Amplitude} \times 100 \qquad (7.2)$$

From the results of table 7.2, there is a clear trend where the more the injection rate is increased, the more improvement can be seen in the performance of the system, where an injection rate of 3.0ns^{-1} and frequency detuning of -4.5GHz gives the greatest improvement of almost 45% relative to the uncoupled laser, hence showing a significant reduction in the introduced perturbations. It can be seen that between the injection rates of 0.1ns^{-1} with a frequency detuning of 0GHz, to an injection rate of 0.6ns^{-1} with a frequency detuning of -900MHz, the system shows a gradual improvement of between 0.6% and 10.4%, but when the injection rate is increased to 0.8ns^{-1} with an injection rate of -500MHz, there is a slight decrease in improvement, with the percentage falling very slightly to 9%, before increasing once more through to an injection rate of 0.8ns^{-1} with a frequency detuning of -1GHz where there is an improvement of 15.3%. There is again a slight fall off in improvement for an injection rate of 1.0ns^{-1} and a frequency detuning of -1GHz, where the percentage again falls very slightly, to a value of 14.1%, before again increasing once more through to an injection rate of 1.0ns^{-1} and a frequency detuning of -1.6GHz, where there is an improvement of 21.5%. There is a very steep increase in improvement from 1.0ns^{-1} with a frequency detuning of -1.6GHz to an injection rate of 2.0ns^{-1} with a frequency detuning of -2.8GHz, where the improvement increases to 33.6%, and will then continually increase through to an injection rate of 3.0ns^{-1} with a frequency detuning of -4.5GHz, where the biggest percentage improvement of 44.1% can be seen.

It is clear from these results, that the more the injection rate is increased, the better the system is at suppressing the perturbations that have been introduced into the system, and that the best location for this is at an injection rate of 3.0ns^{-1} and a frequency detuning of -4.5GHz; and this point is the single locking region point in figures 6.6 & 6.7 before synchronisation between the two lasers is lost. If the injection rate was increased further, no further locking regions would be observed, unlike the case for conventional injection locking observed in chapter five. As previously discussed, the more the injection rate was increased, the smaller the locking range would become after 0.6ns^{-1}, before tapering off to a single point at an injection rate of 3.0ns^{-1} and a detuning frequency of -4.5GHz, this would therefore suggest that the optimum operating region for this system would be at this point.

Injection Rate, κ_c	Frequency Detuning (Hz)	Percentage Improvement
0.1ns^{-1}	0GHz	0.59%
0.6ns^{-1}	0GHz	4.69%
0.6ns^{-1}	-500MHz	8.38%
0.6ns^{-1}	-900MHz	10.36%
0.8ns^{-1}	-500MHz	9.03%
0.8ns^{-1}	-750MHz	12.37%
0.8ns^{-1}	-1GHz	15.31%
1.0ns^{-1}	-1GHz	14.11%
1.0ns^{-1}	-1.3GHz	19.22%
1.0ns^{-1}	-1.6GHz	21.46%
2.0ns^{-1}	-2.8GHz	33.64%
2.0ns^{-1}	-3GHz	34.26%
2.0ns^{-1}	-3.2GHz	35.30%
3.0ns^{-1}	-4.5GHz	44.06%

Table 7.2: *Percentage improvement of the resulting phasor compared to the uncoupled laser for injection rates of 0.1ns^{-1}, 0.6ns^{-1}, 1.0ns^{-1}, 2.0ns^{-1} and 3.0ns^{-1} and detuning frequencies between 0GHz and -4.5GHz. The optimal locking point is at an injection rate of 3.0ns^{-1} with a detuning frequency of -4.5GHz where the system shows an improvement of 44.06% over the uncoupled laser.*

7.5 – Summary and Conclusion

This chapter has built on the work of chapters five and six in order to establish a conclusion on the overall performance of the three laser FWM system under consideration. In order to do this, perturbations were introduced to the first laser in order to investigate the system's modulation response when perturbations are introduced to the system compared to the uncoupled laser.

A clear result from the analysis is that with a low modulation frequency (~10MHz), the first and the second laser's oscillations would be out of phase with each other, where the second laser would lead the oscillations of the first laser by approximately 180°. When the modulation frequency had been increased to ~3GHz, the system had gone through a 90° change of phase, whereby the second laser was still leading the first laser oscillations. This is consistent with a first order system. When the modulation frequency had been increased to ~9GHz, both the first and second lasers' oscillations were completely in phase. As the modulation frequency was increased to ~12GHz, the second laser

would now be lagging the first laser oscillations by approximately -90°. The change in phase from 90° to -90° (180° change of phase) is now consistent with a second order system; the whole three laser FWM system under consideration is therefore behaving like a first order system in series with a second order system. This is consistent no matter what the injection rate used.

In order to establish whether or not the three laser FWM system provided a performance improvement over the uncoupled laser, the phasor difference between the first and the second lasers' amplitudes was calculated in order to find the resultant waveform. This was then compared to the uncoupled laser amplitude. What was clear from the results is that the more the injection rate and detuning frequency was increased, the more the three laser FWM system would supress the introduced perturbations, thus improving the performance of the system.

From the results, it generally appears as though the three laser FWM system shows a gradual improvement in performance over the uncoupled laser as the injection rates and detuning frequency are increased, however, there is an exception to this, with an injection rate of $0.6ns^{-1}$ and a detuning frequency of 0GHz, where the amplitude of the resultant wave is slightly worse when compared to the uncoupled laser, hence suggesting that the three laser FWM system increases the amplitude of the perturbations here, rather than suppressing them.

The final part of analysis for the three laser FWM system was to investigate, as a percentage, how much the three laser FWM supresses the introduced perturbations, and to identify if there was an optimal locking point present in the system. As was seen in the results, the percentage improvement would increase the more the injection rate was increased, and an optimal locking point was found where the three laser FWM reduces the introduced perturbations by 44.1%, hence it is possible to conclude that the single optimal locking is with an injection rate of $3.0ns^{-1}$ and a frequency detuning of -4.5GHz. A further increase in injection rate and detuning frequency resulted in a loss of synchronisation between the lasers.

As a final conclusion, and as an advantage over the injection locking scheme, in the locked condition here, there is a nonzero frequency spacing between the first and the second lasers' frequency in the locked condition, as opposed to a zero frequency separation in the injection locking scheme, thus providing the foundation for generating a frequency spacing within the THz frequency range.

REFERENCES

[1] **M. Zanola**, M. J. Strain, G. Giuliani, M. Sorel, “Monolithically integrated DFB lasers for tunable and narrow linewidth millimeter-wave generation”, IEEE J. Quantum Electron., vol. 19, no. 4, Paper ID. 1500406, Jul/Aug. 2013.

[2] **L. A. Coldren**, S. W. Corzine, Chapter 2 in Diode Lasers and Photonic Integrated Circuits, Wiley, New York, pp.200-201, 1995.

CHAPTER EIGHT

CONCLUSIONS AND FUTURE WORK

This work has been devoted to the exploration of potential schemes for realising terahertz radiation. Three different methods have been discussed within this thesis, (with one of these methods providing a stepping stone for one of the other considered methods); these include the dual-wavelength VECSEL, where the wavelength separation would lie within the THz range, the injection locking scheme, investigating both unidirectional and bidirectional injection locking, and the scheme of four-wave mixing (FWM), whereby two distributed-feedback lasers (DFB) are injected into a third, auxiliary, DFB where the FWM process generates two new conjugate FWM signals that are clones of DFB1 and DFB2. The proposal in the future would be to then shine the output from both the dual-wavelength laser device and the FWM scheme onto a photoconductive antenna (PCA) [1]-[6] with the potential of generating THz radiation, where the author has already looked in detail at the mathematical approach employed by Saeedkia *et al*. to describe the physical phenomena that are apparent in a typical photoconductive photomixing scheme from [1], where two linearly polarized laser beams, whose difference in central frequencies falls within the THz spectrum, are applied to a DC biased photoconductor film.

The previously proposed dual-wavelength VECSEL [7] had a large wavelength separation (58nm, 16.97THz), and the work in this thesis explored the possibility of reducing this spacing down to 5nm (1.54THz) in order to potentially improve the performance of the device. In addition, the locations of the quantum-wells (QW) were improved in order to reduce the cross-absorption of the short wavelength light in the deep QWs. In addition, the effect of linewidth broadening was explored as a potential constraint in the design of dual-wavelength VECSELs, paying particular attention to calculations of the Schawlow-Townes [8] linewidth for both structures.

The final chapters of this work investigated laser injection locking and the FWM scheme. The injection locking schemes investigated in chapter five investigated both unidirectional and bidirectional injection locking in order to provide the building blocks for the three laser FWM system presented in chapters six and seven.

The previous work [9] proposed a monolithically integrated DFB which would generate narrow linewidth, millimetre-waves. Here, simulations were carried out in order to explore the locking regions present in such a device with varying injection rates, detuning frequency values, and modulation frequencies, which had not been conducted before. The benefit to the FWM scheme over the injection

locking approach is the fact that in the locked condition, there is a nonzero frequency separation between the first and the second lasers' in the locked condition, enabling the potential to generate a frequency spacing between the two in the THz range. As previously mentioned, the proposal is to then shine the output from this scheme onto a PCA in order to generate THz radiation.

8.1 – Conclusions

This thesis work proposes two new schemes for generating THz radiation; the dual-wavelength VECSEL, and the four-wave mixing (FWM) scheme. The contributions to the dual-wavelength VECSEL are detailed in chapters two to four. Chapter two details the contribution made to the design of a new dual-wavelength VECSEL inspired by Leinonen *et al* [7]; this was undertaken with a view of improving the performance of the device. Leinonen *et al*. proposed a device with a short wavelength, λ_S, of 984nm and a long wavelength, λ_L, of 1042nm, hence giving a wavelength separation of 58nm; this translates to a frequency spacing of 16.97THz. During the course of their work, Leinonen *et al*. reported that their VECSEL device would emit coherent, continuous wave light at both λ_L and λ_S up to a pump power of 2.4W, where several distinct lines were visible in the emission spectrum. However, beyond 2.4W of pump power, the VECSEL would begin to show signs of self-pulsation, where the sinusoidal component of the long and short wavelength pulse components were in strong phase correlation, riding on top of the CW components. Leinonen *et al*. suggested that this may be due to the Q-switching of the short wavelength component by residual absorption in the deep QWs, which are not actually located exactly at the nodes of the short wavelength standing wave pattern. This led to the proposal of significantly reducing the wavelength separation from 58nm down to 5nm (1.54THz), and re-positioning the QWs in order to reduce the effect of cross-absorption of the short wavelength light in the deep QWs. The main conclusions from this work are as follows:

1. A structure has been proposed to generate dual-wavelength emission with greatly reduced wavelength separation to that reported by Leinonen *et al*., reducing the wavelength separation from 58nm down to 5nm, which translates to 1.54THz in frequency separation.
2. In addition to the reduced wavelength separation, the locations of the QWs have been improved in order to reduce the cross-absorption of the short wavelength light in the deep QWs. In reducing the separation between λ_S and λ_L, and by improving the positions of the QWs, the newly designed structure has also been designed to yield much smaller overlap values between λ_S, λ_L and the corresponding QWs in both the long and short wavelength active regions.

3. Reducing the overlap should improve the performance of the VECSEL structure, allowing the VECSEL to operate at higher pumping levels, hence suggesting a reduction in the effect of self-pulsation having reduced the residual absorption in the deep QWs.

It should be noted that in the design of the dual-wavelength VECSEL, it has been assumed that there are no effects due to carrier density, and as such there will be no effect of refractive index changes due to carrier density, and hence a so called 'cold cavity' response has been assumed. As such, the assumptions made here may give rise to limitations on the final utility of the results.

The effect that must be carefully considered in a dual-wavelength VECSEL when two wavelengths are close together (only 5nm (1.54THz) apart in this case), is linewidth broadening. When the separation between the two wavelengths are so close, it is possible that only one broad peak will appear in the lasing spectrum of the laser, rather than two narrow peaks, hence this effect must be carefully considered.

Chapter three went into detail on the derivations for the linewidths of laser lines, paying particular attention to the work of Schawlow and Townes [8], and how the Schawlow-Townes linewidth derivation was modified by Melvin Lax [10], and enhanced by Charles Henry [11]. In their work, they discovered that the linewidth of a laser line will occur as a result of the fluctuations in phase at the output of the optical field. These fluctuations occur as a result of either spontaneous emission, or carrier density fluctuations.

The modified Schawlow-Townes linewidth equation was applied to the original dual-wavelength VECSEL structure by Leinonen *et al*. and to the newly designed VECSEL structure proposed in chapter two. This was undertaken in order to establish a fundamental limit on how close the two wavelengths may be together in a dual-wavelength VECSEL before only one broad peak will be apparent in the spectrum, rather than two narrow peaks defining the two individual wavelengths.

This was discussed in chapter four, and the main conclusions from this work are as follows:

1. A model of a dual-wavelength VECSEL was simulated in FORTRAN (the code for which can be found in Appendix B) in order to establish the linewidths of both λ_S and λ_L in the original and new VECSEL structure designs.
2. The structures were simulated with the calculated overlap percentages, and through this, the steady-state values for the carrier and photon densities were obtained in order to calculate the Schawlow-Townes linewidth for both structures.
3. The linewidth for λ_S stayed the same for both structures, at a value of 7.669MHz; this is due to the fact that no light is being injected from λ_L into λ_S, only the converse

(unidirectional injection). The linewidth for λ_L reduced from 6.45MHz to 4.88MHz for increasing overlap percentages from 19.45% to 82.05% in the original VECSEL structure, whereas λ_L only reduced from 6.65MHz down to 6.48MHz for increasing overlap percentages from 15.305% to 18.768% for the newly designed VECSEL structure.

4. In order to establish a fundamental limit on the wavelength separation in the dual-wavelength VECSEL, the frequency linewidths (MHz) needed to be converted into wavelength linewidths (nm). The calculations showed that λ_S never changed from 0.02pm, whereas λ_L was calculated as 0.017pm for the original VECSEL structure, and 0.021pm for the new VECSEL structure design.
5. As these values are so close to zero, it would seem apparent that there is no limit due to the Schawlow-Townes linewidth for the minimal separation between the two wavelength values where it would not be possible to see two resolved lines in the spectrum; hence, the linewidth does not appear to be a limiting factor in the design of a dual-wavelength VECSEL.
6. A limiting factor in the design of a dual-wavelength VECSEL could be the molar compositions of the QWs. As discussed in chapter two, an approximation for the molar compositions for the shallow and deep QWs would be $In_{0.17}Ga_{0.83}As$ and $In_{0.18}Ga_{0.82}As$ respectively for the newly designed structure (compared with $In_{0.17}Ga_{0.83}As$ and $In_{0.23}Ga_{0.77}As$ for the original structure). Further work would have to be conducted in order to establish whether or not such a device could be constructed with such similar molar compositions for the shallow and deep QWs.

The results and conclusions of the work from chapters two through to four would allow the design of a dual-wavelength VECSEL with a minimum separation of 5nm (1.54THz) between the two wavelengths, with the ultimate goal of realizing terahertz radiation. As mentioned previously, a future potential field of work would be the possibility of shining the output from a dual-wavelength laser onto a PCA [1]-[6].

Chapter five looked at the laser injection locking scheme as another potential method of realising THz radiation, which would prove the building blocks for the three laser FWM system presented in chapters six and seven.

Chapter five looked in detail at the injection locking scheme, investigating both unidirectional and bidirectional injection locking. Both schemes employed a two laser configuration; for unidirectional injection locking, a fraction of the light from the first laser was injected into the cavity of the second

laser, and for bidirectional injection locking, a fraction of the light from the second laser was also injected into the cavity of the first laser. Here, the various locking regions and behaviours of both schemes was explored in detail. The work in chapter five was modelled in FORTRAN based upon the rate equations from the work of Peters-Flynn *et al*. [12], [13]. It should be noted that everything in the model was kept identical, except for the wavelength. This was justifiable in this work as this chapter served as a 'building block' for the work presented in chapters six and seven. In practice, the gains etc. would not be identical for both lasers. The main conclusions from this work are as follows:

1. In both schemes, four distinct behavioural regions are present; firstly, where the lasers' carrier and photon output response would oscillate periodically, secondly where a potentially chaotic behaviour was present in the carriers and photons output response, thirdly where a locked condition was observed, whereby the carriers and photons in both the first and the second lasers' would settle to a constant value (with no oscillations), and finally, the unlocked condition whereby the carriers and photons would simply oscillate at a beat frequency of the same value as the detuning frequency.
2. For the unidirectional locking scheme, the locking region was highly asymmetrical, as a result of the linewidth enhancement factor, α, and also due to the singular direction of detuning frequency which was only applied to the second laser in this scheme.
3. For the bidirectional scheme, the locking region was highly symmetrical, as a result of the bidirectional detuning frequencies set to $+\Delta\omega$ in the second laser and $-\Delta\omega$ in the first laser.
4. In the unidirectional injection locking scheme where periodicity was apparent, these regions would often exhibit more than one harmonic in the carriers' and photons output oscillations response. In addition, these oscillations seemed to be unrelated to the detuning frequency value. These potential additional harmonics were confirmed from FFT plots of the photons output.
5. In the bidirectional scheme, in the regions of periodicity, only a single harmonic would be present in the carriers' and photons output response, but again, they would oscillate at a frequency unrelated to the detuning frequency. Again, this single harmonic was confirmed in the FFT plot.
6. For both the unidirectional and bidirectional injection locking schemes, when operating outside of the locking regions, the second lasers' carriers and photons (for the case of unidirectional injection locking) and the second laser and first lasers' carriers and photons (for the case of bidirectional injection locking) would simply oscillate at a beat frequency

of the same value as the detuning frequency; this indicated that both schemes were operating outside of the locking region.

7. Both schemes exhibited a potential chaotic behaviour, where the carrier's and photons output response would oscillate in a potential chaotic manner. In these regions, multiple harmonics were apparent, again oscillating at a frequency unrelated to the detuning frequency. In the case of unidirectional injection locking, multiple regions of potential chaotic behaviour were observed at each injection rate, excluding an injection rate of $90ns^{-1}$. However, with the bidirectional injection locking scheme, only two chaotic regions were observed at $30ns^{-1}$ and $80ns^{-1}$. Again, this potential chaotic behaviour was confirmed from FFT plots of the photons output.
8. Both schemes exhibited the injection locked condition, whereby both the first and second lasers would settle to a constant steady-state value after the relaxation oscillations. In the unidirectional scheme, the carriers in the second laser would settle to a different steady-state value than the first laser. This was expected due to the fact that the first laser light is being injected into the cavity of the second laser, causing an increase in photons in the cavity of the second laser. As a consequence, the carriers in the cavity of the second laser would decrease. In the bidirectional scheme, the first and the second lasers' carriers would settle to the exact same value of steady-state carriers. This is again to be expected due to the fact that the light from the first laser is being injected into the cavity of the second laser, and vice-versa.
9. The locking regions in both schemes would increase as the injection rate was increased, with the widest locking regions observed at $90ns^{-1}$ for both schemes.
10. As a result of the bidirectional scheme, and due to the fact that both the first and second lasers' carriers and photons settle to the same steady-state value, the locked condition will always give a zero frequency separation between the two locked lasers.

A clear disadvantage to the injection locking scheme is the zero frequency separation between the first and second laser in the locked condition. As a result, the work on injection locking provides the building blocks for the three laser FWM system presented in chapters six and seven, whereby a nonzero frequency separation between the lasers' in the locked condition is required, where the difference in the frequency separation lies within the THz frequency range.

Chapters six and seven investigated the FWM scheme, whereby two distributed-feedback lasers are injected into a third, auxiliary, DFB where the FWM process generated two new conjugate FWM

signals; these are clones of DFB1 and DFB2. These clones are then injected back into the original signals where the locking takes place. Similar to chapter five, the locking regions and behaviours were investigated and an optimal locking region was proposed.

Chapter six provided a significant contribution to modelling a three laser FWM system, utilising the injection locking scheme, as a potential method for realising THz radiation. The work was based on the work of Zanola *et al*. [9], and the work was modelled in FORTRAN, again based on an evolution of the rate equations from the work of Peters-Flynn *et al*. [12], [13]. The main conclusions from this work are as follows:

1. In this scheme, there are five distinct regions of behaviour present in the system. Firstly, a region of periodicity in the carriers' and photons output, where at certain points, the periodicity would exhibit additional harmonics at the troughs of the carrier output, and at the peaks of the photon output of the waveforms. Secondly, an area where the carriers and photons would oscillate as an undistorted sine wave at the same frequency as the relaxation oscillation frequency. Thirdly, a potential chaotic behaviour similar to that observed in chapter five. The fourth area was where the carriers and photons would oscillate with potential multiple harmonics in the response, and finally, where the carriers and the photons of the first and second lasers would settle to a constant stead-state value, representing the locked condition.
2. The additional harmonics were investigated further with FFT plots of the photons outputs, and it was found that even though multiple oscillations were apparent in the response of the photons, these did not translate into multiple harmonics in the power spectrum. The only exception to this was when the system exhibited a potential chaotic behaviour, and when the carriers and photons were clearly oscillating periodically with varying oscillations.
3. The locking condition was observed for much lower injection rates than those observed in the injection locking scheme.
4. The locking region was highly symmetrical for injection rates between $0.1ns^{-1}$ and $0.6ns^{-1}$, similar to that observed with bidirectional injection locking, and between $0.7ns^{-1}$ and $8.0ns^{-1}$ the locking region became highly symmetrical, as per unidirectional injection locking.
5. In the symmetrical region, the locking condition would increase in width, however, in the asymmetrical region, the locking region would gradually taper off as the injection rate

increased to just a single point as an injection rate of 3.0ns^{-1} and a frequency detuning of -4.5GHz.

6. In the locked condition, the carriers and photons for both the first and the second lasers would settle to a constant steady-state value, whereby there was a nonzero frequency separation between them.

In order to establish whether or not the three laser FWM system under consideration holds a performance advantage over an uncoupled laser, chapter seven introduced perturbations to the first laser, and hence investigated the modulation response of the three laser FWM system. From this, the phasor difference between the first and the second lasers was calculated in order to find the resultant waveform. The amplitude of his resultant wave was then compared to the amplitude of the uncoupled laser in order to establish whether or not the three laser FWM system supresses any of the introduced perturbations. The main conclusions from this work are as follows:

1. In terms of the phase changes between the first and the second lasers' oscillations, for low modulation frequencies (~10MHz), the second laser would lead the first laser oscillations by 180°. When increasing the modulation frequency to ~3GHz, the second laser would lead the first lasers' oscillations by 90°, thus showing that the system had gone through a phase change of 90°; this response is consistent with a first order system.
2. When increasing the modulation frequency to ~12GHz, the second laser would now be lagging the first laser oscillations by approximately -90°, thus showing that the system had now gone through a phase change of 180°; this is now consistent with a second order system.
3. The phasor difference between the first and the second lasers' amplitudes was calculated and compared to the uncoupled lasers amplitude in order to see whether or not the three laser FWM system suppresses any of the introduced perturbations.
4. The more the injection rate was increased, the more the three laser FWM system would supress the introduced perturbations, thus improving the performance of the system up to a maximum injection rate of 3ns^{-1} and a detuning frequency of -4.5GHz. With injection rates above 3.0ns^{-1}, no further locking regions were observed.
5. As a percentage improvement, for an injection rate of 3.0ns^{-1} and detuning frequency of -4.5GHz, the three laser FWM system showed a 44.1% improvement over the uncoupled laser, and this corresponds to the optimal operating point for this system.

As a closing conclusion here, the three laser FWM system has an overall advantage over the injection locking scheme as there is a nonzero frequency difference between the first and the second lasers frequency while operating in the locked condition. This provides a foundation for generating a frequency spacing within the THz frequency range.

As previously discussed, the output from the scheme could potentially be injected onto a photoconductive antenna (PCA) [1]-[6], whereby THz radiation may be produced.

8.2 – Original Contributions

This thesis incudes several original contributions. Firstly, a new VECSEL structure has been proposed to generate dual-wavelength emission with greatly reduced wavelength separation to that reported by Leinonen *et al*. [7] and reduced cross-absorption of the short wavelength light in the deep QWs. This has the potential to improve the performance of the VECSEL, allowing the laser to operate at higher pumping power levels.

Secondly, the injection locking scheme has been investigated in detail, paying particular attention to the unidirectional and bidirectional injection locking schemes. In both schemes, the locking regions have been thoroughly investigated, and the different behaviours of both systems at numerous injection rates and detuning frequencies has been explored, which has not previously been conducted in such detail. It is important to understand and investigate the scheme of injection locking as it provided the foundation for the three laser FWM system.

A three laser FWM system was modelled, utilising the injection locking scheme, in order to produce a nonzero frequency difference between the first and the second laser. For the first time, a thorough investigation of the locking regions was undertaken at varying injection rates and detuning frequencies, exploring the different behaviours the system exhibited in each region.

A thorough investigation was also undertaken on the resilience of the new three laser FWM system to introduced perturbations. In this work, the phase and frequency response of the system was investigated in detail and it was found that the three laser FWM scheme improved the overall performance of the system over the uncoupled laser.

8.3 – Proposals for Future Work

There are numerous areas of future research arising from this work which should be pursued.

Firstly, arising from the work of chapters two to four, a physical dual-wavelength VECSEL device and system may be built based on the calculated parameters, in order to establish whether there are any performance enhancements in the new VECSEL structure design compared to the original VECSEL structure proposed by Leinonen *et al*.; namely, when operating above 2.4W of pump power, has the

new VECSEL structure design successfully suppressed any of the effects of self-pulsation above this power, or have other phenomena come into play that have been overlooked. Also, does the newly designed VECSEL structure emit two resolved lines in the lasing spectrum, corresponding to each of the emitting wavelengths.

Another consideration that should be investigated are the percentages of molar compositions for the shallow and deep QWs. In the proposed new structure design, the molar compositions are required to be very similar to each other, which could be a cause for concern for constructing such a dual-wavelength VECSEL.

Arising from this is the possibility of simulating, and experimentally shining the output from the dual-wavelength laser onto a photoconductive antenna (PCA), with the potential of generating THz radiation.

It would also be of great interest to investigate the work of Belkin *et al*. [14], and Razeghi *et al*. [15], [16] whereby they have developed monolithic THz sources based on the difference-frequency generation.

Following on from the work of chapters six and seven, it would be beneficial to investigate the behaviour of the three laser FWM system when a change in current is introduced to the first laser after settling to the steady-state to see how this would affect the second laser, i.e. would the second laser follow the frequency of the first laser, or do something different.

Another consideration could be the construction of a monolithic FWM device, similar to that of Zanola *et al*. [9] in order to conduct real-world experiments to see how the results compare to those of the simulations. Also, similar to the consideration for the dual-wavelength laser is the possibility of simulating and experimentally shining the output from the FWM scheme onto a PCA with the potential of generating THZ radiation.

A final consideration would be the construction of a system with three separate devices in order to compare the performance to that of the deice by Zanola *et al*., and to compare the behavioural patterns to what was observed in the three laser FWM system considered in this thesis.

REFERENCES

[1] **D. Saeedkia**, R. R. Mansour, S. Safavi-Naeini, "The interaction of laser and photoconductor in a continuous-wave terahertz photomixer", IEEE J. Quantum Electron., vol. 41, no. 9, pp. 1188-1196, Sept. 2005.

[2] **D. Saeedkia**, R. R. Mansour, S. Safavi-Naeini, "Analysis and design of a continuous-wave terahertz photoconductive photomixer array source", IEEE Trans. Ant and Prop., vol. 53, no. 12, pp. 4044-4050, Dec. 2005.

[3] **D. Saeedkia**, A. H. Majedi, S. Safavi-Naeini, R. R. Mansour, "Analysis and design of a photoconductive integrated photomixer/antenna for terahertz applications", IEEE J. Quantum Electron., vol. 41, no. 2, pp. 234-241, Feb. 2005.

[4] **D. Saeedkia**, A. H. Majedi, S. Safavi-Naeini, "CW photoconductive photomixer/antenna array source for THz applications", Proc. IEEE Micro. Photon. Conf., Oct. 2004, pp. 317-320.

[5] **D. Saeedkia**, S. Safavi-Naeoni, "A comprehensive model for photomixing in ultrafast photoconductors", IEEE Photon Technol Lett., vol. 18, no. 13, pp. 1457-1459, Jul. 2006.

[6] **D. Saeedkia**, A. H. Majedi, S. Safavi-Naeini, R. R. Mansour, "High-temperature superconductive photomixer patch antenna: Theory and design", IEICE Trans. Electron., vol. E86-C, no. 7, pp. 1318-1327, Jul. 2003.

[7] **T. Leinonen**, Y. A. Morozov, A. Härkönen, M. Pessa, "Vertical external-cavity surface-emitting laser for dual-wavelength generation", IEEE Photon. Technol. Lett., vol. 17, no. 12, pp. 2508-2510, Dec. 2005.

[8] **A. L. Schawlow**, C. H. Townes, "Infrared and optical masers", Phys. Rev., vol. 112, no. 6, pp. 1940-1949, Dec. 1958.

[9] **M. Zanola**, M. J. Strain, G. Giuliani, M. Sorel, "Monolithically integrated DFB lasers for tunable and narrow linewidth millimeter-wave generation", IEEE J. Quantum Electron., vol. 19, no. 4, Paper ID. 1500406, Jul/Aug. 2013.

[10] **M. Lax**, "Classical noise V. Noise in self-sustained oscillators", Phys. Rev., vol. 160, no. 2 p. 290, Aug. 1967.

[11] **C. H. Henry**, "Theory of the linewidth of semiconductor lasers", IEEE J. Quantum Electron., vol. 18, no. 2, pp. 259-264, Feb 1982.

[12] **S. Peters-Flynn**, P. S. Spencer, S. Sivaprakasam, I. Pierce, K. A. Shore, "Identification of the optimum time-delay for chaos synchronization regimes of semiconductor lasers", IEEE J. Quantum Electron., vol. 42, no. 4, pp. 427-434, Apr. 2006.

[13] **S. Peters-Flynn**, I. Pierce, P. S. Spencer, P. Rees, "Synchronisation recovery in unidirectionally coupled semiconductor lasers", IEE Proc. Optoelectron., vol. 153, no. 1, pp. 8-12, Feb. 2006.

[14] **K. Vijayraghavan**, M. Jang, A. Jiang, X. Wang, M. Troccoli, M. A. Belkin, "THz difference-frequency generation in MOVPE-Grown quantum cascade lasers", IEEE Photon. Technol. Lett., vol. 26, no. 4, pp. 391-394, Feb. 2014.

[15] **Q. Y. Lu**, N. Bandyopadhyay, S. Slivken, Y. Bai, M. Razeghi, "Continuous operation of a monolithic semiconductor terahertz source at room temperature", Appl. Phys. Lett., vol. 104, no. 22, pp. 221105-1 – 221105-5, Jun. 2014.

[16] **Q. Y. Lu**, S. Slivken, N. Bandyopadgyay, Y. Bai, M. Razeghi, "Widely tunable room temperature semiconductor terahertz source", Appl. Phys. Lett., vol. 105, no. 20, pp. 201102-1 – 201102-5, Nov. 2014.

APPENDIX A

PUBLICATIONS AND CONFERENCE CONTRIBUTIONS

The following is a list of journal papers (accepted for publication by the journals), and conference papers (presented and accepted) that have arisen from the work in this thesis.

1. **Journal Papers**
    - Daniel Roberts and Iestyn Pierce, “Cynllunio Laser Donfedd Ddeuol”. Submitted to the Welsh journal publication ‘Gwerddon’, January 2015; Accepted for publication in the October 2016 edition.

2. **Conference Papers**
    - Daniel Roberts and Iestyn Pierce, “Cynllunio Laser Donfedd Ddeuol”. Coleg Cymraeg Cenedlaethol Welsh Medium Science Conference, Aberystwyth, June the 9th 2014.

    - Daniel Roberts and Iestyn Pierce, “Cynllunio Laser Donfedd Ddeuol”. Coleg Cymraeg Cenedlaethol Multi-Disciplinary Conference, Newtown, June the 19th 2014.

    - Daniel Roberts and Iestyn Pierce, “Ehangiad Lled-Llinell Laser ‘Tonfedd-Ddeuol”. Coleg Cymraeg Cenedlaethol Welsh Medium Science Conference, Aberystwyth, June the 8th 2015.

APPENDIX B

FORTRAN COUPLED VCSEL MODEL

```
program ColdrenCorzineCoupledVCSEL

    implicit none

    integer, parameter :: dbl = selected_real_kind(15,307)
    real(dbl) :: Jg1, Jg2, vg, confin
    real(dbl) :: deltaT, t
    integer :: wellw
    real(dbl) :: ng1, ng2
    real(dbl) :: gain1, gain2
    real(dbl) :: S1, S2
    real(dbl) :: fg, tp, betaspon
    real(dbl) :: epsilon

    wellw=2.4_dbl              !cm^-3
    vg=3e10_dbl                !cm/s
    confin=0.05_dbl
    ng1=0.0_dbl
    ng2=0.0_dbl
    Jg1=0.5e-3*0.8_dbl         !I*ni
    Jg2=0.5e-3*0.8_dbl         !I*ni
    S1=0.0_dbl
    S2=0.0_dbl
    fg=1.0_dbl
    tp=2.20e-12_dbl            !ps
    betaspon=2e-4_dbl
    epsilon=0.0_dbl

                open (unit=99, file="datateststhort.dat")
                open (unit=98, file="datatestlong.dat")

                t=0.0_dbl
                deltaT=1.0e-12_dbl

                do while (t<1e-7_dbl)

                                call runge_ng1(t,deltaT,ng1,S1,gain1)
                                call runge_ng2(t,deltaT,ng2,S2,gain2)
                                call runge_S1(t,deltaT,S1,gain1,ng1)
                                call runge_S2(t,deltaT,S2,gain2,ng2)
                                t=t+deltaT
                print*, ng1, S1, t
                write(99, *)ng1, S1, t
                write(98, *)ng2, S2, t
                end do
                close(unit=99)
                close(unit=98)

contains

   subroutine runge_ng1(t,deltaT,ng1,S1,gain1)
   real(dbl) :: Jg1, vg, confin
```

```
integer :: wellw
real(dbl) :: t, deltaT
real(dbl) :: ng1, S1
real(dbl) :: gain1
real(dbl) :: k1, k2, k3, k4

k1=deltaT*ng1cal(t,ng1,S1,gain1)
k2=deltaT*ng1cal((t+(deltaT/2)),(ng1+(k1/2)),S1,gain1)
k3=deltaT*ng1cal((t+(deltaT/2)),(ng1+(k2/2)),S1,gain1)
k4=deltaT*ng1cal(t+deltaT,ng1+k3,S1,gain1)
ng1=ng1+(k1/6)+(k2/3)+(k3/3)+(k4/6)
end subroutine runge_ng1

real(dbl) function ng1cal(t,ng1,S1,gain1)
real(dbl) :: t
real(dbl) :: ng1
real(dbl) :: gain1, S1
real(dbl) :: k1, k2, k3, k4

gain1=4.11e-16_dbl*(ng1-1.8e18_dbl)/(1+(epsilon*S1))

ng1cal=(Jg1/(1.602e-19_dbl*(wellw*1e-12_dbl)))-(gain1*S1*vg)-(1e-
10_dbl*ng1**2)

end function ng1cal

subroutine runge_ng2(t,deltaT,ng2,S2,gain2)
real(dbl) :: Jg2, vg, confin
integer :: wellw
real(dbl) :: t, deltaT
real(dbl) :: ng2, S2
real(dbl) :: gain2
real(dbl) :: k1, k2, k3, k4

k1=deltaT*ng2cal(t,ng2,S2,gain2)
k2=deltaT*ng2cal((t+(deltaT/2)),(ng2+(k1/2)),S2,gain2)
k3=deltaT*ng2cal((t+(deltaT/2)),(ng2+(k2/2)),S2,gain2)
k4=deltaT*ng2cal(t+deltaT,ng2+k3,S2,gain2)
ng2=ng2+(k1/6)+(k2/3)+(k3/3)+(k4/6)
end subroutine runge_ng2

real(dbl) function ng2cal(t,ng2,S2,gain2)
real(dbl) :: t
real(dbl) :: ng2
real(dbl) :: gain2, S2
real(dbl) :: k1, k2, k3, k4

gain2=4.11e-16_dbl*(ng2-1.8e18_dbl)/(1+(epsilon*S2))

ng2cal=(Jg2/(1.602e-19_dbl*(wellw*1e-12_dbl)))-(gain2*S2*vg)-(1e-
10_dbl*ng2**2)-(gain2*S1*vg*0.18768)

end function ng2cal

subroutine runge_S1(t,deltaT,S1,gain1val,ng1)
real(dbl) :: vg, confin
real(dbl) :: fg
real(dbl) :: tp, betaspon
real(dbl) :: t, deltaT
real(dbl) :: ng1
real(dbl) :: gain1val, S1
```

```
    real(dbl) :: k1,k2,k3,k4

    k1=deltaT*S1cal(t,S1,gain1val,ng1)
    k2=deltaT*S1cal((t+(deltaT/2)),(S1+(k1/2)),gain1val,ng1)
    k3=deltaT*S1cal((t+(deltaT/2)),(S1+(k2/2)),gain1val,ng1)
    k4=deltaT*S1cal(t+deltaT,S1+k3,gain1val,ng1)
    S1=S1+(k1/6)+(k2/3)+(k3/3)+(k4/6)
    end subroutine runge_S1

    real(dbl) function S1cal(t,S1,gain1val,ng1)
    real(dbl) :: t
    real(dbl) :: ng1
    real(dbl) :: gain1val, S1
    real(dbl) :: k1, k2, k3, k4

    S1cal=((gain1val*fg*vg*confin)-(1.0_dbl/tp))*S1+confin*betaspon*1e-
    10_dbl*ng1**2

    end function S1cal

    subroutine runge_S2(t,deltaT,S2,gain2val,ng2)
    real(dbl) :: vg, confin
    real(dbl) :: fg
    real(dbl) :: tp, betaspon
    real(dbl) :: t, deltaT
    real(dbl) :: ng2
    real(dbl) :: gain2val, S2
    real(dbl) :: k1,k2,k3,k4

    k1=deltaT*S2cal(t,S2,gain2val,ng2)
    k2=deltaT*S2cal((t+(deltaT/2)),(S2+(k1/2)),gain2val,ng2)
    k3=deltaT*S2cal((t+(deltaT/2)),(S2+(k2/2)),gain2val,ng2)
    k4=deltaT*S2cal(t+deltaT,S2+k3,gain2val,ng2)
    S2=S2+(k1/6)+(k2/3)+(k3/3)+(k4/6)
    end subroutine runge_S2

    real(dbl) function S2cal(t,S2,gain2val,ng2)
    real(dbl) :: t
    real(dbl) :: ng2
    real(dbl) :: gain2val, S2
    real(dbl) :: k1, k2, k3, k4

    S2cal=((gain2val*fg*vg*confin)-(1.0_dbl/tp))*S2+confin*betaspon*1e-
    10_dbl*ng2**2+(gain2val*fg*vg*confin*0.18768*S1)

    end function S2cal

end program ColdrenCorzineCoupledVCSEL
```

APPENDIX C

FORTRAN UNIDIRECTIONAL INJECTION LOCKING MODEL

```
program FourWaveMixing

    implicit none

    integer, parameter :: dbl = selected_real_kind(15,307)
    real(dbl) :: Jg1, Jg2
    real(dbl) :: deltaT, t
    real(dbl) :: ng1, ng2
    real(dbl) :: gain1, gain2
    real(dbl) :: tn, tp
    complex(dbl) :: A1, A2
    real(dbl) :: alpha
    real(dbl) :: kc
    real(dbl) :: dW
    real(dbl) :: dF
    real(dbl) :: Pi
    real(dbl) :: Phi, Phi2
    real(dbl) :: Phi_old, Phi2_old
    real(dbl) :: dp1, dp2
    real(dbl) :: epsilon
    complex(dbl), parameter :: i=(0.0_dbl,1.0_dbl)

    Phi=0.0_dbl
    Phi2=0.0_dbl
    ng1=0.0_dbl
    ng2=0.0_dbl
    Jg1=5.0e-2_dbl
    Jg2=5.0e-2_dbl
    tn=2.0e-9_dbl
    tp=2.0e-12_dbl
    A1=(1.0_dbl,1.0_dbl)
    A2=(1.0_dbl,1.0_dbl)
    alpha=5.0_dbl
    kc=10.0e9_dbl
    Pi=4*atan(1.0_16)
    dF=-21.0e9_dbl
    dW=2.0_dbl*Pi*dF
    epsilon=1.5e-17_dbl

            open (unit=99, file="philaser1.dat")
            open (unit=98, file="carrierphotonlaser1.dat")
            open (unit=97, file="philaser2.dat")
            open (unit=96, file="carrierphotonlaser2.dat")
            open (unit=95, file="dphidt.dat")
            open (unit=94, file="gainlaser1.dat")
            open (unit=93, file="gainlaser2.dat")
            open (unit=92, file="realimaglaser1.dat")
            open (unit=91, file="realimaglaser2.dat")

            t=0.0_dbl
```

```
            deltaT=1.0e-13_dbl

            do while (t<1e-7_dbl)

                        call runge_ng1(t,deltaT,ng1,A1,gain1)
                        call runge_ng2(t,deltaT,ng2,A2,gain2)
                        call runge_A1(t,deltaT,A1,gain1)
                        call runge_A2(t,deltaT,A2,gain2)
                        t=t+deltaT
                        Phi_old=Phi
                        Phi2_old=Phi2
                        Phi=atan2(aimag(A1), real(A1))
                        Phi2=atan2(aimag(A2), real(A2))
                        dp1=(Phi-Phi_old)/deltaT
                        dp2=(Phi2-Phi2_old)/deltaT

            print*, ng2, abs(A2**2), t
            write(99, *) t, Phi
            write(98, *) t, abs(A1**2), ng1
            write(97, *) t, Phi2
            write(96, *) t, abs(A2**2), ng2
            write(95, *) t, dp1, dp2
            write(94, *) t, gain1, (gain1-(1.0_dbl/tp))
            write(93, *) t, gain2, (gain2-(1.0_dbl/tp))
            write(92, *) t, aimag(A1), real(A1)
            write(91, *) t, aimag(A2), real(A2)

            end do

            close(unit=99)
            close(unit=98)
            close(unit=97)
            close(unit=96)
            close(unit=95)
            close(unit=94)
            close(unit=93)
            close(unit=92)
            close(unit=91)

contains

   subroutine runge_ng1(t,deltaT,ng1,A1,gain1)
   real(dbl) :: Jg1
   real(dbl) :: t, deltaT
   real(dbl) :: ng1
   complex(dbl) :: A1
   real(dbl) :: gain1
   real(dbl) :: tn
   real(dbl) :: k1, k2, k3, k4

   k1=deltaT*ng1cal(t,ng1,A1,gain1)
   k2=deltaT*ng1cal((t+(deltaT/2)),(ng1+(k1/2)),A1,gain1)
   k3=deltaT*ng1cal((t+(deltaT/2)),(ng1+(k2/2)),A1,gain1)
   k4=deltaT*ng1cal(t+deltaT,ng1+k3,A1,gain1)
   ng1=ng1+(k1/6)+(k2/3)+(k3/3)+(k4/6)
   end subroutine runge_ng1

   real(dbl) function ng1cal(t,ng1,A1,gain1)
   real(dbl) :: t
   real(dbl) :: ng1
   complex(dbl) :: A1
```

```
   real(dbl) :: gain1
   real(dbl) :: k1, k2, k3, k4

   gain1=15e3_dbl*(ng1-1.5e8_dbl)/(1+epsilon*(A1*conjg(A1)))

   ng1cal=(Jg1/1.602e-19_dbl)-(ng1/tn)-(gain1*(A1*conjg(A1)))

   end function ng1cal

   subroutine runge_ng2(t,deltaT,ng2,A2,gain2)
   real(dbl) :: Jg2
   real(dbl) :: t, deltaT
   real(dbl) :: ng2
   complex(dbl) :: A2
   real(dbl) :: gain2
   real(dbl) :: tn
   real(dbl) :: k1, k2, k3, k4

   k1=deltaT*ng2cal(t,ng2,A2,gain2)
   k2=deltaT*ng2cal((t+(deltaT/2)),(ng2+(k1/2)),A2,gain2)
   k3=deltaT*ng2cal((t+(deltaT/2)),(ng2+(k2/2)),A2,gain2)
   k4=deltaT*ng2cal(t+deltaT,ng2+k3,A2,gain2)
   ng2=ng2+(k1/6)+(k2/3)+(k3/3)+(k4/6)
   end subroutine runge_ng2

   real(dbl) function ng2cal(t,ng2,A2,gain2)
   real(dbl) :: t
   real(dbl) :: ng2
   complex(dbl) :: A2
   real(dbl) :: gain2
   real(dbl) :: k1, k2, k3, k4

   gain2=15e3_dbl*(ng2-1.5e8_dbl)/(1+epsilon*(A2*conjg(A2)))

   ng2cal=(Jg2/1.602e-19_dbl)-(ng2/tn)-(gain2*(A2*conjg(A2)))

   end function ng2cal

   subroutine runge_A1(t,deltaT,A1,gain1val)
   real(dbl) :: gain1val
   complex(dbl) :: A1
   real(dbl) :: tp
   real(dbl) :: deltaT, t
   complex(dbl) :: k1, k2, k3, k4

   k1=deltaT*a1cal(t,A1,gain1val)
   k2=deltaT*a1cal((t+(deltaT/2)),(A1+(k1/2)),gain1val)
   k3=deltaT*a1cal((t+(deltaT/2)),(A1+(k2/2)),gain1val)
   k4=deltaT*a1cal(t+deltaT,A1+k3,gain1val)
   A1=A1+(k1/6)+(k2/3)+(k3/3)+(k4/6)
   end subroutine runge_A1

   complex(dbl) function a1cal(t,A1,gain1val)
   real(dbl) :: t
   complex(dbl) :: A1
   real(dbl) :: gain1val
   complex(dbl) :: k1, k2, k3, k4

   a1cal=0.5_dbl*((1.0_dbl+(i*alpha))*(gain1val-(1.0_dbl/tp)))*A1
!+kc*A2*exp(i*dW*t)
```

```
   end function a1cal

   subroutine runge_A2(t,deltaT,A2,gain2val)
   real(dbl) :: gain2val
   complex(dbl) :: A2
   real(dbl) :: tp
   real(dbl) :: deltaT, t
   complex(dbl) :: k1, k2, k3, k4

   k1=deltaT*a2cal(t,A2,gain2val)
   k2=deltaT*a2cal((t+(deltaT/2)),(A2+(k1/2)),gain2val)
   k3=deltaT*a2cal((t+(deltaT/2)),(A2+(k2/2)),gain2val)
   k4=deltaT*a2cal(t+deltaT,A2+k3,gain2val)
   A2=A2+(k1/6)+(k2/3)+(k3/3)+(k4/6)
   end subroutine runge_A2

   complex(dbl) function a2cal(t,A2,gain2val)
   real(dbl) :: t
   complex(dbl) :: A2
   real(dbl) :: gain2val
   complex(dbl) :: k1, k2, k3, k4

   a2cal=(0.5_dbl*((1.0_dbl+(i*alpha))*(gain2val-
(1.0_dbl/tp)))*A2)+kc*A1*exp(i*dW*t)

   end function a2cal

end program FourWaveMixing
```

APPENDIX D

UNIDIRECTIONAL INJECTION LOCKING DATA

The data in the following table represents the data used to plot figure 5.5 from chapter five. The figure has been reproduced here for convenience.

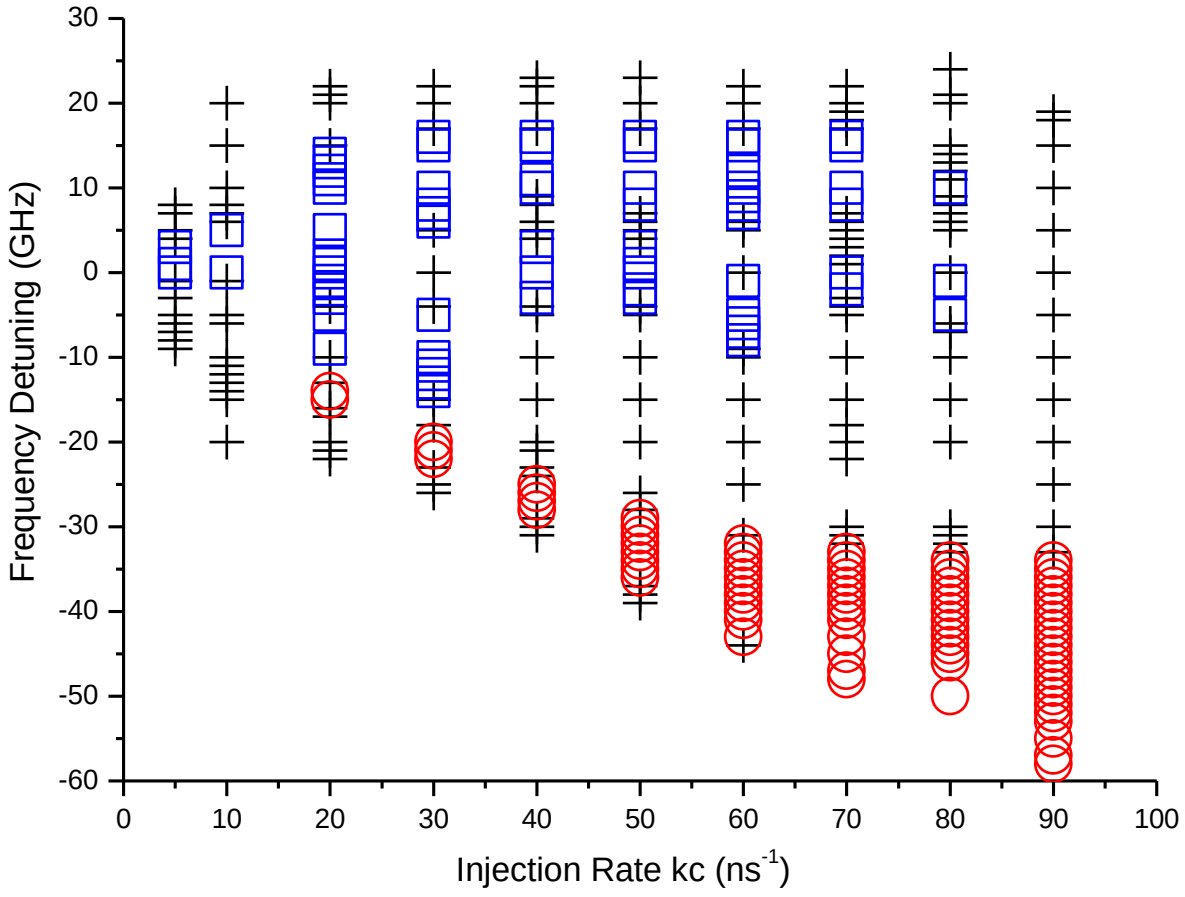

Figure 5.5: *Behavioural plot for the case of unidirectional injection with various values for detuning and injection rates.*

$\kappa_c = 5ns^{-1}$		
Frequency Detuning, Δf	**Locked / Periodic / Chaos**	**Frequency of Oscillations**
0GHz	Chaos	Unmeasurable
-5GHz	Periodic	≈3.38GHz
-6GHz	Periodic	≈4.81GHz
-7GHz	Periodic	≈5.45GHz
-8GHz	Periodic	≈6.34GHz

+7GHz	Periodic	≈5.45GHz
+8GHz	Periodic	≈6.22GHz
+9GHz	Periodic	≈10.47GHz
$\kappa_c = 10ns^{-1}$		
Frequency Detuning, Δf	**Locked / Periodic / Chaos**	**Frequency of Oscillations**
0GHz	Chaos	Unmeasurable
-1GHz	Periodic	≈8.74GHz
-5GHz	Periodic	≈9.26GHz
-6GHz	Periodic	≈9.43GHz
-10GHz	Periodic	≈3.34GHz
-11GHz	Periodic	≈3.37GHz
-12GHz	Periodic	≈3.25GHz
-13GHz	Periodic	≈3.14GHz
-14GHz	Periodic	≈3.21GHz
-15GHz	Periodic	≈3.33GHz
-20GHz	Periodic	≈10.14GHz
-21GHz	Periodic	≈21.37GHz
+5GHz	Chaos	Unmeasurable
+6GHz	Periodic	≈5.05GHz
+7GHz	Periodic	≈10.71GHz
+8GHz	Periodic	≈11.32GHz
+10GHz	Periodic	≈6.20GHz
+15GHz	Periodic	≈4.44GHz
+20GHz	Periodic	≈10.70GHz
+21GHz	Periodic	≈21.25GHz
$\kappa_c = 20ns^{-1}$		
Frequency Detuning, Δf	**Locked / Periodic / Chaos**	**Frequency of Oscillations**
0GHz	Chaos	Unmeasurable
-1GHz	Chaos	Unmeasurable
-2GHz	Chaos	Unmeasurable
-3GHz	Chaos	Unmeasurable
-4GHz	Periodic	≈4.17GHz
-5GHz	Chaos	Unmeasurable
-9GHz	Chaos	Unmeasurable
-10GHz	Periodic	≈4.88GHz
-13GHz	Periodic	≈9.99GHz
-14GHz	Locked	Flat Response
-15GHz	Locked	Flat Response
-16GHz	Periodic	≈5.50GHz
-17GHz	Periodic	≈5.09GHz
-20GHz	Periodic	≈3.55GHz

-21GHz	Periodic	≈11.60GHz
-22GHz	Periodic	≈11.56GHz
-24GHz	Periodic	≈24.92GHz
+1GHz	Chaos	Unmeasurable
+2GHz	Chaos	Unmeasurable
+5GHz	Chaos	Unmeasurable
+10GHz	Chaos	Unmeasurable
+11GHz	Chaos	Unmeasurable
+12GHz	Chaos	Unmeasurable
+13GHz	Chaos	Unmeasurable
+14GHz	Chaos	Unmeasurable
+15GHz	Periodic	≈10.20GHz
+20GHz	Periodic	≈11.40GHz
+21GHz	Periodic	≈11.40GHz
+22GHz	Periodic	≈11.57GHz
+23GHz	Periodic	≈23.86GHz
$\kappa_c = 30ns^{-1}$		
Frequency Detuning, Δf	**Locked / Periodic / Chaos**	**Frequency of Oscillations**
0GHz	Periodic	≈6.29GHz
-4GHz	Periodic	≈5.21GHz
-5GHz	Chaos	Unmeasurable
-10GHz	Chaos	Unmeasurable
-11GHz	Chaos	Unmeasurable
-12GHz	Chaos	Unmeasurable
-13GHz	Chaos	Unmeasurable
-14GHz	Chaos	Unmeasurable
-15GHz	Periodic	≈5.19GHz
-19GHz	Periodic	≈10.63GHz
-20GHz	Locked	Flat Response
-21GHz	Locked	Flat Response
-22GHz	Locked	Flat Response
-23GHz	Periodic	≈12.64GHz
-24GHz	Periodic	≈25.85GHz
-25GHz	Periodic	≈5.09GHz
-26GHz	Periodic	≈3.00GHz
-27GHz	Periodic	≈27.98GHz
+5GHz	Periodic	≈9.78GHz
+6GHz	Chaos	Unmeasurable
+7GHz	Chaos	Unmeasurable
+8GHz	Chaos	Unmeasurable
+10GHz	Chaos	Unmeasurable
+15GHz	Chaos	Unmeasurable

+16GHz	Chaos	Unmeasurable
+17GHz	Periodic	≈9.10GHz
+20GHz	Periodic	≈12.11GHz
+22GHz	Periodic	≈12.35GHz
+23GHz	Periodic	≈24.76GHz
$\kappa_c = 40ns^{-1}$		
Frequency Detuning, Δf	**Locked / Periodic / Chaos**	**Frequency of Oscillations**
0GHz	Chaos	Unmeasurable
-3GHz	Chaos	Unmeasurable
-4GHz	Periodic	≈6.60GHz
-5GHz	Periodic	≈13.14GHz
-10GHz	Periodic	≈8.91GHz
-15GHz	Periodic	≈6.14GHz
-20GHz	Periodic	≈11.13GHz
-21GHz	Periodic	≈11.20GHz
-23GHz	Periodic	≈11.47GHz
-24GHz	Periodic	≈11.59GHz
-25GHz	Locked	Flat Response
-26GHz	Locked	Flat Response
-27GHz	Locked	Flat Response
-28GHz	Locked	Flat Response
-29GHz	Periodic	≈4.99GHz
-30GHz	Periodic	≈1.53GHz
-31GHz	Periodic	≈5.1GHz
-32GHz	Periodic	≈33.4GHz
+3GHz	Chaos	Unmeasurable
+4GHz	Periodic	≈10.46GHz
+5GHz	Periodic	≈10.22GHz
+7GHz	Periodic	≈10.70GHz
+8GHz	Periodic	≈5.39GHz
+9GHz	Chaos	Unmeasurable
+10GHz	Chaos	Unmeasurable
+15GHz	Chaos	Unmeasurable
+16GHz	Chaos	Unmeasurable
+17GHz	Periodic	≈9.55GHz
+20GHz	Periodic	≈6.28GHz
+22GHz	Periodic	≈12.85GHz
+23GHz	Periodic	≈12.98GHz
+24GHz	Periodic	≈26.86GHz
$\kappa_c = 50ns^{-1}$		
Frequency Detuning, Δf	**Locked / Periodic / Chaos**	**Frequency of Oscillations**

0GHz	Chaos	Unmeasurable
-4GHz	Chaos	Unmeasurable
-5GHz	Chaos	Unmeasurable
-6GHz	Periodic	≈3.71GHz
-10GHz	Periodic	≈13.66GHz
-15GHz	Periodic	≈11.59GHz
-20GHz	Periodic	≈11.64GHz
-25GHz	Periodic	≈12.11GHz
-28GHz	Periodic	≈12.29GHz
-29GHz	Locked	Flat Response
-30GHz	Locked	Flat Response
-31GHz	Locked	Flat Response
-32GHz	Locked	Flat Response
-33GHz	Locked	Flat Response
-34GHz	Locked	Flat Response
-35GHz	Locked	Flat Response
-36GHz	Locked	Flat Response
-37GHz	Periodic	≈4.99GHz
-38GHz	Periodic	≈4.73GHz
-39GHz	Periodic	≈4.51GHz
-40GHz	Periodic	≈40.99GHz
+1GHz	Chaos	Unmeasurable
+3GHz	Chaos	Unmeasurable
+4GHz	Periodic	≈11.24GHz
+5GHz	Periodic	≈11.35GHz
+6GHz	Periodic	≈5.72GHz
+7GHz	Periodic	≈5.75GHz
+8GHz	Chaos	Unmeasurable
+10GHz	Chaos	Unmeasurable
+15GHz	Chaos	Unmeasurable
+16GHz	Chaos	Unmeasurable
+17GHz	Periodic	≈8.99GHz
+20GHz	Periodic	≈6.56GHz
+23GHz	Periodic	≈13.58GHz
+24GHz	Periodic	≈27.57GHz
$\kappa_c = 60ns^{-1}$		
Frequency Detuning, Δf	**Locked / Periodic / Chaos**	**Frequency of Oscillations**
0GHz	Periodic	≈6.55GHz
-1GHz	Chaos	Unmeasurable
-5GHz	Chaos	Unmeasurable
-6GHz	Chaos	Unmeasurable
-7GHz	Chaos	Unmeasurable

-8GHz	Chaos	Unmeasurable
-9GHz	Periodic	≈7.90GHz
-10GHz	Periodic	≈7.78GHz
-15GHz	Periodic	≈14.43GHz
-20GHz	Periodic	≈13.42GHz
-25GHz	Periodic	≈13.02GHz
-31GHz	Periodic	≈13.27GHz
-32GHz	Locked	Flat Response
-33GHz	Locked	Flat Response
-34GHz	Locked	Flat Response
-35GHz	Locked	Flat Response
-36GHz	Locked	Flat Response
-37GHz	Locked	Flat Response
-38GHz	Locked	Flat Response
-39GHz	Locked	Flat Response
-40GHz	Locked	Flat Response
-41GHz	Locked	Flat Response
-42GHz	Periodic	≈43.43GHz
-43GHz	Locked	Flat Response
-44GHz	Periodic	≈4.10GHz
-45GHz	Periodic	≈45.82GHz
-46GHz	Periodic	≈47.01GHz
+5GHz	Periodic	≈11.87GHz
+6GHz	Periodic	≈6.06GHz
+7GHz	Chaos	Unmeasurable
+8GHz	Chaos	Unmeasurable
+9GHz	Chaos	Unmeasurable
+10GHz	Chaos	Unmeasurable
+12GHz	Chaos	Unmeasurable
+15GHz	Chaos	Unmeasurable
+16GHz	Chaos	Unmeasurable
+17GHz	Periodic	≈4.75GHz
+20GHz	Periodic	≈13.80GHz
+22GHz	Periodic	≈13.82GHz
+23GHz	Periodic	≈28.58GHz
$\kappa_c = 70ns^{-1}$		
Frequency Detuning, Δf	**Locked / Periodic / Chaos**	**Frequency of Oscillations**
0GHz	Chaos	Unmeasurable
-2GHz	Chaos	Unmeasurable
-3GHz	Periodic	≈6.79GHz
-4GHz	Periodic	≈6.59GHz
-5GHz	Periodic	≈6.31GHz

-10GHz	Periodic	≈8.61GHz
-15GHz	Periodic	≈16.08GHz
-20GHz	Periodic	≈14.97GHz
-22GHz	Periodic	≈14.85GHz
-30GHz	Periodic	≈14.25GHz
-31GHz	Periodic	≈14.21GHz
-32GHz	Periodic	≈14.27GHz
-33GHz	Locked	Flat Response
-34GHz	Locked	Flat Response
-35GHz	Locked	Flat Response
-36GHz	Locked	Flat Response
-37GHz	Locked	Flat Response
-38GHz	Locked	Flat Response
-39GHz	Locked	Flat Response
-40GHz	Locked	Flat Response
-41GHz	Locked	Flat Response
-42GHz	Periodic	≈43.87GHz
-43GHz	Locked	Flat Response
-44GHz	Periodic	≈45.46GHz
-45GHz	Locked	Flat Response
-46GHz	Periodic	≈47.44GHz
-47GHz	Locked	Flat Response
-48GHz	Locked	Flat Response
-49GHz	Periodic	≈50.19GHz
-50GHz	Periodic	≈51.29GHz
-51GHz	Periodic	≈51.96GHz
+1GHz	Periodic	≈2.71GHz
+2GHz	Periodic	≈2.73GHz
+3GHz	Periodic	≈11.13GHz
+4GHz	Periodic	≈11.57GHz
+5GHz	Periodic	≈12.02GHz
+6GHz	Periodic	≈12.27GHz
+7GHz	Periodic	≈6.21GHz
+8GHz	Chaos	Unmeasurable
+10GHz	Chaos	Unmeasurable
+15GHz	Chaos	Unmeasurable
+16GHz	Chaos	Unmeasurable
+17GHz	Periodic	≈6.80GHz
+18GHz	Periodic	≈6.93GHz
+19GHz	Periodic	≈13.91GHz
+20GHz	Periodic	≈13.89GHz
+22GHz	Periodic	≈14.23GHz
+23GHz	Periodic	≈29.04GHz

+24GHz	Periodic	≈29.36GHz
$\kappa_c = 80ns^{-1}$		
Frequency Detuning, Δf	**Locked / Periodic / Chaos**	**Frequency of Oscillations**
0GHz	Periodic	≈2.16GHz
-1GHz	Chaos	Unmeasurable
-5GHz	Chaos	Unmeasurable
-6GHz	Periodic	≈4.87GHz
-7GHz	Periodic	≈4.77GHz
-10GHz	Periodic	≈9.25GHz
-15GHz	Periodic	≈17.20GHz
-20GHz	Periodic	≈16.51GHz
-30GHz	Periodic	≈15.33GHz
-31GHz	Periodic	≈15.39GHz
-32GHz	Periodic	≈15.46GHz
-33GHz	Periodic	≈15.23GHz
-34GHz	Locked	Flat Response
-35GHz	Locked	Flat Response
-36GHz	Locked	Flat Response
-37GHz	Locked	Flat Response
-38GHz	Locked	Flat Response
-39GHz	Locked	Flat Response
-40GHz	Locked	Flat Response
-41GHz	Locked	Flat Response
-42GHz	Locked	Flat Response
-43GHz	Locked	Flat Response
-44GHz	Locked	Flat Response
-45GHz	Locked	Flat Response
-46GHz	Locked	Flat Response
-47GHz	Periodic	≈48.92GHz
-48GHz	Periodic	≈48.88GHz
-49GHz	Periodic	≈50.89GHz
-50GHz	Locked	Flat Response
-51GHz	Periodic	≈52.19GHz
-52GHz	Periodic	≈53.27GHz
+5GHz	Periodic	≈12.31GHz
+6GHz	Periodic	≈12.68GHz
+7GHz	Periodic	≈12.77GHz
+8GHz	Periodic	≈6.34GHz
+9GHz	Periodic	≈6.35GHz
+10GHz	Chaos	Unmeasurable
+11GHz	Periodic	≈3.25GHz
+12GHz	Periodic	≈3.31GHz

+13GHz	Periodic	≈3.31GHz
+14GHz	Periodic	≈6.88GHz
+15GHz	Periodic	≈6.92GHz
+20GHz	Periodic	≈5.28GHz
+21GHz	Periodic	≈14.43GHz
+22GHz	Periodic	≈29.55GHz
+23GHz	Periodic	≈29.77GHz
+24GHz	Periodic	≈11.19GHz
+25GHz	Periodic	≈31.02GHz
+26GHz	Periodic	≈31.67GHz
$\kappa_c = 90ns^{-1}$		
Frequency Detuning, Δf	**Locked / Periodic / Chaos**	**Frequency of Oscillations**
0GHz	Periodic	≈11.02GHz
-5GHz	Periodic	≈10.36GHz
-10GHz	Periodic	≈9.74GHz
-15GHz	Periodic	≈18.73GHz
-20GHz	Periodic	≈17.75GHz
-25GHz	Periodic	≈17.10GHz
-30GHz	Periodic	≈16.50GHz
-33GHz	Periodic	≈16.38GHz
-34GHz	Locked	Flat Response
-35GHz	Locked	Flat Response
-36GHz	Locked	Flat Response
-37GHz	Locked	Flat Response
-38GHz	Locked	Flat Response
-39GHz	Locked	Flat Response
-40GHz	Locked	Flat Response
-41GHz	Locked	Flat Response
-42GHz	Locked	Flat Response
-43GHz	Locked	Flat Response
-44GHz	Locked	Flat Response
-45GHz	Locked	Flat Response
-46GHz	Locked	Flat Response
-47GHz	Locked	Flat Response
-48GHz	Locked	Flat Response
-49GHz	Locked	Flat Response
-50GHz	Locked	Flat Response
-51GHz	Locked	Flat Response
-52GHz	Locked	Flat Response
-53GHz	Locked	Flat Response
-54GHz	Periodic	≈55.45GHz
-55GHz	Locked	Flat Response

+5GHz	Periodic	≈12.41GHz
+10GHz	Periodic	≈13.45GHz
+15GHz	Periodic	≈14.04GHz
+18GHz	Periodic	≈14.36GHz
+19GHz	Periodic	≈14.58GHz
+20GHz	Periodic	≈29.40GHz
+21GHz	Periodic	≈29.78GHz
+22GHz	Periodic	≈30.46GHz
+23GHz	Periodic	≈30.89GHz

APPENDIX E

BIDIRECTIONAL INJECTION LOCKING DATA

The data in the following table represents the data used to plot figure 5.8 from chapter five. The figure has been reproduced here for convenience.

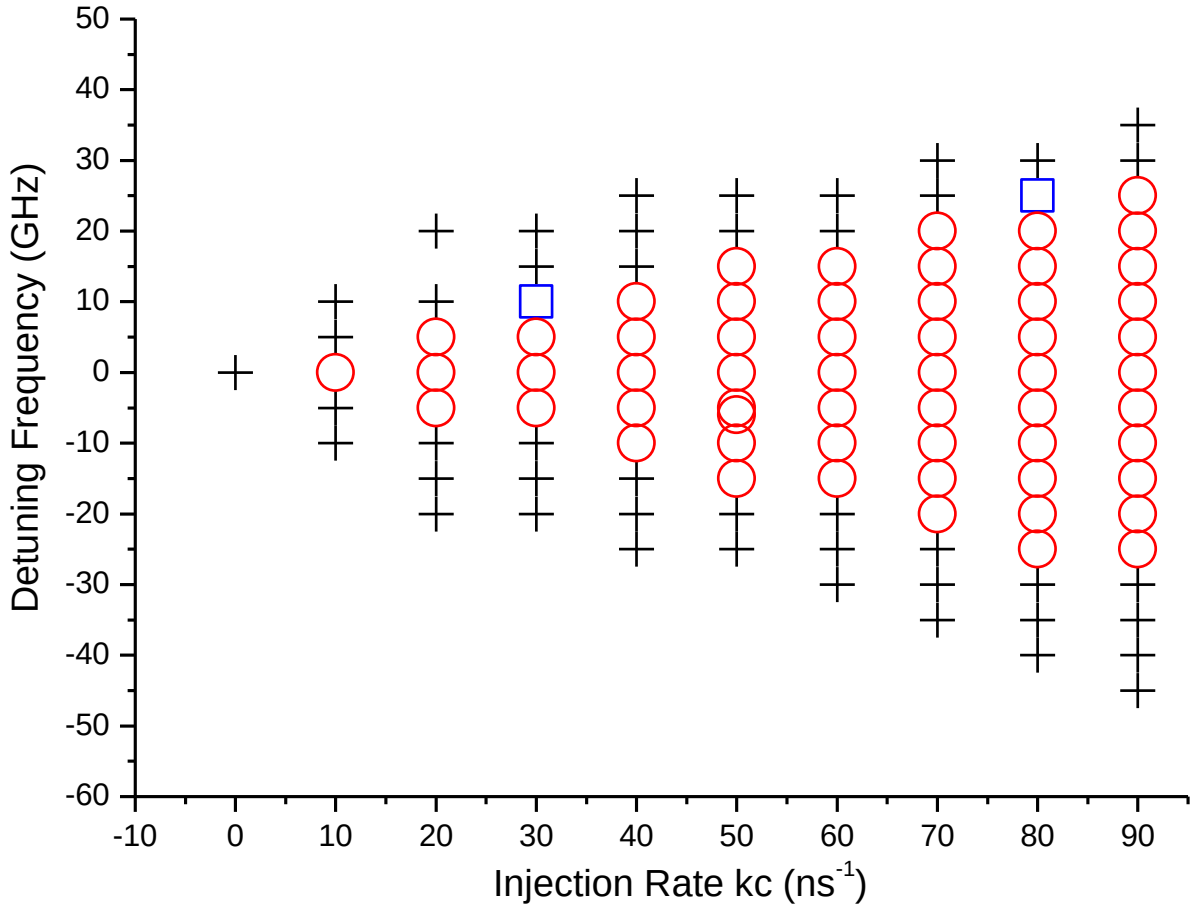

Figure 5.10: *Behavioural plot for the case of bidirectional injection with various values for detuning and injection rate.*

$\kappa_c = 0ns^{-1}$		
Frequency Detuning, Δf	**Locked / Periodic / Chaos**	**Frequency of Oscillations**
0GHz	Locked	Flat Response
$\kappa_c = 10ns^{-1}$		
Frequency Detuning, Δf	Locked / Periodic / Chaos	Frequency of Oscillations
0GHz	Locked	Flat Response

-5GHz	Periodic	≈3.88GHz
-10GHz	Periodic	≈9.52GHz
-15GHz	Periodic	≈14.68GHz
+5GHz	Periodic	≈3.88GHz
+10GHz	Periodic	≈9.52GHz
+15GHz	Periodic	≈14.47GHz
$\kappa_c = 20ns^{-1}$		
Frequency Detuning, Δf	**Locked / Periodic / Chaos**	**Frequency of Oscillations**
0GHz	Locked	Flat Response
-5GHz	Locked	Flat Response
-10GHz	Periodic	≈7.71GHz
-15GHz	Periodic	≈6.76GHz
+5GHz	Locked	Flat Response
+10GHz	Periodic	≈7.78GHz
+15GHz	Periodic	≈13.55GHz
+20GHz	Periodic	≈9.52GHz
+25GHz	Periodic	≈23.99GHz
$\kappa_c = 30ns^{-1}$		
Frequency Detuning, Δf	**Locked / Periodic / Chaos**	**Frequency of Oscillations**
0GHz	Locked	Flat Response
-5GHz	Locked	Flat Response
-10GHz	Periodic	≈2.70GHz
-15GHz	Periodic	≈11.44GHz
-20GHz	Periodic	≈8.71GHz
-25GHz	Periodic	≈23.17GHz
+5GHz	Locked	Flat Response
+10GHz	Chaos	Unmeasurable
+15GHz	Periodic	≈11.81GHz
+20GHz	Periodic	≈8.71GHz
+25GHz	Periodic	≈23.22GHz
$\kappa_c = 40ns^{-1}$		
Frequency Detuning, Δf	**Locked / Periodic / Chaos**	**Frequency of Oscillations**
0GHz	Locked	Flat Response
-5GHz	Locked	Flat Response
-10GHz	Locked	Flat Response
-15GHz	Periodic	≈7.70GHz
-20GHz	Periodic	≈7.61GHz
-25GHz	Periodic	≈7.10GHz
-30GHz	Periodic	≈27.16GHz
+5GHz	Locked	Flat Response

+10GHz	Locked	Flat Response
+15GHz	Periodic	≈8.17GHz
+20GHz	Periodic	≈7.81GHz
+25GHz	Periodic	≈7.19GHz
+30GHz	Periodic	≈27.42GHz
$\kappa_c = 50ns^{-1}$		
Frequency Detuning, Δf	**Locked / Periodic / Chaos**	**Frequency of Oscillations**
0GHz	Locked	Flat Response
-5GHz	Locked	Flat Response
-6GHz	Locked	Flat Response
-10GHz	Locked	Flat Response
-15GHz	Locked	Flat Response
-20GHz	Periodic	≈5.87GHz
-25GHz	Periodic	≈3.17GHz
-30GHz	Periodic	≈25.21GHz
-35GHz	Periodic	≈30.76GHz
-40GHz	Periodic	≈36.58GHz
+5GHz	Locked	Flat Response
+10GHz	Locked	Flat Response
+15GHz	Locked	Flat Response
+20GHz	Periodic	≈12.47GHz
+25GHz	Periodic	≈9.81GHz
+30GHz	Periodic	≈25.47GHz
$\kappa_c = 60ns^{-1}$		
Frequency Detuning, Δf	**Locked / Periodic / Chaos**	**Frequency of Oscillations**
0GHz	Locked	Flat Response
-5GHz	Locked	Flat Response
-10GHz	Locked	Flat Response
-15GHz	Locked	Flat Response
-20GHz	Periodic	≈5.58GHz
-25GHz	Periodic	≈2.62GHz
-30GHz	Periodic	≈7.64GHz
-35GHz	Periodic	≈28.92GHz
-40GHz	Periodic	≈34.84GHz
+5GHz	Locked	Flat Response
+10GHz	Locked	Flat Response
+15GHz	Locked	Flat Response
+20GHz	Periodic	≈6.92GHz
+25GHz	Periodic	≈8.22GHz
+30GHz	Periodic	≈23.36GHz

$\kappa_c = 70ns^{-1}$		
Frequency Detuning, Δf	**Locked / Periodic / Chaos**	**Frequency of Oscillations**
0GHz	Locked	Flat Response
-5GHz	Locked	Flat Response
-10GHz	Locked	Flat Response
-15GHz	Locked	Flat Response
-20GHz	Locked	Flat Response
-25GHz	Periodic	≈2.65GHz
-30GHz	Periodic	≈9.72GHz
-35GHz	Periodic	≈8.78GHz
-40GHz	Periodic	≈32.76GHz
+5GHz	Locked	Flat Response
+10GHz	Locked	Flat Response
+15GHz	Locked	Flat Response
+20GHz	Locked	Flat Response
+25GHz	Periodic	≈2.44GHz
+30GHz	Periodic	≈10.32GHz
+35GHz	Periodic	≈33.29GHz
$\kappa_c = 80ns^{-1}$		
Frequency Detuning, Δf	**Locked / Periodic / Chaos**	**Frequency of Oscillations**
0GHz	Locked	Flat Response
-5GHz	Locked	Flat Response
-10GHz	Locked	Flat Response
-15GHz	Locked	Flat Response
-20GHz	Locked	Flat Response
-25GHz	Locked	Flat Response
-30GHz	Periodic	≈3.70GHz
-35GHz	Periodic	≈3.89GHz
-40GHz	Periodic	≈30.23GHz
+5GHz	Locked	Flat Response
+10GHz	Locked	Flat Response
+15GHz	Locked	Flat Response
+20GHz	Locked	Flat Response
+25GHz	Locked	Flat Response
+30GHz	Periodic	≈4.17GHz
+35GHz	Periodic	≈24.70GHz
$\kappa_c = 90ns^{-1}$		
Frequency Detuning, Δf	**Locked / Periodic / Chaos**	**Frequency of Oscillations**
0GHz	Locked	Flat Response
-5GHz	Locked	Flat Response
-10GHz	Locked	Flat Response

-15GHz	Locked	Flat Response
-20GHz	Locked	Flat Response
-25GHz	Locked	Flat Response
-30GHz	Periodic	≈2.26GHz
-35GHz	Periodic	≈9.44GHz
-40GHz	Periodic	≈8.99GHz
-45GHz	Periodic	≈33.60GHz
+5GHz	Locked	Flat Response
+10GHz	Locked	Flat Response
+15GHz	Locked	Flat Response
+20GHz	Locked	Flat Response
+25GHz	Locked	Flat Response
+30GHz	Periodic	≈10.84GHz
+35GHz	Periodic	≈10.57GHz
+40GHz	Periodic	≈28.82GHz

APPENDIX F
FOUR-WAVE MIXING: MATHEMATICAL REPRESENTATION

The following is a mathematical representation of the FWM scheme employed in the work of chapters six and seven. The equation defines all of the different frequency components that can be obtained from the FWM scheme. The highlighted frequencies are equivalent frequencies, for example, all of the red highlighted frequencies are equal to $\pm(2\omega_1 \pm \omega_1)$.

$$\widetilde{\boldsymbol{E}}(\boldsymbol{t}) = \boldsymbol{E_1 e^{-i(\omega_1)t}} + \boldsymbol{E_2 e^{-i(\omega_2)t} E_3 e^{-i(\omega_3)t}} + \boldsymbol{c.c}$$
$$= \left[\boldsymbol{E_1 e^{-i(\omega_1)t}} + \boldsymbol{E_1}^{*}\boldsymbol{e^{i(\omega_1)t}} + \boldsymbol{E_2 e^{-i(\omega_2)t}} + \boldsymbol{E_2}^{*}\boldsymbol{e^{i(\omega_2)t}} + \boldsymbol{E_3 e^{-i(\omega_3)t}} + \boldsymbol{E_3}^{*}\boldsymbol{e^{i(\omega_3)t}}\right]$$

$$\tilde{E}(t)^2 = \left(E_1 e^{-i(\omega_1)t} + {E_1}^{*} e^{i(\omega_1)t} + E_2 e^{-i(\omega_2)t} + {E_2}^{*} e^{i(\omega_2)t} + E_3 e^{-i(\omega_3)t} + {E_3}^{*} e^{i(\omega_3)t}\right) \times$$
$$\left(E_1 e^{-i(\omega_1)t} + {E_1}^{*} e^{i(\omega_1)t} + E_2 e^{-i(\omega_2)t} + {E_2}^{*} e^{i(\omega_2)t} + E_3 e^{-i(\omega_3)t} + {E_3}^{*} e^{i(\omega_3)t}\right)$$

$$= \begin{pmatrix} {E_1}^{2} e^{-i(2\omega_1)t} + E_1 {E_1}^{*} + E_1 E_2 e^{-i(\omega_1+\omega_2)t} + \\ E_1 {E_2}^{*} e^{i(\omega_2-\omega_1)t} + E_1 E_3 e^{-i(\omega_1+\omega_3)t} + E_1 {E_3}^{*} e^{i(\omega_3-\omega_1)t} \end{pmatrix}$$
$$+ \begin{pmatrix} {E_1}^{*} E_1 + {E_1}^{*2} e^{i(2\omega_1)t} + {E_1}^{*} E_2 e^{i(\omega_1-\omega_2)t} + \\ {E_1}^{*} {E_2}^{*} e^{i(\omega_1+\omega_2)t} + {E_1}^{*} E_3 e^{i(\omega_1-\omega_3)t} + {E_1}^{*} {E_3}^{*} e^{i(\omega_1+\omega_3)t} \end{pmatrix}$$
$$+ \begin{pmatrix} E_2 E_1 e^{-i(\omega_2+\omega_1)t} + E_2 {E_1}^{*} e^{i(\omega_1-\omega_2)t} + {E_2}^{2} e^{-i(2\omega_2)t} + \\ E_2 {E_2}^{*} + E_2 E_3 e^{-i(\omega_2+\omega_3)t} + E_2 {E_3}^{*} e^{i(\omega_3-\omega_2)t} \end{pmatrix}$$
$$+ \begin{pmatrix} {E_2}^{*} E_1 e^{i(\omega_2-\omega_1)t} + {E_2}^{*} {E_1}^{*} e^{i(\omega_2+\omega_1)t} + {E_2}^{*} E_2 + \\ {E_2}^{*2} e^{i(2\omega_2)t} + {E_2}^{*} E_3 e^{i(\omega_2-\omega_3)t} + {E_2}^{*} {E_3}^{*} e^{i(\omega_2+\omega_3)t} \end{pmatrix}$$
$$+ \begin{pmatrix} E_3 E_1 e^{-i(\omega_3+\omega_1)t} + E_3 {E_1}^{*} e^{i(\omega_1-\omega_3)t} + E_3 E_2 e^{-i(\omega_3+\omega_2)t} + \\ E_3 {E_2}^{*} e^{i(\omega_2-\omega_3)t} + {E_3}^{2} e^{-i(2\omega_3)t} + E_3 {E_3}^{*} \end{pmatrix}$$
$$+ \begin{pmatrix} {E_3}^{*} E_1 e^{i(\omega_3-\omega_1)t} + {E_3}^{*} {E_1}^{*} e^{i(\omega_3+\omega_1)t} + {E_3}^{*} E_2 e^{i(\omega_3-\omega_2)t} + \\ {E_3}^{*} {E_2}^{*} e^{i(\omega_3+\omega_2)t} + {E_3}^{*} E_3 + {E_3}^{*2} e^{i(2\omega_3)t} \end{pmatrix}$$

$$\tilde{E}(t)^3 =$$
$$\begin{pmatrix} E_1 e^{-i(\omega_1)t} + {E_1}^{*} e^{i(\omega_1)t} + E_2 e^{-i(\omega_2)t} + \\ {E_2}^{*} e^{i(\omega_2)t} + E_3 e^{-i(\omega_3)t} + {E_3}^{*} e^{i(\omega_3)t} \end{pmatrix} \begin{pmatrix} {E_1}^{2} e^{-i(2\omega_1)t} + E_1 {E_1}^{*} + E_1 E_2 e^{-i(\omega_1+\omega_2)t} + \\ E_1 {E_2}^{*} e^{i(\omega_2-\omega_1)t} + E_1 E_3 e^{-i(\omega_1+\omega_3)t} + E_1 {E_3}^{*} e^{i(\omega_3-\omega_1)t} \end{pmatrix}$$
$$+ \begin{pmatrix} {E_1}^{*} E_1 + {E_1}^{*2} e^{i(2\omega_1)t} + {E_1}^{*} E_2 e^{i(\omega_1-\omega_2)t} + \\ {E_1}^{*} {E_2}^{*} e^{i(\omega_1+\omega_2)t} + {E_1}^{*} E_3 e^{i(\omega_1-\omega_3)t} + {E_1}^{*} {E_3}^{*} e^{i(\omega_1+\omega_3)t} \end{pmatrix}$$
$$+ \begin{pmatrix} E_2 E_1 e^{-i(\omega_2+\omega_1)t} + E_2 {E_1}^{*} e^{i(\omega_1-\omega_2)t} + {E_2}^{2} e^{-i(2\omega_2)t} + \\ E_2 {E_2}^{*} + E_2 E_3 e^{-i(\omega_2+\omega_3)t} + E_2 {E_3}^{*} e^{i(\omega_3-\omega_2)t} \end{pmatrix}$$

$$+\begin{pmatrix} E_2{}^*E_1e^{i(\omega_2-\omega_1)t} + E_2{}^*E_1{}^*e^{i(\omega_2+\omega_1)t} + E_2{}^*E_2 + \\ E_2{}^{*2}e^{i(2\omega_2)t} + E_2{}^*E_3e^{i(\omega_2-\omega_3)t} + E_2{}^*E_3{}^*e^{i(\omega_2+\omega_3)t} \end{pmatrix}$$

$$+\begin{pmatrix} E_3E_1e^{-i(\omega_3+\omega_1)t} + E_3E_1{}^*e^{i(\omega_1-\omega_3)t} + E_3E_2e^{-i(\omega_3+\omega_2)t} + \\ E_3E_2{}^*e^{i(\omega_2-\omega_3)t} + E_3{}^2e^{-i(2\omega_3)t} + E_3E_3{}^* \end{pmatrix}$$

$$+\begin{pmatrix} E_3{}^*E_1e^{i(\omega_3-\omega_1)t} + E_3{}^*E_1{}^*e^{i(\omega_3+\omega_1)t} + E_3{}^*E_2e^{i(\omega_3-\omega_2)t} + \\ E_3{}^*E_2{}^*e^{i(\omega_3+\omega_2)t} + E_3{}^*E_3 + E_3{}^{*2}e^{i(2\omega_3)t} \end{pmatrix}$$

$$=\begin{pmatrix} E_1{}^3e^{-i(3\omega_1)t} + E_1{}^2E_1{}^*e^{-i(\omega_1)t} + E_1{}^2E_2e^{-i(2\omega_1-\omega_2)t} + \\ E_1{}^2E_2{}^*e^{i(\omega_2-2\omega_1)t} + E_1{}^2E_3e^{-i(\omega_3-2\omega_1)t} + E_1{}^2E_3{}^*e^{i(\omega_3-2\omega_1)t} \end{pmatrix}$$

$$+\begin{pmatrix} E_1{}^2E_1{}^*e^{-i(\omega_1)t} + E_1E_1{}^{*2}e^{i(\omega_1)t} + E_1E_1{}^*E_2e^{-i(\omega_2)t} + \\ E_1E_1{}^*E_2{}^*e^{i(\omega_2)t} + E_1E_1{}^*E_3e^{-i(\omega_3)t} + E_1E_1{}^*E_3{}^*e^{i(\omega_3)t} \end{pmatrix}$$

$$+\begin{pmatrix} E_1{}^2E_2e^{-i(2\omega_1+\omega_2)t} + E_1E_2E_1{}^*e^{i(\omega_2)t} + E_1E_2{}^2e^{-i(\omega_1)t} + \\ E_1E_2E_2{}^*e^{-i(\omega_1+2\omega_2)t} + E_1E_2E_3e^{-i(\omega_1+\omega_2-\omega_3)t} + E_1E_2E_3{}^*e^{-i(\omega_1+\omega_2+\omega_3)t} \end{pmatrix}$$

$$+\begin{pmatrix} E_1{}^2E_2{}^*e^{i(\omega_2-2\omega_1)t} + E_1E_2{}^*E_1{}^*e^{i(\omega_2)t} + E_1E_2{}^*E_2e^{-i(\omega_1)t} + \\ E_1E_2{}^{*2}e^{i(2\omega_2-\omega_1)t} + E_1E_2{}^*E_3e^{i(\omega_2-\omega_1-\omega_3)t} + E_1E_2{}^*E_3{}^*e^{i(\omega_2-\omega_1+\omega_3)t} \end{pmatrix}$$

$$+\begin{pmatrix} E_1{}^2E_3e^{-i(2\omega_1+\omega_3)t} + E_1E_3E_1{}^*e^{i(\omega_3)t} + E_1E_3E_2e^{-i(\omega_1+\omega_3-\omega_2)t} + \\ E_1E_3E_2{}^*e^{-i(\omega_1+\omega_3+\omega_2)t} + E_1E_3{}^2e^{-i(\omega_1)t} + E_1E_3{}^*e^{-i(\omega_1+2\omega_3)t} \end{pmatrix}$$

$$+\begin{pmatrix} E_1{}^2E_3{}^*e^{i(\omega_3-2\omega_1)t} + E_1E_3{}^*E_1{}^*e^{i(\omega_3)t} + E_1E_3{}^*E_2e^{i(\omega_3-\omega_1-\omega_2)t} + \\ E_1E_3{}^*E_2{}^*e^{i(\omega_3-\omega_1+\omega_2)t} + E_1E_3{}^*E_3e^{-i(\omega_1)t} + E_1E_3{}^{*2}e^{i(2\omega_3-\omega_1)t} \end{pmatrix}$$

$$+\begin{pmatrix} E_1{}^*E_1{}^2e^{-i(\omega_1)t} + E_1{}^{*2}E_1e^{i(\omega_1)t} + E_1{}^*E_1E_2e^{-i(\omega_2)t} + \\ E_1{}^*E_1E_2{}^*e^{i(\omega_2)t} + E_1{}^*E_1E_3e^{-i(\omega_3)t} + E_1{}^*E_1E_3{}^*e^{i(\omega_3)t} \end{pmatrix}$$

$$+\begin{pmatrix} E_1{}^{*2}E_1e^{i(\omega_1)t} + E_1{}^{*3}e^{i(3\omega_1)t} + E_1{}^{*2}E_2e^{i(2\omega_1-\omega_2)t} + \\ E_1{}^{*2}E_2{}^*e^{i(2\omega_1+\omega_2)t} + E_1{}^{*2}E_3e^{i(2\omega_1-\omega_3)t} + E_1{}^{*2}E_3{}^*e^{i(2\omega_1+\omega_3)t} \end{pmatrix}$$

$$+\begin{pmatrix} E_1{}^*E_2E_1e^{-i(\omega_2)t} + E_1{}^{*2}E_2e^{i(2\omega_1-\omega_2)t} + E_1{}^*E_2{}^2e^{i(\omega_1-2\omega_2)t} + \\ E_1{}^*E_2E_2{}^*e^{i(\omega_1)t} + E_1{}^*E_2E_3e^{i(\omega_1-\omega_2-\omega_3)t} + E_1{}^*E_2E_3{}^*e^{i(\omega_1-\omega_2+\omega_3)t} \end{pmatrix}$$

$$+\begin{pmatrix} E_1{}^*E_2{}^*E_1e^{i(\omega_2)t} + E_1{}^{*2}E_2{}^*e^{i(2\omega_1+\omega_2)t} + E_1{}^*E_2{}^*E_2e^{i(\omega_1)t} + \\ E_1{}^*E_2{}^{*2}e^{i(\omega_1+2\omega_2)t} + E_1{}^*E_2{}^*E_3e^{i(\omega_1+\omega_2-\omega_3)t} + E_1{}^*E_2{}^*E_3{}^*e^{i(\omega_1+\omega_2+\omega_3)t} \end{pmatrix}$$

$$+\begin{pmatrix} E_1{}^*E_3E_1e^{-i(\omega_3)t} + E_1{}^{*2}E_3e^{i(2\omega_1-\omega_3)t} + E_1{}^*E_3E_2e^{i(\omega_1-\omega_3-\omega_2)t} + \\ E_1{}^*E_3E_2{}^*e^{i(\omega_1-\omega_3+\omega_2)t} + E_1{}^*E_3{}^2e^{i(\omega_1-2\omega_3)t} + E_1{}^*E_3E_3{}^*e^{i(\omega_1)t} \end{pmatrix}$$

$$+\begin{pmatrix} E_1{}^*E_3{}^*E_1e^{i(\omega_3)t} + E_1{}^{*2}E_3{}^*e^{i(2\omega_1+\omega_3)t} + E_1{}^*E_3{}^*E_2e^{i(\omega_1+\omega_3-\omega_2)t} + \\ E_1{}^*E_3{}^*E_2{}^*e^{i(\omega_1+\omega_2+\omega_3)t} + E_1{}^*E_3{}^*E_3e^{i(\omega_1)t} + E_1{}^*E_3{}^{*2}e^{i(\omega_1+2\omega_3)t} \end{pmatrix}$$

$$+\begin{pmatrix} E_2E_1{}^2e^{-i(\omega_2)t} + E_2E_1E_1{}^*e^{-i(\omega_2+2\omega_1)t} + E_2{}^2E_1e^{-i(2\omega_2+\omega_1)t} + \\ E_2E_1E_2{}^*e^{i(\omega_1)t} + E_2E_1E_3e^{-i(\omega_2+\omega_1-\omega_3)t} + E_2E_1E_3{}^*e^{-i(\omega_1+\omega_2+\omega_3)t} \end{pmatrix}$$

$$+\begin{pmatrix} E_2E_1{}^*E_1e^{-i(\omega_2)t} + E_2E_1{}^{*2}e^{i(2\omega_1-\omega_2)t} + E_2{}^2E_1{}^*e^{i(\omega_1-2\omega_2)t} + \\ E_2E_1{}^*E_2{}^*e^{i(\omega_1)t} + E_2E_1{}^*E_3e^{i(\omega_1-\omega_2-\omega_3)t} + E_2E_1{}^*E_3{}^*e^{i(\omega_1-\omega_2+\omega_3)t} \end{pmatrix}$$

$$+\begin{pmatrix} E_2{}^2E_1e^{-i(2\omega_2-\omega_1)t} + E_2{}^2E_1{}^*e^{-i(2\omega_2+\omega_1)t} + E_2{}^3e^{-i(3\omega_2)t} + \\ E_2{}^2E_2{}^*e^{-i(\omega_2)t} + E_2{}^2E_3e^{-i(2\omega_2-\omega_3)t} + E_2{}^2E_3{}^*e^{-i(2\omega_2+\omega_3)t} \end{pmatrix}$$

$$+\begin{pmatrix}E_2E_2{}^*E_1e^{-i(\omega_1)t}+E_2E_2{}^*E_1{}^*e^{i(\omega_1)t}+E_2{}^2E_2{}^*e^{-i(\omega_2)t}+\\E_2E_2{}^{*2}e^{i(\omega_2)t}+E_2E_2{}^*E_3e^{-i(\omega_3)t}+E_2E_2{}^*E_3{}^*e^{i(\omega_3)t}\end{pmatrix}$$

$$+\begin{pmatrix}E_2E_3E_1e^{-i(\omega_2+\omega_3-\omega_1)t}+E_2E_3E_1{}^*e^{-i(\omega_2+\omega_3+\omega_1)t}+E_2{}^2E_3e^{-i(2\omega_2+\omega_3)t}+\\E_2E_3E_2{}^*e^{i(\omega_3)t}+E_2E_3{}^2e^{-i(\omega_2)t}+E_2E_3E_3{}^*e^{-i(\omega_2+2\omega_3)t}\end{pmatrix}$$

$$+\begin{pmatrix}E_2E_3{}^*E_1e^{i(\omega_3-\omega_2-\omega_1)t}+E_2E_3{}^*E_1{}^*e^{i(\omega_3-\omega_2+\omega_1)t}+E_2{}^2E_3{}^*e^{i(\omega_3-2\omega_2)t}+\\E_2E_3{}^*E_2{}^*e^{i(\omega_3)t}+E_2E_3{}^*E_3e^{-i(\omega_2)t}+E_2E_3{}^{*2}e^{i(2\omega_3-\omega_2)t}\end{pmatrix}$$

$$+\begin{pmatrix}E_2{}^*E_1{}^2e^{i(\omega_2-2\omega_1)t}+E_2{}^*E_1E_1{}^*e^{i(\omega_2)t}+E_2{}^*E_1E_2e^{-i(\omega_1)t}+\\E_2{}^{*2}E_1e^{i(2\omega_2-\omega_1)t}+E_2{}^*E_1E_3e^{i(\omega_2-\omega_1-\omega_3)t}+E_2{}^*E_1E_3{}^*e^{i(\omega_2-\omega_1+\omega_3)t}\end{pmatrix}$$

$$+\begin{pmatrix}E_2{}^*E_1{}^*E_1e^{i(\omega_2)t}+E_2{}^*E_1{}^{*2}e^{i(\omega_2+2\omega_1)t}+E_2{}^*E_1{}^*E_2e^{i(\omega_1)t}+\\E_2{}^{*2}E_1{}^*e^{i(2\omega_2+\omega_1)t}+E_2{}^*E_1{}^*E_3e^{i(\omega_2+\omega_1-\omega_3)t}+E_2{}^*E_1{}^*E_3{}^*e^{i(\omega_2+\omega_1+\omega_3)t}\end{pmatrix}$$

$$+\begin{pmatrix}E_2{}^*E_2E_1e^{-i(\omega_1)t}+E_2{}^*E_2E_1{}^*e^{i(\omega_1)t}+E_2{}^*E_2{}^2e^{-i(\omega_2)t}+\\E_2{}^{*2}E_2e^{i(\omega_2)t}+E_2{}^*E_2E_3e^{-i(\omega_3)t}+E_2{}^*E_2E_3{}^*e^{i(\omega_3)t}\end{pmatrix}$$

$$+\begin{pmatrix}E_2{}^{*2}E_1e^{i(2\omega_2-\omega_1)t}+E_2{}^{*2}E_1{}^*e^{i(2\omega_2+\omega_1)t}+E_2{}^{*2}E_2e^{i(\omega_2)t}+\\E_2{}^{*3}e^{i(3\omega_2)t}+E_2{}^{*2}E_3e^{i(2\omega_2-\omega_3)t}+E_2{}^{*2}E_3{}^*e^{i(2\omega_2+\omega_3)t}\end{pmatrix}$$

$$+\begin{pmatrix}E_2{}^*E_3E_1e^{i(\omega_2-\omega_3-\omega_1)t}+E_2{}^*E_3E_1{}^*e^{i(\omega_2-\omega_3+\omega_1)t}+E_2{}^*E_3E_2e^{-i(\omega_3)t}+\\E_2{}^{*2}E_3e^{i(2\omega_2-\omega_3)t}+E_2{}^*E_3{}^2e^{i(\omega_2-2\omega_3)t}+E_2{}^*E_3E_3{}^*e^{i(\omega_2)t}\end{pmatrix}$$

$$+\begin{pmatrix}E_2{}^*E_3{}^*E_1e^{i(\omega_2+\omega_3-\omega_1)t}+E_2{}^*E_3{}^*E_1{}^*e^{i(\omega_2+\omega_3+\omega_1)t}+E_2{}^*E_3{}^*E_2e^{i(\omega_3)t}+\\E_2{}^{*2}E_3{}^*e^{i(2\omega_2+\omega_3)t}+E_2{}^*E_3{}^*E_3e^{i(\omega_2)t}+E_2{}^*E_3{}^{*2}e^{i(\omega_2+2\omega_3)t}\end{pmatrix}$$

$$+\begin{pmatrix}E_3E_1{}^2e^{-i(\omega_3)t}+E_3E_1E_1{}^*e^{-i(\omega_3+2\omega_1)t}+E_3E_1E_2e^{-i(\omega_3+\omega_1-\omega_2)t}+\\E_3E_1E_2{}^*e^{-i(\omega_3+\omega_1+\omega_2)t}+E_3{}^2E_1e^{-i(2\omega_3+\omega_1)t}+E_3E_1E_3{}^*e^{i(\omega_1)t}\end{pmatrix}$$

$$+\begin{pmatrix}E_3E_1{}^*E_1e^{-i(\omega_3)t}+E_3E_1{}^{*2}e^{i(2\omega_1-\omega_3)t}+E_3E_1{}^*E_2e^{i(\omega_1-\omega_3-\omega_2)t}+\\E_3E_1{}^*E_2{}^*e^{i(\omega_1-\omega_3+\omega_2)t}+E_3{}^2E_1{}^*e^{i(\omega_1-2\omega_3)t}+E_3E_1{}^*E_3{}^*e^{i(\omega_1)t}\end{pmatrix}$$

$$+\begin{pmatrix}E_3E_2E_1e^{-i(\omega_3+\omega_2-\omega_1)t}+E_3E_2E_1{}^*e^{-i(\omega_3+\omega_2+\omega_1)t}+E_3E_2{}^2e^{-i(\omega_3)t}+\\E_3E_2E_2{}^*e^{-i(\omega_3+2\omega_2)t}+E_3{}^2E_2e^{-i(2\omega_3+\omega_2)t}+E_3E_2E_3{}^*e^{i(\omega_2)t}\end{pmatrix}$$

$$+\begin{pmatrix}E_3E_2{}^*E_1e^{i(\omega_2-\omega_3-\omega_1)t}+E_3E_2{}^*E_1{}^*e^{i(\omega_2-\omega_3+\omega_1)t}+E_3E_2{}^*E_2e^{-i(\omega_3)t}+\\E_3E_2{}^{*2}e^{i(2\omega_2-\omega_3)t}+E_3{}^2E_2{}^*e^{i(\omega_2-2\omega_3)t}+E_3E_2{}^*E_3{}^*e^{i(\omega_2)t}\end{pmatrix}$$

$$+\begin{pmatrix}E_3{}^2E_1e^{-i(2\omega_3-\omega_1)t}+E_3{}^2E_1{}^*e^{-i(2\omega_3+\omega_1)t}+E_3{}^2E_2e^{-i(2\omega_3-\omega_2)t}+\\E_3{}^2E_2{}^*e^{-i(2\omega_3+\omega_2)t}+E_3{}^3e^{-i(3\omega_3)t}+E_2{}^2E_2{}^*e^{-i(\omega_3)t}\end{pmatrix}$$

$$+\begin{pmatrix}E_3E_3{}^*E_1e^{-i(\omega_1)t}+E_3E_3{}^*E_1{}^*e^{i(\omega_1)t}+E_3E_3{}^*E_2e^{-i(\omega_2)t}+\\E_3E_3{}^*E_2{}^*e^{i(\omega_2)t}+E_3{}^2E_3{}^*e^{-i(\omega_3)t}+E_3E_3{}^{*2}e^{i(\omega_3)t}\end{pmatrix}$$

$$+\begin{pmatrix}E_3{}^*E_1{}^2e^{i(\omega_3-2\omega_1)t}+E_3{}^*E_1E_1{}^*e^{i(\omega_3)t}+E_3{}^*E_1E_2e^{i(\omega_3-\omega_1-\omega_2)t}+\\E_3{}^*E_1E_2{}^*e^{i(\omega_3-\omega_1+\omega_2)t}+E_3{}^*E_1E_3e^{-i(\omega_1)t}+E_3{}^{*2}E_2e^{i(2\omega_3-\omega_1)t}\end{pmatrix}$$

$$+\begin{pmatrix}E_3{}^*E_1{}^*E_1e^{i(\omega_3)t}+E_3{}^*E_1{}^{*2}e^{i(\omega_3+2\omega_1)t}+E_3{}^*E_1{}^*E_2e^{i(\omega_3+\omega_1-\omega_2)t}+\\E_3{}^*E_1{}^*E_2{}^*e^{i(\omega_3+\omega_1+\omega_2)t}+E_3{}^*E_1{}^*E_3e^{i(\omega_1)t}+E_3{}^{*2}E_1{}^*e^{i(2\omega_3+\omega_1)t}\end{pmatrix}$$

$$+\begin{pmatrix}E_3{}^*E_2E_1e^{i(\omega_3-\omega_2-\omega_1)t}+E_3{}^*E_2E_1{}^*e^{i(\omega_3-\omega_2+\omega_1)t}+E_3{}^*E_2{}^2e^{i(\omega_3-2\omega_2)t}+\\E_3{}^*E_2E_2{}^*e^{i(\omega_3)t}+E_3{}^*E_2E_3e^{-i(\omega_2)t}+E_3{}^{*2}E_2e^{i(2\omega_3-\omega_2)t}\end{pmatrix}$$

$$+\begin{pmatrix}E_3{}^*E_2{}^*E_1e^{i(\omega_3+\omega_2-\omega_1)t}+E_3{}^*E_2{}^*E_1{}^*e^{i(\omega_3+\omega_2+\omega_1)t}+E_3{}^*E_2{}^*E_2e^{i(\omega_3)t}+\\E_3{}^*E_2{}^{*2}e^{i(\omega_3+2\omega_2)t}+E_3{}^*E_2{}^*E_3e^{i(\omega_2)t}+E_3{}^{*2}E_2{}^*e^{i(2\omega_3+\omega_2)t}\end{pmatrix}$$

$$+\begin{pmatrix} {E_3}^* E_3 E_1 e^{-i(\omega_1)t} + {E_3}^* E_3 {E_1}^* e^{i(\omega_1)t} + {E_3}^* E_3 E_2 e^{-i(\omega_2)t} + \\ {E_3}^* E_3 {E_2}^* e^{i(\omega_2)t} + {E_3}^* {E_3}^2 e^{-i(\omega_3)t} + {E_3}^{*2} E_3 e^{i(\omega_3)t} \end{pmatrix}$$

$$+\begin{pmatrix} {E_3}^{*2} E_1 e^{i(2\omega_3-\omega_1)t} + {E_3}^{*2} {E_1}^* e^{i(2\omega_3+\omega_1)t} + {E_3}^{*2} E_2 e^{i(2\omega_3-\omega_2)t} + \\ {E_3}^{*2} {E_2}^* e^{i(2\omega_3+\omega_2)t} + {E_3}^{*2} E_3 e^{i(\omega_3)t} + {E_3}^{*3} e^{i(3\omega_3)t} \end{pmatrix}$$

APPENDIX G

PHASE CONJUGATE FOUR-WAVE MIXING DATA

The data in the following table represents the data used to plot figures 6.5-6.7 from chapter six. The figures have been reproduced here for convenience.

It should be noted in the table of data that the yellow highlighted numbers represent regions where the photon steady-state numbers for the two lasers have settled to different numbers, and the turquoise highlighted numbers represent regions where the photon numbers never settle at all.

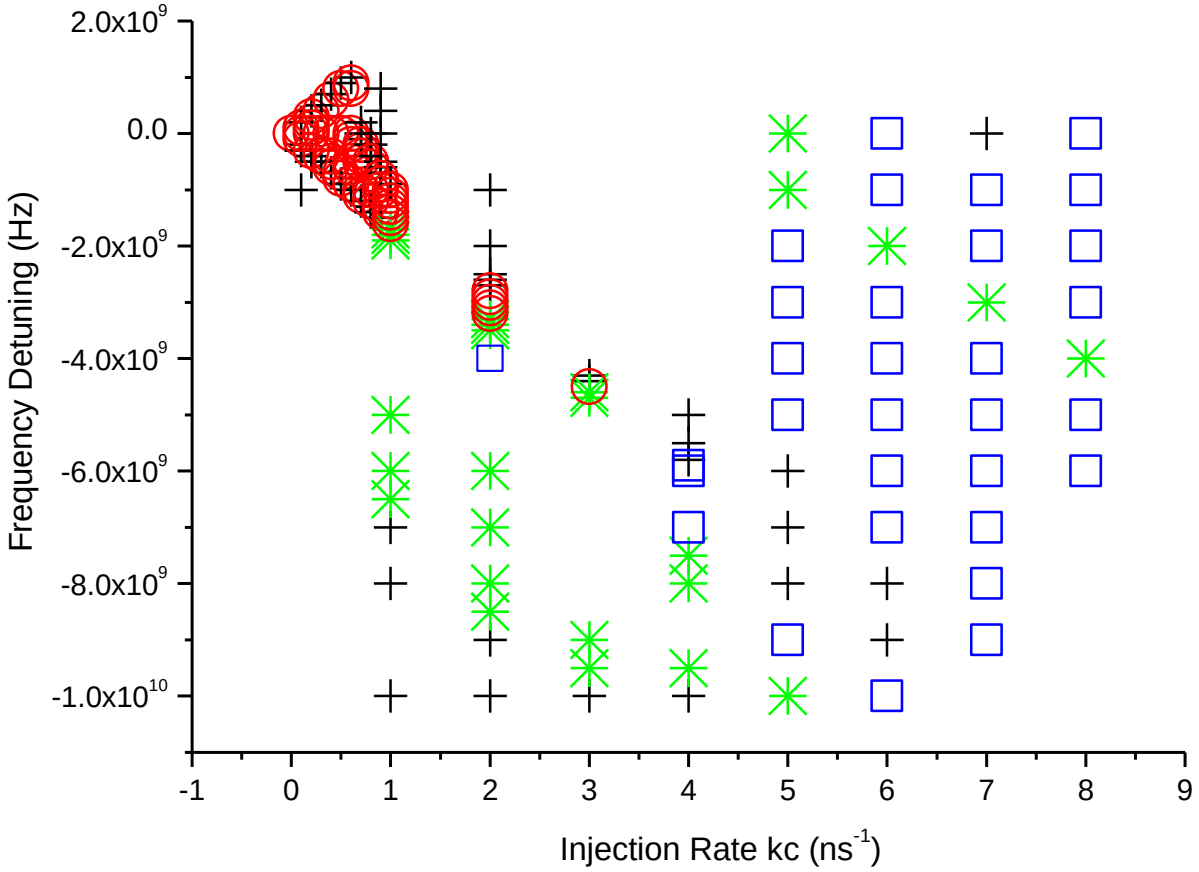

Figure 6.6: *Behavioural plot for the case of bidirectional phase conjugate injection, with frequency detuning values of -10GHz to 1GHz and injection rates of 0.1ns^{-1} to 8ns^{-1}.*

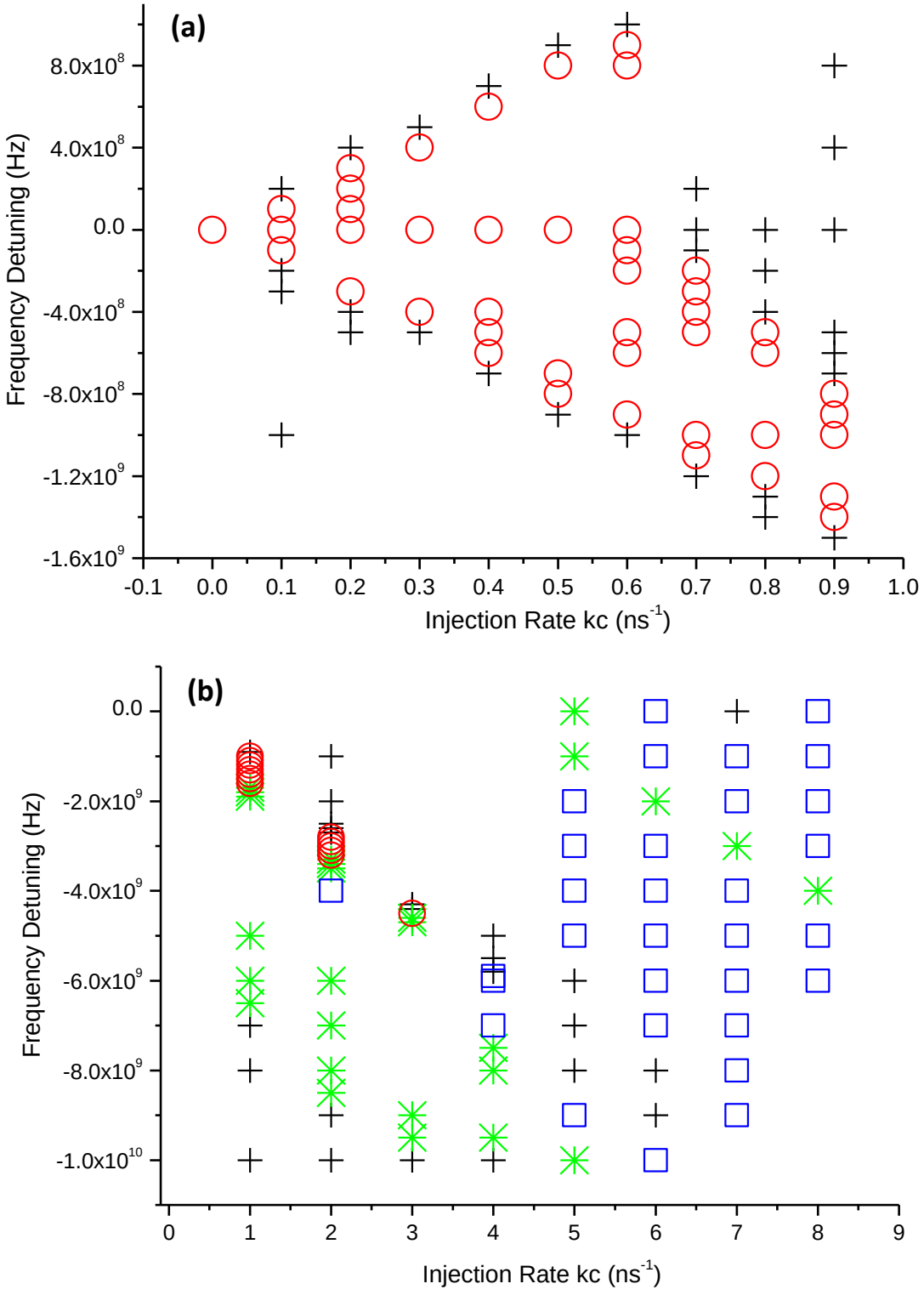

Figure 6.7: *Behavioural plot for the case of bidirectional phase conjugate injection, with frequency detuning values of -1.6GHz to 1GHz and injection rates of 0.1ns^{-1} to 0.9ns^{-1} (figure (a), and the behavioural plot for the case of bidirectional phase conjugate injection, with frequency detuning values of 0GHz to -10GHz and injection rates of 1.0ns^{-1} to 8.0ns^{-1} figure (b).*

$\kappa_c = 0.1ns^{-1}$				
Frequency Detuning, Δf	**Locked / Periodic / Chaos**	**Frequency of Oscillations**	**Photon Number**	
			First Laser	**Second Laser**
0GHz	Locked	Flat Response	440923.595783275	440923.595793274
-100MHz	Locked	Flat Response	441030.339459268	441030.335557557
-200MHz	Periodic	Humps @ ≈116MHz	441075.293401573	441075.294377275
-300MHz	Periodic	Humps @ ≈251MHz	440703.045422488	440703.050175485
-1GHz	Periodic	≈0.99GHz	441130.581953780	441130.576849877
+100MHz	Locked	Flat Response	440801.105715029	440801.111036857
+200MHz	Periodic	-Humps @ ≈117MHz	440723.138538666	440723.134823715
$\kappa_c = 0.2ns^{-1}$				
Frequency Detuning, Δf	**Locked / Periodic / Chaos**	**Frequency of Oscillations**	**Photon Number**	
			First Laser	**Second Laser**
0GHz	Locked	Flat Response	440960.805395599	440960.805395599
-300MHz	Locked	Flat Response	441258.908137543	441258.901221456
-400MHz	Periodic	Humps @ ≈233.17MHz	441217.150607039	441216.968994206
-500MHz	Periodic	Humps @ ≈381.15MHz	440465.784732537	440465.803512679
+100MHz	Locked	Flat Response	440842.573103232	440842.584940901
+200MHz	Locked	Flat Response	440715.844769744	440715.866054116
+300MHz	Locked	Flat Response	440571.209564675	440571.229425082
+400MHz	Periodic	-Humps @ ≈232.9MHz	440537.591930112	440537.578811231
$\kappa_c = 0.3ns^{-1}$				
Frequency Detuning, Δf	**Locked / Periodic / Chaos**	**Frequency of Oscillations**	**Photon Number**	
			First Laser	**Second Laser**
0GHz	Locked	Flat Response	440998.020849008	440998.020847222
-400MHz	Locked	Flat Response	441409.021621136	441408.993127488
-500MHz	Periodic	Humps @ ≈113.30MHz	441275.412611023	441275.371681024
+400MHz	Locked	Flat Response	440491.931468393	440491.982934864
+500MHz	Periodic	-Humps @ ≈114MHz	440491.643523376	440491.696379514
$\kappa_c = 0.4ns^{-1}$				
Frequency Detuning, Δf	**Locked / Periodic / Chaos**	**Frequency of Oscillations**	**Photon Number**	
			First Laser	**Second Laser**
0GHz	Locked	Flat Response	441035.242139604	441035.242139774
-400MHz	Locked	Flat Response	441462.729934390	441462.667742997
-500MHz	Locked	Flat Response	441555.281226519	441555.224606659
-600MHz	Locked	Flat Response	441632.016889355	441631.989202429
-700MHz	Periodic	Humps @ ≈260.9MHz	441548.892515437	441548.800708825

+600MHz	Locked	Flat Response	440256.425939057	440256.505332003
+700MHz	Periodic	Humps @ ≈261.6MHz	440157.321760314	440157.364481967
$\kappa_c = 0.5ns^{-1}$				
Frequency Detuning, Δf	**Locked / Periodic / Chaos**	**Frequency of Oscillations**	**Photon Number**	
			First Laser	**Second Laser**
0GHz	Locked	Flat Response	441072.469274211	441072.469273955
-700MHz	Locked	Flat Response	441784.434818382	441784.366503844
-800MHz	Locked	Flat Response	441836.339390776	441836.346219004
-900MHz	Periodic	Humps @ ≈388MHz	441209.385108057	441209.519974165
+800MHz	Locked	Flat Response	440002.445268652	440002.530473161
+900MHz	Periodic	-Humps @ ≈388MHz	440923.687708762	440923.538819890
$\kappa_c = 0.6ns^{-1}$				
Frequency Detuning, Δf	**Locked / Periodic / Chaos**	**Frequency of Oscillations**	**Photon Number**	
			First Laser	**Second Laser**
0GHz	Locked	Flat Response	441109.702252894	441109.702252894
-100MHz	Locked	Flat Response	441223.273853041	441223.239675031
-200MHz	Locked	Flat Response	441334.495953383	441334.430148657
-500MHz	Locked	Flat Response	441652.234157844	441652.101527022
-600MHz	Locked	Flat Response	441751.447854223	441751.307844675
-900MHz	Locked	Flat Response	442005.719659249	442005.657318380
-1GHz	Periodic	Humps @ ≈226.2MHz	442014.434543121	442014.485924238
+800GHz	Locked	Flat Response	440098.075137201	440098.280845125
+900MHz	Locked	Flat Response	439942.040332974	439942.218857937
+1GHz	Periodic	-Humps @ ≈227MHz	443111.499042271	443111.748919823
$\kappa_c = 0.7ns^{-1}$				
Frequency Detuning, Δf	**Locked / Periodic / Chaos**	**Frequency of Oscillations**	**Photon Number**	
			First Laser	**Second Laser**
0GHz	Periodic	≈9.20GHz	441146.931349270	441146.931736886
-100MHz	Periodic	≈9.16GHz	441260.702946614	441260.662892059
-200MHz	Locked	Flat Response	441372.468854339	441372.391129534
-300MHz	Locked	Flat Response	441482.160515715	441482.048508087
-400MHz	Locked	Flat Response	441589.639107469	441589.497291982
-500MHz	Locked	Flat Response	441694.685387662	441694.519437574
-1GHz	Locked	Flat Response	442159.470744171	442159.348287924
-1.1GHz	Locked	Flat Response	442215.899941379	442215.864406875
-1.2GHz	Periodic	Humps @ ≈383.3MHz	442202.997604523	442202.937125546
+200MHz	Periodic	≈9.17GHz	440792.933214919	440793.099218053

$\kappa_c = 0.8ns^{-1}$				
Frequency Detuning, Δf	**Locked / Periodic / Chaos**	**Frequency of Oscillations**	**Photon Number**	
			First Laser	**Second Laser**
0GHz	Periodic	≈9.18GHz	517505.574024363	517581.754280594
-200MHz	Periodic	≈9.13GHz	394720.754219669	394226.296371964
-400MHz	Periodic	≈9.18GHz	441623.183195356	441622.993925818
-500MHz	Locked	Flat Response	441736.559215366	441734.578803523
-600MHz	Locked	Flat Response	441840.951472767	441838.719088978
-1GHz	Locked	Flat Response	442226.116654729	442225.889879318
-1.2GHz	Locked	Flat Response	442380.017848605	442379.906939746
-1.3GHz	Periodic	Humps @ ≈631.7MHz	442385.145265983	442385.253888598
-1.4GHz	Periodic	Humps @ ≈518.7MHz	441853.064800596	441851.585147334
$\kappa_c = 0.9ns^{-1}$				
Frequency Detuning, Δf	**Locked / Periodic / Chaos**	**Frequency of Oscillations**	**Photon Number**	
			First Laser	**Second Laser**
0GHz	Periodic	≈9.26GHz	353596.403207046	352251.719786034
-500MHz	Periodic	≈8.95GHz	493117.012063605	493058.937965698
-600MHz	Periodic	≈9.17GHz	429610.277788893	428860.591836773
-700MHz	Periodic	≈9.14GHz	441986.424805567	441983.539994253
-800MHz	Locked	Flat Response	442087.890901555	442084.824312943
-900MHz	Locked	Flat Response	442186.631092822	442183.478225560
-1GHz	Locked	Flat Response	442282.098645673	442278.976625581
-1.3GHz	Locked	Flat Response	442534.695126583	442534.504398715
-1.4GHz	Locked	Flat Response	442592.506994892	442592.437751190
-1.5GHz	Periodic	Humps @ ≈338.1MHz	442116.973115757	442117.452696923
+400MHz	Periodic	≈9.10GHz	559714.751801424	559602.887534476
+800MHz	Periodic	≈9.18GHz	448753.238392759	448977.688152818
$\kappa_c = 1.0ns^{-1}$				
Frequency Detuning, Δf	**Locked / Periodic / Chaos**	**Frequency of Oscillations**	**Photon Number**	
			First Laser	**Second Laser**
-900MHz	Periodic	≈9.16GHz	442502.242075868	442502.119360925
-1GHz	Locked	Flat Response	442329.984938244	442329.595585347
-1.1GHz	Locked	Flat Response	442425.711337362	442425.324659741
-1.2GHz	Locked	Flat Response	442517.859084684	442517.489447237
-1.3GHz	Locked	Flat Response	442605.303276375	442604.969022503
-1.4GHz	Locked	Flat Response	442685.953653698	442685.679916576
-1.5GHz	Locked	Flat Response	442754.912861550	442754.739439168
-1.6GHz	Locked	Flat Response	442790.093345149	442790.120708859

-1.7GHz	Periodic	Humps @ ≈449.7MHz	444436.361919420	44434.9079478010
-1.8GHz	Periodic	Humps @ ≈771MHz	443272.388219583	443272.878596207
-1.9GHz	Periodic	Humps @ ≈1.83GHz	438451.538487353	438450.962122649
-5GHz	Periodic	≈4.67GHz	N/A	N/A
-6GHz	Periodic	≈5.70GHz	N/A	N/A
-6.5GHz	Periodic	≈6.16GHz	N/A	N/A
-7GHz	Periodic	≈6.6GHz	N/A	N/A
-8GHz	Periodic	≈7.5GHz	N/A	N/A
-10GHz	Periodic	≈12.45GHz	N/A	N/A
$\kappa_c = 2.0ns^{-1}$				
Frequency Detuning, Δf	**Locked / Periodic / Chaos**	**Frequency of Oscillations**	**Photon Number**	
			First Laser	**Second Laser**
-1GHz	Periodic	≈9.04GHz	599193.397757902	599283.789106598
-2GHz	Periodic	≈9.34GHz	380478.783473364	380263.578631839
-2.5GHz	Periodic	≈9.27GHz	398086.918649935	398067.205135623
-2.6GHz	Periodic	≈9.30GHz	455568.033144978	455692.276718741
-2.7GHz	Periodic	≈9.25GHz	429297.026667805	429241.730456609
-2.8GHz	Locked	Flat Response	444499.498658601	444498.349849733
-2.9GHz	Locked	Flat Response	444573.000621988	444572.076737470
-3GHz	Locked	Flat Response	444638.389756019	444637.693531404
-3.1GHz	Locked	Flat Response	444690.186314767	444689.800638701
-3.2GHz	Locked	Flat Response	444709.112753571	444709.222619563
-3.3GHz	Periodic	Humps @ ≈733.2MHz	450470.696461817	450509.833044999
-3.4GHz	Periodic	Humps @ ≈1.19GHz	437349.493329829	437316.366768604
-3.5GHz	Periodic	Humps @ ≈1.48GHz	439464.836902127	439461.157751783
-4GHz	Chaos	Unmeasurable	N/A	N/A
-6GHz	Periodic	≈5.05GHz	N/A	N/A
-7GHz	Periodic	≈5.80GHz	N/A	N/A
-8GHz	Periodic	≈6.71GHz	N/A	N/A
-8.5GHz	Periodic	≈7.15GHz	N/A	N/A
-9GHz	Periodic	≈7.57GHz	N/A	N/A
-10GHz	Periodic	≈11.12GHz	N/A	N/A
$\kappa_c = 3.0ns^{-1}$				
Frequency Detuning, Δf	**Locked / Periodic / Chaos**	**Frequency of Oscillations**	**Photon Number**	
			First Laser	**Second Laser**
-4.3GHz	Periodic	≈9.19GHz	N/A	N/A
-4.4GHz	Periodic	≈4.75GHz	N/A	N/A
-4.5GHz	Locked	Flat Response	446537.000506435	446535.428239901
-4.6GHz	Periodic	≈4.70GHz	N/A	N/A

-4.7GHz	Periodic	≈4.78GHz	N/A	N/A
-9GHz	Periodic	≈6.70GHz	N/A	N/A
-9.5GHz	Periodic	≈7.09GHz	N/A	N/A
-10GHz	Periodic	≈7.80GHz	N/A	N/A
$\kappa_c = 4.0ns^{-1}$				
Frequency Detuning, Δf	**Locked / Periodic / Chaos**	**Frequency of Oscillations**	**Photon Number**	
			First Laser	**Second Laser**
-5GHz	Periodic	≈9.22GHz	N/A	N/A
-5.5GHz	Periodic	≈9.42GHz	N/A	N/A
-5.8GHz	Periodic	≈9.26GHz	N/A	N/A
-5.9GHz	Chaos	Unmeasurable	N/A	N/A
-6GHz	Chaos	Unmeasurable	N/A	N/A
-7GHz	Chaos	Unmeasurable	N/A	N/A
-7.5GHz	Periodic	≈5.10GHz	N/A	N/A
-8GHz	Periodic	≈5.42GHz	N/A	N/A
-9.5GHz	Periodic	≈6.41GHz	N/A	N/A
-10GHz	Periodic	≈12.45GHz	N/A	N/A
$\kappa_c = 5.0ns^{-1}$				
Frequency Detuning, Δf	**Locked / Periodic / Chaos**	**Frequency of Oscillations**	**Photon Number**	
			First Laser	**Second Laser**
0GHz	Periodic	≈3.11GHz	N/A	N/A
-1GHz	Periodic	≈3.3GHz	N/A	N/A
-2GHz	Chaos	Unmeasurable	N/A	N/A
-3GHz	Chaos	Unmeasurable	N/A	N/A
-4GHz	Chaos	Unmeasurable	N/A	N/A
-5GHz	Chaos	Unmeasurable	N/A	N/A
-6GHz	Periodic	≈9.24GHz	N/A	N/A
-7GHz	Periodic	≈9.20GHz	N/A	N/A
-8GHz	Periodic	≈8.99GHz	N/A	N/A
-9GHz	Chaos	Unmeasurable	N/A	N/A
-10GHz	Periodic	≈3.34GHz	N/A	N/A
$\kappa_c = 6.0ns^{-1}$				
Frequency Detuning, Δf	**Locked / Periodic / Chaos**	**Frequency of Oscillations**	**Photon Number**	
			First Laser	**Second Laser**
0GHz	Chaos	Unmeasurable	N/A	N/A
-1GHz	Chaos	Unmeasurable	N/A	N/A
-2GHz	Periodic	≈4.43GHz	N/A	N/A
-3GHz	Chaos	Unmeasurable	N/A	N/A

-4GHz	Chaos	Unmeasurable	N/A	N/A
-5GHz	Chaos	Unmeasurable	N/A	N/A
-6GHz	Chaos	Unmeasurable	N/A	N/A
-7GHz	Chaos	Unmeasurable	N/A	N/A
-8GHz	Periodic	≈9.17GHz	N/A	N/A
-9GHz	Periodic	≈9.34GHz	N/A	N/A
-10GHz	Chaos	Unmeasurable	N/A	N/A
$\kappa_c = 7.0ns^{-1}$				
Frequency Detuning, Δf	**Locked / Periodic / Chaos**	**Frequency of Oscillations**	**Photon Number**	
			First Laser	**Second Laser**
0GHz	Periodic	≈8.71GHz	N/A	N/A
-1GHz	Chaos	Unmeasurable	N/A	N/A
-2GHz	Chaos	Unmeasurable	N/A	N/A
-3GHz	Periodic	≈8.65GHz	N/A	N/A
-4GHz	Chaos	Unmeasurable	N/A	N/A
-5GHz	Chaos	Unmeasurable	N/A	N/A
-6GHz	Chaos	Unmeasurable	N/A	N/A
-7GHz	Chaos	Unmeasurable	N/A	N/A
-8GHz	Chaos	Unmeasurable	N/A	N/A
-9GHz	Chaos	Unmeasurable	N/A	N/A
-10GHz	Periodic	≈9.25GHz	N/A	N/A
$\kappa_c = 8.0ns^{-1}$				
Frequency Detuning, Δf	**Locked / Periodic / Chaos**	**Frequency of Oscillations**	**Photon Number**	
			First Laser	**Second Laser**
0GHz	Chaos	Unmeasurable	N/A	N/A
-1GHz	Chaos	Unmeasurable	N/A	N/A
-2GHz	Chaos	Unmeasurable	N/A	N/A
-3GHz	Chaos	Unmeasurable	N/A	N/A
-4GHz	Periodic	≈8.63GHz	N/A	N/A
-5GHz	Chaos	Unmeasurable	N/A	N/A
-6GHz	Chaos	Unmeasurable	N/A	N/A